

A mechanistic approach to assessment
of the geochemical evolution of
low sulfide mine-waste rock

by

David Wilson

A thesis
presented to the University of Waterloo
in fulfillment of the
thesis requirement for the degree of
Doctor of Philosophy
in
Earth and Environmental Sciences

Waterloo, Ontario, Canada, 2018

©David Wilson 2018

Examining committee membership

The following served on the Examining Committee for this thesis. The decision of the Examining Committee is by majority vote.

External Examiner

Dr. Rene Lefebvre

Professor

Supervisors

Dr. David Blowes

Professor

Dr. Richard Amos

Assistant Professor

Internal Members

Dr. Carol Ptacek

Professor

Dr. Edward Sudicky

Adjunct Professor

Internal-external Member

Dr. Marek Stastna

Professor

Author's Declaration

This thesis consists of material all of which I authored or co-authored: see Statement of Contributions included in the thesis. This is a true copy of the thesis, including any required final revisions, as accepted by my examiners.

I understand that my thesis may be made electronically available to the public.

Statement of contributions

This thesis consists of a series of co-authored papers. As first author on each paper I was primarily responsible for development and implementation of the modelling approaches, data interpretation, and paper writing. The following summarizes the contributions of co-authors.

Chapter 1: This chapter was written solely by David Wilson

Chapter 2: The conceptual model was developed primarily by David Wilson with input from Richard Amos, David Blowes, and Jeff Langman. David Wilson implemented the conceptual model with the reactive transport code MIN3P, analyzed the results and wrote the paper. All other authors provided feedback on the paper.

Chapter 3: The design and implementation of the modelling approach were completed by David Wilson with input from Richard Amos and David Blowes. David Wilson interpreted the results and wrote the paper with feedback from Richard Amos and David Blowes. All other authors provided feedback on the paper.

Chapter 4: The design and implementation of the modelling approach were completed by David Wilson with input from Richard Amos and David Blowes. David Wilson interpreted the results and wrote the paper with feedback from Richard Amos and David Blowes. All other authors provided feedback on the paper.

Chapter 5: The sample collection programs were designed by Colleen Atherton and Lianna Smith and conducted by Colleen Atherton, David Wilson, Lianna Smith, and David Barsi with assistance from many others. The geostatistical analysis process was designed and conducted by David Wilson with feedback from David Blowes, Leslie Smith, and Richard Amos. David Wilson wrote the paper with feedback from David Blowes, Richard Amos, and Leslie Smith.

Chapter 6: Modeling approach and implementation were designed by David Wilson with input from David Blowes and Richard Amos. David Wilson conducted the simulations with assistance on parallel computing from Danyang Su. David Wilson interpreted the results and wrote the paper with feedback from Richard Amos and David Blowes.

Chapter 7: This chapter was written solely by David Wilson.

Abstract

The potential for mine wastes to generate elevated concentrations of solutes including metals, sulfate, and reduced pH exists wherever mine-waste rock is stockpiled at the Earth's surface representing one of the world's largest environmental problems. The assessment of the long-term geochemical evolution of mine wastes is of critical importance in the process of mine-life planning because of the potential for adverse impacts of released solutes and low pH effluent to receiving environments. The Diavik Waste Rock Project included laboratory and field experiments investigating the geochemical evolution of low-sulfide mine-waste rock at different scales. The experiments included small-scale humidity cells (0.1 m high; laboratory), medium-scale lysimeters (2 m high; field), and large-scale test piles (15 m high; field) to facilitate development of a mechanistic approach to scaling results of the laboratory experiments to make assessments regarding the geochemical evolution at the larger field experiments. This process, generally referred to scale-up, often involves the use of humidity cell experiment results coupled with empirical scale factors to make predictions about the long term geochemistry of effluent released from mine-waste stockpiles. The empirical factors used typically include parameters known to influence rates of sulfide oxidation including mineral content, particle-size distribution, temperature, moisture content, and oxygen availability. These scale-up factors often fail to account for site specific heterogeneities in physical and chemical properties that can strongly influence the prediction process. Mechanistic approaches (*i.e.*, the use of geochemical models including reactive transport models) have the potential to include complex heterogeneities that facilitate a quantitative assessment of the long-term geochemical evolution of mine wastes.

A conceptual model of the geochemical evolution of low-sulfide waste rock was developed to facilitate numerical simulations of the small-scale experiments and then was used to simulate the geochemical evolution in the larger scale field experiments. The conceptual model, based on oxidation of sulfide minerals coupled with the geochemical weathering of host minerals present in waste rock produced at the Diavik Diamond Mine (NT, Canada), was implemented using the reactive transport code MIN3P. The 1-D model was calibrated to capture the effluent concentrations from the laboratory-scale experiments then used to simulate the geochemical evolution at the larger scale field experiments, without further calibration, to assess the efficacy of the mechanistic scale-up approach. Geostatistical analyses of mineralogical and particle-size distribution samples were conducted to assess the heterogeneity of S, C, and saturated hydraulic conductivity. The results of the geostatistical

analyses were used to inform spatial distributions of S, C, and saturated hydraulic conductivity as input to reactive transport simulations of the large-scale field experiment. The 2-D simulations were conducted to assess the influence of heterogeneity in S, C, and saturated hydraulic conductivity on the geochemical evolution of the waste rock.

The results of the humidity cell simulations indicate that the conceptual model represents the primary geochemical processes of the low-sulfide waste rock weathering. The simulated effluent concentrations compares well with the measured solute concentrations from the humidity cells, although some divergence for specific parameters was observed. Mineral surface area, mineral content, temperature, and pH were identified as important factors controlling the geochemical evolution of the waste rock. The results of the model developed and calibrated at the humidity-cell scale suggested that the conceptual model could be representative of the DWRP waste rock weathering in general and the implemented model could be used to simulate waste rock weathering for the field scale experiments.

The implementation of the conceptual model at the medium-scale field experiments involved inclusion of measured temporally dynamic temperature and infiltration to better represent the physical conditions at the field experiments. Implementation at the large-scale test pile experiments included providing spatially dynamic temperature. Inclusion of these parameters as model input facilitated completion of multi-year simulations essential to making long-term assessments of the geochemical evolution of waste rock. Scaling the humidity cell conceptual model to simulate the geochemical evolution at the field-experiment scales resulted in good visual agreement between measured and simulated concentrations and mass flux of most parameters. The pH was generally over estimated in the medium- and large-scale field simulations. Supplemental simulations indicate that calcite availability was lower for the field experiments (approximately 20% of measured content).

The field experiment simulations did not rely on geochemical data for calibration; however, these simulations did rely on site-specific physical data, including mineralogy-related parameters such as volume fraction, hydrology-related parameters including hydraulic conductivity, grain-size distribution, porosity, and water-retention curve values, and environmental parameters including temperature, precipitation, and O₂ concentration (the field systems were not O₂ limited); to facilitate an assessment of the geochemical evolution of waste rock. The reactive transport simulations demonstrated that a comprehensive, integrated conceptual model representing the geochemical

evolution of low-sulfide waste rock, implemented and calibrated at the humidity-cell scale can be applied to field-scale experiments using a small number of measurable parameters to constrain the simulations. Parameters should include mineral content, bulk mineral surface area, and particle-size distribution, water flow and infiltration characteristics as well as general climatic conditions (specifically temperature and precipitation). The reliance on readily available, measurable parameters suggests that this approach could be implemented at other sites using the appropriate site specific parameters. This mechanistic approach provides the basis for predictive scale-up.

Consideration of the influence of temperature on the geochemical reactions was a major factor facilitating the scale-up of the model. The humidity cell experiments were conducted at temperatures 5 °C and 22 °C to allow calibration for the influence of temperature, which was a critical component in the scale-up process because of the varied temperatures at which surface-stored waste rock is exposed. Measurement of temperature at the field scale would be an important component of any scale-up program.

The results of the geostatistical analyses indicate the spatial distributions of S, C, and saturated hydraulic conductivity in the test-pile experiments could be approximated using a log normal distribution with mean and standard deviation calculated from samples collected during test pile construction for each parameter. A lack of spatial dependence for matrix hydraulic conductivity was significant because the matrix material exerted strong control over the flow of water through the test-pile experiments. The spatial distributions of S, C, and saturated hydraulic conductivity in the test piles experiments provides a foundation from which full-scale waste-rock piles could be characterized using the geostatistical methods described. The spatial dependence of saturated hydraulic conductivity in larger piles may also depend on the influence of features which were not present in the test-pile experiments (*e.g.*, traffic surfaces).

The investigation of the influence of mineralogical and physical heterogeneity on the geochemical evolution in the Type III test-pile suggested that heterogeneous distributions of S and C mineralogy and saturated hydraulic conductivity field resulted in variations of effluent concentrations that were at times, consistent with the measured variation. Analysis of the results of the heterogeneous simulations indicate that the distribution of solute mass fluxes from the test-pile experiment for most parameters could be best approximated with a log normal probability density function.

Acknowledgements

The Diavik Waste Rock Project is a joint research project by the University of Waterloo, the University of British Columbia, and the University of Alberta. Funding for this research was provided by: Diavik Diamond Mines Inc.; a grant from the Natural Science and Engineering Research Council of Canada Collaborative Research and Development program awarded to David Blowes, Principal Investigator; an award from the Canadian Foundation for Innovation Fund awarded to James Barker, Principal Investigator; the Mine Environment Neutral Drainage Program; the International Network for Acid Prevention; the Northern Scientific Training Program; and the Ontario Graduate Scholarship program.

Throughout the course of this project, I was fortunate to work with many interesting and entertaining people who all helped me in large and/or small ways to complete the research documented in this thesis.

I would first like to acknowledge the mentorship and leadership I received from both of my supervisors, Dr. David Blowes and Dr. Richard Amos. Thanks to many meetings and conversations with Dave and Rich I have received valuable training and advice that stretched well beyond Earth Science and will be with me for many years. I would also like to thank Dr. Leslie Smith, Dr. David Segó, Dr. Ed Sudicky, Dr. Marek Stastna, and Dr. Rene Lefebvre for their contributions to the project in general and specifically their timely constructive criticism of my research.

Because of the immense scope of this project, a good portion of the data used in this thesis was collected by others before I even started and it is this work by previous researchers (some of whom I have not met) that made this thesis possible. I would like to thank all of the previous graduate students including Lianna Smith, Steve Momeyer, Mike Gupton, Brenda Bailey, Sheldon Chi, Ashley Stanton, Mandy Moore, Stacey Hannam, Sivaram Mullapudi, Matt Neuner, Nathan Fretz, Andrew Krentz, Jordan Zak, Laurier Collette, Renata Klassen, Nam Pham, David Barsi, and Hilary Smith for their contributions. I would also like to thank current and former GGR staff Jeff Bain, Mike Moncur, Laura Groza, Joy Hu, Julia Jamieson-Hanes, Matt Lindsay and the hordes of co-op students who were all instrumental in this research. This project would not have been possible without the ongoing support from personnel at Diavik Diamond Mines; thank you to Gord Macdonald, David Wells,

Darcy Bourassa, Dianne Dul, Justin Grandjambe, Kyla Gray, Dan Guigon, Steve Pinter, and Dave Mohler for your help over the years.

I would especially like to thank fellow test-pilers Sean Sinclair, Colleen Atherton, and Steve Holland for all of the ‘problem solving’ sessions and for never allowing things to get too serious. Thank you to Jeff Langman for his optimism during the early stages and thank you to Danyang Su for his knowledge and patience during the high performance computing stages of my thesis.

Most importantly, I would like to express sincere gratitude to the ones who set me on, and kept me on, this path: Dr. Carol Ptacek for suggesting this outrageous thing be attempted; Reed and Donella Wilson for enthusiastically encouraging acceptance of that outrageous suggestion; and, most of all, Katherine Appleby for her patience and mettle in supporting the subsequent five years of outrageous husband behaviour.

Dedication

This thesis is dedicated to Donella Wilson.

She said 'David, you have to do this'; as always, she was right.

Table of Contents

Examining committee membership	ii
Author's Declaration.....	iii
Statement of contributions	iv
Abstract.....	vi
Acknowledgements.....	ix
Dedication.....	xi
Table of Contents.....	xii
List of Figures.....	xv
List of Tables	xxii
Chapter 1 Introduction	1
1.1 Diavik Waste Rock Project.....	2
1.2 Geochemical Evolution of Sulfidic Waste Rock	8
1.3 Concept of scale-up.....	10
1.4 Heterogeneity.....	12
1.5 Reactive Transport Modelling	14
1.6 Thesis Structure	16
Chapter 2 A conceptual model for temperature and sulfide content dependent geochemical evolution of waste rock – Laboratory scale	19
2.1 Humidity Cell Methodology.....	20
2.2 Conceptual Model.....	22
2.3 Model Parameters	28
2.4 Results.....	32
2.5 Discussion.....	38
2.5.1 Mineral Volume Fraction.....	39
2.5.2 Temperature	40
2.5.3 Sulfide Oxidation Mechanism and Rate	42
2.5.4 Acid Neutralization.....	43
2.6 Conclusions.....	45
Chapter 3 Scale-up of a reactive transport model for temperature and sulfide-content dependent geochemical evolution of waste rock.....	46

3.1 Active Zone Lysimeter Methodology.....	48
3.2 Conceptual Model	51
3.3 Model Parameters.....	59
3.4 Results	62
3.5 Discussion	74
3.5.1 Temperature.....	77
3.5.2 Infiltration.....	77
3.5.3 Mineral Volume Fraction	78
3.5.4 Secondary Mineral Control	78
3.5.5 Acid Neutralization	79
3.6 Conclusions	80
Chapter 4 Simulation of the geochemical evolution of large test piles using a scaled temperature and sulfide content dependent reactive transport conceptual model.....	82
4.1 Test Pile Methodology	85
4.2 Conceptual Model	86
4.3 Model Parameters.....	94
4.4 Results	98
4.5 Discussion	111
4.5.1 Temperature.....	113
4.5.2 Infiltration.....	114
4.5.3 Mineral Volume Fraction	114
4.5.4 Secondary Mineral Control	115
4.5.5 Acid Neutralization	116
4.6 Conclusions	119
Chapter 5 Geostatistical analysis of sulfur, carbon, and hydraulic conductivity distribution in a mine waste-rock test pile.....	120
5.1 Methodology	121
5.2 Results	123
5.2.1 Calculation of Hydraulic Conductivity.....	123
5.2.2 Statistical Distribution.....	124
5.2.3 Stationarity	127

5.2.4 Experimental Semi-variogram Estimation.....	128
5.2.5 Theoretical Semi-variogram Fitting.....	130
5.3 Discussion.....	132
5.3.1 Statistical Comparison of Construction Samples.....	133
5.3.2 Theoretical Semi-variogram Fitting.....	133
5.4 Conclusions.....	135
Chapter 6 Influence of heterogeneity in S, C, and hydraulic conductivity on the geochemical evolution of large-scale test piles using reactive transport simulations.....	137
6.1 Simulation Methodology.....	140
6.2 Conceptual Model.....	143
6.3 Model Parameters.....	149
6.4 Results.....	153
6.5 Discussion.....	159
6.5.1 Temperature.....	160
6.5.2 Influence of Heterogeneous S and C Distribution.....	160
6.5.3 Influence of Heterogeneous Hydraulic Conductivity Distribution.....	166
6.5.4 Variability of Effluent Geochemistry.....	169
6.6 Conclusions.....	172
Chapter 7 Conclusions.....	174
7.1 Overview of Research.....	174
7.2 Summary of Major Findings.....	175
7.3 Future Work.....	179
7.3.1 Temperature.....	179
7.3.2 Heterogeneity.....	180
7.3.3 Other sites.....	180
Bibliography.....	182

List of Figures

Figure 1.1 Location of Diavik Diamond Mine (from Smith et al., 2013a).....	2
Figure 1.2 Cold temperature humidity cell experiment configuration.	3
Figure 1.3 A: Cross-sectional conceptual diagram of DWRP active zone lysimeter experiment. B: Active zone lysimeter experiment prior to emplacement of run-of-mine rock.	4
Figure 1.4 Typical tipping bucket and sample cell configuration at test pile instrumentation trailers. .	5
Figure 1.5 Overview of Test Piles Research Area at Diavik.....	6
Figure 1.6 A: Main drainage network and liner at the base of the Type III test pile. B: Basal collection lysimeter drainage network at the base of the Type III test pile (adapted from Smith et al., 2013a).....	7
Figure 1.7 A: Conceptual cross-section of DWRP Type III test pile experiment indicating approximate location of basal collection lysimeters. B: Construction of basal collection lysimeters prior to run-of-mine material placement at Type III test pile.....	7
Figure 1.8 Conceptual illustration of the internal structure of a waste-rock pile constructed in two benches with horizontal stratification in the core of the pile, sloped stratification near the edges, and larger boulders congregated near the bottoms of the benches (adapted from Anterrieu et al., 2010). .	12
Figure 2.1 Average concentrations of mineral weathering products SO_4 , Ni, Co, Cu, Zn, Fe, Al, Ca, Mg, K, Na, and H_4SiO_4 [mol L^{-1}], pH [-], and alkalinity [as $\text{mg L}^{-1} \text{CaCO}_3$] versus time [weeks] measured in the two Type III warm temperature humidity cell effluent compared to aqueous concentrations exiting the simulation domain.	34
Figure 2.2 Average concentrations of mineral weathering products SO_4 , Ni, Co, Cu, Zn, Fe, Al, Ca, Mg, K, Na, and H_4SiO_4 [mol L^{-1}], pH [-], and alkalinity [as $\text{mg L}^{-1} \text{CaCO}_3$] versus time [weeks] measured in the two Type III cold temperature humidity cell effluent compared to aqueous concentrations exiting the simulation domain.	35
Figure 2.3 Average concentrations of mineral weathering products SO_4 , Ni, Co, Cu, Zn, Fe, Al, Ca, Mg, K, Na, and H_4SiO_4 [mol L^{-1}], pH [-], and alkalinity [as $\text{mg L}^{-1} \text{CaCO}_3$] versus time [weeks] measured in the six Type I warm temperature humidity cell effluent compared to aqueous concentrations exiting the simulation domain.	36
Figure 2.4 Average concentrations of mineral weathering products SO_4 , Ni, Co, Cu, Zn, Fe, Al, Ca, Mg, K, Na, and H_4SiO_4 [mol L^{-1}], pH [-], and alkalinity [as $\text{mg L}^{-1} \text{CaCO}_3$] versus time [weeks]	

measured in the six Type I cold temperature humidity cell effluent compared to aqueous concentrations exiting the simulation domain.	37
Figure 2.5 Rate of sulfide oxidation [$\text{mol m}^{-2} \text{ mineral s}^{-1}$] versus time [weeks] as estimated from measured SO_4 concentrations in Type I and Type III warm and cold temperature humidity cell effluent compared to simulation results.	38
Figure 2.6 Simulated rates of pyrrhotite oxidation [$\text{mol m}^{-2} \text{ mineral s}^{-1}$] by $\text{O}_{2(\text{aq})}$ and Fe^{3+} versus time [weeks] in Type I and Type III warm and cold humidity cell experiments.	42
Figure 2.7 Simulated rates of calcite, dolomite, biotite, and gibbsite dissolution/ precipitation [$\text{mol L}^{-1} \text{ bulk d}^{-1}$] versus time [weeks] in Type I and Type III warm and cold humidity cell experiments. Rates greater than zero indicate mineral precipitation; rates less than zero indicate mineral dissolution.	44
Figure 3.1 A: Cross-sectional conceptual diagram of DWRP active zone lysimeter experiment. B: Active zone lysimeter experiment prior to emplacement of run-of-mine rock within and surrounding containers. Active zone lysimeter containers are filled and surrounded with Type III or Type I run-of-mine material.	49
Figure 3.2 Precipitation (rain only) at the DWRP research area for the period 2008 to 2011 and average daily air temperature and average daily AZL internal temperature for the period 2009 to 2015.	51
Figure 3.3 Daily outflow [L d^{-1}] versus time [year] measured and simulated for the Type III and Type I AZLs.	64
Figure 3.4 Simulated Cl^- concentration [mmol L^{-1}] (dashed line) in Type III AZL effluent versus time [month-year] following injection on June 16, 2008 (vertical dotted line). Peak effluent tracer concentration occurred on August 25, 2008, approximately 70 days after tracer injection.	64
Figure 3.5 Cumulative annual outflow [L] and cumulative annual estimated infiltration (using FAO-Penman Monteith method) versus time [year] measured and simulated at the Type III and Type I AZLs.	64
Figure 3.6 Volumetric water content [$\text{m}^3 \text{ m}^{-3}$] versus time [year] measured and simulated at approximately 1.0 m depth at the Type III AZL. Measured values are available only for periods where $\text{AZL T} > 0^\circ\text{C}$; simulated values were calculated by the model for all periods regardless of temperature condition.	65

Figure 3.7 Concentrations of mineral weathering products SO ₄ , Fe, Ni, Co, Cu, Zn, Al, Si, Ca, Mg, K, and Na [mol L ⁻¹], pH [-], and alkalinity [as mg L ⁻¹ CaCO ₃] versus time [year] measured in Type III AZL effluent compared to aqueous concentration exiting the simulation domain. Measured concentrations are available only for periods of AZL flow and are the average of the two Type III AZL concentrations where applicable; simulated concentrations are calculated by the model for all periods regardless of flow condition.	68
Figure 3.8 Concentrations of mineral weathering products SO ₄ , Fe, Ni, Co, Cu, Zn, Al, Si, Ca, Mg, K, and Na [mol L ⁻¹], pH [-], and alkalinity [as mg L ⁻¹ CaCO ₃] versus time [year] measured in Type I AZL effluent compared to aqueous concentration exiting the simulation domain. Measured concentrations are available only for periods of AZL flow and are the average of the two Type III AZL concentrations where applicable; simulated concentrations are calculated by the model for all periods regardless of flow condition.	69
Figure 3.9 Total annual mass of mineral weathering products SO ₄ , Fe, Ni, Co, Cu, Zn, Al, Si, Ca, Mg, K, and Na [g m ⁻² yr ⁻¹] versus time [year] measured in Type III AZL effluent compared to total mass exiting the simulation domain. Predicted values are from Bailey, 2013.	70
Figure 3.10 Total annual mass of mineral weathering products SO ₄ , Fe, Ni, Co, Cu, Zn, Al, Si, Ca, Mg, K, and Na [g m ⁻² yr ⁻¹] versus time [year] measured in Type I AZL effluent compared to total mass exiting the simulation domain.	71
Figure 3.11 Daily mass flux of mineral weathering products SO ₄ , Fe, Ni, Co, Cu, Zn, Al, Si, Ca, Mg, K, and Na [g m ⁻² d ⁻¹] versus time [year] measured in Type III AZL effluent compared to daily mass flux exiting the simulation domain.	72
Figure 3.12 Daily mass flux of mineral weathering products SO ₄ , Fe, Ni, Co, Cu, Zn, Al, Si, Ca, Mg, K, and Na [g m ⁻² d ⁻¹] versus time [year] measured in Type I AZL effluent compared to daily mass flux exiting the simulation domain.	73
Figure 3.13 pH [-] versus time [year] measured in Type III AZL effluent compared to aqueous concentration exiting the simulation domain with measured calcite contribution (short dash) and decreased calcite contribution (dotted).	74
Figure 3.14 Reaction rate of pyrrhotite [mol L ⁻¹ d ⁻¹] versus versus time [year] simulated in Type III AZL compared to model temperature [°C].	77

Figure 4.1 Precipitation (rain only) at the DWRP research station and average daily air temperature at Diavik for the period 2006-2012. Note that precipitation measurements began at the research station on September 1, 2006.	83
Figure 4.2 A: Conceptual cross-section of DWRP Type III test pile experiment indicating approximate location of basal collection lysimeters (BCL). B: Construction of basal collection lysimeters prior to run-of-mine material placement at Type III test pile.	86
Figure 4.3 Interpolated simulation temperature and measured temperature [°C] at 2 m, 3 m, 5 m, 7 m, 9 m, and 12.5 m (measured from test pile crest) versus time [year]. Input temperatures for the simulations were provided for depths 0 m, 2.5 m, 4.5 m, 6.5 m, 8.5 m, 10.5 m, and 12.5 m (measured from test pile crest).	100
Figure 4.4 A: Daily outflow [L d ⁻¹] versus time [year] measured and simulated for the Type III test pile experiment. B: Measured and simulated cumulative annual outflow [L] and cumulative annual estimated infiltration (using FAO-Penman Monteith method) versus time [year] for the Type III test pile.	101
Figure 4.5 Simulated Cl ⁻ concentration [mmol L ⁻¹] (dashed line) from the Type III test pile core versus time [year] following injection on September 13, 2007 (vertical dotted line). Peak simulated tracer concentration occurred on December 31, 2012, approximately 5.3 years after tracer injection.	102
Figure 4.6 Concentrations of mineral weathering products SO ₄ , Fe, Ni, Co, Cu, Zn, Al, Si, Ca, Mg, K, and Na [mmol L ⁻¹], pH [-], and alkalinity [as mg L ⁻¹ CaCO ₃] versus time [year] measured in Type III test pile effluent compared to aqueous concentration exiting the simulation domain. Measured concentrations are available only for periods of test pile core flow; simulated concentrations are calculated by the model for all periods regardless of flow condition.	105
Figure 4.7 Total annual mass of mineral weathering products SO ₄ , Fe, Ni, Co, Cu, Zn, Al, Si, Ca, Mg, K, and Na [g m ⁻² yr ⁻¹] versus time [year] measured in Type III test pile effluent compared to total mass exiting the simulation domain.	106
Figure 4.8 Concentrations of mineral weathering products SO ₄ , Fe, Ni, Co, Cu, Zn, Al, Si, Ca, Mg, K, and Na [mmol L ⁻¹], pH [-], and alkalinity [as mg L ⁻¹ CaCO ₃] versus time [year] measured in Type III test pile effluent compared to aqueous concentration exiting the calibrated (calcite reduction to 20% of measured) simulation domain. Measured concentrations are available only for periods of test	

pile core flow; simulated concentrations are calculated by the model for all periods regardless of flow condition.	107
Figure 4.9 Total annual mass of mineral weathering products SO_4 , Fe, Ni, Co, Cu, Zn, Al, Si, Ca, Mg, K, and Na [$\text{g m}^{-2} \text{yr}^{-1}$] versus time [year] measured in Type III test pile effluent compared to total mass exiting the calibrated (calcite reduction to 20% of measured) simulation domain.	108
Figure 4.10 Average annual concentrations of mineral weathering products Al, Fe [mmol L^{-1}], pH [-], and alkalinity [as $\text{mg L}^{-1} \text{CaCO}_3$] versus depth [m] measured from test pile crest, measured in samples collected at soil water solution samplers installed in the Type III test pile compared to calibrated simulation aqueous concentration.	109
Figure 4.11 Average annual concentrations of mineral weathering products SO_4 , Ni, Cu, and Zn [mmol L^{-1}] versus depth [m], measured from test pile crest, measured in samples collected at soil water solution samplers installed in the Type III test pile compared to calibrated simulation aqueous concentration.	111
Figure 4.12 Simulated rates of calcite, gibbsite, and ferrihydrite dissolution and/or precipitation [$\text{mol L}^{-1} \text{bulk d}^{-1}$] versus time [year] in the Type III test pile. Rates greater than zero indicate mineral precipitation; rates less than zero indicate mineral dissolution. Rates of zero indicate that the test pile is frozen and reactions have stopped or that a mineral has been exhausted.	118
Figure 5.1 Location and spatial distribution of S and C measurements and saturated K estimates at the 15 m profile of the Type I test pile. (▪) indicates a sample location and the black line indicates the outline of the test pile. The linear interpolation method was used to present the data.	125
Figure 5.2 Frequency histograms for Type I deconstruction wt.% S, wt.% C, K (m s^{-1}), $\text{Ln}(S)$, $\text{Ln}(C)$, and $\text{Ln}(K)$	127
Figure 5.3 Mean and variance of $\text{Ln}(S)$, $\text{Ln}(C)$, and $\text{Ln}(K_S)$ from the deconstruction samples calculated by deconstruction bench. PSD analysis was conducted for samples from benches 1 to 5 only.	128
Figure 5.4 Horizontal and vertical experimental semi-variograms for $\text{Ln}(S)$, $\text{Ln}(C)$, and $\text{Ln}(K_S)$ using classical, Cressie-Hawkins, and SMAD estimators.	130
Figure 5.5 Theoretical semi-variogram fits to classical horizontal and vertical semi-variogram estimates for $\text{Ln}(S)$, $\text{Ln}(C)$, and $\text{Ln}(K_S)$. The pure nugget model is fit to $\text{Ln}(S)$ and $\text{Ln}(C)$ experimental semi-variograms; the Gaussian model is fit to $\text{Ln}(K_S)$ experimental semi-variograms.	132

Figure 6.1 (A): Conceptual cross-section of DWRP Type III test pile experiment indicating approximate location of basal collection lysimeters (BCL). (B): Construction of basal collection lysimeters prior to run-of-mine material placement at Type III test pile.	139
Figure 6.2 A single realization of the spatial distribution of pyrrhotite and calcite volume fractions for the Type III test pile simulation domain based on mean and standard deviation of samples collected as part of test pile construction and log normal distribution of samples collected as part of the Type I test pile deconstruction.	141
Figure 6.3 A single realization of spatial distribution of hydraulic conductivity for the Type III test pile simulation domain based on mean and standard deviation of samples collected as part of test pile construction and log normal distribution of samples collected as part of the Type I test pile deconstruction.	142
Figure 6.4 Example statistical distributions for three generated S, C, and K_S realizations (realization 1, realization 9, and realization 47) showing log normal distribution. Mean and standard deviation of measured log transformed S [wt. %], C [wt. %], and K_S ($m s^{-1}$) are -2.94 and 0.68, -3.56 and 0.32, and -11.62 and 0.88 respectively.	142
Figure 6.5 A: Measured and simulated (80 2-D simulations, homogeneous K_S) daily outflow [$L d^{-1}$] versus time [year] for the Type III test pile experiment. B: Measured and simulated (80 2-D simulations, homogeneous K_S) cumulative annual outflow [L] versus time [year] for the Type III test pile.	154
Figure 6.6 A: Measured and simulated (80 2-D simulations, heterogeneous K_S) daily outflow [$L d^{-1}$] versus time [year] for the Type III test pile experiment. B: Measured and simulated (80 2-D simulations, heterogeneous K_S) cumulative annual outflow [L] versus time [year] for the Type III test pile.	155
Figure 6.7 Concentrations of mineral weathering products SO_4 , Fe, Ni, Al, Ca [$mmol L^{-1}$] and pH [-] versus time [year] measured in Type III test pile effluent compared to aqueous concentration exiting the simulation domain. Simulated concentrations are from 1 2-D simulations (16 points along x-axis) with homogeneous hydraulic conductivity (SC_1) and heterogeneous hydraulic conductivity ($SC-K_{S1}$). Measured concentrations are available only for periods of test pile core flow; simulated concentrations are calculated by the model for all periods regardless of flow condition.	157
Figure 6.8 Concentrations of mineral weathering products SO_4 , Fe, Ni, Al, Ca [$mmol L^{-1}$] and pH [-] versus time [year] measured in Type III test pile effluent compared to aqueous concentration exiting	

the simulation domain. Simulated concentrations are from 80 2-D simulations (16 points along x-axis) with homogeneous hydraulic conductivity (SC₁₋₈₀) and heterogeneous hydraulic conductivity (SC-K_{S1-80}). Measured concentrations are available only for periods of test pile core flow; simulated concentrations are calculated by the model for all periods regardless of flow condition..... 158

Figure 6.9 Total annual mass of mineral weathering products SO₄, Fe, Ni, Al, and Ca [mmol m⁻² yr⁻¹] versus time [year] measured in Type III test pile effluent compared to simulated total mass exiting the 2-D homogeneous hydraulic conductivity (SC₁₋₈₀), 2-D heterogeneous hydraulic conductivity (SC-K_{S1-80}) and 1-D simulation domains. Circles represent the measured values from the core of the test pile, empty triangles represent 80 2-D simulation results, solid triangles represent the 1-D simulation results (Chapter 4). 159

Figure 6.10 Histograms indicating the distribution of the log-transformed daily mass flux [mmol m⁻²] from the 2-D homogeneous hydraulic conductivity simulation domain compared to the fitted normal distribution for parameters SO₄, Fe, and Ni on September 9 of each year. 162

Figure 6.11 Histograms indicating the distribution of the log-transformed annual mass flux [mmol m⁻²] from the 2-D homogeneous hydraulic conductivity simulation domain compared to the fitted normal distribution for the parameters SO₄, Fe, and Ni. 163

Figure 6.12 Residual of mean annual mass flux of mineral weathering products SO₄, Fe, Ni, Co, Cu, Zn, Al, Si, Ca, Mg, K, and Na [mmol m⁻² yr⁻¹] versus time [year] exiting the SC₁₋₈₀ and SC-K_{S1-80} simulation domains and exiting the 1-D simulation domain. 165

Figure 6.13 Residuals of mean annual mass flux of mineral weathering products SO₄, Fe, Ni, Co, Cu, Zn, Al, Si, Ca, Mg, K, and Na [mmol m⁻² yr⁻¹] versus time [year] exiting the homogeneous (SC₁₋₈₀) and heterogeneous hydraulic conductivity (SC-K_{S1-80}) simulation domains. 168

Figure 6.14 Concentrations of mineral weathering products SO₄, Fe, Ni, Al, Ca [mmol L⁻¹], and pH [-] versus time [year] measured in Type III test pile effluent compared to the mean aqueous concentration exiting the simulation domain. Simulated concentrations are from a single 2-D heterogeneous simulation (SC-K_{S1}) and the entire set of 2-D heterogeneous simulations (SC-K_{S1-80}). Confidence intervals (95th percentile) are shown in blue shading around the daily mean values. Measured concentrations are available only for periods of test pile core flow; simulated concentrations are calculated by the model for all periods regardless of flow condition..... 171

List of Tables

Table 2.1 Reaction stoichiometry and solubility products (K) for sulfide minerals	26
Table 2.2 Reaction stoichiometry and solubility products (K) for host and secondary minerals	27
Table 2.3 Rate expressions for dissolution of host and secondary minerals.....	28
Table 2.4 Physical parameters used in simulations.....	29
Table 2.5 Initial volume fractions and calibrated diffusion coefficients (<i>D</i>) for sulfide minerals and initial volume fraction and rate data for host and secondary minerals in Type III and Type I simulations	30
Table 3.1 Reaction stoichiometry minerals included in simulations	57
Table 3.2 Rate expressions for dissolution of host and secondary minerals.....	59
Table 3.3 Physical parameters used in simulations.....	60
Table 3.4 Initial volume fraction and rate data for sulfide minerals in AZL experiment simulations	61
Table 3.5 Initial volume fraction and rate data for host and secondary minerals in Type III and Type I simulations	62
Table 3.6 Summary of the root mean square error of annual mass flux [mol m^{-2}] residual from the Type I humidity cell, Type III humidity cell, and Type III AZL simulation cases.....	76
Table 4.1 Reaction stoichiometry and solubility products (K) for sulfide, host, and secondary minerals.....	92
Table 4.2 Rate expressions for dissolution of host and secondary minerals.....	93
Table 4.3 Physical parameters used in simulations.....	96
Table 4.4 Initial volume fraction and rate data for sulfide minerals in Type III test pile experiment simulations	97
Table 4.5 Initial volume fraction and rate data for host and secondary minerals in Type III test pile simulations	98
Table 4.6 Summary of the root mean square error of annual mass flux residual [mol m^{-2}] from the Type I humidity cell, Type III humidity cell, and Type III test pile simulation cases.....	113
Table 5.1 Summary of mean, standard deviation, and number of data points for $\text{Ln}(S)$ and $\text{Ln}(C)$ at Type I and Type III test pile	125
Table 5.2 Summary of mean, standard deviation, and number of data points for $\text{Ln}(K_S)$ at Type I and Type III test pile.....	126
Table 6.1 Reaction stoichiometry and solubility products (K) for sulfide minerals	147

Table 6.2 Reaction stoichiometry and solubility products (K) for host and secondary minerals.....	148
Table 6.3 Rate expressions for dissolution of host and secondary minerals	149
Table 6.4 Physical parameters used in the Type III test pile experiment 2-D heterogeneous simulations.....	151
Table 6.5 Initial volume fraction generation statistics and diffusion coefficient data for sulfide and carbonate minerals in Type III test pile experiment 2-D heterogeneous simulations	152
Table 6.6 Initial volume fraction and rate data for host and secondary minerals in Type III simulations.....	153
Table 6.7 Summary of the root mean square error of mean total mass flux residual [mmol m ⁻²] from the heterogeneous 2-D and homogeneous 1-D simulation cases for selected parameters.....	164
Table 6.8 Flow simulation statistic comparison for homogeneous and heterogeneous hydraulic conductivity distributions.....	167

Chapter 1

Introduction

The generation of mine waste and subsequent reduced quality effluent from sulfide mineral weathering is an environmental issue of global scale. In order to evaluate and mitigate the environmental impacts of mine wastes it is important that significant stakeholders (*i.e.*, mining companies, impacted communities and regulators) have a reliable and efficient means of assessing the severity of impacts to the receiving environment before waste emplacement. The potential for mine waste-rock to generate acid, elevated metals and sulfate concentrations in effluent, and the associated long-term effects to the receiving environment are typically characterized using the results of small-scale laboratory experiments. The laboratory experiments include kinetic tests (humidity cells), wherein a relatively small sample (1 kg) of waste rock is subjected to regular flooding events. The water quality of the effluent samples collected from these experiments are used to calculate sulfide-mineral weathering rates, which form the basis of predictions of effluent quality from the associated waste-rock dump. The process of extrapolating weathering rates derived from small-scale laboratory experiments is often referred to as scale-up. In addition to weathering rates calculated from laboratory experiments, the scale-up process often incorporates the use of empirical factors to estimate solute release rates for mine-waste dumps (Kempton, 2012; Amos et al., 2015). Scale-up factors often fail to encompass site specific heterogeneity associated with flow and mineralogical variability (Amos et al., 2015). Reactive transport modelling is capable of accounting for specific complexities such as secondary-mineral precipitation, adsorption, temperature dependence, and variable flow regimes, in a constrained manner, facilitating a quantitative assessment of the geochemical evolution of mine-waste rock. This mechanistic approach can potentially serve as a viable alternative or quality check for traditional methods of scale-up.

The research documented in this thesis focuses on the use of reactive transport modelling codes MIN3P (Mayer et al., 2002) and MIN3P-THCm (Su et al., 2017) to assess the significant geochemical processes controlling oxidation of sulfide minerals, and the subsequent release of dissolved metals and SO_4 , from the laboratory experiments. The conceptual model developed for the laboratory experiments is scaled to conduct simulations of the geochemical evolution of larger field experiments and provides a foundation for scale-up to a full-size waste-rock pile.

1.1 Diavik Waste Rock Project

The Diavik Waste Rock Project (DWRP) consisted of laboratory-scale and field-scale experiments with a primary goal of investigating a mechanistic scale-up technique to assess impacts of mine wastes. The project included the detailed geochemical and physical characterization of sulfidic waste rock produced at Diavik Diamond Mine (Diavik), which is located in the arctic climate of NT, Canada (Figure 1.1). The experiments consisted of small-scale (1 kg sample) humidity cells, intermediate-scale (~9,300 kg) active zone lysimeters, and large-scale (8.2×10^7 kg) heavily instrumented waste-rock test piles. Combined, these experiments provided a data set specifically designed to facilitate scale-up research.

The Diavik mine is located approximately 300 km northeast of Yellowknife, NT, in the continuous permafrost zone. The mean annual air temperature is approximately -9 °C; the area receives an average of 280 mm of precipitation per year, with approximately 40% as rain.



Figure 1.1 Location of Diavik Diamond Mine (from Smith et al., 2013a).

Waste rock used in the DWRP experiments has been characterized as approximately 75% granite, 14% pegmatitic granite, 10% biotite schist, and 1% diabase (Blowes & Logsdon, 1998). The biotite schist component has been identified as the primary host of metal sulfide minerals at the site, containing a mean sulfide content of 0.24 wt.% S (Langman et al., 2014). Pyrrhotite was the primary

metal sulfide present in the biotite schist with minor substitution of Ni and Co for Fe in the approximate ratio: $[\text{Fe}_{0.852}\text{Ni}_{0.004}\text{Co}_{0.001}\text{S}]$ (Jambor, 1997). Minor amounts of metal sulfide minerals chalcopyrite $[\text{CuFeS}_2]$, sphalerite $[\text{ZnS}]$, and pentlandite $[(\text{Fe,Ni})_9\text{S}_8]$ were also noted by Langman et al. (2014). Waste rock at Diavik is separated into three waste streams based on the total sulfur content: Type I (< 0.04 wt.% S); Type II (> 0.04 wt.% S and < 0.08 wt.% S); and Type III (> 0.08 wt.% S).

The laboratory experiments consisted of 36 humidity cells (Figure 1.2), with one set of 18 cells maintained at room temperature (approximately 22 °C) and a replicate set of 18 cells maintained at a cold temperature (approximately 5 °C). The experiments were conducted over a period of approximately 9 years. Each 18 cell set included duplicate cells such that there were six cells containing Type I waste rock, six cells containing Type II waste rock, and six cells containing Type III waste rock in each temperature group. All cells were constructed with 1 kg of < 6.3 mm diameter waste rock. Only the results of the Type I and Type III simulations are discussed in this thesis.



Figure 1.2 Cold temperature humidity cell experiment configuration.

The humidity cell experiments were flooded weekly according to the American Society for Testing and Materials (ASTM) method for humidity cell testing (ASTM, 1996). The effluent was collected

and analyzed for a suite of inorganic parameters that included SO₄, Fe, Ni, Co, Cu, Zn, Al, Si, Ca, Mg, K, Na, pH, and alkalinity.

An intermediate field-scale experiment was conducted at the Diavik site (Figure 1.3). This experiment consisted of four 2 m diameter HDPE active zone lysimeters (AZL) with two duplicate cells containing Type I waste-rock and two duplicate cells containing Type III waste-rock (Bailey et al., 2015; Neuner et al., 2013). Each of the lysimeters contained approximately 9,300 kg of < 1 m diameter waste-rock, which was exposed to atmospheric temperature and precipitation for the duration of the experiments.

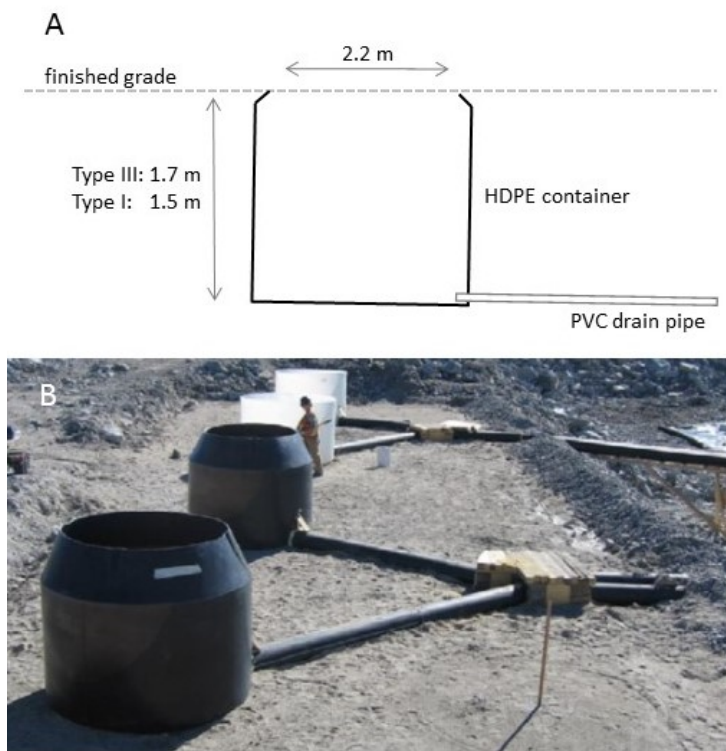


Figure 1.3 A: Cross-sectional conceptual diagram of DWRP active zone lysimeter experiment. B: Active zone lysimeter experiment prior to emplacement of run-of-mine rock.

Water flow volume was measured using individual rain-gauge tipping buckets connected to drain lines from the AZL experiments (Figure 1.4). Effluent samples were collected every 2 to 5 days, during periods of water flow, from the drain lines.



Figure 1.4 Typical tipping bucket and sample cell configuration at test pile instrumentation trailers.

The test pile experiments, located at the Diavik Test Piles Research Area (Figure 1.5) consisted of one pile constructed using Type III waste-rock material, one pile constructed with Type I waste-rock material, and a third pile constructed following the proposed closure concept for the Diavik waste rock. This cover concept includes a layered system wherein a core of Type III material was covered with a 1.5 m layer of till material (hydraulic barrier), then covered by a 3 m layer of Type I material (thermal barrier). The focus of the work in this thesis was simulation of the geochemical evolution of the waste rock in the Type III test pile only.

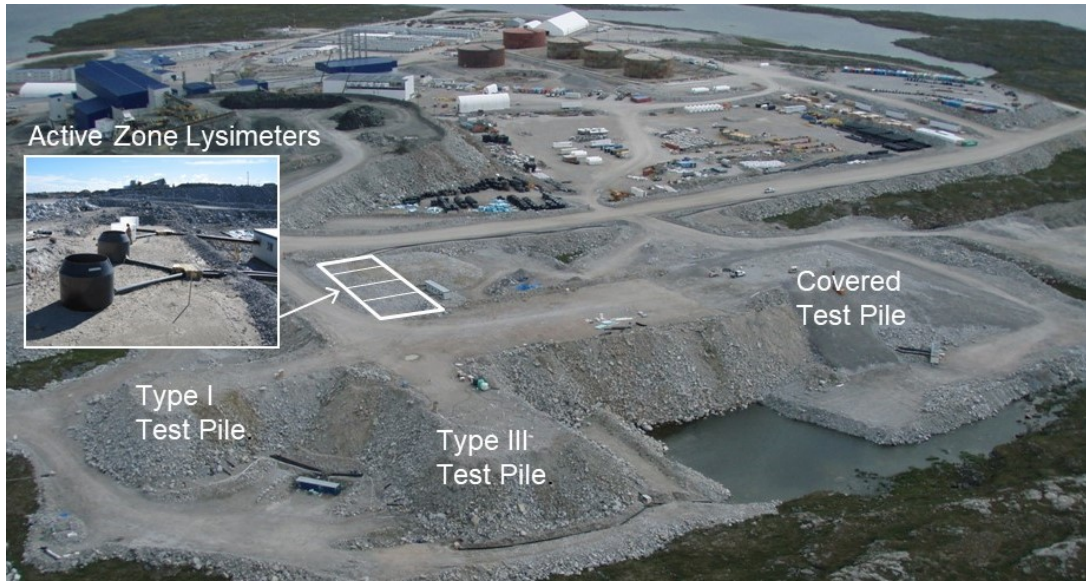


Figure 1.5 Overview of Test Piles Research Area at Diavik.

The Type III experiment measured approximately 50 m x 60 m at the base and was approximately 15 m high. The test pile was exposed to atmospheric temperature and precipitation conditions throughout the 7 year experiment. The test pile experiments were lined at the bottom and were constructed with drain piping that directed effluent to accessible sampling locations near the edges of the piles (Figure 1.6). In addition, twelve box-style lysimeters were installed within each of the piles to capture effluent from the core of the piles. These basal collection lysimeters (BCLs) were installed near the base of the pile and intercepted a portion of the flow through the piles to the main drain system (Figure 1.7).

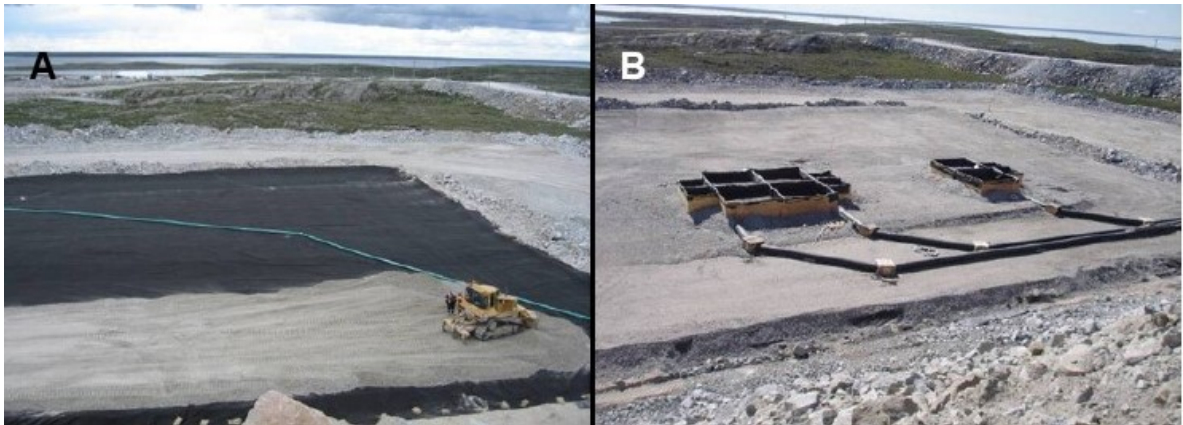


Figure 1.6 A: Main drainage network and liner at the base of the Type III test pile. B: Basal collection lysimeter drainage network at the base of the Type III test pile (adapted from Smith et al., 2013a).

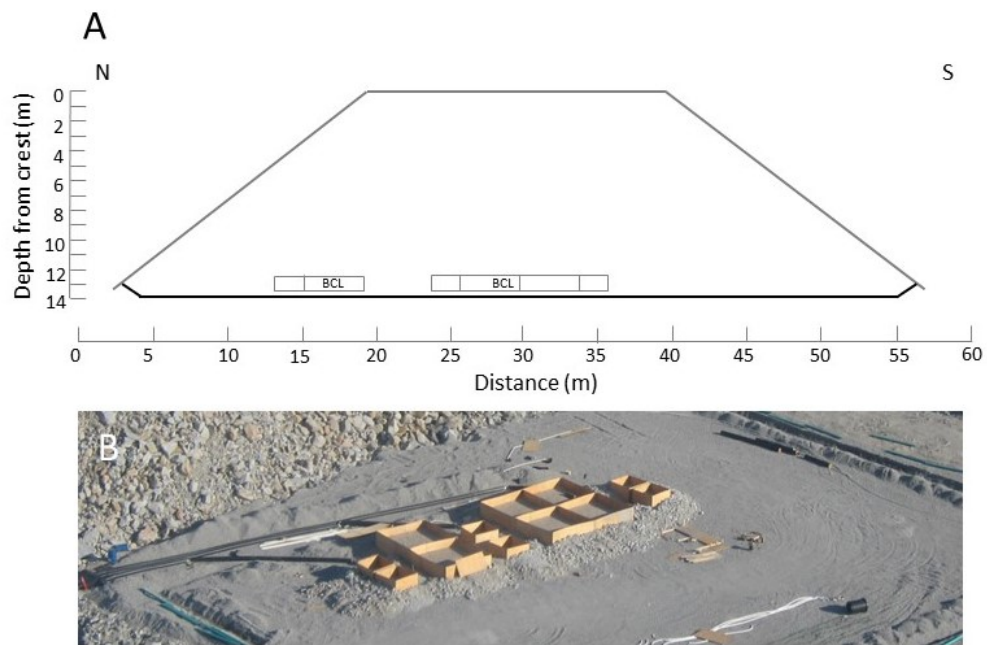


Figure 1.7 A: Conceptual cross-section of DWRP Type III test pile experiment indicating approximate location of basal collection lysimeters. B: Construction of basal collection lysimeters prior to run-of-mine material placement at Type III test pile.

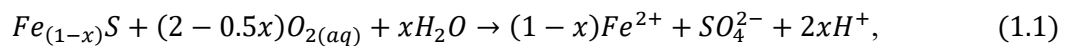
Similar to the AZL experiments, effluent samples were collected from the main drains and BCLs every 3 to 5 days during periods of water flow. Soil water samplers (SWS) were installed at depths of 1 m, 2 m, 3 m, 5 m, 7 m, and 9 m with the core of the test pile experiments to facilitate collection of pore water samples from the unsaturated zone. Samples are collected at SWS locations by applying suction and represent point measurements of unsaturated zone pore water geochemistry. Water samples from the main drains, BCL drains, and SWSs were analyzed for inorganic parameters that included SO₄, Fe, Ni, Co, Cu, Zn, Al, Si, Ca, Mg, K, Na, pH, and alkalinity.

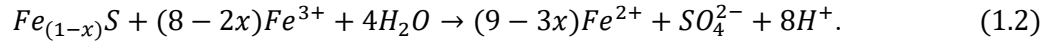
The Type I test pile was deconstructed in 2014 to investigate the geochemical evolution of the DWRP waste rock. The pile was excavated in lifts of approximately 3 m; parallel trenches were excavated into each bench to facilitate the collection of samples for analysis of mineralogical, geochemical, physical, and microbiological parameters. The samples were spatially located facilitating geostatistical analysis of key parameters including S and C mineralogy and particle size distribution.

1.2 Geochemical Evolution of Sulfidic Waste Rock

The integrated conceptual model of the geochemical evolution of sulfidic waste rock developed as part of the laboratory simulations (Chapter 2) forms the centrepiece of the thesis approach. The work in each of the first three research chapters is based on the integrated conceptual model and differs primarily in the scale of the experiment. In the context of the work documented in this thesis integrated is defined as the linking of the various geochemical aspects of sulfide waste rock weathering. Waste-rock mass, water infiltration and temperature, used to reflect the measured conditions at each of the experiments also differentiates each of the scales. Sulfur and C content and surface area parameters are scale dependent and based on values measured at each of the experiments.

It is commonly recognized that the primary driver of elevated solute load and reduced pH in sulfidic mine-waste material is the oxidation of sulfide minerals upon exposure to atmospheric O₂ and moisture (Nordstrom & Southam, 1997; Blowes et al., 2003). Using generic pyrrhotite as an example, the overall oxidation reactions for the key sulfide mineral oxidizing components, considered as part of the integrated conceptual model, O_{2(aq)} and Fe³⁺, can be represented as follows (Nicholson and Scharer, 1998; Janzen et al., 2000; Belzile et al., 2004):

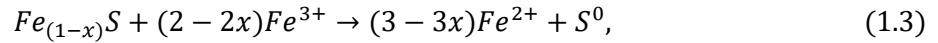




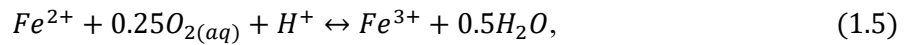
The oxidation of $Fe_{0.852}Ni_{0.004}Co_{0.001}S$, $CuFeS_2$, ZnS , and $(Fe,Ni)_9S_8$ by $O_{2(aq)}$ can be represented by equation 1.1 balanced for each of the sulfide minerals (see Wilson et al., 2018a).

The Fe^{3+} oxidation of sulfide minerals can be represented by three reactions following the pathway proposed by Schippers and Sand (1999). The Schippers and Sand (1999) reaction sequence for oxidation by Fe^{3+} includes pathways wherein partially oxidized S species may be briefly produced (e.g., H_2S_x , HS_x^- , S_x^{2-} , S^0) and subsequently oxidized in a process that leads to the end member product SO_4 . Because elemental S is commonly the dominant S intermediate species in the Schippers and Sand (1999) reaction sequence, it can be used to represent a single proxy for all intermediary S components in the reaction sequence.

Inserting elemental S as a proxy for intermediary S species results in the following generalized reaction sequence (Nicholson and Scharer, 1998); reaction stoichiometry specific to each sulfide mineral is provided in Chapter 2:



The availability of Fe^{3+} via the oxidation of Fe^{2+} is an important process in the oxidation of sulfide minerals and can be represented by the following reaction (Singer and Stumm, 1970; Schippers and Sand, 1999; Rohwerder et al., 2003):



Reduced pH resulting from sulfide mineral oxidation is often partially or fully consumed by acid neutralization minerals including carbonates, aluminosilicates, and secondary Al and Fe precipitates (Blowes et al., 2003). Depending on the mineralogy of the mine waste, acid neutralization follows a consistent sequence whereby carbonate minerals are consumed first, followed by secondary hydroxide and oxyhydroxide minerals resulting from the dissolution of Fe-bearing and aluminosilicate minerals (Jurjovec et al., 2002).

Dissolution of the carbonate mineral calcite, for example, can maintain the pH to approximately neutral and can be represented by the following reaction:



Dissolution of Al hydroxide and/or Fe oxyhydroxide minerals can maintain the pH of sulfide oxidation impacted effluent to 4.0-4.5 in the presence of Al hydroxide minerals such as gibbsite and to 2.5-3.5 in the presence of Fe oxyhydroxide minerals such as ferrihydrite (Blowes et al., 2003). Aluminosilicate minerals including biotite, muscovite, and albite represent a longer term partial acid neutralization capacity within waste rock because the dissolution of this type of mineral is typically too slow to buffer effluent pH to a specific value (Blowes et al., 2003). The contribution of aluminosilicate minerals is important when considering the geochemical evolution of waste rock because of the increased metal load, especially Al, which can result from aluminosilicate dissolution. The precipitation of secondary Al as hydroxide and hydroxysulfate phases provides an acid consuming capacity that slows the extreme acidification of the pore water.

1.3 Concept of scale-up

Research and practice in earth science disciplines is replete with the use of scaling smaller experiments or using representative samples to make conclusions about much larger systems. A common scale-up approach in mining involves assessment of site specific characteristics to derive scale factors (empirical and mechanistic) to facilitate the use of small-scale testing to predict the geochemical evolution of mega-scale waste-rock piles and mill tailings impoundments. Scale factors include considerations for parameters thought to influence mineral weathering rates including temperature, particle-size distribution, sulfide-mineral content and surface area, pore-water pH, moisture content, water-rock contact time, and O₂ concentration (Kempton, 2012; Amos et al., 2015). For example, Malmström et al. (2000) scaled the results of column experiments using the scaling factor approach through consideration of temperature, pH, mineral content, and particle size distribution to estimate weathering rates at the field scale to within one order of magnitude.

Scale factors are routinely assumed to be representative of an averaged parameter which can lead to the masking of heterogeneity. Kempton (2012) provided a review of the research regarding the scale factor approach to scale-up and suggested that the method results in loss of site specific heterogeneity for the sake of maintaining the relative simplicity of the method. Andrina et al. (2012) measured weathering rates of mine waste rock at three experimental scales over 10 years and found that scale

factors relating the weathering rates of the laboratory scale experiment to the field scale varied significantly, suggesting that temporally constant scale factors are not appropriate.

The scale-factor method relies on parameters that are commonly empirical (Amos et al., 2015) suggesting that well constrained mechanistic methods (*e.g.*, reactive transport models) may provide a path to advanced scale-up techniques. Studies incorporating mechanistic approaches to scale-up are limited. Bailey (2013) and Sinclair et al. (2015) used mechanistic methods to assess the solute load from the DWRP AZL and test pile experiments respectively, using the results of small-scale laboratory experiments. The solute loads calculated by Bailey (2013) and Sinclair et al. (2015) did not include comprehensively simulated flow regimes or the effects of secondary mineral formation and adsorption reactions. Blackmore et al. (2014) used dual porosity methods to simulate tracer tests in column and large-scale field experiments to investigate the effects of scale-up on flow regimes as part of the Antamina Waste Rock Project. An analysis of the flow regime at the Diavik site suggests that the contribution of the macropore component to the overall flow system at the Diavik site is modest (Neuner et al., 2013). Blackmore et al. (2014) presented a valuable treatment of scale-up with respect to flow regime, but the investigation did not include the geochemical evolution of waste rock.

The research documented in this thesis builds on the work of Bailey (2013), who scaled sulfide-mineral weathering rates that were calculated using DWRP humidity cell experimental effluent data and sulfide mineral surface areas, to predict mass loading from the DWRP AZL experiments. The results of the Bailey (2013) scale-up assessment indicated mass loading of conservative parameters (*e.g.*, Zn, Cu) could be predicted with sufficient accuracy to support waste-rock management strategy selection. The method did not include more complex processes such as secondary-mineral precipitation and adsorption. Sinclair et al. (2015) also used a mechanistic approach related to scale-up by simulating SO₄ production in one of the DWRP test piles using a relatively simple loading model. In the model, a temperature corrected SO₄ release rate, calculated from the results of the DWRP humidity cell experiments, and constant water velocity corrected for depth dependent temperature were assumed and resulted in a reasonable assessment of SO₄ release from the core of the test pile.

1.4 Heterogeneity

Heterogeneity in earth sciences research and practice is also a common theme that is typically addressed through the use of averaged parameters. Stochastic methods can extend the concept of averaged parameters and refine our treatment of the role of heterogeneity in earth systems.

Waste-rock piles are inherently heterogeneous. The wide range of particle size distribution along with construction methods can result in large spatial variability in mineralogy and physical characteristics (Fala et al., 2013; Anterrieu et al., 2010). Common methods of waste-rock pile construction include: i) push-dumping, where loads are dumped short of the tip face then pushed over the tip face with earth moving equipment, and ii) end-dumping, where loads are dumped directly over the tip face edge. Anterrieu et al. (2010) presented a conceptual model of the internal structure of typical waste-rock piles that includes a series of horizontally oriented layers of loose coarse material interbedded with finer grained compacted layers caused by mine equipment traffic, and angle of repose zones resulting from end-dumping and push-dumping where material segregation can result in a fining upward sequence. This conceptual model provides a good illustration of the heterogeneity of waste-rock piles (Figure 1.8).

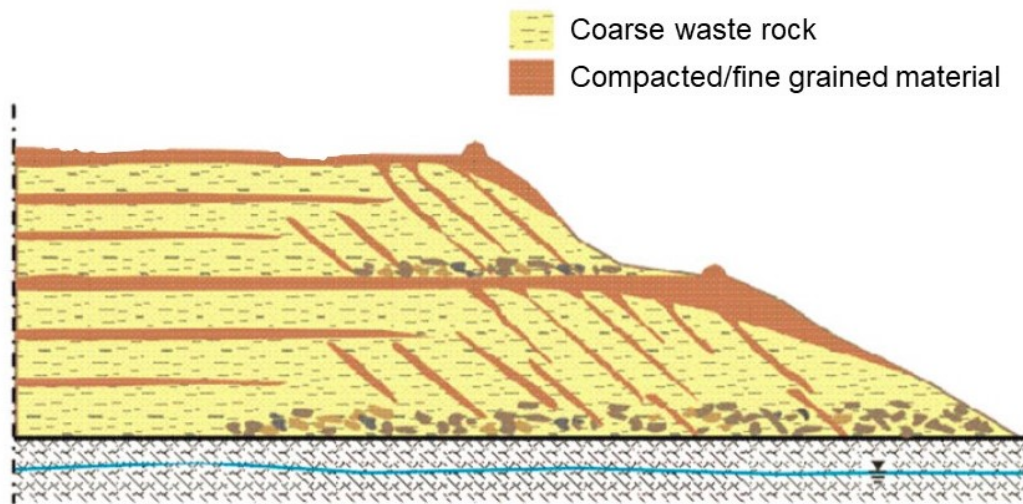


Figure 1.8 Conceptual illustration of the internal structure of a waste-rock pile constructed in two benches with horizontal stratification in the core of the pile, sloped stratification near the edges, and larger boulders congregated near the bottoms of the benches (adapted from Anterrieu et al., 2010).

The DWRP test piles were built using typical waste-rock dump construction methods (Smith et al., 2013a); however, no traffic surfaces were created on the Type I and Type III piles because the piles were constructed in a single lift. Barsi (2017) studied the spatial distribution of particle sizes in the Type I test pile as part of the deconstruction investigation in 2014. Analysis of spatially located samples collected from the core of the pile indicated a fining upward sequence likely introduced by the construction methods used (Barsi, 2017). This sequence was likely a result of particle separation that occurred as material was pushed or dumped over the active tip face resulting in larger material migrating to the bottom of the tip face and more fine material remaining near the top. Chi (2010) conducted an image analysis study on the DWRP test pile experiments and also concluded that a fining upward sequence was present. Atherton (2017) suggested that heterogeneity within the test pile led to pronounced zones of reduced pore water pH and elevated concentrations of SO_4 and metals parameters. These findings indicate that the heterogeneity present in full-size waste-rock piles was replicated by the test piles experiments.

The methodology of the scale factor approach results in elimination of most aspects of heterogeneity in waste-rock piles. The use of a single averaged parameter to scale weathering rates does not account for heterogeneity of mineralogy and physical parameters within piles but also does not account for variability in external influences including climatic drivers such as temperature and infiltration of precipitation.

Stochastic approaches have been used to represent heterogeneous porous media by many authors including Gelhar and Axness (1983), Sudicky (1986), Burr et al. (1994), Zhang and Lu (2004), Malmström et al. (2008), Sudicky et al. (2010), and Fala et al. (2013). Gelhar and Axness (1983) provided a theoretical study on the use of stochastic methods specifically applied to heterogeneous porous media and provided analytical solutions. Sudicky (1986) used geostatistics based on high resolution hydraulic conductivity measurements and the stochastic expressions of Gelhar and Axness (1983) and Dagan (1982) to estimate macro-dispersivity in porous media defined by a heterogeneous hydraulic conductivity field. Burr et al. (1994) used stochastic methods to define heterogeneous hydraulic conductivity and distribution coefficient fields and conducted numerical simulations using multiple realizations of the random fields. Burr et al. (1994) also provided a preliminary treatment of prediction uncertainty. Stochastic methods were used by Zhang and Lu (2004) to delineate and provide uncertainty regarding well capture zones. Sudicky et al. (2010) used geostatistical analyses

and stochastic theory to estimate a hydraulic conductivity tensor and dispersivity parameters used to model plume migration at a landfill. The results of the modelling were consistent with measured plume extents suggesting the approach of combining geostatistics, stochastic theory, and modelling works well to evaluate heterogeneous systems. Moving to reactive transport and stochastic methods, Malmström et al. (2008) used a probabilistic model with heterogeneous hydraulic conductivity and mineralogy fields to assess Zn migration from a mine tailings impoundment. The results indicate that mineralogical and flow heterogeneity can heavily influence transport of solutes and in some cases mask typically easily identifiable geochemical processes. Fala et al. (2013) studied the influence of heterogeneity in physical parameters (K, pressure, and volumetric water content) and mineralogy on the flow patterns and geochemical evolution of a hypothetical waste-rock pile. These studies demonstrate the evolution and effectiveness of using stochastic methods in evaluating parameters to define heterogeneous physical and geochemical systems.

In this thesis heterogeneity in S and C mineralogy and hydraulic conductivity was quantified for the test pile experiments using the results of a detailed sampling program conducted during the deconstruction of one of the test piles at the Diavik site. Observations from this program were used to define spatially heterogeneous realizations of S and C content and hydraulic conductivity, which were used to conduct a series of reactive transport simulations to assess the influence of heterogeneity on the geochemical evolution of the Diavik waste rock.

1.5 Reactive Transport Modelling

Reactive transport models have been used to simulate the geochemical evolution of mine wastes in a number of studies including Walter et al. (1994), Wunderley et al. (1996), Bain et al. (2001), Mayer et al. (2002), Amos et al. (2004), Jurjovec et al. (2004), Molson et al. (2005), Brookfield et al. (2006), Fala et al. (2013), and Demers et al. (2013). Each of these studies focused on a single scale of characterization (laboratory scale or field scale). The intent of many of the studies was to replicate data collected from laboratory experiments (Jurjovec et al., 2004; Amos et al., 2004) or field measurements (Mayer et al., 2002, Brookfield et al., 2006, and Demers et al. 2013) to enhance the evaluation of the geochemical mechanisms of the simulated systems.

These studies also demonstrated the capabilities of reactive transport modelling to capture the significant processes of geochemical evolution of minerals. Demers et al. (2013) used a reactive

transport model to demonstrate the role of adsorption in the delay of Ni release based on results of a medium-scale field experiment but did not consider temperature variation associated with waste rock exposed to atmospheric conditions. Bain et al. (2001) used reactive transport simulations to demonstrate the potential effects on the geochemical evolution of water down gradient of an abandoned uranium mine, but this study was limited somewhat by the lack of measured data. Molson et al. (2005) and Fala et al. (2013) used reactive transport simulations to demonstrate the influence of the physical characteristics of waste-rock piles on the flow and weathering regimes. The simulations of Molson et al. (2005) and Fala et al. (2013) were based on primarily hypothetical waste-rock pile configurations.

Most of the studies referenced previously in this section focused on homogenous porous media or waste rock. The role of heterogeneity in porous media has been investigated using numerical models (including reactive transport models) by several authors (*e.g.*, Burr et al., 1994; Malmström et al., 2008; Fala et al., 2013; Lahmira et al., 2017; Pedretti et al., 2017).

The reactive transport code used in this research was MIN3P (Mayer et al., 2002). MIN3P is a multi-component reactive transport model that provides a generalized framework to simulate kinetically controlled reactions. The model allows for customization of reaction stoichiometry and kinetics including the shrinking core model, which is commonly used to simulate the geochemical evolution of sulfide minerals. MIN3P uses one governing equation for simulation of variably saturated flow (Richards equation) coupled with a geochemical network defined by processes including mineral dissolution and precipitation, adsorption, complexation, and oxidation-reduction. Pore gas transport is implemented in MIN3P as a diffusion controlled process.

Reactive transport codes MIN3P (Mayer et al., 2002) and MIN3P-THCm (Su et al., 2017) were used to implement a conceptual model of geochemical evolution of the waste rock used in the humidity cell experiments. This implementation was then scaled to simulate the geochemical evolution of the similar waste rock used to construct the field scale experiments. Finally the implemented conceptual model was used to quantify the influence of heterogeneity in S and C and hydraulic conductivity on the geochemical evolution of the Diavik waste rock. Although not included in this thesis, all input files, database files, and the code executable used to conduct the simulations documented in this chapter have been archived to facilitate future reference.

1.6 Thesis Structure

The thesis consists of five research chapters documenting work conducted to answer the following research questions:

1. Can a mechanistic conceptual model of geochemical evolution of mine waste-rock, implemented with a reactive transport model, reasonably simulate the effluent geochemistry of small-scale laboratory experiments?
2. Can a mechanistic conceptual model of geochemical evolution of waste rock, developed for laboratory experiments, be scaled to reasonably simulate the effluent geochemistry from intermediate-scale field experiments while incorporating temporally dynamic flow and temperature conditions?
3. Can a mechanistic conceptual model of geochemical evolution of waste rock developed for laboratory experiments, be scaled to reasonably describe the effluent water geochemistry at a large-scale field experiment while incorporating temporally and spatially variable flow and temperature conditions ?
4. Can geostatistical methods be used to quantify the spatial heterogeneity in the waste-rock pile S and C concentration distributions and the hydraulic conductivity distribution?
5. What is the influence of heterogeneity in S and C distributions and hydraulic conductivity distribution on the geochemical evolution of the waste-rock pile?

The research portion of the thesis begins with the development and implementation of an integrated conceptual model of geochemical weathering at the small laboratory scale. The implementation was conducted with the reactive transport model MIN3P. The mineralogy and physical characteristics derived from the DWRP humidity cell experiments (Langman et al., 2014) were used to constrain the simulations and the results were compared to the effluent geochemistry from samples collected during these experiments. Chapter 2 demonstrates the implementation of a conceptual model that captured the significant geochemical processes of sulfidic waste rock weathering (research question 1).

Following simulation of the small-scale laboratory experiments, the integrated conceptual model was implemented at the medium-scale DWRP active zone lysimeter (AZL) field experiments. The simulations were conducted by maintaining the conceptual model used in the humidity cell simulations and changing only the S and C content to reflect the differing sulfide and carbonate

contents of the field experiments compared to the laboratory experiments. The infiltration (temporally variable) and temperature regimes (temporally variable, assumed to be spatially constant) of the AZL experiments were included in the simulations. The initial simulations, which were run without calibration, provided a reasonable assessment of waste rock weathering at the AZL scale. Minor calibration was subsequently completed to refine the pH of these simulations. Chapter 3 demonstrates that the conceptual model developed for the laboratory experiments could be scaled to provide a reasonable assessment of medium-sized field experiments (research question 2).

The mineralogy of the large-scale field experiment (Type III test pile) was similar to that of the Type III AZL experiments; the simulations of the large-scale field experiment were conducted using the mineral content used for the associated AZL simulations. The infiltration (temporally variable) and temperature regimes (temporally and spatially variable) of the test pile experiment were included in the simulations. Simulations were run with and without calibration. The calibrated simulations confirmed the results of the AZL simulations suggesting that carbonate minerals may be less available for H^+ neutralization in the field experiments when compared to laboratory experiments. Chapter 4 demonstrates that the conceptual model developed for the laboratory experiments can be scaled to provide a reasonable assessment of a large sized field experiment (research question 3).

Analysis of S, C, and particle-size distribution results from construction of the Type I and Type III test piles and deconstruction of the Type I test pile was used to assess the efficacy of using geostatistics to characterize the heterogeneity of the test pile experiments. Chapter 5 demonstrates that limited spatial heterogeneity can be detected in S, C, and particle size distribution parameters at the sampling density used during deconstruction of the large-scale field experiment (research question 4).

The generation of realizations of S, C, and hydraulic conductivity, facilitated by the geostatistical analysis, enabled assessment of heterogeneity within the test pile experiments. Multiple simulations were conducted to generate probability density functions for important waste rock effluent parameters. Chapter 6 demonstrates the role of heterogeneity in S, C, and hydraulic conductivity in the geochemical evolution of the effluent and constrains the error associated with reactive transport simulations of a waste rock system (research question 5).

The final chapter provides a summary of conclusions of the research chapters and puts forth global conclusions of the thesis. Suggestions for future research regarding the use of reactive transport

models to scale the results of laboratory experiments for prediction of the geochemical evolution of mine waste rock are also outlined.

Chapter 2

A conceptual model for temperature and sulfide content dependent geochemical evolution of waste rock – Laboratory scale

This chapter is modified from:

Wilson, D., Amos, R.T., Blowes, D.W., Langman, J.B., Ptacek, C.J., Smith, L., Segeo, D.C. 2018. The Diavik Waste Rock Project: A conceptual model for temperature and sulfide-content dependent geochemical evolution of waste rock – laboratory scale. *Appl. Geochem.* 89, 160-172.

Laboratory-scale experiments such as humidity cells are often used to characterize the geochemical evolution of sulfidic waste rock and the associated impacts on effluent water quality (*i.e.*, decreased pH and increased solute concentrations) generated as part of mine operations (Lapakko, 2003; Ardaud et al., 2009; Sapsford et al., 2009). The mineral leaching rates derived from humidity cell experiments are commonly extrapolated to anticipate the geochemical evolution of full-scale waste-rock piles using empirical scale factors, a process typically referred to as scale-up. Scale factors usually incorporate one or more parameters understood to influence effluent quality, such as pH, grain or particle size distribution, moisture content, temperature, oxygen availability, and mineral surface area (Kempton, 2012; Amos et al., 2015). Site-specific heterogeneities in physical and geochemical characteristics often render empirically based scale-up methods ineffective for accurate prediction of effluent quality (Amos et al., 2015). The capacity of reactive transport models to account for site heterogeneity and coupled geochemical processes leads to the potential to address scale-up using a detailed, mechanistic, and quantitative approach.

The Diavik Waste Rock Project (DWRP) was developed, in part, to assess scale-up techniques through the implementation of laboratory- and field-scale experiments conducted using sulfidic mine waste rock produced at Diavik Diamond Mine (Diavik), Northwest Territories, Canada. DWRP experiments involve small-scale (1-kg sample) humidity cells, medium-scale (~9,300 kg) *in situ* collection lysimeters, large-scale ($\sim 8.2 \times 10^7$ kg) densely instrumented waste-rock test piles, and instrumentation within the full-scale waste-rock pile, thus providing detailed datasets specifically designed to quantify scale-up processes.

Scale-up studies already conducted as part of the DWRP include preliminary calculations summarized by Bailey (2013) and Sinclair et al. (2015). Bailey (2013) normalized sulfide oxidation rates from the humidity cell experiments to sulfide mineral surface area to estimate the mass loading expected from the *in situ* collection lysimeters. This approach was determined to be relatively accurate for more conservative parameters (*e.g.*, Cu and Zn) but less suitable for estimation of solutes involved in multiple coupled processes (*e.g.*, Fe and Al). Sinclair et al. (2015) developed a loading-rate model to evaluate hypotheses regarding the geochemical evolution of pore water in one of the waste-rock test piles (15-m scale) and indicated this approach can be used to simulate the migration of solutes not affected by secondary mineral formation at the larger field scale.

The DWRP humidity cell experiments were conducted over a period of approximately nine years using run-of-mine waste rock collected at Diavik. The waste rock is sorted into three types according to sulfur content: Type I < 0.04 wt.%, Type II 0.04 to 0.08 wt.%, and Type III > 0.08 wt.% S (Smith et al., 2013a). The experiments were conducted as one component in a strategy to quantify the primary geochemical mechanisms controlling effluent quality from waste rock at the mine site.

The reactive transport model MIN3P (Mayer et al., 2002) was used to simulate the effluent geochemistry resulting from the humidity cell experiments and allow assessment of the primary weathering processes involved. The simulations were used to develop an integrated robust conceptual model of the geochemical evolution of the Diavik waste rock, which was applied to all of the humidity cell experiments to account for a range of sulfide contents and temperatures. This chapter presents a conceptual model of metal sulfide weathering in low sulfide waste rock using the results of humidity cell effluent quality sampling, the resulting estimated weathering rates, and mineralogical and hydraulic properties from the DWRP humidity cell and field-scale experiments. The simulations provide a geochemical conceptual model that can subsequently be adapted for simulations of the larger scale field experiments towards the development of an integrated conceptual model of sulfide weathering.

2.1 Humidity Cell Methodology

The humidity cell experiments involved a total of 36 cells, half of which were allocated to a warm cell group maintained at room temperature (approximately 22 °C) and the other half to a replicate cold cell group maintained at a lower temperature (approximately 5 °C) (Langman et al., 2014).

Replicate cells were constructed within each 18-cell experiment so that both temperature groups included six cells of each of the three types (Type I, Type II, and Type III) of waste-rock material. The results of the Type II simulations are not discussed here because of their similarity to the results of the Type I simulations.

Waste rock used in the humidity cell experiments was collected in 2004 and 2005 and was characterized as approximately 75% granite (primarily quartz [SiO_2], K-feldspar [KAlSi_3O_8], and albite [$\text{NaAlSi}_3\text{O}_8$]), 14% pegmatitic granite, 10% biotite schist, and 1% diabase (Blowes & Logsdon, 1998; Langman et al., 2014). Biotite schist is the primary host of metal sulfide minerals at the site, and is primarily composed of albite (35–55%), quartz (20–50%), and biotite [$\text{KMg}_{1.6}\text{Fe}_{1.4}\text{AlSi}_3\text{O}_{10}(\text{OH})_2$] (10–25%) and contains a mean sulfide content of 0.24 wt.% S (Langman et al., 2014). Pyrrhotite is the dominant metal sulfide mineral present in the waste rock wherein minor substitution of Ni and Co for Fe has occurred in the approximate ratio [$\text{Fe}_{0.852}\text{Ni}_{0.004}\text{Co}_{0.001}\text{S}$] (Jambor, 1997). Langman et al. (2014) also note smaller but significant metal sulfide contributions of chalcopyrite [CuFeS_2], sphalerite [ZnS], and pentlandite [$(\text{Fe},\text{Ni})_9\text{S}_8$]. Given the relatively low sulfide content of the waste rock, the humidity cell experiments were used to assess the potential for acid generation and the release of elevated concentrations of metals, including Fe, Ni, Co, Cu, and Zn, as well as other dissolved constituents such as sulfate [SO_4].

Initial host mineralogy of the waste rock was obtained from Jambor (1997). The mineralogical study of the Diavik waste rock included transmitted and reflected light optical microscopy to identify the silicate, carbonate, and sulfide minerals. In addition, scanning electron microscopy with energy dispersion analysis and microprobe analyses were conducted to obtain compositional data on the silicate and sulfide minerals. X-ray diffraction was used to provide quantitative estimates of the abundance of silicate minerals in the primary lithological units at Diavik. Similar analyses were conducted to identify secondary phases on a previous series of column experiments. The total S and C contents were determined by Langman et al. (2014). Additional work conducted by Langman et al. (2015) focussed on the application of synchrotron based techniques to characterize and identify secondary phases associated with the weathered sulfide minerals from the humidity cell experiment.

Each humidity cell contained 1 kg of waste rock, and was flooded on a weekly basis with deionized water following the American Society for Testing and Materials (ASTM) method D5477-96 for humidity cell testing (ASTM, 1996). Increased flooding occurred in the early stages according to the

method modification described by Lapakko and White (2000). The added water was held for approximately 1 h then allowed to drain from the cells. Draining of the cells generally lasted for 4 to 6 h but was allowed to continue for 24 h followed by periods of forced dry air flow (3 d at < 10% relative humidity) and forced humid air flow (3 d at >95% relative humidity) to complete the weekly cycle (Langman et al., 2014). Further details regarding the methodology and results of the humidity cell experiments are presented by Langman et al. (2014).

2.2 Conceptual Model

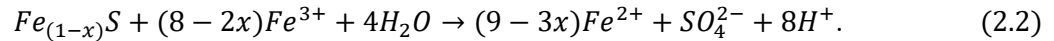
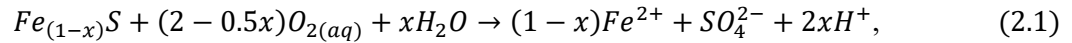
The conceptual model presented here was developed to simulate the geochemical evolution of sulfidic mine-waste rock exposed to atmospheric oxygen under wetting conditions. The conceptual model is based on the interpretation of the DWRP humidity cell experiments provided by Langman et al. (2014). Due to the relatively constant moisture and availability of oxygen within the humidity cell system, sulfide mineral oxidation is hypothesized to be the primary driver of elevated concentrations of SO₄, Ni, Co, Cu, and Zn in the humidity cell effluent. As a result, the conceptual model is focused on sulfide oxidation processes including oxidation by O_{2(aq)} and Fe³⁺. The development of the conceptual model and subsequent calibration were based on effluent geochemistry obtained from the Type I and III warm and cold humidity cell experiments (Langman et al., 2014).

Water flow through the humidity cells was simulated as continuous infiltration at a rate of 500 mL·wk⁻¹, which resulted in partially saturated conditions throughout the modelled period. The humidity cells were flooded on a weekly basis (*i.e.*, 500 mL over a period of 4 to 6 h); however, simulating this flow as continuous infiltration was considered a reasonable approximation because: i) fully saturated conditions represented a very low proportion of the total experiment time (2 – 4 %) and ii) evaporation was likely limited during the weekly dry cycle and did not result in a significant reduction of moisture content.

Several key components were included in the geochemical portion of the conceptual model to create a robust, generalized set of equations to represent the oxidation of sulfide minerals in systems beyond the scope of the humidity cells and the associated DWRP field experiments. Key oxidants, including O_{2(aq)} and Fe³⁺ with various microbial communities acting as catalysts (Nordstrom & Southam, 1997; Blowes et al., 2003), were included in the development of the conceptual model. Bacterial enumeration data collected as part of the DWRP humidity cell experiments (Langman et al.,

2014) indicated that neutrophilic sulfur oxidizing bacteria were the dominant microbiological catalyst in the system. The pH of the Type III cells initially declined to 4-4.5 then rose slightly to 4.5-5 after a period of stabilization while the pH of the Type I cells remained circumneutral throughout the experiments (Langman et al., 2014).

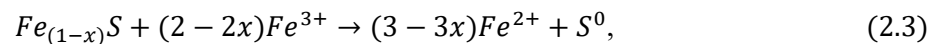
Using pyrrhotite as an example, the overall oxidation reactions can be represented as follows (Nicholson and Scharer, 1998; Janzen et al., 2000; Belzile et al., 2004):



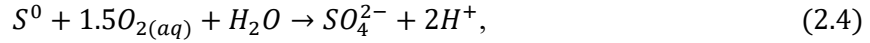
The oxidation of $Fe_{0.852}Ni_{0.004}Co_{0.001}S$, $CuFeS_2$, ZnS , and $(Fe,Ni)_9S_8$ by $O_{2(aq)}$ was represented in the simulations by versions of Equation 2.1 specific to each of the metal sulfide minerals (Table 2.1). The pentlandite present in the system was assumed to contain Ni and Co in the same ratio as noted for pyrrhotite, resulting in the stoichiometry $Fe_{4.5}Ni_{3.6}Co_{0.9}S_8$.

The oxidation of sulfide minerals by Fe^{3+} was represented by three parallel reactions following the sulfide mineral oxidation pathway proposed by Schippers and Sand (1999). Their reaction mechanism included polysulfide and thiosulfate pathways wherein partially oxidized S species (such as H_2S_x , HS_x^- , S_x^{2-} , and S^0) can be produced and subsequently oxidized as part of a sequence that proceeds towards the fully oxidized end member product SO_4 . Langman et al. (2015) examined the oxidation states of S on weathered pyrrhotite grains collected from the humidity cell and field experiments of the DWRP. The presence of S oxidation products $S_2O_3^{2-}$, SO_3^{2-} , and S^0 suggested a sequence of alteration that is more consistent with the thiosulfate pathway. Elemental S was selected as a proxy for the intermediary S components in the MIN3P simulations because it is included in both the polysulfide and thiosulfate pathways and is commonly the dominant S intermediary component in the oxidation process (Schippers and Sand, 1999). The inclusion of S^0 in the reaction sequence can be implemented in this numerical model in a straightforward manner. The addition of other reaction products would add complexity that cannot be constrained by the current data set.

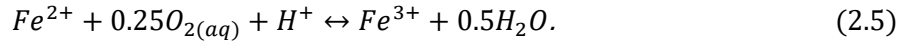
Elemental S was introduced into the geochemical system as an intermediary component using the following generalized reaction sequence (Nicholson and Scharer, 1998), where



represents a chemical oxidation process and



represents a biologically mediated oxidation process (Table 2.1). These reactions were driven in the simulations by the availability of Fe^{3+} , which is dependent on the rate of oxidation of Fe^{2+} and the pH. A kinetically controlled reaction was included to represent the replenishment of Fe^{3+} via oxidation of Fe^{2+} (Singer and Stumm, 1970; Schippers and Sand, 1999; Rohwerder et al., 2003):



For each of the metal sulfide minerals included in the simulations, a rate expression representing the shrinking core model (Levenspiel, 1972; Davis and Ritchie, 1986; Wunderly et al., 1996; Mayer et al., 2002) was used to simulate the rate of oxidation according to the representative reaction stoichiometry (Table 2.1). An example of the rate expression used for the oxidation of Diavik pyrrhotite by $O_{2(aq)}$ (after Mayer et al., 2002) is

$$R_{Po\ ox} = -10^3 S_{Fe_{0.852}Ni_{0.004}Co_{0.001}S} \left[\frac{r_p}{(r_p - r_r)r_r} \right] D_{O_{2(aq)}} \left[\frac{O_{2(aq)}}{1.9285} \right], \quad (2.6)$$

where $R_{Po\ ox}$ represents the rate of pyrrhotite oxidation [$mol\ L^{-1}\ d^{-1}$] and $S_{Fe_{0.852}Ni_{0.004}Co_{0.001}S}$, r_p , r_r , and $D_{O_{2(aq)}}$ represent the reactive surface area [$m^2\ mineral\ L^{-1}\ porous\ medium$], average particle radius [m], unreacted particle radius [m], and effective diffusion coefficient [$m^2\ s^{-1}$] for $O_{2(aq)}$ diffusion to the unreacted surface, respectively. Similar rate expressions were used to simulate the rate of sulfide mineral oxidation by Fe^{3+} so that the rate of oxidation of each sulfide mineral was represented by two rate equations (one for oxidation by $O_{2(aq)}$ and one for oxidation by Fe^{3+}) that acted separately on the same mineral volume fraction. The rate expression used for the oxidation of Diavik pyrrhotite by Fe^{3+} (after Mayer et al., 2002) was

$$R_{Po\ ox} = -10^3 S_{Fe_{0.852}Ni_{0.004}Co_{0.001}S} \left[\frac{r_p}{(r_p - r_r)r_r} \right] D_{Fe^{3+}} \left[\frac{Fe^{3+}}{1.714} \right]. \quad (2.7)$$

Biotic oxidation was represented in the rate expressions associated with Equations 2.4 and 2.5 by simulating the increase in reaction rate with increasing substrate (in these cases S^0 and Fe^{2+}) concentration to represent the increase in microbial activity.

The rate of Fe²⁺ oxidation (Equation 2.5) was simulated using the rate expression (after Singer and Stumm, 1970; Mayer et al., 2002; Roden, 2008)

$$R_{Fe^{2+}-Fe^{3+}} = -S_1 k_{1_{Fe^{2+}-Fe^{3+}}} [Fe^{2+}] [O_{2(aq)}] - S_2 k_{2_{Fe^{2+}-Fe^{3+}}} [Fe^{2+}] [O_{2(aq)}] [OH^-]^2 - S_3 k_{3_{Fe^{2+}-Fe^{3+}}} \left[\frac{[Fe^{2+}]}{K_s + [Fe^{2+}]} \right], \quad (2.8)$$

where $R_{Fe^{2+}-Fe^{3+}}$ represents the rate of Fe²⁺ oxidation [mol L⁻¹ d⁻¹]. The first two terms on the right side of Equation 2.8 represent the chemical oxidation of Fe²⁺ by aqueous oxygen, with S_1 , $k_{1_{Fe^{2+}-Fe^{3+}}}$, and $k_{2_{Fe^{2+}-Fe^{3+}}}$ representing a scaling factor [-] and reaction rate constants for pH < ~ 3.5 [L mol⁻¹ d⁻¹] and pH > ~ 4.5 [L³ mol⁻³ d⁻¹] (Singer and Stumm, 1970), respectively. The final term on the right hand side represents the biotic oxidation of Fe²⁺, where $k_{3_{Fe^{2+}-Fe^{3+}}}$ and K_s represent the reaction rate constant [mol L⁻¹ d⁻¹] and half-saturating concentration [mol L⁻¹], respectively.

Humidity cell effluent SO₄ concentrations derived from oxidation of sulfide minerals by Fe³⁺ were simulated by the microbially catalyzed oxidation of S⁰ to SO₄ by O_{2(aq)}, corresponding to the reaction stoichiometry in Equation 2.4. Due to the abundance of O_{2(aq)} in the system (unsaturated cells open to atmospheric O₂ levels), the rate of S⁰ oxidation is only dependent on the availability of the reaction substrate (S⁰) and is represented by (after Roden, 2008):

$$R_{S^0-SO_4} = -k_{S^0-SO_4} \left[\frac{[S^0]}{K_s + [S^0]} \right], \quad (2.9)$$

where $R_{S^0-SO_4}$ represents the rate of biotic S⁰ oxidation by oxygen [mol L⁻¹ d⁻¹] and $k_{S^0-SO_4}$ and K_s represent the reaction rate constant [mol L⁻¹ d⁻¹] and half-saturating concentration [mol L⁻¹], respectively.

Dissolution of host minerals was simulated as surface-controlled reactions according to the reaction stoichiometry and rate expressions presented in Tables 2.2 and 2.3.

Iron-bearing oxides and hydroxysulfates are expected to precipitate in association with the geochemical weathering of sulfide minerals (Blowes et al., 2003; Jambor, 2003). Secondary minerals were selected based on calculations of saturation indices conducted using the geochemical speciation software PHREEQC (Parkhurst and Appelo, 1999) and minerals considered representative of the geochemical evolution of the Diavik waste rock. The geochemical speciation modelling indicated that the humidity cell effluent water was saturated or supersaturated with respect to Fe(III) (oxy)hydroxide

minerals (represented in this study by ferrihydrite [Fe(OH)₃]) at various times in the experiments. Ferrihydrite was allowed to precipitate or dissolve during the MIN3P simulations according to equilibrium-controlled rate expression (Tables 2.2 and 2.3). Saturation index calculations indicated that gypsum [CaSO₄·2H₂O], jarosite [KFe₃(SO₄)₂(OH)₆], gibbsite [Al(OH)₃], and siderite [FeCO₃] may precipitate at the field scale (Bailey et al., 2015; Sinclair et al., 2015). In anticipation of scaling the conceptual model to simulate field experiments, supplemental secondary minerals gypsum, jarosite, gibbsite, and siderite were allowed to precipitate according to equilibrium constraints (Tables 2.2 and 2.3). To prevent excess Si build-up resulting from aluminosilicate weathering, amorphous silica [SiO₂] was included in the simulations and allowed to precipitate according to an equilibrium-controlled rate expression (Tables 2.2 and 2.3).

Comparison of effluent concentrations indicated a Ni to Co molar ratio of approximately 3.5 from the Type III cells and less than 1 from the Type I cells, suggesting the influence of adsorption on Ni concentrations in the Type I humidity cells. Adsorption of Ni, Co, Cu, and Zn to hydrous ferric oxide was therefore included in the simulations using the general two-layer model (Dzombak and Morel, 1990). Competitive adsorption of Ni, Co, Cu, and Zn was incorporated into the simulations using constant available surface area (600 m² g⁻¹; Dzombak and Morel, 1990) and adsorption site density (0.056 nm⁻² strong sites and 2.3 nm⁻² weak sites; Dzombak and Morel, 1990), intrinsic surface complexation constants (from Balistriero et al., 2003), and a total Fe concentration of 1.0 mg L⁻¹.

Table 2.1 Reaction stoichiometry and solubility products (K) for sulfide minerals

Mineral	Sulfide Mineral Reactions	log <i>K_i</i>
pyrrhotite	$Fe_{0.852}Ni_{0.004}Co_{0.001}S + 0.143H_2O + 1.9285O_{2(aq)} \rightarrow$ $0.852Fe^{2+} + 0.004Ni^{2+} + 0.001Co^{2+} + SO_4^{2-} + 0.286H^+$ $Fe_{0.852}Ni_{0.004}Co_{0.001}S + 1.714Fe^{3+}$ $\rightarrow 2.566Fe^{2+} + 0.004Ni^{2+} + 0.001Co^{2+} + S^0$	134.66
sphalerite	$ZnS + 2O_{2(aq)} \rightarrow Zn^{2+} + SO_4^{2-}$ $ZnS + 2Fe^{3+} \rightarrow 2Fe^{2+} + Zn^{2+} + S^0$	--
chalcopyrite	$CuFeS_2 + 4O_{2(aq)} \rightarrow Cu^{2+} + Fe^{2+} + 2SO_4^{2-}$ $CuFeS_2 + 4Fe^{3+} \rightarrow 5Fe^{2+} + Cu^{2+} + 2S^0$	--

	$Fe_{4.5}Ni_{3.6}Co_{0.9}S_8 + 16.5O_{2(aq)} + 2H^+ \rightarrow$	
pentlandite	$4.5Fe^{2+} + 3.6Ni^{2+} + 0.9Co^{2+} + 8SO_4^{2-} + H_2O$	--
	$Fe_{4.5}Ni_{3.6}Co_{0.9}S_8 + 18Fe^{3+} \rightarrow 22.5Fe^{2+} + 3.6Ni^{2+} + 0.9Co^{2+} + 8S^0$	

Table 2.2 Reaction stoichiometry and solubility products (K) for host and secondary minerals

Mineral	Host Mineral Reactions	log K_i
calcite	$CaCO_3 \rightarrow Ca^{2+} + CO_3^{2-}$	-8.48
dolomite	$MgCa(CO_3)_2 \rightarrow Mg^{2+} + Ca^{2+} + 2CO_3^{2-}$	-17.09
biotite	$KMg_{1.6}Fe_{1.4}(AlSi_3O_{10})(OH)_2 + 10H^+ \rightarrow K^+ + 2Mg^{2+} + Fe^{2+} + Al^{3+} + 3H_4SiO_4$	--
muscovite	$KAl_2(AlSi_3O_{10})(OH)_2 + 10H^+ \rightarrow K^+ + 3Al^{3+} + 3H_4SiO_4$	--
albite	$NaAlSi_3O_8 + 4H_2O + 4H^+ \rightarrow Na^+ + Al^{3+} + 3H_4SiO_4$	--
Secondary Mineral Reactions		
Fe(III) (oxy)hydroxide	$Fe(OH)_{3(am)} + 3H^+ \leftrightarrow Fe^{3+} + 3H_2O$	4.89
jarosite	$KFe_3(SO_4)_2(OH)_6 + 6H^+ \leftrightarrow K^+ + 3Fe^{3+} + 2SO_4^{2-} + 6H_2O$	-9.21
silica(am)	$SiO_2 + 2H_2O \leftrightarrow H_4SiO_4$	-2.71
gibbsite	$Al(OH)_{3(am)} + 3H^+ \leftrightarrow Al^{3+} + 3H_2O$	8.11
gypsum	$CaSO_4 \cdot 2H_2O \leftrightarrow Ca^{2+} + SO_4^{2-} + 2H_2O$	-4.58
siderite	$FeCO_3 \rightarrow Fe^{2+} + CO_3^{2-}$	-10.93

Table 2.3 Rate expressions for dissolution of host and secondary minerals

Host Minerals	Rate Expression
calcite	$R = -S_{CaCO_3} [10^{-0.05}[H^+] + 10^{-6.19}[H_2O] + 10^{-3.30}[H_2CO_3]] \left[1 - \frac{IAP}{10^{-8.48}} \right]$
dolomite	$R = -S_{MgCa(CO_3)_2} [10^{-2.59}[H^+]^{0.75} + 10^{-7.66} + 10^{-4.00}[H_2CO_3]^{0.75}] \left[1 - \frac{IAP}{10^{-17.09}} \right]$
biotite	$R = -S_{KMg_{1.6}Fe_{1.4}(AlSi_3O_{10})(OH)_2} k_1 [H^+]^{0.25}$
muscovite	$R = -S_{KAl_2(AlSi_3O_{10})(OH)_2} [k_1 [H^+]^{0.08} + k_2 [H^+]^{-0.1}]$
albite	$R = -S_{NaAlSi_3O_8} [k_1 [H^+]^{0.49} + k_2 [H^+]^{-0.3}]$
Secondary Minerals	
Fe(III) (oxy)hydroxide	$R = k_{Fe(OH)_3}^{eff} \left[1 - \frac{IAP}{10^{4.89}} \right]$
jarosite	$R = k_{KFe_3(SO_4)_2(OH)_6}^{eff} \left[1 - \frac{IAP}{10^{-9.21}} \right]$
silica(am)	$R = k_{SiO_2}^{eff} \left[1 - \frac{IAP}{10^{-2.71}} \right]$
gibbsite	$R = k_{Al(OH)_3}^{eff} \left[1 - \frac{IAP}{10^{-8.11}} \right]$
gypsum	$R = k_{CaSO_4 \cdot 2H_2O}^{eff} \left[1 - \frac{IAP}{10^{4.58}} \right]$
siderite	$R = k_{FeCO_3}^{eff} \left[1 - \frac{IAP}{10^{10.93}} \right]$

2.3 Model Parameters

The simulation domain was constructed as a 0.1-m deep 1-D column discretized as 101 1 mm control volumes. The simulations were run for 3285 d, corresponding to the approximately nine-year period of the longest running humidity cell experiments. The inflow boundary condition for gas phase O₂ and CO₂ was set to their respective atmospheric partial pressures because i) humidity-adjusted

atmospheric air was pumped through the cells during the air flow portions of the experiment and ii) the deionized water used for weekly flooding events was not isolated from atmospheric conditions. To be consistent with the temperature conditions of the experiment, the warm and cold simulations were conducted at 22 and 5 °C, respectively.

Physical characteristics such as porosity, hydraulic conductivity, and hydraulic function parameters (Table 2.4) were based on Neuner et al. (2013) or on analysis of humidity cell data. Because of the relatively short flow path (0.1 m) and the rapid flushing of solutes from the column, dispersivity was ignored. Mineral volume fraction (ϕ_i) values (Table 2.5) for sulfide and carbonate minerals were calculated using values obtained from carbon and sulfur analyses (Langman et al., 2014). The total sulfide content of the Type I and Type III humidity cells was 0.02 wt.% and 0.16 wt.%, respectively. The ϕ_i values for CuFeS_2 and ZnS were calculated using the results of bulk metal analysis conducted on humidity cell samples; the ϕ_i value for $\text{Fe}_{4.5}\text{Ni}_{3.6}\text{Co}_{0.9}\text{S}_8$ was calibrated as part of the simulations. Host ϕ_i values were based on the general waste-rock content documented by Jambor (1997). The effective surface area of each host mineral was used as a calibration parameter in conjunction with secondary mineral precipitation (in some cases) to capture the concentrations of Al, Ca, K, Fe, Mg, Na, and Si.

The dissolution of sulfide minerals was irreversible and transport controlled with reaction rates calculated using separate effective diffusion coefficients for oxidants $\text{O}_{2(\text{aq})}$ and Fe^{3+} . The effective diffusion coefficients were used as calibration parameters to capture the concentrations of SO_4 and cations Ni, Co, Cu, and Zn (along with adsorption processes) in the humidity cell effluent.

Table 2.4 Physical parameters used in simulations

Parameter	Value
hydraulic conductivity ¹	2.5×10^{-4}
van Genuchten hydraulic parameters ²	α 8.8 n 1.7
infiltration rate ³	1.0×10^{-9}
porosity ⁴	0.26

¹Hydraulic conductivity based on humidity cell grain size data in m s^{-1} .

²Van Genuchten parameters based on Neuner et al. (2013); α in m^{-1} , n is unitless.

³Infiltration rate in m s^{-1} .

⁴Porosity based on humidity cell dry and saturated weights; data courtesy of Mandy Moore (unpublished).

Table 2.5 Initial volume fractions and calibrated diffusion coefficients (D) for sulfide minerals and initial volume fraction and rate data for host and secondary minerals in Type III and Type I simulations

Mineral	Type III $\phi_i^{1,2}$	Type I $\phi_i^{1,2}$	$D^{eff}/k/k^{eff}$	E_a^3	S_i (calibrated)
pyrrhotite – $O_{2(aq)}$	1.6×10^{-3}	2.0×10^{-4}	$2.2 \times 10^{-13}, 8.0 \times 10^{-14}$	--	--
pyrrhotite – Fe^{3+}			$1.0 \times 10^{-9}, 3.7 \times 10^{-10}$		
chalcopyrite - $O_{2(aq)}$	4.9×10^{-5}	6.1×10^{-6}	$3.0 \times 10^{-13}, 1.2 \times 10^{-13}$	--	--
chalcopyrite - Fe^{3+}			$1.0 \times 10^{-9}, 4.0 \times 10^{-10}$		
sphalerite - $O_{2(aq)}$	5.3×10^{-5}	6.7×10^{-6}	$4.0 \times 10^{-14}, 1.6 \times 10^{-14}$	--	--
sphalerite - Fe^{3+}			$1.0 \times 10^{-9}, 4.0 \times 10^{-10}$		
pentlandite - $O_{2(aq)}$	2.0×10^{-5}	2.5×10^{-6}	$4.0 \times 10^{-13}, 1.6 \times 10^{-13}$	--	--
pentlandite - Fe^{3+}			$1.0 \times 10^{-9}, 4.0 \times 10^{-10}$		
calcite	2.1×10^{-4}	2.3×10^{-4}	$k_1 = 10^{-0.05}$ $k_2 = 10^{-6.19}$ $k_3 = 10^{-3.30}$	21	--
dolomite	2.4×10^{-4}	2.7×10^{-4}	$k_1 = 10^{-2.59}$ $k_2 = 10^{-7.66}$ $k_3 = 10^{-4.00}$	42	--
biotite ⁴	4.7×10^{-2}	2.6×10^{-2}	$10^{-10.97}$	63	100
muscovite ⁴	1.6×10^{-2}	1.6×10^{-2}	$k_1 = 10^{-12.60}$ $k_2 = 10^{-13.50}$	22	35
albite ⁴	1.5×10^{-1}	1.0×10^{-1}	$k_1 = 10^{-9.69}$ $k_2 = 10^{-14.15}$	58	30
Fe(III) (oxy)hydroxide ⁵	--	--	10^{-8}	--	--
k-jarosite ⁵	--	--	10^{-8}	--	--
gibbsite ⁵	--	--	10^{-12}	--	--
silica(am) ⁵	--	--	10^{-6}	--	--
gypsum ⁵	--	--	10^{-6}	--	--
siderite ⁵	--	--	10^{-9}	--	--

Input files, database files, and the code executable used to conduct the simulations documented here have been archived to facilitate future reference.

Reactions are transport controlled with $r^p = 0.0625$ mm (after Langman et al., 2014); calibrated effective diffusion coefficient (D^{eff}) in $m^2 s^{-1}$; reactive surface area was calculated in m^2 mineral L^{-1} porous media, based on particle size, mineral volume fraction, and an estimated surface area of $1 m^2 g^{-1}$ (Langman et al., 2014).

¹Total sulfide and carbonate mineral contents based on results of static testing after Langman et al. (2014);

chalcopyrite and sphalerite content based on Cu and Zn content from whole rock analysis; pentlandite content calibrated based on Ni and Co concentrations in humidity cell effluent; mineral content of host minerals based on results presented in Jambor (1997).

²For sulfide minerals: calculated using density specific to each mineral in m^3 mineral m^{-3} porous medium. For non-sulfide minerals: calculated using $\rho_b = 1.62 \text{ g cm}^{-3}$ in m^3 mineral m^{-3} porous medium and adjusted during simulation calibration.

³Activation energy in kJ mol^{-1} .

⁴For this phase, surface area calibrated in m^2 mineral L^{-1} porous medium based on mineral volume fraction and bulk surface area after Langman et al. (2014) and adjusted to fit measured effluent parameters. Calibrated activation energy.

⁵For this phase, effective rate constant calibrated in mol L^{-1} porous medium s^{-1} .

The dissolution of host minerals was kinetically controlled and irreversible (with the exception of calcite and dolomite dissolution). Reactions involving carbonate minerals and all secondary minerals were simulated as kinetically controlled and reversible, meaning that calcite, dolomite, and the secondary minerals could precipitate and/or dissolve as the geochemical conditions evolved.

2.4 Results

The simulated effluent geochemistry for the Type III humidity cells (warm and cold) generally captured the overall trend and concentration of solutes in the measured humidity cell effluent (Figures 2.1 and 2.2). Concentrations of solutes derived from sulfide oxidation (SO_4 , Ni, Co, Cu, and Zn) in the Type III column effluent generally increased uniformly, from low concentrations to relatively sharp peak concentrations as the rate of sulfide mineral oxidation increased. Peak concentrations were followed by generally monotonic declines to relatively stable minimum concentrations in the latter half of the humidity cell experiment, reflecting the decline in sulfide mineral availability that is attributed to the formation of secondary solids on the outer rims of the particle surfaces (Langman et al., 2014). Type III effluent pH decreased from approximately neutral (pH 6.5) in conjunction with increasing metal concentrations, reaching lows of slightly below 4 in both the warm and cold temperature cell effluent (70-80 weeks). In general, warm temperature effluent peak solute concentrations occurred earlier in the experiment and were higher than those for the cold temperature effluent, reflecting the influence of temperature on the weathering process. Maximum concentrations were observed at 10 to 50 weeks in the warm temperature experiments but at 25 to 100 weeks in the cold temperature experiments; the warm temperature concentrations were also generally twice the corresponding cold temperature concentrations.

The evolution of indicator solutes followed a slightly different reaction pathway in the Type I warm and cold humidity cell effluents (Figures 2.3 and 2.4). In general, the highest solute concentrations for both warm and cold cells occurred within the first 10 weeks, followed by monotonic decreases to the end of the experiment. The Type I effluent pH was generally stable, ranging from 6.0 to 8.0 for both temperatures. Peak concentrations of solutes associated with sulfide weathering were generally higher for the room temperature cells compared to the cold temperature cells, again indicating the effect of temperature on weathering rates; notably, the effect was not as pronounced as in the Type III effluent, likely due to the lower ϕ_i of the sulfide minerals present in the Type I waste rock.

Effluent pH was controlled primarily by the oxidation of sulfide minerals and dissolution of carbonate minerals. Acid neutralization in the Type III cells was provided initially by the dissolution of calcite; longer term consumption of H^+ was influenced by the dissolution of gibbsite, dolomite, and biotite. Acid production was also mitigated at later times by the decline in sulfide mineral availability, which resulted in increased pH after peak sulfide weathering had occurred. Acid neutralization in the Type I effluent was associated with calcite dissolution throughout the experiment because of the lower sulfide mineral content. The concentration of aqueous iron was controlled by the rate of Fe^{2+} oxidation and by the precipitation of secondary minerals Fe(III) (oxy)hydroxide and jarosite. Although the precipitation of siderite was allowed, it did not occur in any of the simulations.

The simulated rates of sulfide oxidation compared well to the rates of sulfide oxidation for Type III and Type I waste rock calculated using the concentrations of SO_4 (Langman et al., 2014) (Figure 2.5). Oxidation rates and the overall decreasing trend are consistent with the hypothesis that increasing pH and declining solute concentrations are the result of decreasing availability of sulfide minerals in the system (Langman et al., 2014).

Individual simulation run times averaged approximately 1.5 minutes on a single processor laptop machine. MIN3P uses an adaptive time stepping scheme that minimizes convergence issues by limiting time step size based on the complexity of the simulation (Mayer, 1999).

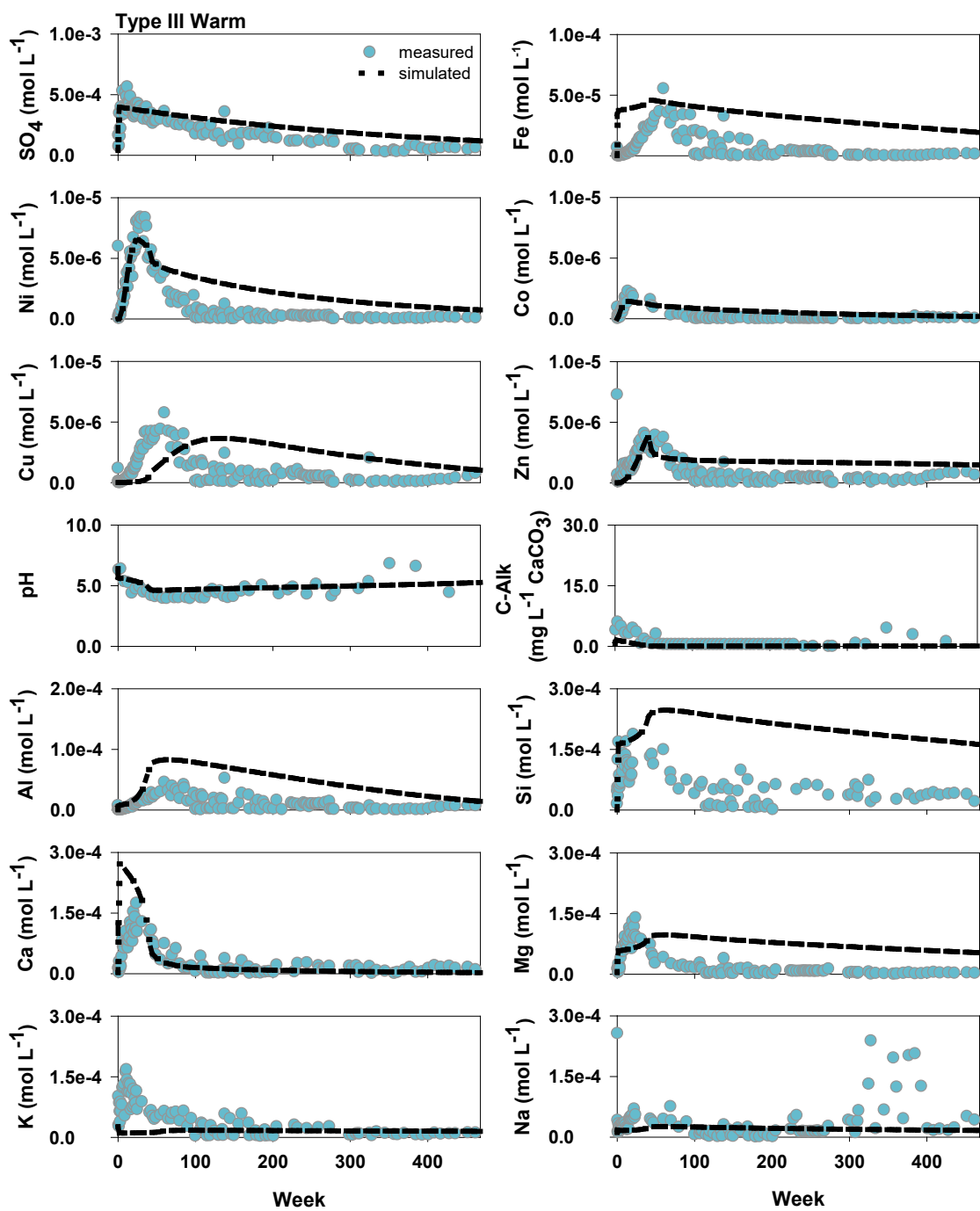


Figure 2.1 Average concentrations of mineral weathering products SO₄, Ni, Co, Cu, Zn, Fe, Al, Ca, Mg, K, Na, and H₄SiO₄ [mol L⁻¹], pH [-], and alkalinity [as mg L⁻¹ CaCO₃] versus time [weeks] measured in the two Type III warm temperature humidity cell effluent compared to aqueous concentrations exiting the simulation domain.

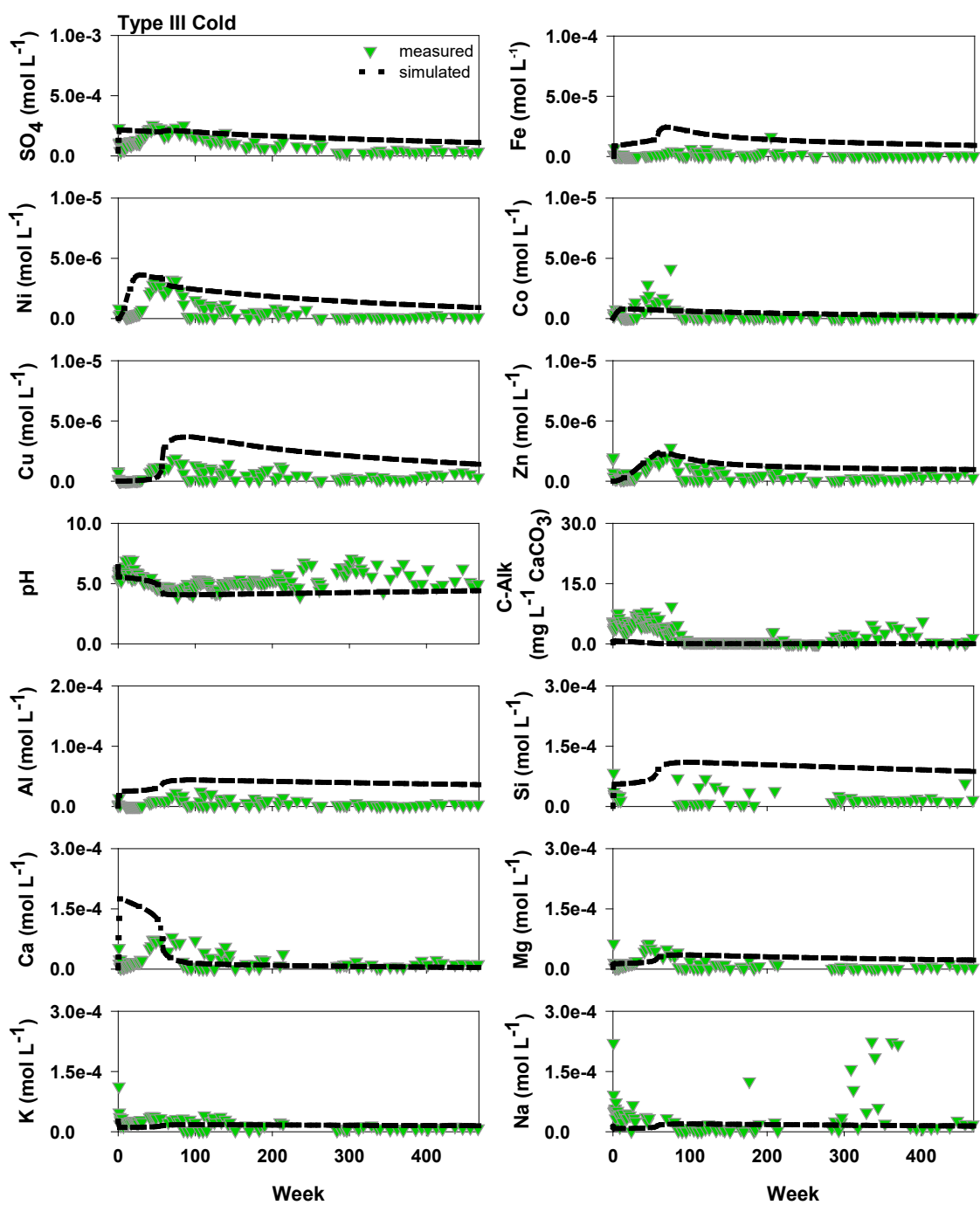


Figure 2.2 Average concentrations of mineral weathering products SO_4 , Ni, Co, Cu, Zn, Fe, Al, Ca, Mg, K, Na, and H_4SiO_4 [mol L^{-1}], pH [-], and alkalinity [$\text{mg L}^{-1} \text{CaCO}_3$] versus time [weeks] measured in the two Type III cold temperature humidity cell effluent compared to aqueous concentrations exiting the simulation domain.

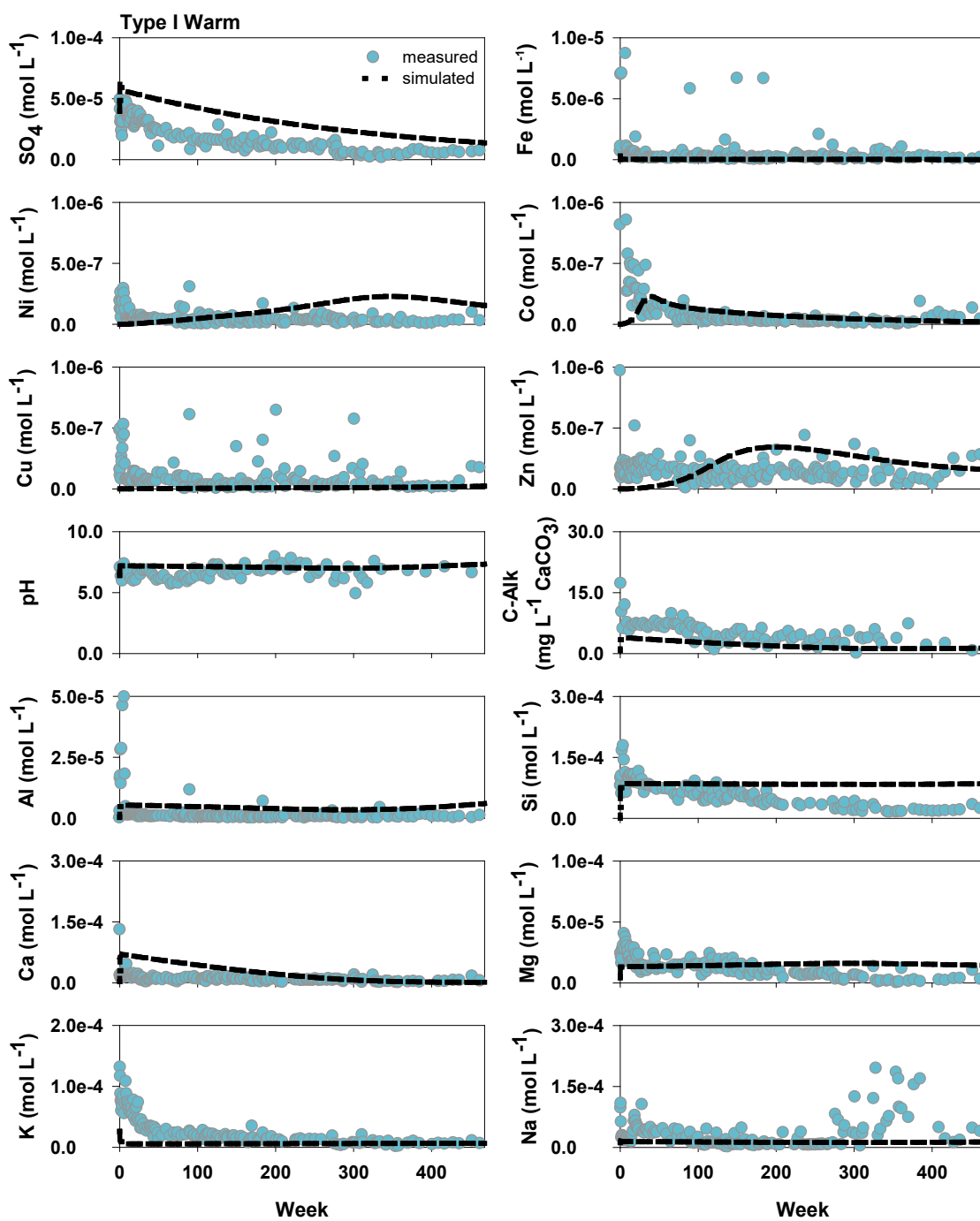


Figure 2.3 Average concentrations of mineral weathering products SO₄, Ni, Co, Cu, Zn, Fe, Al, Ca, Mg, K, Na, and H₄SiO₄ [mol L⁻¹], pH [-], and alkalinity [as mg L⁻¹ CaCO₃] versus time [weeks] measured in the six Type I warm temperature humidity cell effluent compared to aqueous concentrations exiting the simulation domain.

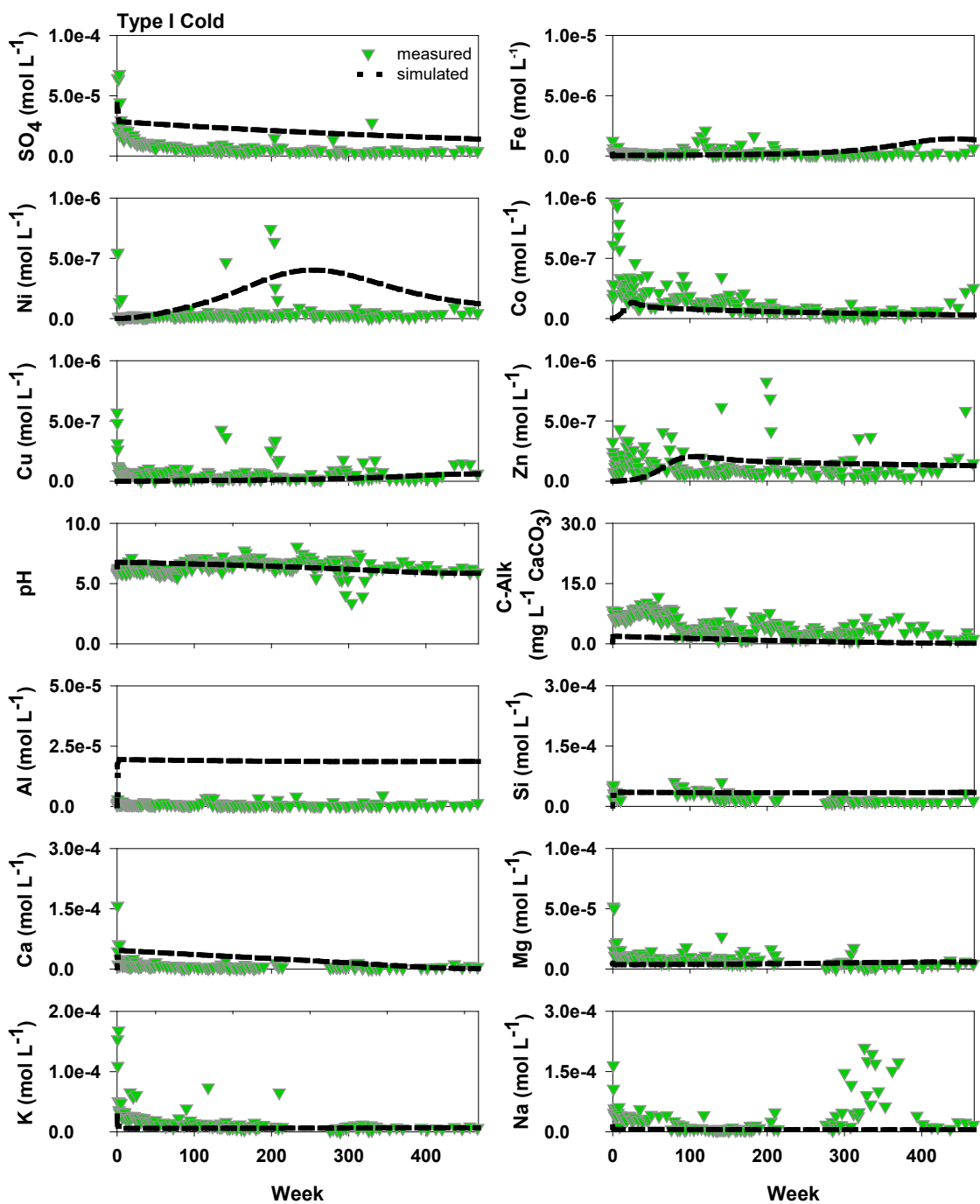


Figure 2.4 Average concentrations of mineral weathering products SO_4 , Ni, Co, Cu, Zn, Fe, Al, Ca, Mg, K, Na, and H_4SiO_4 [mol L^{-1}], pH [-], and alkalinity [as $\text{mg L}^{-1} \text{CaCO}_3$] versus time [weeks] measured in the six Type I cold temperature humidity cell effluent compared to aqueous concentrations exiting the simulation domain.

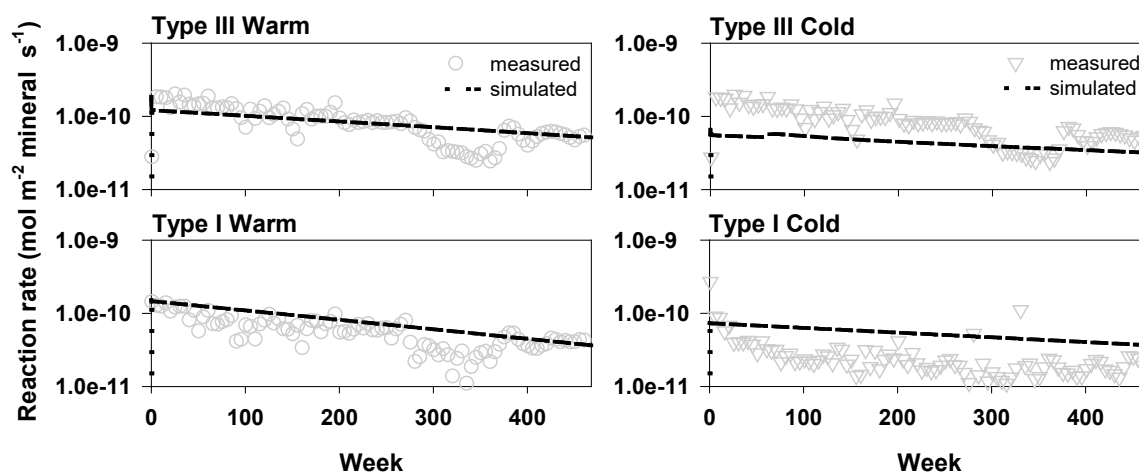


Figure 2.5 Rate of sulfide oxidation [$\text{mol m}^{-2} \text{ mineral s}^{-1}$] versus time [weeks] as estimated from measured SO_4 concentrations in Type I and Type III warm and cold temperature humidity cell effluent compared to simulation results.

2.5 Discussion

The conceptual model presented here was implemented for use in baseline simulations with the intent of developing an integrated conceptual model of sulfide mineral weathering for larger scale field systems. An integrated conceptual model was required to provide a mechanistic description capable of simulating geochemical systems governing smaller scale laboratory and/or field experiments towards the goal of scaling these results to facilitate simulation of the geochemical evolution of full-size waste-rock dumps. The conceptual model and the simulations presented here captured the overall trends and concentrations of the humidity cell effluent quality data. The simulations were conducted such that the best visual fit to all four experimental conditions was obtained and minor divergence between the simulations and measured data occurred, most notably for elements such as Al and Fe for which a large number of processes can potentially control concentrations. For example, the simulated effluent Al concentrations were generally higher than the measured concentrations. This situation arose from implementation of the conceptual model so that it could be scaled to field experiments. Because Al was associated with the dissolution of all of the non-carbonate host minerals, calibration of the simulations to capture the Al effluent concentrations resulted in poorer capture of effluent concentrations than for most of the other elements. Similarly, Fe is associated with reactions

involving a number of solid phases, including sulfide and aluminosilicate minerals and secondary minerals Fe(III)(oxy)hydroxide and jarosite, potentially accounting for the deviations for this element. Differences between simulated and measured concentrations for cations, most notably Cu (Type III warm) and Ni (Type I cold), were likely the result of temperature effects on surface complexation processes that were not accounted for in the simulations. In order to implement a conceptual model that could be scaled, no attempt was made to calibrate adsorption parameters to fit the individual simulations.

The geochemical simulations presented were calibrated to measured solute concentrations in Type III and Type I humidity cell effluents. Simulation parameter adjustment was minimized to maximize parameter consistency and the applicability of the simulations over differing mineralogy while still providing an acceptable fit to all four sets of measured data. The calibration focused on solutes that indicated sulfide mineral oxidation (including SO₄, Ni, Co, Cu, Zn, Fe), pH, and parameters that indicated acid neutralization processes (including Al, Ca, Mg, K, and Na). All hydraulic parameters were fixed during the calibration process. Elevated concentrations of SO₄ and cations at early time (*i.e.*, the first week) were predominantly oxidation products released from blasting and do not reflect long term weathering processes. As such, these were not considered in the simulations because of the focus of the study is the prediction of the long term geochemical evolution of the Diavik waste rock.

2.5.1 Mineral Volume Fraction

Mineral content and the associated parameter mineral surface area are closely tied to sulfide mineral weathering rates (Belzile et al., 2004; Kempton, 2012). For sulfide minerals, the mineral volume fraction was adjusted according to measured S content of differing rock types (*e.g.*, simulating Type I and Type III effluent from cells at 22 °C). Chalcopyrite and ZnS contents were estimated based on Cu and Zn concentrations measured using whole rock analysis of Type III material under the assumption that CuFeS₂ and ZnS were the exclusive sources of Cu and Zn, respectively. The CuFeS₂ and ZnS contents of the Type I material were assumed to represent a corresponding proportion of total sulfide (*i.e.*, the Type III material has ~8 times the sulfide wt.% of the Type I material). The φ_i of Fe_{4.5}Ni_{3.6}Co_{0.9}S₈ was approximated through calibration of the simulations for Type III effluent, then assumed to follow the same proportion as Fe_{0.852}Ni_{0.004}Co_{0.001}S, CuFeS₂, and ZnS when adjusting mineral content to Type I material. In all cases, the calculation of the sulfide mineral contents was constrained by the measured total sulfide mineral content.

An initial particle radius for sulfide minerals of 6.25×10^{-5} m was selected based on observations provided by Langman et al. (2014). After the surface areas (host minerals) and effective rate constants (secondary minerals) of non-sulfide minerals were calibrated for the Type III simulations, no further adjustments were made to parameters involving non-sulfide or secondary minerals when simulating Type I effluent.

Use of the shrinking core model as a central tenet of the conceptual model led to simulation of concentrations of Ni, Co, Cu, Zn, and SO₄ that compared well with measured solute concentrations. This suggests that the shrinking core model is a valid concept for describing sulfide oxidation processes and is consistent with previous studies of the waste rock at Diavik (Langman et al., 2014) and other locations (Wunderly et al., 1996; Brookfield et al., 2006) that indicate the formation of an alteration rim limits the transport of oxidants to the reactive surface. Specifically, the increasing thickness of an alteration rim (resulting from shrinking of the core sulfide grain) leads to a decrease in SO₄ and metal ion release and often to a decline in dissolved solute concentrations. Langman et al. (2015) collected samples from the humidity cell experiments and conducted X-ray absorption spectroscopy and micro X-ray diffraction to investigate the weathering condition of pyrrhotite grains. Analysis of the results indicated the presence of partially and fully oxidized S species within alteration rims that formed on the pyrrhotite grains and the formation of Fe precipitates in close proximity to the pyrrhotite grains (Langman et al., 2015).

2.5.2 Temperature

Given that mine waste rock is commonly stored exposed to ambient temperature, it was important to investigate the effects of temperature on the geochemical evolution of sulfide minerals. Langman et al. (2014) use the Arrhenius expression to represent the temperature dependence of reaction rates for host minerals in the Diavik waste rock, and this approach was also used to account for the temperature dependence of rate expressions in the current study. Reaction rate parameters for non-sulfide minerals were not adjusted between simulations of different material type. To account for the temperature dependence of reaction rates of non-sulfide mineral dissolution, E_a values (Table 2.5) were used to adjust the rate constant according to

$$E_a = \frac{RT_1T_2}{(T_1 - T_2)} \ln \frac{k_1}{k_2}, \quad (2.10)$$

where E_a is activation energy [kJ mol^{-1}], R is the universal gas constant ($8.314 \times 10^{-3} \text{ mol kJ}^{-1} \text{ K}^{-1}$), T_1 and T_2 are temperatures [K], and k_1 and k_2 are rate constants or effective rate constants depending on the mineral being evaluated. Calculations to adjust the rate constant according to temperature were completed internally within MIN3P. The calibrated E_a for calcite was within the range of 8-60 kJ mol^{-1} reported in Morse and Arvidson (2002). The calibrated E_a for dolomite was within the range of values (15-62 kJ mol^{-1}) reported by Gautelier et al. (1999). The calibrated E_a for biotite was within the range of 50-80 kJ mol^{-1} suggested by White et al. (1999) for metal release from silicate minerals. The E_a values for albite and muscovite were not used in the calibration process; the values used for the humidity cell simulations were from Blum and Stillings (1995) and Nagy (1995) respectively.

For the sulfide minerals only, the effective diffusion coefficient was adjusted to fit data from the same material type at a different experimental temperature (*e.g.*, to fit Type III data at 22 and 5 °C). In solid state diffusion, the Arrhenius relationship is often used to describe the temperature dependence of the diffusion coefficient (Borg and Dienes, 1988; Mehrer, 2007) using

$$\Delta H = \frac{RT_1T_2}{(T_1-T_2)} \ln \frac{D_1}{D_2}, \quad (2.11)$$

where ΔH is activation enthalpy [kJ mol^{-1}], R is the universal gas constant ($8.314 \times 10^{-3} \text{ mol kJ}^{-1} \text{ K}^{-1}$), T_1 and T_2 are temperatures [K], and D_1 and D_2 are effective diffusion coefficients [$\text{m}^2 \text{ s}^{-1}$]. After the simulations were calibrated to fit the humidity cell effluent data, activation enthalpies for each of the sulfide minerals were calculated. Note that many authors use the term activation energy when describing the temperature dependence of effective diffusion coefficients in solid state diffusion literature. We use the term activation enthalpy (after Mehrer, 2007) to distinguish the physical temperature dependence of diffusion coefficients from the chemical temperature dependence of rate constants (as described for the temperature dependence of host mineral dissolution). In this context, activation enthalpy refers to the energy required to induce diffusion of an oxidant through the alteration rim of a partially oxidized sulfide mineral. Estimates of ΔH for diffusion of $\text{O}_{2(\text{aq})}$ and Fe^{3+} to the reactive surface of sulfide minerals in the humidity cells (35 kJ mol^{-1}) are required for subsequent simulations of Diavik waste rock in field experiments where a temporally and spatially dynamic temperature regime is present.

2.5.3 Sulfide Oxidation Mechanism and Rate

Separation of sulfide oxidation into oxidant components facilitated assessment of the apparent rates of oxidation by $O_{2(aq)}$ and Fe^{3+} in the simulations (Figure 2.6). The simulated sulfide oxidation reaction rates indicate that sulfide oxidation by $O_{2(aq)}$ dominates the production of SO_4 . The rate of oxidation by Fe^{3+} becomes significant in the Type III simulations as the pH decreases and is closely associated with the peak effluent concentrations of metals Ni, Co, Cu, and Zn. The oxidation rate of the sulfide minerals in the Type I material is dominated by oxidation by $O_{2(aq)}$ throughout the experiment; oxidation by Fe^{3+} does not play a significant role. This observation is consistent with the similar carbonate contents of the Type I and Type III materials and the lower sulfide content of the Type I material, the oxidation of which did not result in a significant decrease in pH.

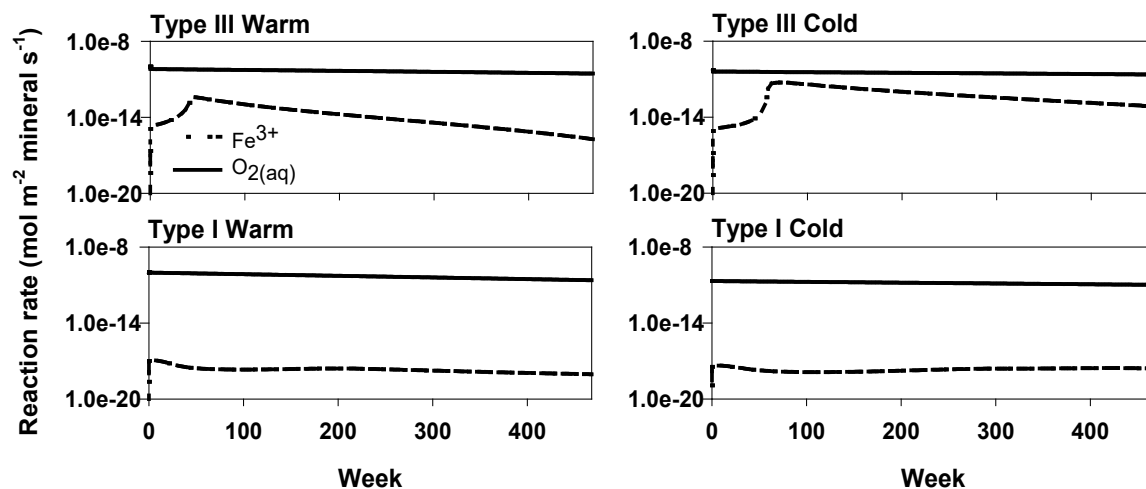


Figure 2.6 Simulated rates of pyrrhotite oxidation [$\text{mol m}^{-2} \text{mineral s}^{-1}$] by $O_{2(aq)}$ and Fe^{3+} versus time [weeks] in Type I and Type III warm and cold humidity cell experiments.

Separation of the $O_{2(aq)}$ and Fe^{3+} oxidation mechanisms facilitated interpretation of the respective effective diffusion coefficients (D). The calibrated effective diffusion coefficients for $O_{2(aq)}$ were consistent for the Type I and Type III sulfide minerals. The lower D ($O_{2(aq)}$) value for ZnS in Type III and Type I simulations could indicate that the estimated volume fraction for ZnS was too high.

Effective diffusion coefficient values for oxidation by Fe^{3+} were consistent among the sulfide minerals; however, the values were approximately eight orders of magnitude higher than values

presented in Mayer et al. (2002), which were consistent with solid state diffusion through iron oxide minerals (Gorski et al., 2012). The higher D^{eff} for Fe^{3+} suggests an alternate process of sulfide oxidation by Fe^{3+} (*i.e.*, not solid state diffusion of Fe^{3+} through the alteration rim on the sulfide grains). Gorski et al. (2012) and Handler et al. (2009) indicate electron conduction is a possible mechanism to explain relatively rapid Fe isotope exchange between Fe^{2+} rich waters and iron oxide minerals. Yanina and Rosso (2008) explain this mechanism is dependent on the introduction of an electric potential gradient across a thickness of material that has low electrical resistivity (*e.g.*, iron oxide minerals) such that redox reactions occurring at one water-mineral interface become coupled to those at a separate water-mineral interface on another face of a crystal. This process is conceptualized by Handler et al. (2009) as a redox-driven conveyor belt and is somewhat analogous to the oxidation of sulfide minerals by Fe^{3+} , in which electron exchange at the Fe(III) (oxy)hydroxide-sulfide mineral interface is coupled to the reduction of Fe^{3+} at the water-Fe(III) (oxy)hydroxide interface. The higher diffusion coefficient for Fe^{3+} oxidation of sulfide minerals, necessary to represent the geochemistry of the humidity cell effluent, is more consistent with the redox-driven conveyor belt mechanism than for solid state diffusion of Fe^{3+} through an iron oxyhydroxide sulfide alteration rim.

The simulated sulfide mineral oxidation reaction rates are consistent (within an order of magnitude) with those calculated by Langman et al. (2014). The consistency in measured and simulated sulfide oxidation rates indicates the simulations of the Type III and Type I humidity cells captured the main oxidation processes of the system.

2.5.4 Acid Neutralization

Analysis of the simulation results highlights the acid neutralization sequence within the humidity cells. Langman et al. (2014) propose an acid neutralization sequence for the Type III material initiated with the dissolution of calcite and followed by dissolution of aluminosilicate and secondary Al minerals (represented in the simulations by gibbsite). Figure 2.7 shows the precipitation and dissolution rates of the main acid-consuming minerals calcite, biotite, and gibbsite. The Type III simulations indicate that the calcite content is exhausted in approximately 100 weeks in the warm temperature cells and in approximately 150 weeks in the cold temperature cells, although the consumption of H^+ ceases prior to this time. The evolution of the acid-neutralization processes results in a steady pH decline as the capacity of calcite to consume H^+ is overwhelmed. Near calcite exhaustion, in the cold cells only, gibbsite dissolution began buffering the effluent to around pH 4.

Gibbsite was present in the system as a result of earlier precipitation and its dissolution subsequently ceases, indicating the increasing effluent pH is a result of declining H^+ production (*i.e.*, reduced sulfide mineral weathering resulting from reduced reactive surface area or increased alteration rim thickness). The dissolution of dolomite and biotite proceeds at a relatively low rate (compared to calcite) throughout the experiment and provides some additional buffering capacity. The pH of the Type III system does not decrease to a value below which Fe(III) (oxy)hydroxide dissolution occurs. Type III simulations conducted with biotite and dolomite excluded from the mineral assemblage indicate that long-term mitigation of acid production from Type III material is likely influenced more by reduced availability of sulfide minerals than by dissolution of these minerals. Simulations involving the Type I mineral assemblage indicate that the calcite volume fraction is large enough to buffer the acid generation resulting from sulfide mineral oxidation until the acid generation is diminished by other processes (*i.e.*, reduction of sulfide mineral availability due to an increased alteration rim thickness).

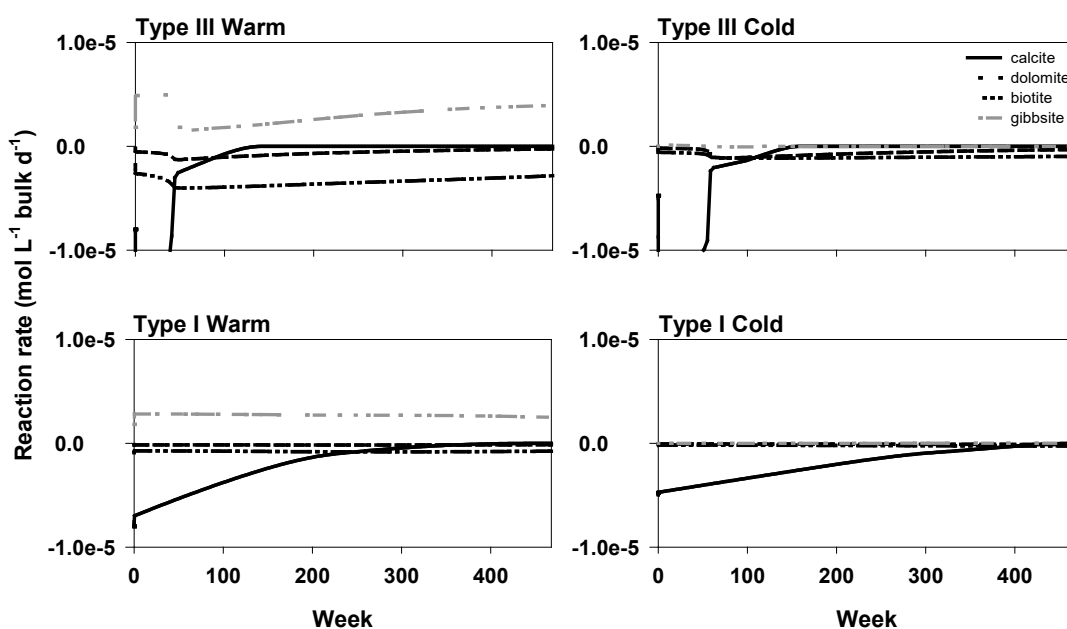


Figure 2.7 Simulated rates of calcite, dolomite, biotite, and gibbsite dissolution/ precipitation [$\text{mol L}^{-1} \text{bulk d}^{-1}$] versus time [weeks] in Type I and Type III warm and cold humidity cell experiments. Rates greater than zero indicate mineral precipitation; rates less than zero indicate mineral

dissolution.

2.6 Conclusions

The close agreement of model results with measured solute concentrations indicates that the integrated conceptual model presented here captured the geochemical evolution of the Diavik waste rock considering both variable temperature and variable sulfide mineral content. Using data collected as part of the DWRP, the simulations identify the significant processes controlling the geochemical evolution of Diavik waste rock, *i.e.*, low quality effluent produced as a result of sulfide mineral oxidation with acid consumed in the short term by carbonate dissolution and improved quality effluent in the longer term primarily due to depletion of the available sulfide minerals. The three major components controlling oxidation of the sulfide minerals identified by the modelling study are mineral surface area, temperature, and pH. Successfully simulating the humidity cell effluent through use of the shrinking core model indicates reduction of available sulfide surface area leads to a declining rate of sulfide oxidation.

Overall, the results suggest that the conceptual model presented here can be used to simulate the geochemical evolution of the DWRP field experiments provided that the dynamic temperature regime and more complex flow system are incorporated. It is unclear at this stage of the scale-up simulation process how the differences between the simulated concentrations and measured concentrations at the humidity cell experiments will impact the scale-up of the conceptual model as implemented; however, it is possible that a larger scale field experiment would provide a better representation of the geochemical conditions within a full size waste-rock pile. This use of primarily DWRP data also indicates that site-specific system characterization is beneficial for mechanistic approaches using reactive transport models to successfully simulate the geochemical evolution of mine waste rock. Characterization should include accurate determination of the average and range of sulfide and carbonate mineral content, measurements to assess the available reactive surface area of sulfide minerals, and grain-size analysis to determine the portion of total mineral content most likely to be geochemically active. Assessment of bulk mineral surface area and water flow and infiltration characteristics as well as general climatic conditions (specifically temperature) are also important considerations when applying reactive transport models to geochemical evolution problems.

Chapter 3

Scale-up of a reactive transport model for temperature and sulfide-content dependent geochemical evolution of waste rock

This chapter is modified from:

Wilson, D., Amos, R.T., Blowes, D.W., Langman, J.B., Smith, L., Segó, D.C. 2018. The Diavik Waste Rock Project: Scale-up of a reactive transport model for temperature and sulfide-content dependent geochemical evolution of waste rock. *Appl. Geochem.* 96, 177-190.

The characterization of the geochemical evolution of mine-waste rock is an important component of mine planning. Elevated concentrations of solutes in effluent water from mine wastes, including metals and SO₄, can result in detrimental impacts to receiving environments such as surface water bodies and groundwater. The issue of waste effluent quality prediction has been problematic for stakeholders for decades requiring development of advanced techniques in this field. Medium-scale field experiments (>1,000 kg and <10,000 kg) such as test cells or barrel experiments are often used to provide specific components of the geochemical evolution of mine waste rock (Demers et al., 2013; Smith et al., 2013a; Parbhakar-Fox and Lottermoser, 2015). The results of medium-scale field experiments can be combined with laboratory scale experiments such as humidity cells to improve the characterization of the geochemical evolution of waste rock beyond that of using humidity cell experiments alone by including field related influences on weathering. Similar to mineral weathering rates derived from humidity cell experiments, weathering rates derived from medium-scale field experiments can be extrapolated to assess the geochemical evolution of full-scale waste-rock piles. This process is commonly referred to as scale-up and typically makes use of empirical scale factors that involve a variety of parameters understood to influence effluent quality. Empirical scale-up factors often include consideration of pH, grain size, moisture content, temperature, oxygen availability, mineral surface area, and water-mineral contact (Kempton, 2012; Amos et al., 2015). Physical heterogeneity (*e.g.*, particle size and mineral distribution) and variable temperatures often limit the application of empirically derived scale-up methods to accurately predict effluent quality at waste-rock dumps (Andrina et al., 2012; Amos et al., 2015). Furthermore, the lack of experimental

testing and large variability in waste-rock characteristics renders empirical scale factors challenging to reliably define for predictive purposes (Amos et al., 2015). Reactive transport models capable of accounting for heterogeneity and variability in physical and geochemical characteristics (*i.e.*, dynamic temperature regime, variably distributed minerals) have the potential to overcome the deficiencies of empirical scale-up factors, providing a more accurate mechanistic approach to scale-up.

The Diavik Waste Rock Project (DWRP) consisted of laboratory and field experiments conducted using waste rock from the Diavik Diamond Mine (Diavik), which is located at Lac de Gras approximately 300 km northeast of Yellowknife, NT, Canada. The different experiment scales of the DWRP were designed to facilitate investigation of mechanistic approaches (*i.e.*, model simulation of physical and chemical processes constrained by measured parameters) to scale-up. The laboratory experiments consisted of small-scale (1 kg sample) humidity cells that were conducted over a period of 9 years. The field experiments comprised medium scale (~9,300 kg) barrel style active zone lysimeter (AZL) experiments and large-scale (~8.2 x 10⁷ kg) highly instrumented test piles both constructed with Diavik waste rock. The three experimental scales provided a large data set that has been used to constrain the reactive transport components of this scale-up research.

Scale-up work conducted previously as part of the DWRP included loading calculations (Bailey, 2013; Sinclair et al., 2015) and conceptual model development using the reactive transport model MIN3P (Wilson et al., 2018a). The development of an integrated conceptual model of sulfide mineral oxidation by simulating the geochemical evolution of Diavik waste rock in humidity cell experiments (Wilson et al., 2018a) is directly related to the work outlined in this paper. In addition, sulfide mineral weathering rates calculated using humidity cell effluent data and sulfide-mineral surface area were used to estimate mass loading from the Type III AZL experiments (Bailey, 2013). The results of these calculations indicated mass loading of more conservative parameters (*e.g.*, Zn, Cu) could be predicted with a reasonable degree of accuracy, however the method was less effective for elements influenced by more complex processes such as secondary mineral precipitation and adsorption. Sinclair et al. (2015) simulated the production of SO₄ in the Type III test pile using a loading-rate model and evaluated hypotheses with respect to the temperature and residence time dependence of the geochemical evolution of the waste rock. The work of other researchers including Mayer et al. (2002), Brookfield et al. (2006), and Demers et al. (2013) have shown the efficacy of mechanistic approaches to the characterization of the mine-waste weathering.

The reactive transport code MIN3P (Mayer et al., 2002) was used to simulate the flow and effluent geochemistry from the AZL experiments. MIN3P is a multi-component reactive transport code through which water flow and kinetically controlled geochemical reactions can be simulated. The code's structure facilitates customized reaction stoichiometry and kinetics, which provide a geochemical framework that is coupled to a governing equation for simulation of variably saturated flow. Geochemical reactions can include mineral dissolution and precipitation, adsorption, complexation, and oxidation-reduction. The simulations were based on the integrated conceptual model of mineral weathering developed for the DWRP humidity cell simulations (Wilson et al., 2018a) using the mineral content associated with the field experiments. The approach used in the study was to adopt the geochemical calibration obtained from the laboratory experiments directly, only the boundary conditions associated with the AZL experiments (infiltration and temperature) and the properties of the waste rock were modified to reflect the measured characteristics at the AZL experiments. No adjustments to the geochemical calibration were made in the simulations documented in this paper. The objective of the simulations of the medium-scale field experiments was to test the efficacy of this mechanistic scale-up approach using the integrated conceptual model developed at the laboratory scale under the dynamic flow and temperature conditions of a field experiment.

3.1 Active Zone Lysimeter Methodology

The AZL experiments were conducted over a period of more than 11 years, from 2005 to 2016, as a component of the DWRP focused on investigating the geochemical evolution of waste rock at the medium scale in the active zone (the upper zone of a waste-rock pile that is most subject to freeze/thaw conditions). The AZL experiments were constructed with two types of waste rock according to sulfur content (Type I = 0.035 wt.% S and Type III = 0.053 wt.% S) (Smith et al., 2013a). Waste rock at Diavik was segregated according to S content as follows: Type I < 0.04 wt.% S and Type III > 0.08 wt.% S. The wt.% S of the Type III AZL experiments was below the Diavik threshold for Type III designation; however, to remain consistent with other DWRP publications the experiment identifiers were not changed to reflect this. The S content of the AZL experiments was not measured directly; however, the experiments were constructed during the same period as the larger DWRP field experiment test piles; the S content of the larger field experiment was used for the AZL simulations. Sulfide-mineral volume fractions of the Type I and Type III AZL experiment waste rock

were slightly different from the sulfide-mineral volume fraction of Diavik humidity cell experiments (0.02 wt.% S and 0.18 wt.% S respectively).

The AZL experiment consisted of four cells in total, with two duplicate cells constructed using Type I waste-rock material and two duplicate cells constructed with Type III waste-rock material. The AZL experiments were contained in HDPE containers measuring approximately 2.2 m in diameter and between 1.5 m (Type I) and 1.7 m (Type III) in height (Bailey et al., 2015; Neuner et al., 2013) (Figure 3.1). The waste-rock material in the AZL cells consisted of rock < 1 m in diameter.

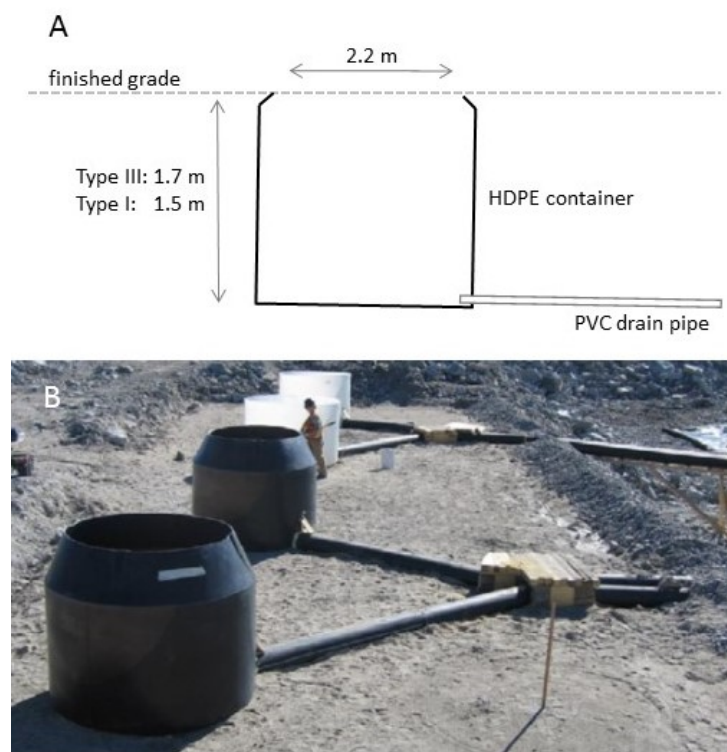


Figure 3.1 A: Cross-sectional conceptual diagram of DWRP active zone lysimeter experiment. B: Active zone lysimeter experiment prior to emplacement of run-of-mine rock within and surrounding containers. Active zone lysimeter containers are filled and surrounded with Type III or Type I run-of-mine material.

The waste rock contained in the AZL experiments was extracted from the same source rock as the material used in the humidity cells and test piles and included approximately 75% granite (primarily quartz [SiO₂], K-feldspar [KAlSi₃O₈], and albite [NaAlSi₃O₈]), 14% pegmatitic granite, 10% biotite

schist, and 1% diabase (Blowes & Logsdon, 1998; Langman et al., 2014). The primary source of metal sulfide minerals was biotite schist, which was composed primarily of albite (35–55%), quartz (20–50%), and biotite [$\text{KMg}_2\text{FeAlSi}_3\text{O}_{10}(\text{OH})_2$] (10–25%), and contained a mean sulfide content of 0.24 wt.% S (Langman et al., 2014). The primary metal sulfide mineral in the waste material was pyrrhotite [$\text{Fe}_{(1-x)}\text{S}$] with minor substitution of Ni and Co for Fe in the following approximate ratio: $\text{Fe}_{0.852}\text{Ni}_{0.004}\text{Co}_{0.001}\text{S}$ (Jambor, 1997). Smaller portions of other metal-sulfide minerals were present in the waste rock including chalcopyrite [CuFeS_2], sphalerite [ZnS], and pentlandite [$(\text{Fe,Ni})_9\text{S}_8$] (Langman et al., 2014). Variation in mineralogy between and within the experiments was expected due to differences in haul truck loads used for construction.

AZL simulation sulfide-mineral volume fractions were modified to reflect the measured mineral volume fraction of the Type I and Type III AZL experiments. In keeping with the integrated conceptual model, mineral volume fractions for CuFeS_2 , ZnS , and $(\text{Fe,Ni})_9\text{S}_8$ were assumed to follow the same proportions established by Wilson et al. (2018a). In all cases the measured total sulfide-mineral content was used to constrain the sulfide-mineral content calculations.

Mineral volume fractions for all sulfide and host minerals were reduced to 20% of their calculated value to reflect the mineral volume fraction that represented the matrix material as a portion of the bulk material in the AZL experiment. Neuner et al. (2013) reported a value of ~18% of the bulk material as being matrix material (< 5 mm diameter). Smith et al. (2013c) indicated that variation in the proportion of matrix material between Type I and Type III material was likely due to the biotite schist content (higher biotite schist in Type III material led to higher matrix material proportion of the bulk material). The variability in matrix material proportion with waste-rock type was not considered as part of the simulations documented in this paper.

Each of the AZLs contained approximately 9,300 kg of waste rock, which was exposed to atmospheric conditions throughout the experiments. Precipitation was measured using rain gauge tipping buckets located at the DWRP research area (Figure 3.2). Supplemental water (total volume of ~233 L) was added to the Type III experiment in 2007 and 2008 during a tracer test; this additional water was included in the flow portion of the simulations. The water for the tracer tests was obtained from Lac de Gras and had circumneutral pH and concentrations of cation and anion parameters that were typically at least an order of magnitude below AZL effluent concentrations. Flow volume at the AZL experiments was measured using tipping bucket rain gauges (Bailey et al., 2015). Samples of the

AZL experiment effluent were collected every 3-5 days throughout the 2007 to 2016 flow seasons (generally May to October of each year) and analyzed for cation and anion parameters including Fe, Ni, Co, Cu, Zn, Al, Si, Ca, Mg, K, Na, and SO₄ and general parameters including pH and alkalinity (Bailey et al., 2015).

The mean annual air temperature (1998-2007) in the Diavik area was approximately -9 °C with considerable seasonal variation from an average maximum summer temperature of 18 °C to an average minimum winter temperature of -31 °C (Smith et al., 2013a). The temperature of the AZL experiments developed a somewhat muted response to seasonal variations of air temperature (Bailey et al., 2015), resulting in fully thawed conditions during approximately 4 months of the spring, summer, and fall seasons and fully frozen conditions during approximately 8 months of the fall, winter, and spring periods (Figure 3.2).

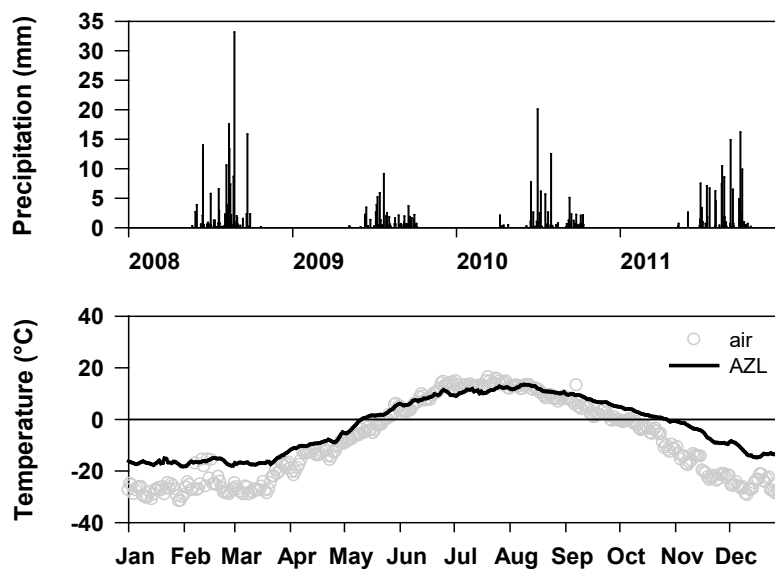


Figure 3.2 Precipitation (rain only) at the DWRP research area for the period 2008 to 2011 and average daily air temperature and average daily AZL internal temperature for the period 2009 to 2015.

3.2 Conceptual Model

The conceptual model presented here was based on the integrated conceptual model presented by

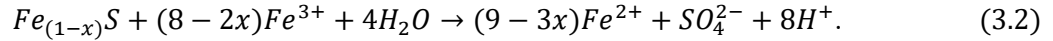
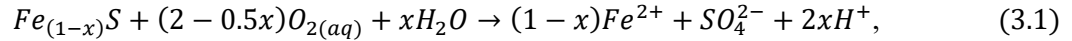
Wilson et al. (2018a) for the simulation of weathering of low-sulfide waste rock. The term integrated was used to refer to a conceptual model based on measurable parameters (*e.g.*, mineral surface area and volume fraction) that can be scaled to larger experiments and includes considerations for temporally variable infiltration and temperature. The mineralogy included in the version of the integrated conceptual model described here was specific to this site. The integrated conceptual model was designed specifically to simulate sulfide-mineral weathering in a mechanistic manner accounting for temperature variation for use in a scale-up capacity. The physical parameters were based on the DWRP AZL experiments described by Smith et al. (2013a) and Neuner et al. (2013).

Water flow through the AZL experiments was simulated as temporally discontinuous events based on precipitation data (Figure 3.2) collected as part of the DWRP at the test-piles research area. The net infiltration volume was estimated using the FAO Penman-Monteith (FAO P-M) method to calculate evaporative losses from the AZL experiments for periods when the ground temperature was above 0°C (Neuner et al., 2013). With the exception of two supplemental, manually applied precipitation events (tracer tests) at the Type III AZL experiment in 2007 and 2008, the infiltration at both the Type I and Type III AZL experiments was the same throughout the simulations. Infiltration through the AZL system was dominated by flow through the matrix material (Neuner et al., 2013) indicating that flow can be simulated appropriately using the Richards equation. Simulated infiltrating water quality was determined from geochemical analysis of 13 rain samples that were collected during 2014 and 2015. Average precipitation sample concentrations of Fe, Ni, Co, Cu, Zn, Al, Si, Ca, Mg, K, Na, and SO₄ were typically at least two orders of magnitude lower than in the AZL experiment effluent.

The effects of water freezing were not considered as part of the AZL experiment simulations. Because water flow through the domain was mainly driven by pore-water displacement, very low or zero outflow occurred during periods of no infiltration. The periods of zero infiltration were closely related to periods when temperatures within the AZL experiments were below freezing (typically late October to early May) or during dry summer periods with little to no precipitation. In an average year, there were typically two primary infiltration periods, the first during late May and June with a second in late September and early October. Infiltration of snow melt was not considered a significant factor in the infiltration calculations because most snow was removed from the surface of the AZL experiments by wind scour before melting occurred (Neuner et al., 2013).

Temperature for the simulations was based on the average of three temperature sensors located at depths of 0.3, 0.6, and 1.0 m. Temperature data was collected at the AZL experiments during the period of 2009 to 2015 using Decagon Devices 5TM soil moisture and temperature probes.

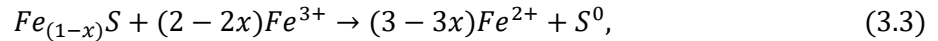
Similar to the conceptual model developed for the DWRP humidity cell experiments, elevated concentrations of SO₄, Ni, Co, Cu, and Zn from the AZL experiments were the result of sulfide-mineral oxidation processes. Commonly recognized sulfide mineral oxidants O_{2(aq)} and Fe³⁺ (Nordstrom & Southam, 1997; Blowes et al., 2003) were considered to be the drivers of the dominant geochemical processes in the simulations. The oxidation of pyrrhotite by O_{2(aq)} and Fe³⁺ can be represented with the following reaction stoichiometry (Nicholson and Scharer, 1998; Janzen et al., 2000; Belzile et al., 2004):



Pyrrhotite, CuFeS₂, ZnS, and (Fe,Ni)₉S₈ oxidation by O_{2(aq)} were simulated using versions of equation 3.1 specific to each of the metal sulfide minerals (Table 3.1).

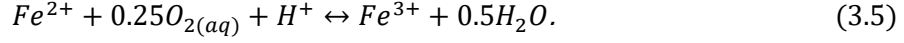
Sulfide-mineral oxidation by Fe³⁺ was described separately from oxidation by O_{2(aq)} using three parallel reactions representing the sulfide-mineral oxidation pathway proposed by Schippers and Sand (1999). The reaction mechanism of metal sulfide-mineral oxidation by Fe³⁺ presented by Schippers and Sand (1999) included intermediary sulfur species, which were represented in the conceptual model by elemental S (S⁰) because it was commonly the primary S intermediary in the oxidation of Fe_(1-x)S (Schippers and Sand, 1999).

The following generalized reaction stoichiometry (Nicholson and Scharer, 1998) represented the introduction of S⁰ (Table 3.1):



Equation 3.5 completes the set of reactions that exert primary control on the oxidation of sulfide minerals in the simulations. The oxidation of Fe²⁺ was a kinetically controlled reaction included to

consider the replenishment of Fe^{3+} in the system (Singer and Stumm, 1970; Schippers and Sand, 1999; Rohwerder et al., 2003):



The shrinking core model (Levenspiel, 1972; Wunderly et al., 1996; Mayer et al., 2002) was used to simulate the rates of sulfide-mineral oxidation. In this instance, the shrinking core model describes mineral dissolution limited by diffusive flux of a reactant through an outer enveloping layer to an unreacted core (Mayer et al., 2002). Rate expressions representing the shrinking core model were used for each of the sulfide minerals to simulate the rate of oxidation by $O_{2(aq)}$ and Fe^{3+} . The following example rate expressions represented the oxidation of Diavik $Fe_{(1-x)}S$ by $O_{2(aq)}$ and Fe^{3+} respectively (after Mayer et al., 2002).

$$R_{Po\ ox} = -10^3 S_{Fe_{0.852}Ni_{0.004}Co_{0.001}S} \left[\frac{r_p}{(r_p - r_r)r_r} \right] D_{O_{2(aq)}} \left[\frac{O_{2(aq)}}{1.9285} \right], \quad (3.6)$$

$$R_{Po\ ox} = -10^3 S_{Fe_{0.852}Ni_{0.004}Co_{0.001}S} \left[\frac{r_p}{(r_p - r_r)r_r} \right] D_{Fe^{3+}} \left[\frac{Fe^{3+}}{1.714} \right], \quad (3.7)$$

where $R_{Po\ ox}$ represented the rate of pyrrhotite oxidation [$mol\ L^{-1}\ d^{-1}$] and $S_{Fe_{0.852}Ni_{0.004}Co_{0.001}S}$, r^p , r^r , and $D_{O_{2(aq)}}$ and $D_{Fe^{3+}}$ represented the reactive surface area [$m^2\ mineral\ L^{-1}\ porous\ medium$], average particle radius [m], unreacted particle radius [m], and effective diffusion coefficient [$m^2\ s^{-1}$] for $O_{2(aq)}$ and Fe^{3+} diffusion to the unreacted surface, respectively. The rate of oxidation of each sulfide mineral was represented by one rate expression for oxidation by $O_{2(aq)}$ and one rate expression for oxidation by Fe^{3+} that acted separately on the same mineral volume fraction.

The following rate expression is associated with Fe^{2+} oxidation (Equation 3.5) (after Singer and Stumm, 1970; Mayer et al., 2002; Roden, 2008):

$$R_{Fe^{2+} \rightarrow Fe^{3+}} = -S_1 k_{1_{Fe^{2+} \rightarrow Fe^{3+}}} [Fe^{2+}] [O_{2(aq)}] - S_2 k_{2_{Fe^{2+} \rightarrow Fe^{3+}}} [Fe^{2+}] [O_{2(aq)}] [OH^-]^2 - S_3 k_{3_{Fe^{2+} \rightarrow Fe^{3+}}} \left[\frac{[Fe^{2+}]}{K_S + [Fe^{2+}]} \right], \quad (3.8)$$

where $R_{Fe^{2+} \rightarrow Fe^{3+}}$ represented the rate of Fe^{2+} oxidation [$mol\ L^{-1}\ d^{-1}$]. The first two terms on the right side of equation 3.8 represented the chemical oxidation of Fe^{2+} by $O_{2(aq)}$ with S , $k_{1_{Fe^{2+} \rightarrow Fe^{3+}}}$, and $k_{2_{Fe^{2+} \rightarrow Fe^{3+}}}$ representing a scaling factor [-], the reaction rate constant for $pH < \sim 3.5$ [$L\ mol^{-1}\ d$

^{1]} (Singer and Stumm, 1970), the reaction rate constant for $\text{pH} > \sim 4.5$ [$\text{mol L}^{-1} \text{d}^{-1}$] (Singer and Stumm, 1970), respectively. The third right hand term in equation 3.8 represented the biotic oxidation of Fe^{2+} where $k_{3_Fe^{2+} \rightarrow Fe^{3+}}$ and K_s are the reaction rate constant [$\text{mol L}^{-1} \text{d}^{-1}$] and half-saturating concentration [mol L^{-1}], respectively. Bailey et al. (2015) indicated Fe-oxidizing bacteria were present in the effluent of one of the Type III AZL experiments.

The following rate expression was associated with the oxidation of S^0 to SO_4 by $\text{O}_{2(\text{aq})}$ (Equation 3.4) (after Roden, 2008):

$$R_{\text{S}^0 \rightarrow \text{SO}_4} = -k_{\text{S}^0 \rightarrow \text{SO}_4} \left[\frac{[\text{S}^0]}{K_s + [\text{S}^0]} \right], \quad (3.9)$$

where $R_{\text{S}^0 \rightarrow \text{SO}_4}$ represented the rate of biotic S^0 oxidation by oxygen [$\text{mol L}^{-1} \text{d}^{-1}$] and $k_{\text{S}^0 \rightarrow \text{SO}_4}$ and K_s represented the reaction-rate constant [$\text{mol L}^{-1} \text{d}^{-1}$] and half-saturating concentration [mol L^{-1}] respectively.

Geochemically active host minerals were included in the simulations to capture the non-sulfide related components of the effluent geochemistry. Weathering of host minerals was simulated as a set of surface controlled reactions according to the reaction stoichiometry and rate expressions presented in Tables 3.1 and 3.2. The dissolution of host minerals was kinetically controlled and irreversible with the exception of the dissolution of calcite and dolomite, which were simulated as reversible.

Geochemical speciation modelling of the AZL experiment effluent indicated that iron-bearing oxide minerals Fe(III) (oxy)hydroxide and goethite, gypsum, hydroxysulfate minerals jarosite and alunite, and the aluminum-bearing oxide mineral gibbsite were at or above saturation for at least a portion of the AZL experiments (Bailey et al., 2015). Secondary minerals commonly observed in association with weathered sulfide minerals including Fe(III) (oxy)hydroxide [$\text{Fe}(\text{OH})_3$], jarosite [$\text{KFe}_3(\text{SO}_4)_2(\text{OH})_6$], gypsum [$\text{CaSO}_4 \cdot 2\text{H}_2\text{O}$], siderite [FeCO_3], and gibbsite [$\text{Al}(\text{OH})_3$] (Blowes et al., 2003; Jambor, 2003) were selected as part of the DWRP humidity cell simulations (Wilson et al., 2018a) to represent the iron or aluminum bearing oxide and hydroxysulfate minerals in the system, and were included in the AZL simulations (Tables 3.1 and 3.2). Amorphous silica [SiO_2] was included in the system due to the likelihood of excess Si derived from aluminosilicate weathering. All secondary minerals were allowed to precipitate or dissolve according to equilibrium constraints specific to each mineral (Tables 3.1 and 3.2).

The exposure of the AZL experiments to atmospheric conditions necessitated the incorporation of temporal temperature variations within the integrated conceptual model. This development was a key component for the implementation of a small to medium size experiment scale-up scheme (specifically when scaling from laboratory to field scale experiments). The results of the humidity cell simulations, combined with the Arrhenius expression, were used to calculate the effects of temperature on the geochemical weathering of the Diavik waste rock (Wilson et al., 2018a). For reactions involving sulfide minerals the temperature dependent diffusion coefficient was adjusted to daily temperature variation using the activation enthalpy calculated as part of the humidity cell simulations (Wilson et al., 2018a). Standard temperature diffusion coefficients (Table 3.4) were calculated with the activation enthalpy and calibrated diffusion coefficients from the humidity cell simulations (Wilson et al., 2018a) using equation 3.10.

$$\Delta H = \frac{RT_1T_2}{(T_1-T_2)} \ln \frac{D_1^{eff}}{D_2^{eff}} \quad (3.10)$$

The MIN3P code was modified to account for the temperature dependence of the diffusion coefficient associated with the weathering of sulfide minerals using equation 3.10 to calculate the temperature dependent diffusion coefficients.

The temperature dependence of non-sulfide mineral weathering rates was considered in the AZL experiment simulations using the activation energy concept outlined in the development of the conceptual model of Diavik waste rock weathering (Wilson et al., 2018a) (*i.e.*, using activation energy and the Arrhenius equation). No adjustments were made to the activation energy values in scaling from the humidity cell experiment simulations to the AZL experiment simulations.

Table 3.1 Reaction stoichiometry minerals included in simulations

Mineral	Sulfide Mineral Reaction	log K_i
pyrrhotite	$Fe_{0.852}Ni_{0.004}Co_{0.001}S + 0.143H_2O + 1.9285O_{2(aq)} \rightarrow$ $0.852Fe^{2+} + 0.004Ni^{2+} + 0.001Co^{2+} + SO_4^{2-} + 0.286H^+$ $Fe_{0.852}Ni_{0.004}Co_{0.001}S + 1.714Fe^{3+}$ $\rightarrow 2.566Fe^{2+} + 0.004Ni^{2+} + 0.001Co^{2+} + S^0$	134.66
sphalerite	$ZnS + 2O_{2(aq)} \rightarrow Zn^{2+} + SO_4^{2-}$ $ZnS + 2Fe^{3+} \rightarrow 2Fe^{2+} + Zn^{2+} + S^0$	--
chalcopyrite	$CuFeS_2 + 4O_{2(aq)} \rightarrow Cu^{2+} + Fe^{2+} + 2SO_4^{2-}$ $CuFeS_2 + 4Fe^{3+} \rightarrow 5Fe^{2+} + Cu^{2+} + 2S^0$	--
pentlandite	$Fe_{4.5}Ni_{3.6}Co_{0.9}S_8 + 16.5O_{2(aq)} + 2H^+ \rightarrow$ $4.5Fe^{2+} + 3.6Ni^{2+} + 0.9Co^{2+} + 8SO_4^{2-} + H_2O$ $Fe_{4.5}Ni_{3.6}Co_{0.9}S_8 + 18Fe^{3+} \rightarrow 22.5Fe^{2+} + 3.6Ni^{2+} + 0.9Co^{2+} + 8S^0$	--
Host Mineral Reaction		
calcite	$CaCO_3 \rightarrow Ca^{2+} + CO_3^{2-}$	-8.48
dolomite	$MgCa(CO_3)_2 \rightarrow Mg^{2+} + Ca^{2+} + 2CO_3^{2-}$	-17.09
biotite	$KMg_2Fe(AlSi_3O_{10})(OH)_2 + 10H^+$ $\rightarrow K^+ + 2Mg^{2+} + Fe^{2+} + Al^{3+} + 3H_4SiO_4$	--
muscovite	$KAl_2(AlSi_3O_{10})(OH)_2 + 10H^+ \rightarrow K^+ + 3Al^{3+} + 3H_4SiO_4$	--
albite	$NaAlSi_3O_8 + 4H_2O + 4H^+ \rightarrow Na^+ + Al^{3+} + 3H_4SiO_4$	--
Secondary Mineral Reaction		
Fe(III) (oxy)hydroxide	$Fe(OH)_{3(am)} + 3H^+ \leftrightarrow Fe^{3+} + 3H_2O$	4.89
jarosite	$KFe_3(SO_4)_2(OH)_6 + 6H^+ \leftrightarrow K^+ + 3Fe^{3+} + 2SO_4^{2-} + 6H_2O$	-9.21
silica(am)	$SiO_2 + 2H_2O \leftrightarrow H_4SiO_4$	-2.71
gibbsite	$Al(OH)_{3(am)} + 3H^+ \leftrightarrow Al^{3+} + 3H_2O$	8.11
gypsum	$CaSO_4 \cdot 2H_2O \leftrightarrow Ca^{2+} + SO_4^{2-} + 2H_2O$	-4.58
siderite	$FeCO_3 \rightarrow Fe^{2+} + CO_3^{2-}$	-10.93

Table 3.2 Rate expressions for dissolution of host and secondary minerals

Host Minerals	Rate Expression
calcite	$R = -S_{CaCO_3} [10^{-0.05}[H^+] + 10^{-6.19}[H_2O] + 10^{-3.30}[H_2CO_3]] \left[1 - \frac{IAP}{10^{-8.46}}\right]$
dolomite	$R = -S_{MgCa(CO_3)_2} [10^{-2.59}[H^+]^{0.75} + 10^{-7.66} + 10^{-4.00}[H_2CO_3]^{0.75}] \left[1 - \frac{IAP}{10^{-17.09}}\right]$
biotite	$R = -S_{KMg_{1.6}Fe_{1.4}(AlSi_3O_{10})(OH)_2} k_1 [H^+]^{0.25}$
muscovite	$R = -S_{KAl_2(AlSi_3O_{10})(OH)_2} [k_1 [H^+]^{0.08} + k_2 [H^+]^{-0.1}]$
albite	$R = -S_{NaAlSi_3O_8} [k_1 [H^+]^{0.49} + k_2 [H^+]^{-0.3}]$
Secondary Minerals	
Fe(III) (oxy)hydroxide	$R = k_{Fe(OH)_3}^{eff} \left[1 - \frac{IAP}{10^{4.89}}\right]$
jarosite	$R = k_{KFe_3(SO_4)_2(OH)_6}^{eff} \left[1 - \frac{IAP}{10^{-9.21}}\right]$
silica(am)	$R = k_{SiO_2}^{eff} \left[1 - \frac{IAP}{10^{-2.71}}\right]$
gibbsite	$R = k_{Al(OH)_3}^{eff} \left[1 - \frac{IAP}{10^{-8.11}}\right]$
gypsum	$R = k_{CaSO_4 \cdot 2H_2O}^{eff} \left[1 - \frac{IAP}{10^{4.58}}\right]$
siderite	$R = k_{FeCO_3}^{eff} \left[1 - \frac{IAP}{10^{10.93}}\right]$

3.3 Model Parameters

The simulations were conducted using domains that reflected the different physical boundaries (depths) of the Type I and Type III AZL experiments. The Type I and Type III domains were constructed as 1-D columns with depths of 1.45 m and 1.70 m and discretized in the z-direction as 145 and 170 1 cm control volumes respectively. The simulations were run for 1461 d that

corresponded to the years 2008-2011 when Diavik experienced relatively stable precipitation with the average annual rainfall within 6% of the longer term (1999-2006) average (Smith et al., 2013a).

Simulation temperature was specified on a daily basis using the average daily temperature (averaged over the 6 year period of collected measurements) and was spatially constant within the AZL simulations. For the simulations the daily temperature of AZL experiments was assumed to be the same from year to year (*e.g.*, simulation temperature on July 1, 2008 was the same as the simulation temperature on July 1, 2011). Physical parameters such as matrix porosity, hydraulic conductivity, and soil hydraulic function parameters (Table 3.3) were based on the work of Neuner et al. (2013). Because water flow through the system was found to be matrix dominated (Neuner et al. 2013), the porosity used in the simulations was the porosity of the matrix material as a proportion of the total volume of the AZL experiments. The porosity of the matrix material as a proportion of the total volume of the waste rock was measured using two different methods by Neuner et al. (2013) who provided a range of 0.05 to 0.07 for this parameter. Sulfide and carbonate mineral volume fractions (ϕ_i) (Tables 3.4 and 3.5) were estimated using values obtained from carbon sulfur analysis on samples of fine fraction (< 4 mm) waste rock used to construct the AZL experiments (Bailey et al., 2015; Langman et al., 2014). Chalcopyrite and ZnS ϕ_i were calculated using the results of bulk metal analysis conducted on humidity cell samples; $\text{Fe}_{4.5}\text{Ni}_{3.6}\text{Co}_{0.9}\text{S}_8$ ϕ_i was calibrated as part of the humidity cell simulations (Wilson et al., 2018a). Host ϕ_i values (Table 3.5) were based on the general waste-rock content documented by Jambor (1997).

Table 3.3 Physical parameters used in simulations

Parameter	Value
hydraulic conductivity ¹	9.0×10^{-6}
van Genuchten hydraulic parameters ²	
α	6.9
n	1.5
infiltration rate ³	variable
porosity ⁴	0.06

¹Hydraulic conductivity based on experiments of Neuner et al. (2013) in m s^{-1} .

²Van Genuchten parameters based on work of Neuner et al. (2013); α in m^{-1} , n is unitless.

³Infiltration rate determined by FAO Penman-Monteith method.

⁴Porosity based on porosity of matrix material as a proportion to the total porosity of the AZL.

Table 3.4 Initial volume fraction and rate data for sulfide minerals in AZL experiment simulations

Mineral	Type III $\phi_i^{1,2}$	Type I $\phi_i^{1,2}$	D^{eff} (25 °C)
pyrrhotite – $O_{2(aq)}$	1.1×10^{-4}	7.0×10^{-5}	2.6×10^{-13}
pyrrhotite – Fe^{3+}			1.2×10^{-9}
chalcopyrite - $O_{2(aq)}$	3.2×10^{-6}	2.2×10^{-6}	3.5×10^{-13}
chalcopyrite - Fe^{3+}			1.2×10^{-9}
sphalerite - $O_{2(aq)}$	3.6×10^{-6}	2.4×10^{-6}	4.6×10^{-14}
sphalerite - Fe^{3+}			1.2×10^{-9}
pentlandite - $O_{2(aq)}$	1.3×10^{-6}	8.8×10^{-7}	4.6×10^{-13}
pentlandite - Fe^{3+}			1.2×10^{-9}

Reactions are transport controlled with $r^p = 0.0625$ mm (after Langman et al., 2014); effective diffusion coefficient (D^{eff}) from Wilson et al. (2018a) in $m^2 s^{-1}$; estimated surface area of $1 m^2 g^{-1}$ (Langman et al., 2014).

¹Total sulfide-mineral content based on results of static testing after Smith et al. (2013b); Bailey et al. (2015); chalcopyrite and sphalerite content based on Cu and Zn content from whole rock analysis; pentlandite content calibrated based on Ni and Co concentrations in humidity cell effluent.

²Calculated using density specific to each mineral in m^3 mineral m^{-3} porous medium.

Table 3.5 Initial volume fraction and rate data for host and secondary minerals in Type III and Type I simulations

Mineral	Type III $\phi_i^{1,2}$	Type I $\phi_i^{1,2}$	k/k^{eff}	E_a^3	S_i
calcite	3.1×10^{-5}	4.8×10^{-5}	$k_1 = 10^{-0.05}$ $k_2 = 10^{-6.19}$ $k_3 = 10^{-3.30}$	21	--
dolomite	3.6×10^{-5}	4.2×10^{-5}	$k_1 = 10^{-2.59}$ $k_2 = 10^{-7.66}$ $k_3 = 10^{-4.00}$	42	--
biotite ⁴	9.4×10^{-3}	5.2×10^{-3}	$10^{-10.97}$	63	20
muscovite ⁴	3.2×10^{-3}	3.2×10^{-3}	$k_1 = 10^{-12.60}$ $k_2 = 10^{-13.50}$	22	7
albite ⁴	3.0×10^{-2}	2.0×10^{-2}	$k_1 = 10^{-9.69}$ $k_2 = 10^{-14.15}$	58	6
Fe(III) (oxy)hydroxide ⁵	--	--	10^{-8}	--	--
k-jarosite ⁵	--	--	10^{-8}	--	--
gibbsite ⁵	--	--	10^{-12}	--	--
silica (am) ⁵	--	--	10^{-6}	--	--
gypsum ⁵	--	--	10^{-6}	--	--
siderite ⁵	--	--	10^{-9}	--	--

¹Mineral content of carbonate minerals based on static testing (after Bailey et al., 2015); mineral content of host minerals based on results presented in Jambor 1997.

²Calculated using $\rho_b = 1.62 \text{ g cm}^{-3}$ in m^3 mineral m^{-3} porous medium and adjusted during simulation calibration.

³Activation energy in kJ mol^{-1} .

⁴Calibrated surface area in m^2 mineral L^{-1} porous medium based on mineral volume fraction and bulk surface area after Langman et al. (2014) and adjusted to fit measured humidity cell effluent parameters (Wilson et al., 2018a). Calibrated activation energy (Wilson et al., 2018a).

⁵Calibrated effective rate constant in mol L^{-1} porous medium s^{-1} (Wilson et al., 2018a).

3.4 Results

Simulated water outflow volume for the Type I and Type III AZL experiments compared to average measured outflow volume indicated the simulations provided an accurate representation of flow

regime at the AZL experiments (Figure 3.3). Infiltration to the simulation domain resulted in outflow 1 to 2 d following infiltration consistent with wetting front velocity ranging from 1.9 m d^{-1} to 0.7 m d^{-1} for the AZL experiments calculated by Neuner et al. (2013). Water residence time estimated using a simulated tracer test was approximately 70 days (Figure 3.4), consistent with a residence time between 72 and 85 days estimated using a pore-water velocity through the AZL experiments calculated by Neuner et al. (2013) of approximately 0.02 m d^{-1} . The average error (*i.e.*, difference between measured outflow volume and simulated outflow volume as a percentage of measured outflow) associated with the flow simulation over the four year period of the simulations was calculated to be less than 10% for both Type I and Type III flow. The simulated cumulative annual outflow compared very well with the FAO P-M estimated annual infiltration and deviated from the measured annual outflow in a similar manner (Figure 3.5). The consistency between the simulated outflow and the FAO P-M infiltration suggested that the FAO P-M estimates were a source of error in the AZL water flow simulations or that the simulation was not fully capturing the water storage mechanism at the AZL experiment. Volumetric water content (VWC) simulated at the Type III AZL compared well with VWC measured at the AZL experiments. The simulated results indicated VWC averaging approximately 0.15, which was consistent with the observed values. These unsaturated conditions facilitated oxygen ingress to the matrix material (Figure 3.6).

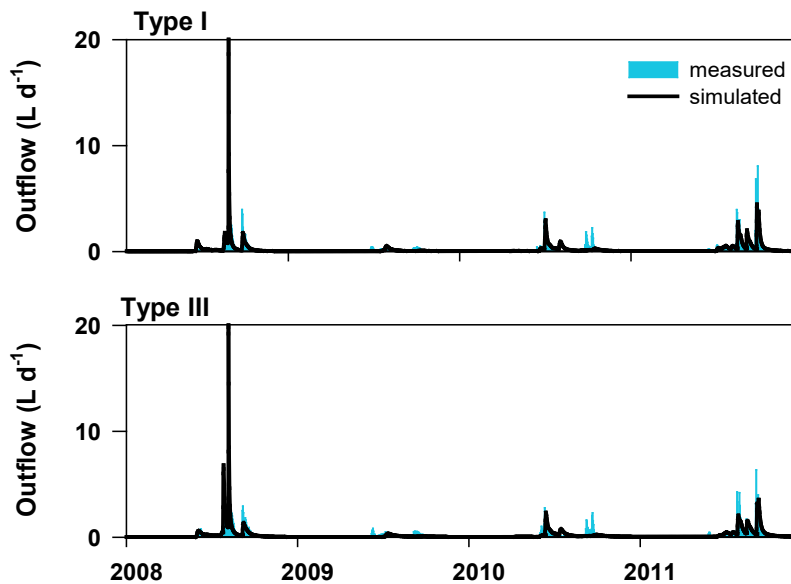


Figure 3.3 Daily outflow [$L d^{-1}$] versus time [year] measured and simulated for the Type III and Type I AZLs.

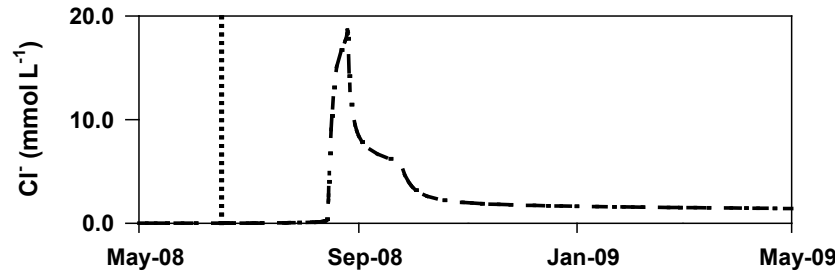


Figure 3.4 Simulated Cl^- concentration [$mmol L^{-1}$] (dashed line) in Type III AZL effluent versus time [month-year] following injection on June 16, 2008 (vertical dotted line). Peak effluent tracer concentration occurred on August 25, 2008, approximately 70 days after tracer injection.

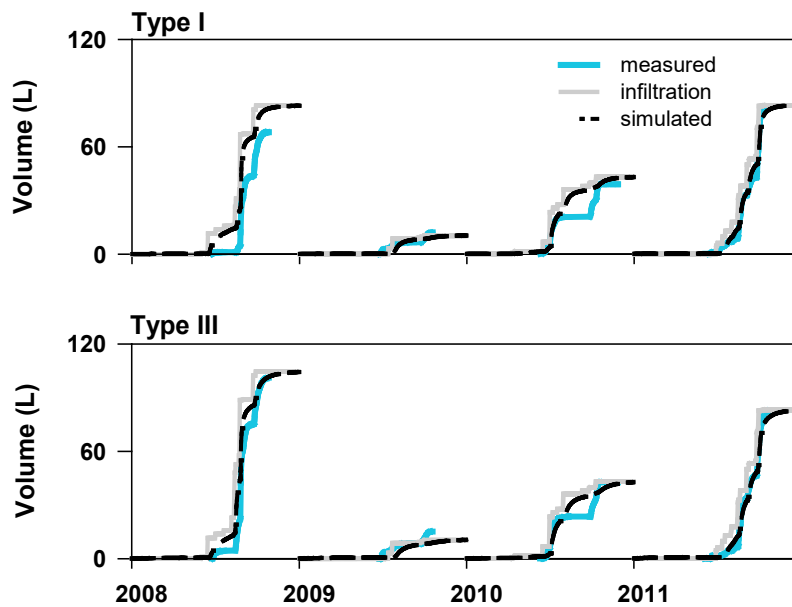


Figure 3.5 Cumulative annual outflow [L] and cumulative annual estimated infiltration (using FAO-Penman Monteith method) versus time [year] measured and simulated at the Type III and Type I AZLs.

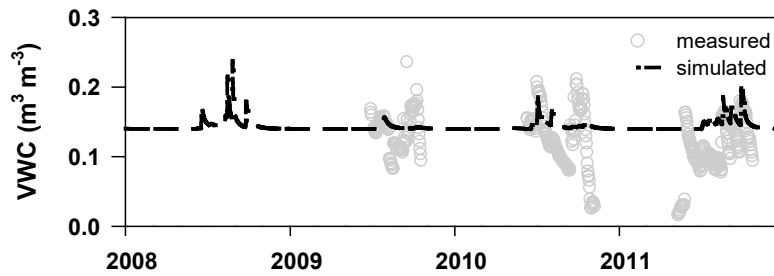


Figure 3.6 Volumetric water content [$\text{m}^3 \text{m}^{-3}$] versus time [year] measured and simulated at approximately 1.0 m depth at the Type III AZL. Measured values are available only for periods where AZL $T > 0^\circ\text{C}$; simulated values were calculated by the model for all periods regardless of temperature condition.

The simulations of effluent geochemistry were compared to the data measured from samples collected at the AZL drains for sulfide-mineral oxidation products SO_4 , Fe, Ni, Co, Cu, and Zn and other solutes and parameters that indicated mineral weathering including Al, Si, Ca, Mg, K, Na, pH, and alkalinity in units of concentration (Figures 3.7 and 3.8) and units of mass flux (Figures 3.9, 3.10, 3.11, and 3.12). The simulation results presented in Figures 3.7 to 3.12 were run using the calibration conducted at the humidity cell scale (Wilson et al., 2018a); no model calibration was conducted at the AZL scale.

The concentrations of most weathering products were consistent year to year with intra-annual variation where concentrations typically started lower then increased to peak mid-season followed by decreased concentrations towards the end of the flow season. Annual average concentrations of Type III sulfide-oxidation indicator solutes SO_4 , Ni, Co, Cu, and Zn generally increased slightly to peak in 2010 (Bailey et al., 2015) followed by slight decreases in concentration in 2011. Solutes that indicated weathering in the non-sulfide portions of the waste rock followed a pattern similar to the annual average concentrations of the sulfide-oxidation indicators. Type III AZL experiment effluent pH declined over the four year period from an average annual value of approximately 4.7 in 2008 to approximately 3.4 in 2011; effluent alkalinity declined from just above zero in 2008 to below detection in 2009 where it remained for the rest of the simulated period. Annual average concentrations of Type I sulfide-oxidation indicator solutes Ni, Co, and Cu increased from 2009 to 2011 while average annual concentrations of SO_4 and Zn decreased or remained stable during the

same period. Average annual concentrations of most other solutes in Type I effluent decreased during the 2008 to 2011 period. The Type I AZL experiment effluent pH remained relatively stable over the four year period at an annual average ranging from 6.7 to 7.2; average annual effluent alkalinity declined from approximately 40 mg L⁻¹ as CaCO₃ in 2008 to 26 mg L⁻¹ as CaCO₃ in 2011. The simulations captured the overall concentration trend for some parameters throughout the 2008 to 2011 period although smaller scale variations within each annual flow cycle were not precisely delineated. Concentrations of SO₄, Ni, and Co were captured reasonably well by the Type I simulations and very well for the Type III simulations suggesting the primary mechanisms of sulfide oxidation and carbonate dissolution were well represented in the simulations. Concentrations of Cu, Al, and Fe were not as well captured in the Type I or Type III simulations indicating that adsorption parameters (for Cu) and dissolution and secondary precipitation processes (for Al and Fe) required supplemental calibration.

The simulation of pH for the Type III experiment deviated slightly from measured values. Supplemental simulations indicated that reduction of ϕ_{CaCO_3} to 20% of the measured value resulted in a pH trend that was consistent with the measured values (Figure 3.13), which indicated that the measured carbonate mineral contribution to the mineralogy of the Type III AZL experiment may have been overestimated. Alkalinity in the reduced CaCO₃ Type III simulation was very low (<1 mg L⁻¹ CaCO₃) by the 2008 flow season and confirmed the measured concentrations that indicated available calcite was exhausted by 2008. Decreased ϕ_{CaCO_3} did not significantly alter the simulation results for other solutes.

The mass fluxes of solutes from the AZL system varied in association with temporal variability in infiltration to the system. Higher annual mass flux of most solutes corresponded to years of higher infiltration (*i.e.*, 2008 and 2011) and lower annual mass flux corresponding with a period of lower infiltration (*i.e.*, 2009). When viewed with time units of days, the mass flux of solutes also varied in association with temperature with higher rates of mass flux associated with periods of higher system temperature, consistent with the conclusions of Bailey et al. (2015). The annual mass flux of sulfide-oxidation indicator solutes SO₄, Fe, Ni, and Co were captured well by the Type III simulation in most years, while the annual mass flux of Cu and Zn were not captured as well for some years by the simulations. The daily mass flux was not captured well for parameters Cu and Al in 2008; this likely resulted from adsorption processes not being fully represented (Cu) and the involvement of multiple

primary and secondary mineral dissolution and precipitation processes (*i.e.*, Al is associated with the dissolution of biotite, muscovite, and albite and the secondary mineral gibbsite). Daily mass fluxes indicated that the simulations were capable of capturing some of the finer resolution temporal variability in mass flux. Overall the simulated mass flux compared well with the measured mass flux (both annual and daily) indicating that scaling of the calibrated model from the small laboratory scale (humidity cell) to the medium field scale (AZL) provided a reasonable assessment of the AZL effluent quality.

Individual simulation run times averaged approximately 3.5 hours on a single processor laptop machine.

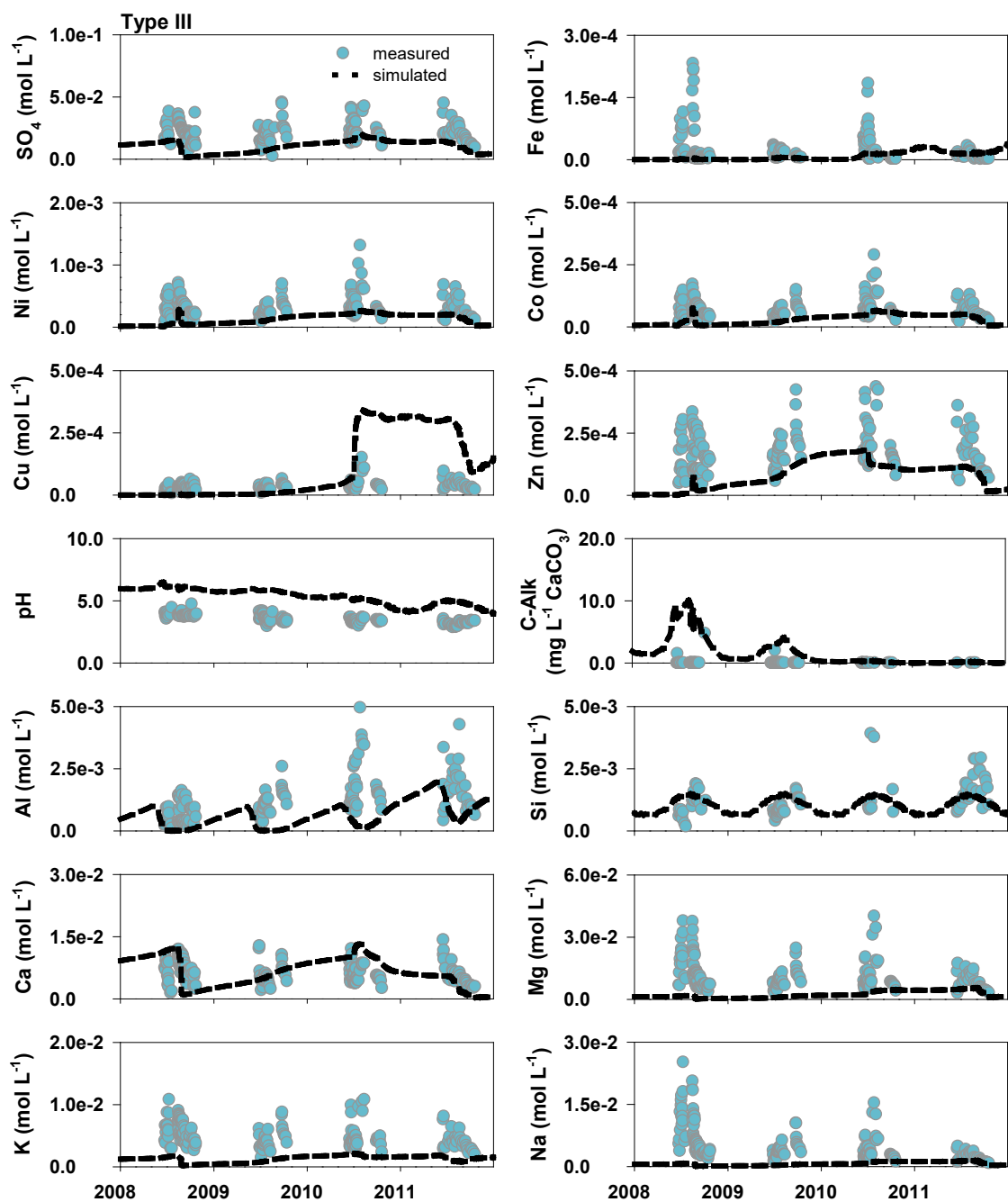


Figure 3.7 Concentrations of mineral weathering products SO₄, Fe, Ni, Co, Cu, Zn, Al, Si, Ca, Mg, K, and Na [mol L⁻¹], pH [-], and alkalinity [as mg L⁻¹ CaCO₃] versus time [year] measured in Type III AZL effluent compared to aqueous concentration exiting the simulation domain. Measured concentrations are available only for periods of AZL flow and are the average of the two Type III AZL concentrations where applicable; simulated concentrations are calculated by the model for all

periods regardless of flow condition.

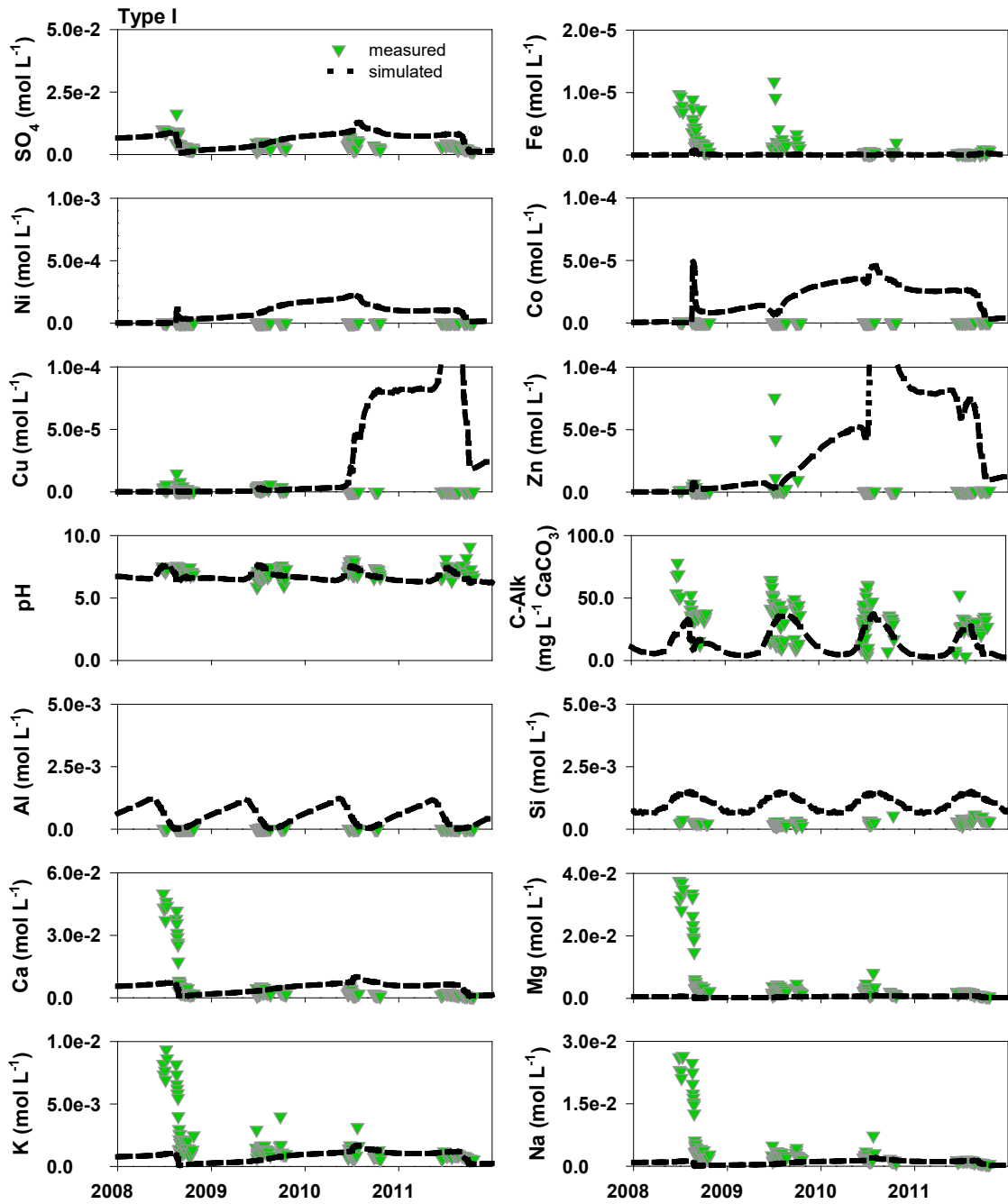


Figure 3.8 Concentrations of mineral weathering products SO_4 , Fe, Ni, Co, Cu, Zn, Al, Si, Ca, Mg, K, and Na [mol L^{-1}], pH [-], and alkalinity [as $\text{mg L}^{-1} \text{CaCO}_3$] versus time [year] measured in Type I

AZL effluent compared to aqueous concentration exiting the simulation domain. Measured concentrations are available only for periods of AZL flow and are the average of the two Type III AZL concentrations where applicable; simulated concentrations are calculated by the model for all periods regardless of flow condition.

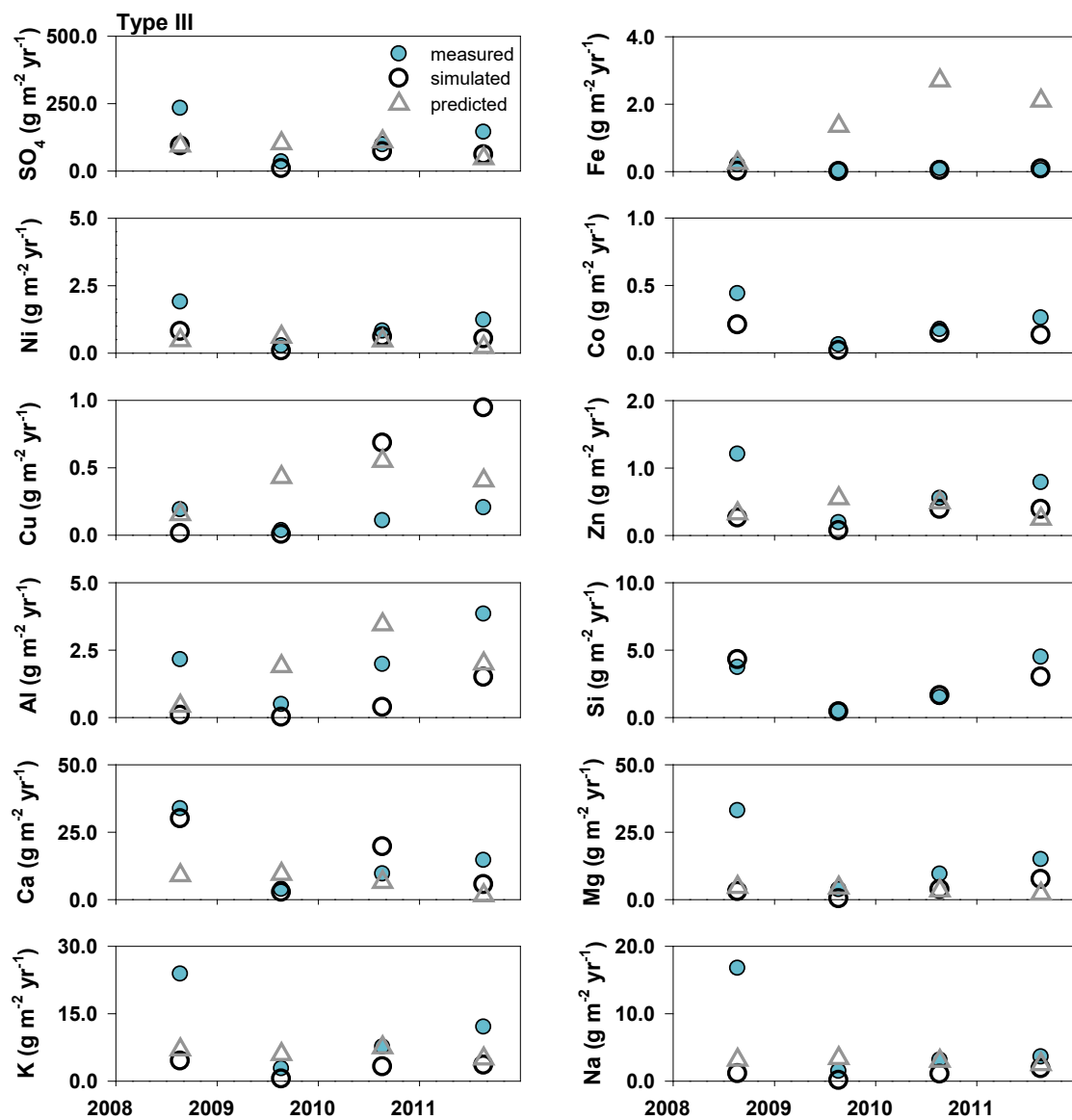


Figure 3.9 Total annual mass of mineral weathering products SO₄, Fe, Ni, Co, Cu, Zn, Al, Si, Ca, Mg, K, and Na [g m⁻² yr⁻¹] versus time [year] measured in Type III AZL effluent compared to total mass exiting the simulation domain. Predicted values are from Bailey, 2013.

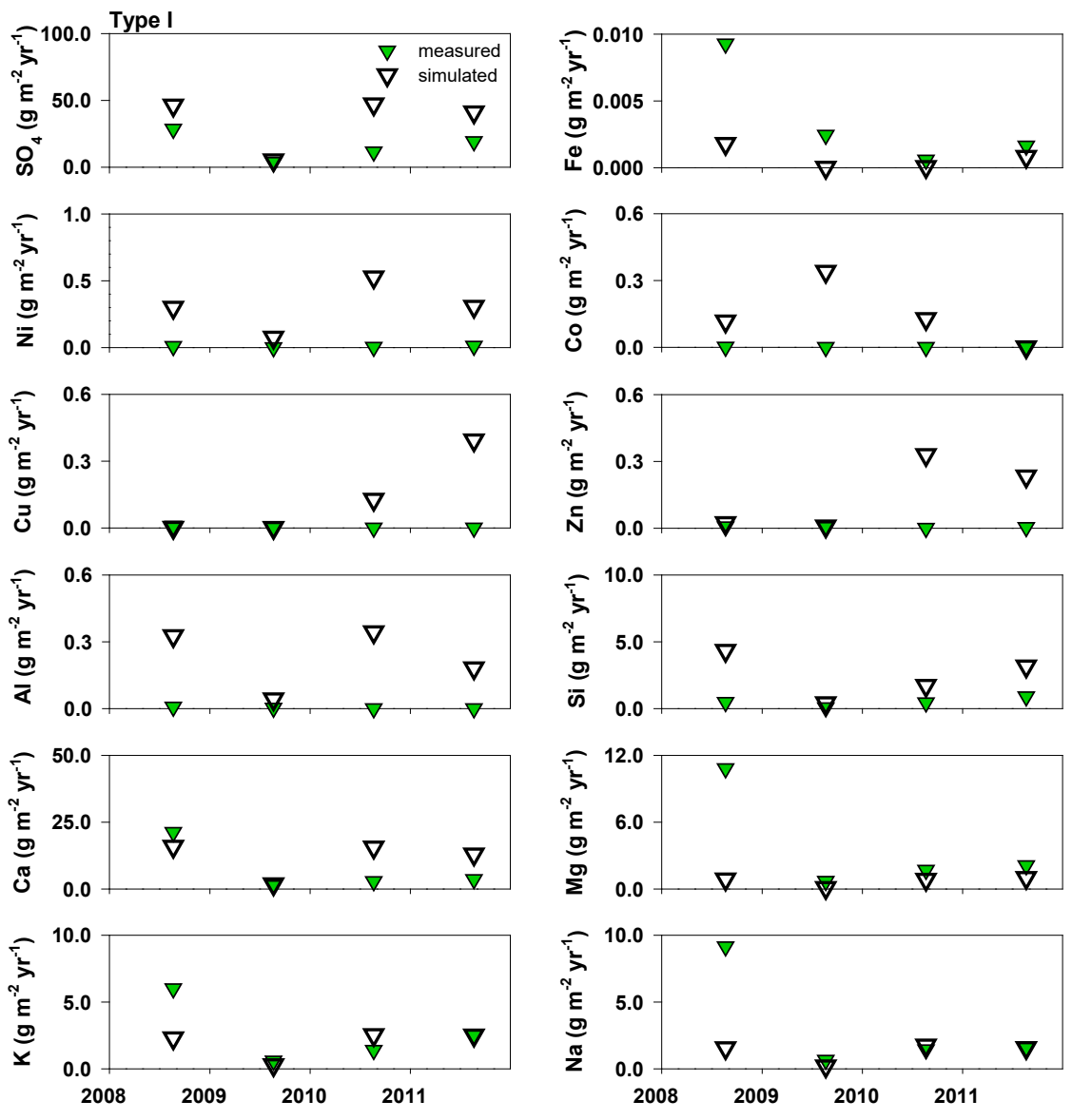


Figure 3.10 Total annual mass of mineral weathering products SO₄, Fe, Ni, Co, Cu, Zn, Al, Si, Ca, Mg, K, and Na [g m⁻² yr⁻¹] versus time [year] measured in Type I AZL effluent compared to total mass exiting the simulation domain.

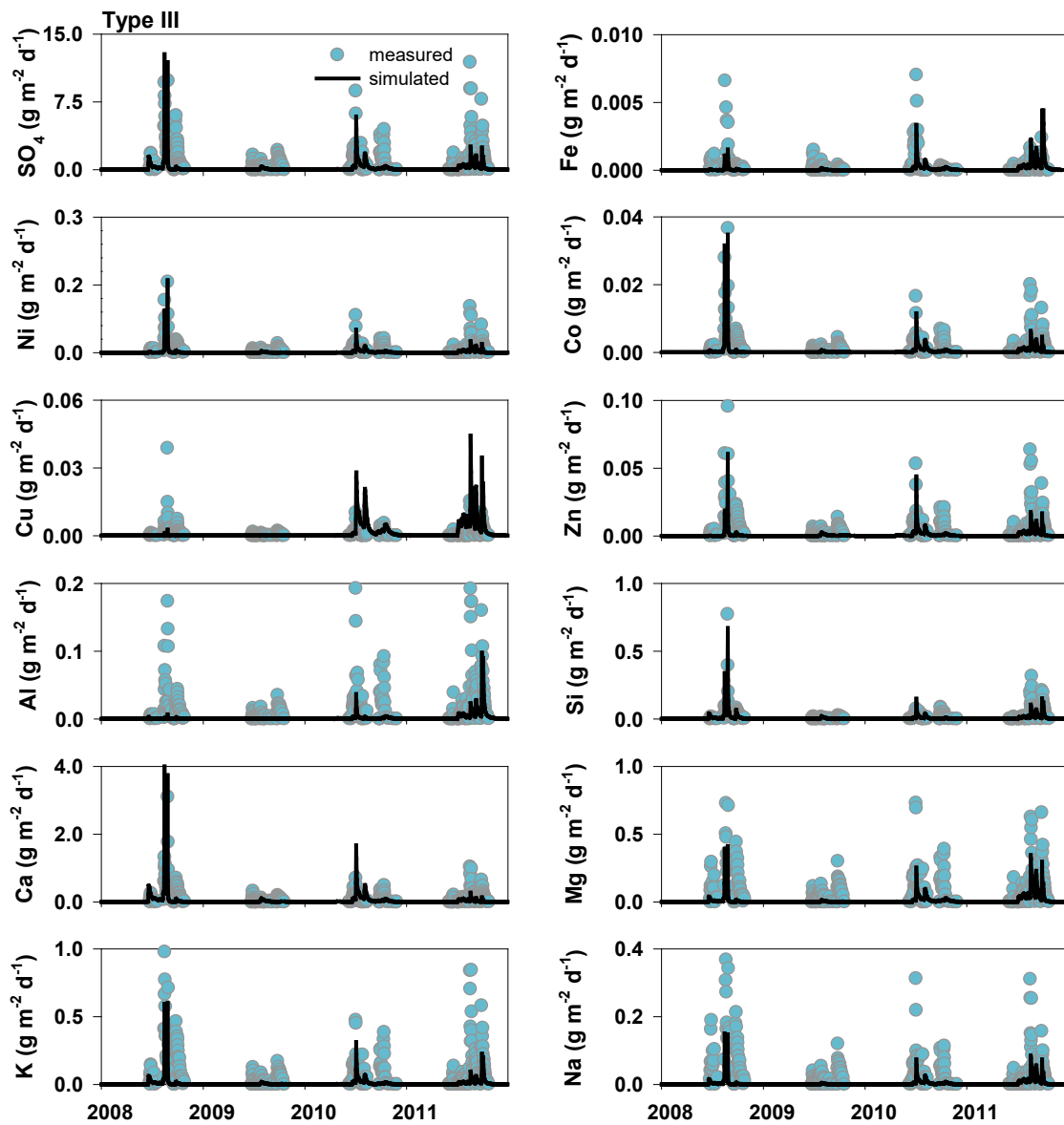


Figure 3.11 Daily mass flux of mineral weathering products SO_4 , Fe, Ni, Co, Cu, Zn, Al, Si, Ca, Mg, K, and Na [$\text{g m}^{-2} \text{d}^{-1}$] versus time [year] measured in Type III AZL effluent compared to daily mass flux exiting the simulation domain.

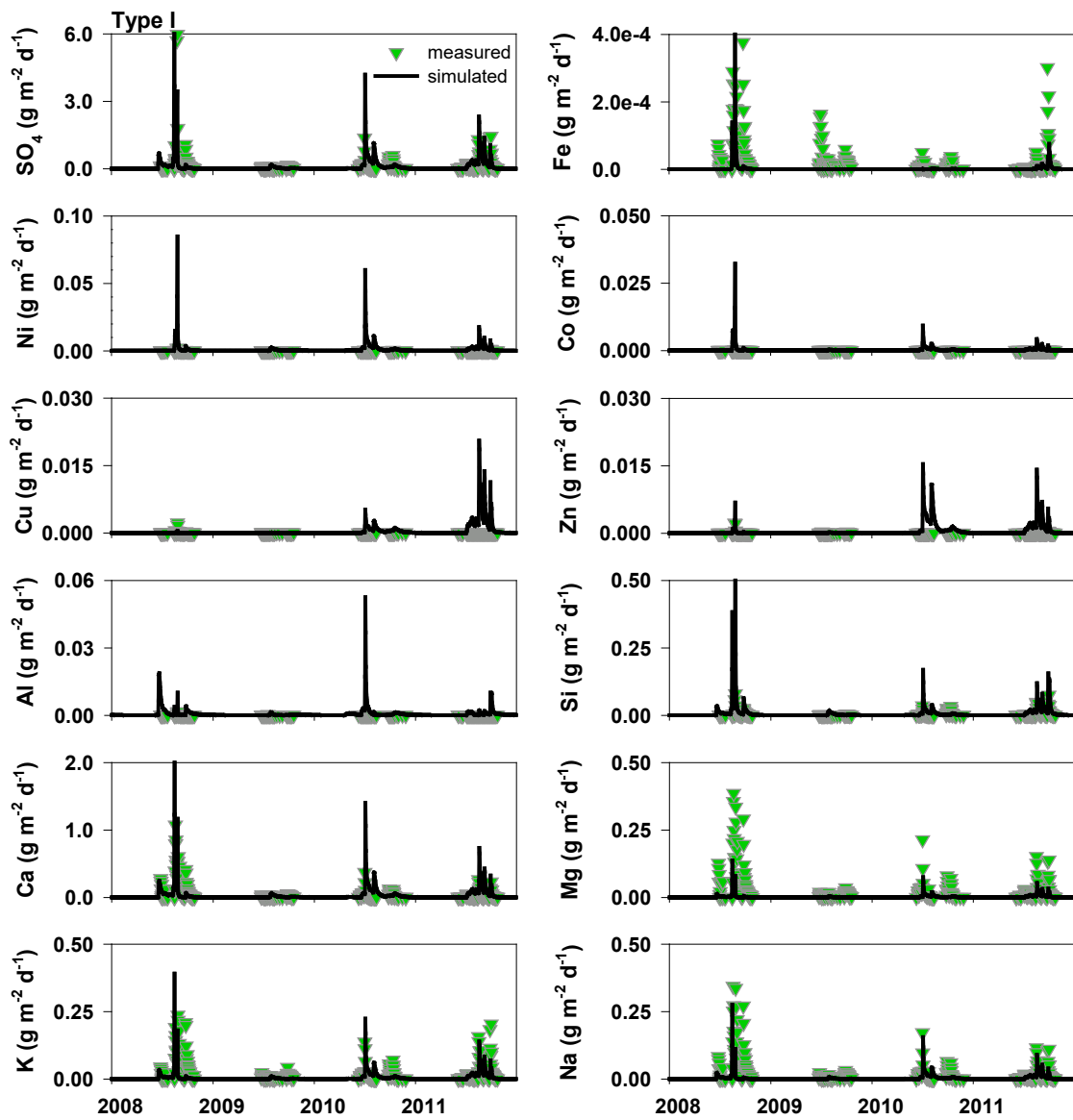


Figure 3.12 Daily mass flux of mineral weathering products SO_4 , Fe, Ni, Co, Cu, Zn, Al, Si, Ca, Mg, K, and Na [$\text{g m}^{-2} \text{d}^{-1}$] versus time [year] measured in Type I AZL effluent compared to daily mass flux exiting the simulation domain.

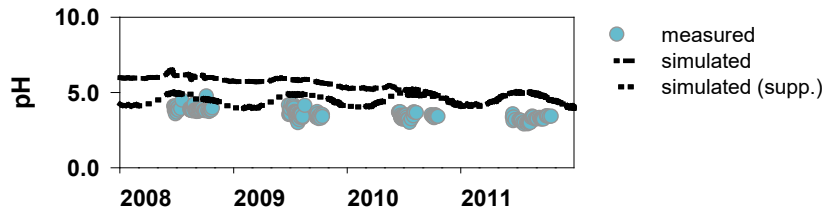


Figure 3.13 pH [-] versus time [year] measured in Type III AZL effluent compared to aqueous concentration exiting the simulation domain with measured calcite contribution (short dash) and decreased calcite contribution (dotted).

3.5 Discussion

The simulations of geochemical evolution of the AZL experiments presented here were conducted by scaling the calibrated model presented by Wilson et al. (2018a) and represented an implementation of an integrated conceptual model of waste-rock weathering for medium-scale field systems. The integrated conceptual model made use of site specific mineralogy and physical parameters; however, the conceptual model was designed such that core elements including the shrinking-core model, use of measurable parameters (mineral surface area and volume fraction), and consideration of temporally variable temperature and infiltration could be coupled with site specific mineralogy and physical parameters to simulate the geochemical evolution of waste rock at other sites. The AZL simulations were intended to illustrate the use of the integrated conceptual model, and, as such, it was recognized that smaller scale variations in the concentrations of sulfide-oxidation indicator species may not be delineated in a precise manner.

Scale-up mass load values predicted by Bailey (2013) were included for the Type III simulations (Figure 3.9). For many parameters (specifically Ni, Cu, Zn, and major ions) the Bailey (2013) predictions were consistent with the measured and simulated values indicating that mechanistic approaches based on measurable parameters (*e.g.*, mineral surface area and volume fraction), in general, could be used to predict the mass load of solutes from waste rock. The Bailey (2013) predictions also highlighted the importance of including secondary processes that influence solute effluent load (specifically SO_4 and Fe for the AZL experiments).

To assess the AZL simulation fit to measured data with respect to the scale-up approach, the root mean square error of the annual mass flux residual [mol m^{-2}] from the Type III AZL and the cold

temperature humidity cells were compared (Table 3.6). The Type I and Type III humidity cell results were used in the comparison to provide a range of error values that included the AZL experiment S content (the S content of the Type I and Type III humidity cells was 0.02 wt.% and 0.18 wt.% respectively). The cold temperature humidity cells were used for the comparison because the average annual temperature at the Type III AZL for days when the temperature was above 0 °C was 6.7 °C (the cold temperature humidity cells were maintained at 5 °C). There were an average of 182 days per year during the 2008-2011 period where the temperature at the AZL experiment was above 0 °C. The humidity cell ‘annual’ mass flux was calculated to correspond with the number of above 0 °C days at the AZL (*e.g.*, year 1, 2008 in the AZL, corresponded to the first 182 days of the humidity cell experiment). The larger mass of matrix material in the AZL was considered in the residual assessment by multiplying the root mean square error for the humidity cell cases by a factor of 3.4 (*i.e.*, the Type III AZL contained approximately 3.4 times the matrix material per m²). The error of the mass flux for parameters at the AZL scale is within the same order of magnitude or lower than the error of the mass flux at the humidity-cell scale for all parameters except K, Na, and Zn. This residual analysis indicates that the scale-up approach provides a fit to the measured AZL data similar to the fit of the humidity cell simulations to the measured data at the laboratory scale.

Table 3.6 Summary of the root mean square error of annual mass flux [mol m^{-2}] residual from the Type I humidity cell, Type III humidity cell, and Type III AZL simulation cases

Parameter	Type I HC	Type III HC	Type III AZL
Al	1.1×10^{-1}	2.0×10^{-1}	4.0×10^{-2}
Ca	2.0×10^{-1}	4.6×10^{-1}	3.1×10^{-1}
Co	6.3×10^{-4}	3.1×10^{-1}	2.0×10^{-3}
Cu	8.6×10^{-5}	1.4×10^{-2}	6.1×10^{-3}
Fe	1.9×10^{-3}	1.1×10^{-1}	7.9×10^{-4}
K	4.4×10^{-2}	8.3×10^{-2}	2.8×10^{-1}
Mg	5.4×10^{-2}	1.9×10^{-1}	5.0×10^{-1}
Na	5.1×10^{-2}	8.8×10^{-2}	3.1×10^{-1}
Ni	5.2×10^{-4}	1.4×10^{-2}	9.8×10^{-3}
Si	1.8×10^{-1}	4.9×10^{-1}	3.3×10^{-2}
SO ₄	1.2×10^{-1}	9.9×10^{-1}	8.6×10^{-1}
Zn	7.0×10^{-4}	8.8×10^{-3}	1.2×10^{-1}
pH	1.9×10^0	1.2×10^0	9.3×10^{-1}

Two significant components were added to the integrated conceptual model that were either not incorporated into, or minimized in, the laboratory scale experiments and simulations: i) variable temperature, and ii) variable infiltration. As part of the laboratory experiments temperature was held constant thereby minimizing mineral weathering rate variability due to temperature fluctuation. Continual temperature variation in the AZL experiments, required internalization of temperature variation within the integrated conceptual model facilitating simulations of sulfide-mineral oxidation using the shrinking-core model. The rate of water infiltration through the system was held constant for the humidity cell simulations. For the AZL simulations constant rate infiltration was not appropriate, resulting in the requirement for incorporation of variable infiltration rates using a variable flux boundary condition in the model.

It is important to reiterate when no calibration of the geochemical component of the AZL simulations was conducted, the simulations produced qualitatively reasonable results. In order to simulate the AZL experiments only the sulfide and carbonate mineral fractions were adjusted to

reflect the slight differences in the measurements of the S and C contents of the AZL experiments. Parameters used for calibration at the humidity cell scale (Wilson et al., 2018a) such as mineral surface areas and diffusion coefficients were not adjusted at the AZL scale. A slight improvement in the simulated pH (Type III AZL simulation only) was obtained by reducing the ϕ_{CaCO_3} to 20% of the measured value, suggesting that the full measured ϕ_{CaCO_3} may not be available for acid neutralization in the field experiments. This apparent difference in carbonate mineral availability between laboratory- and field- scale experiments has important implications for scale-up when assessing the neutralization potential of waste rock.

3.5.1 Temperature

The influence of temperature on sulfide mineral reaction rates, by considering the temperature dependence of the diffusion coefficients, was clearly indicated by plotting the reaction rates for sulfide minerals for the simulated period (Figure 3.14 shows pyrrhotite). The simulated reaction rate for pyrrhotite varied by approximately a factor of four following the dynamic temperature of the system. Inclusion of the temperature influence on the reaction rates of sulfide minerals facilitated the representative simulation of sulfide related parameters.

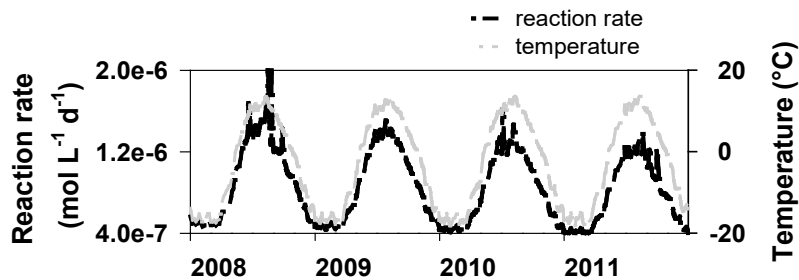


Figure 3.14 Reaction rate of pyrrhotite [$\text{mol L}^{-1} \text{d}^{-1}$] versus versus time [year] simulated in Type III AZL compared to model temperature [$^{\circ}\text{C}$].

3.5.2 Infiltration

The use of measured precipitation data combined with the FAO P-M method to estimate infiltration resulted in reasonable simulation of water flow through the AZL domain. Water flow in the simulations was driven by rainfall events, which induced pressure wave propagation and resident water displacement (Neuner et al., 2013) through the domain resulting in simulated outflow that was

similar in timing and volume to the measured outflow from the Type I and Type III AZL experiments. The saturated hydraulic conductivity of the simulation domain was used to calibrate the resident water displacement to align the timing of the simulated outflow with the measured outflow. The calibration of hydraulic conductivity in the simulations resulted in a value that was consistent with the mean saturated hydraulic conductivity for matrix material of $9 \times 10^{-6} \text{ m s}^{-1}$ reported by Neuner et al. (2013).

3.5.3 Mineral Volume Fraction

The primary driver with respect to simulation of the solute load from the AZL experiment within the integrated conceptual model remained the shrinking-core model. Characterization of the sulfide-mineral surface area available for weathering at both the humidity cell and AZL experiment scales was a crucial component in accurately simulating the geochemical evolution of both experiments. Because of the finer grained nature ($< 6.3 \text{ mm}$) of the waste rock in the DWRP humidity cell experiments, the laboratory scale simulations characterized the geochemical evolution of matrix material. Successful scaling of the calibrated humidity cell model (which accounted for changes in surface area) to the AZL experiments while considering only the geochemical evolution of the matrix material lent confidence to the assertion by Amos et al. (2011) that an important driver of low quality effluent from waste rock was weathering that occurred within the high surface-area matrix material. The simulations of the AZL experiments, using the integrated conceptual model, indicated that the shrinking-core model, and by extension accounting for sulfide-mineral surface area, could be successfully applied to a scale-up scheme.

3.5.4 Secondary Mineral Control

Secondary mineral precipitation was suggested by Bailey et al. (2015) to be a significant control on lower than expected Fe mass release from the AZL experiments. The results of the reactive transport simulations indicated that Fe(III) (oxy)hydroxide precipitation occurred throughout most the Type I and Type III simulation periods and provided agreement to the hypothesis that Fe release from the AZL system was at least partially controlled by secondary Fe(III) (oxy)hydroxide precipitation.

The Fe(III) hydroxysulfate mineral jarosite was included in the simulations and allowed to precipitate or dissolve according to the evolving geochemical conditions. Jarosite precipitation and dissolution occurred throughout the Type III simulation period, which was consistent with the

suggestion by Bailey et al. (2015) that SO_4 release from the Type III AZL experiments was potentially controlled by secondary mineral influences (lower than expected S to Ni and S to Co ratios were observed by Bailey et al., 2015 in the Type III effluent geochemistry). In the simulations, no long-term accumulation of jarosite occurred, with dissolution occurring until the accumulated mass was exhausted during each flow season cycle, suggesting that jarosite acted as a mechanism that delayed SO_4 and Fe release. Jarosite did not precipitate or dissolve in the Type I AZL simulation, which was consistent with the Bailey et al. (2015) observation that S release from the Type I AZL experiments did not appear to be under the influence of secondary mineral control (higher than expected S to Ni and S to Co ratios observed by Bailey et al. (2015) in the Type I effluent geochemistry suggested no control on SO_4 release and/or control on Ni and Co release). Minor control of SO_4 (and Ca) concentrations may have been exerted by the precipitation of gypsum (Bailey et al., 2015). Simulation of the Type I and Type III AZL experiments indicated that gypsum precipitated during portions of the simulated period consistent with the Bailey et al. (2015) suggestion that gypsum may be a secondary control for SO_4 concentrations.

Gibbsite, a secondary Al mineral, was included in the simulations and cycled between precipitation during most of each flow season and limited dissolution near the end of each flow season throughout most of the Type I and Type III simulation domains. Total gibbsite mass accumulated in the systems over the course of the simulations suggesting Al release was controlled at AZL experiments by precipitation of this secondary mineral.

3.5.5 Acid Neutralization

The declining average annual pH (~ 4.7 in 2008 to ~ 3.4 in 2011) and lack of alkalinity after 2008 in effluent from the Type III AZL experiment indicated that the mass of carbonate minerals available for dissolution was likely exhausted. The scaled simulation captured the exhaustion of carbonate minerals (specifically calcite) at the Type III AZL experiments and the resulting decrease in pH. The capability of the model to represent the exhaustion of available calcite was significant because of the importance of this mineral in long-term H^+ consumption processes.

Simulation of the geochemical evolution of the waste rock contained in the Type I AZL experiments indicated that there was sufficient available calcite to neutralize any H^+ produced by sulfide-mineral oxidation. This observation was consistent with the suggestion of Bailey et al. (2015) that the circumneutral pH, the undersaturated conditions with respect to the carbonate minerals calcite and

dolomite, and the continued presence of alkalinity in the Type I AZL effluent indicated that the carbonate mineral supply within the Type I AZL experiment was not exhausted by the end of 2010. The simulations conducted indicated that the neutralization capacity of calcite had not been exhausted by the end of 2011.

3.6 Conclusions

The implementation of an integrated conceptual model to scale simulations of waste-rock weathering from small laboratory experiments (humidity cells) to medium-sized field experiments (AZLs) produced good agreement when comparing simulated concentrations and mass fluxes for sulfide related parameters SO_4 , Ni, Co, and Fe with measured values from the AZL experiments. The good visual agreement suggested that the calibrated model of the geochemical evolution of the Diavik waste rock, developed for laboratory-scale experiments, could be scaled to reasonably assess of the geochemical evolution of the medium-scale field experiments. Minor deviation of the simulations from the measured concentrations was acceptable in the development of a transferable scale-up approach. The goal was to capture the significant weathering processes while incorporating the major factors that influence sulfide oxidation within waste-rock stockpiles including temporal variability in temperature and infiltration. The AZL simulations showed that implementation of the integrated conceptual model was sufficiently versatile to provide realistic multi-year simulations of experiments exposed to atmospheric conditions.

The ability of the model to capture geochemical trends in the AZL experiments without calibration to measured geochemical data lent strength to the use of the integrated conceptual model to scale laboratory experimental results to larger field systems. Although the AZL simulations did not rely on geochemical data for calibration, the simulations did highlight the importance of collecting site specific physical data, specifically mineralogy related parameters such as surface area and volume fraction; hydrology related parameters such as hydraulic conductivity, grain-size distribution, porosity, and water-retention curve values; and environmental related parameters such as temperature and precipitation to facilitate reasonable assessment of the geochemical evolution of waste rock using reactive transport models.

Previous attempts to scale sulfide weathering rates and geochemical conditions from laboratory experiments to field-scale systems have typically relied on empirical scaling factors that vary

dramatically between sites (Amos et al., 2015). The reactive transport simulations shown here have demonstrated that a comprehensive, integrated conceptual model of sulfide weathering and geochemical evolution of low-sulfide waste rock developed from humidity cell experiments could be applied to field-scale experiments using only measurable parameters to scale the simulations. This mechanistic approach provided the basis for predictive scaling.

Chapter 4

Simulation of the geochemical evolution of large test piles using a scaled temperature and sulfide content dependent reactive transport conceptual model

Due to the costs involved in construction, and length of time required to produce results, large-scale field experiments (test piles) are rarely used for the purpose of mine waste-rock characterization. Test piles have been used in research programs focused on the characterization of the geochemical and physical attributes of waste-rock (Blackmore et al., 2014; Smith et al., 2013a; Corazao et al., 2007; Andrina et al., 2006; Stockwell et al., 2006; Nichol et al., 2005). More often, smaller scale field experiments (*e.g.*, barrel experiments) are used to assess the geochemical evolution of waste rock (Demers et al., 2013; Smith et al., 2013a; Parbhakar-Fox and Lottermoser, 2015). Where available, the results of the larger scale field experiments can be used, in a manner similar to the results of smaller scale field experiments, to gain an understanding of the influence of dynamic infiltration and temperature regimes and heterogeneous particle-size distribution on the geochemical evolution of waste rock that can enhance the understanding of laboratory experiments (*e.g.*, humidity cells).

The process of extrapolating the results of small-scale testing to full-scale waste-rock piles is commonly referred to as scale-up. Parameters including pH, particle-size distribution, moisture content, rock/water contact ratios, temperature, oxygen availability, and mineral surface area are understood to influence effluent quality and these relationships are typically scaled using empirical factors (Kempton, 2012; Amos et al., 2015). The capability of empirical scale factors to capture the geochemical evolution of waste rock in full-size dumps can be hampered by heterogeneity in physical parameters (*e.g.*, particle size and mineral distribution) and exposure of the waste rock to atmospheric conditions (*i.e.*, variable temperature and precipitation). Scale-up methods reliant on empirical factors are generally incapable of providing an adequate assessment of waste-rock evolution (Amos et al., 2015). Mechanistic approaches such as reactive transport modelling provide the capacity to incorporate dynamic temperature and precipitation regimes and heterogeneity in physical parameters to address the inherent weaknesses of empirical scale-up methodology.

The experiments conducted as part of the Diavik Waste Rock Project (DWRP) were designed to facilitate investigation of mechanistic approaches to scale-up. Small-scale laboratory experiments

were complemented by intermediate and large-scale field experiments. The laboratory experiments included small-scale (1 kg) humidity cells; the intermediate-scale (~9,300 kg) experiments consisted of 2 m diameter barrel-style active zone lysimeters (AZL) experiments; and the large-scale (~8.2 x 10⁷ kg) experiments included densely instrumented test piles. The field experiments were built and conducted at Diavik Diamond Mine (Diavik), located approximately 300 km northeast of Yellowknife, NT, Canada. The annual temperature at Diavik ranges from an average summer high of 18 °C to an average winter low of -31 °C with an annual mean (1998-2007) of -9 °C (Smith et al., 2013a). Precipitation occurs as approximately 40% rain and 60% snow (Smith et al., 2013a). (Figure 4.1).

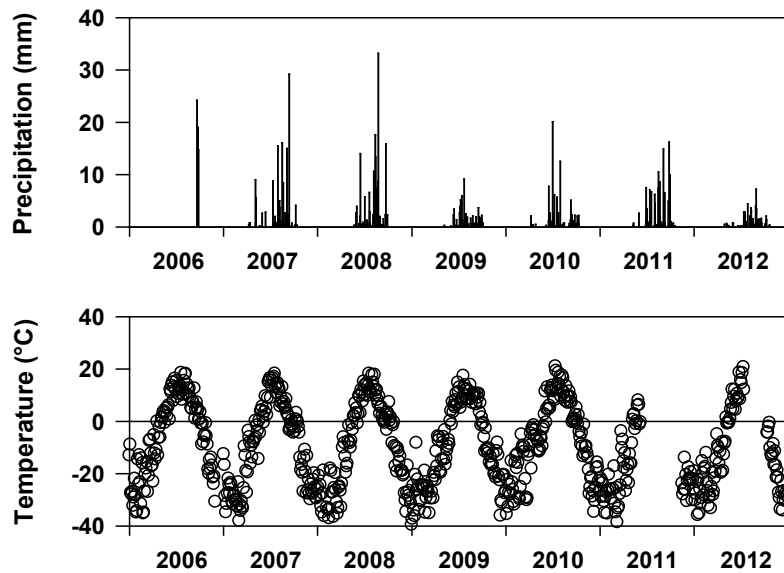


Figure 4.1 Precipitation (rain only) at the DWRP research station and average daily air temperature at Diavik for the period 2006-2012. Note that precipitation measurements began at the research station on September 1, 2006.

Research on scaling laboratory experiment results has been conducted previously as part of DWRP by Bailey (2013), Sinclair et al. (2015), Wilson et al. (2018a), and Wilson et al. (2018b). Bailey (2013) determined sulfide mineral weathering rates using effluent data from the DWRP humidity cell experiments (Langman et al., 2014) and scaled those rates mechanistically to assess solute loading from the intermediate-scale AZL experiment (Bailey et al., 2015). Bailey (2013), using a spreadsheet

model, demonstrated that assessment of mass loading from the AZL experiment could be conducted reasonably well for relatively conservative solutes such as Zn and Cu. The method was limited because geochemical processes known to be active in the systems, including secondary mineral precipitation, ion adsorption, and microbiological catalysis were not considered as part of the calculations.

Sinclair et al. (2015) developed a spreadsheet model that simulated SO_4 production within the core of the Type III test pile. While not strictly related to scale-up, the Sinclair et al. (2015) model suggested that mechanistic approaches to assessment of the geochemical evolution of waste-rock can be applied. Wilson et al. (2018a) and Wilson et al. (2018b) developed an integrated conceptual model of geochemical evolution for the humidity cell experiments and used reactive transport model MIN3P to simulate the effluent concentrations and mass loading from the intermediate-scale AZL experiment. This modelling approach provided a reasonable assessment of the geochemical evolution of the Diavik waste rock while considering secondary mineral precipitation and dissolution, adsorption, and dynamic temperature and infiltration regimes. The work of Bailey (2013) and Wilson et al. (2018b) showed that mechanistic approaches can facilitate a scale-up method that captures the complex processes involved with waste-rock weathering providing realistic assessments of effluent concentrations and mass loading.

The integrated conceptual model developed by Wilson et al. (2018a) was implemented using reactive transport model MIN3P (Mayer et al., 2002) to simulate one dimensional flow and geochemical evolution through the core of the Type III test pile. MIN3P is a multi-component reactive transport code that can be used to simulate water flow through the unsaturated zone and kinetically controlled geochemical reactions. A geochemical framework can be developed using the code that can include mineral dissolution and precipitation, adsorption, complexation, and oxidation-reduction reactions using reaction stoichiometry and kinetics that are project specific. The objective of the simulations was to investigate the capability of the implemented integrated conceptual model to predict the effluent geochemistry when scaled from the small laboratory experiments to the larger field experiment considering dynamic temperature and flow regimes.

4.1 Test Pile Methodology

The test pile experiments were conducted over a period of more than 10 years, starting in 2006, at Diavik. The geochemical evolution of waste-rock was investigated at a large-scale test pile (50 m x 60 m x 15 m high) with a mean S content of 0.053 wt.% (Smith et al., 2013c) and a thermal regime controlled by the Arctic climate and construction of the pile in a continuous permafrost region.

The waste-rock used to build the test pile experiments had mineralogy similar to that of the DWRP humidity cells (Langman et al., 2014; Wilson et al., 2018a) and included approximately 75% granite (primarily quartz [SiO₂], k-feldspar [KAlSi₃O₈], and albite [NaAlSi₃O₈]), 14% pegmatitic granite, 10% biotite schist, and 1% diabase (Blowes & Logsdon, 1998; Langman et al., 2014). The metal sulfide minerals were primarily contained in the biotite schist, of which the major components were albite (35–55%), quartz (20–50%), and biotite [KMg₂FeAlSi₃O₁₀(OH)₂] (10–25%) (Langman et al. 2014). The mean sulfide content of the biotite schist was 0.24 wt.% S (Langman et al., 2014). Pyrrhotite [Fe_(1-x)S] was the primary metal sulfide mineral in the waste material, in which minor substitution of Ni and Co for Fe occurred in the following approximate ratio: Fe_{0.852}Ni_{0.004}Co_{0.001}S (Jambor, 1997). Metal sulfide minerals chalcopyrite [CuFeS₂], sphalerite [ZnS], and pentlandite [(Fe,Ni)₉S₈] were found to be present in small quantities (Langman et al., 2014). Waste rock at Diavik is segregated according to S content with Type I < 0.04 wt.% S, Type II > 0.04 wt.% and < 0.08 wt.%, and Type III > 0.08 wt.% S. The mean S and C contents of samples collected from waste rock used to construct the Type III test pile were 0.053 wt.% and 0.027 wt.% (Smith et al. 2013c).

The Type III test pile was constructed of approximately $\sim 8.2 \times 10^7$ kg of waste rock, exposed to atmospheric temperature and precipitation conditions for the duration the experiment. Water flow from the Type III experiment was measured both from a basal drain system that collected water exiting the entire pile and from a series of basal collection lysimeters (BCLs) constructed near the base of the test pile, which collected water from the core of the pile only (*i.e.*, excluded preferential flow from the sides of the pile) (Figure 4.2).

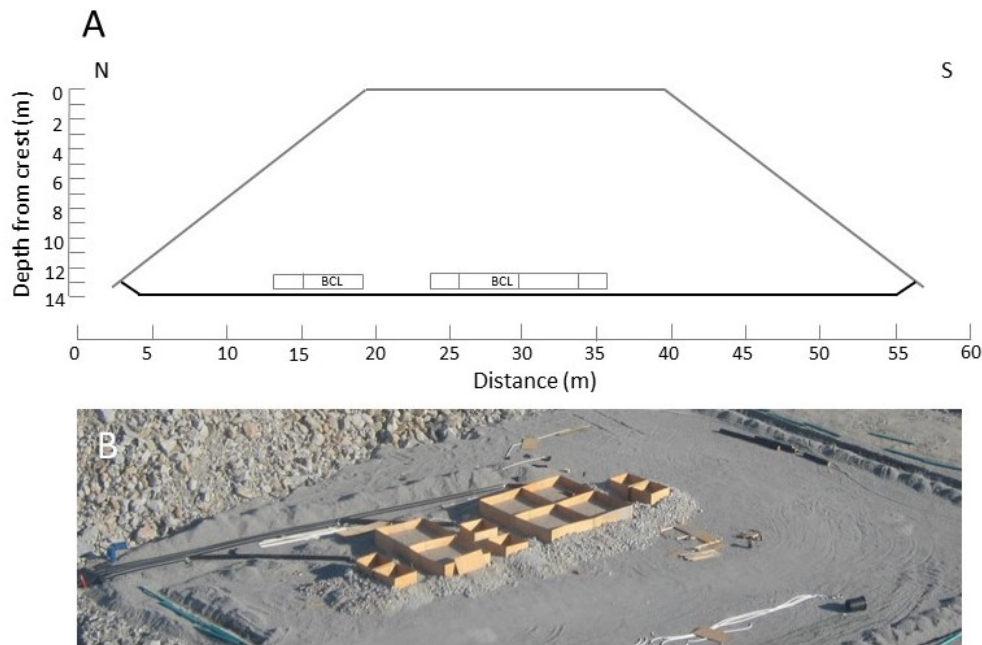


Figure 4.2 **A:** Conceptual cross-section of DWRP Type III test pile experiment indicating approximate location of basal collection lysimeters (BCL). **B:** Construction of basal collection lysimeters prior to run-of-mine material placement at Type III test pile.

The BCLs were installed to facilitate measurement of flow volume and collection of samples for geochemical analysis of water that infiltrated from the crest through the core of the test pile (Smith et al., 2013a). Flow volume from the core of the test pile was measured using rain gauge tipping buckets installed at each BCL drain outlet (Smith et al., 2013a). Effluent samples were collected regularly (every 3-5 days) from the BCL drains during the flow seasons of years 2008 (when flow at the drains started) to 2012. The samples were analyzed for a suite of 42 inorganic and general parameters, which included parameters indicative of Diavik waste rock weathering (Fe, Ni, Co, Cu, Zn, Al, Si, Ca, Mg, K, Na, and SO₄, pH, and alkalinity) (Smith et al., 2013b). Thorough descriptions of the construction of the test pile and drain system and sampling procedures are provided by Smith et al. (2013a) and Sinclair et al. (2015).

4.2 Conceptual Model

The integrated conceptual model for sulfidic mine waste-rock weathering developed by Wilson et al. (2018a) was implemented to simulate the geochemical evolution of the Type III test pile experiment.

The integrated conceptual model developed from site specific data was designed to be scaled and coupled with site specific flow and temperature regimes to provide a realistic assessment of the geochemical evolution of waste rock at Diavik. The integrated conceptual model implemented here contains the same mineralogy used by Wilson et al. (2018b) for simulation of the geochemical evolution at the intermediate DWRP scale; this mineralogy is specific to the DWRP. Due to the larger size of the test pile experiment, it was anticipated that the flow and temperature regimes of the experiment would be more complex when compared to the intermediate-scale simulation described by Wilson et al. (2018b).

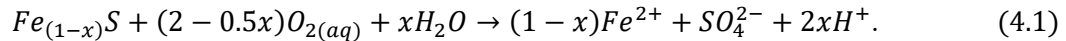
The simulated flow regime was based on the DWRP test pile experiments described by Smith et al. (2013a) and Neuner et al. (2013). Measured precipitation (Figure 4.1) at Diavik was used to estimate infiltration to the test pile through application of the FAO Penman-Monteith (FAO P-M) method described by Neuner et al. (2013). Tracer tests conducted in 2006 and 2007 supplied additional water to the flow system (approximately 34.7 m³ in 2006 and 36.2 m³ in 2007) and were included in the infiltration volume incorporated in the simulations. Tracer water was obtained from Lac de Gras; analyzed samples of the lake water indicated solute concentrations of most parameters at least an order of magnitude below test pile effluent concentrations and circumneutral pH. Neuner et al. (2013) indicated that water flow through the system was dominated by matrix flow (matrix material defined with particle diameter < 5mm), with the matrix material making up approximately 20% of the total material in the Type III test pile. The predominance of matrix flow in the system suggests that the use of Richards equation is appropriate for the simulation of water flow through the test pile. Water flow through the test pile, therefore, was simulated as temporally intermittent events that coincided with the calculated infiltration events under the assumption of a single porosity domain.

The large size of the test pile experiment and its exposure to atmospheric temperature necessitated incorporation of a temperature regime within the pile that was spatially and temporally variable. Temperature was measured during the experiment with a series of instrument strings, with thermistors spaced at regular (approximately 0.5 m) intervals within the core of the test pile. Additional thermistors were installed in boreholes beneath the test pile prior to construction. Automated monitoring of the thermistor network provided temperature measurements approximately every 6 hours from the crest of the pile to approximately 11 m depth, combined with deeper measurements

from approximately 14 m to 16 m below the crest of pile. Smith et al. (2013a) and Pham et al. (2013) provide further details on the construction and operation of the thermal data collection system.

Sinclair et al. (2015) described a conceptual model of freezing and thawing within the test pile that was based on the measured temperatures. Sinclair et al. (2015) showed that the test pile was fully frozen each year from December to May and fully thawed from August to October with transitional periods in June/July, and November. The June/July transitional period was characterized by relatively uniform warming front migration from top and sides to bottom. The November transitional period was characterized by cooling front migration from top and sides to bottom and additional slight cooling front migration up from the bottom of the pile resulting in an inner core of thawed waste-rock surrounded by frozen material. The proposed conceptual model of freezing and thawing suggested a regime of spatially and temporally variable temperature would be required to accurately assess the geochemical evolution of the waste rock at the test pile. To represent the complex temperature regime within the test pile a one dimensional temperature field was generated based on the measured data and varied on a daily basis.

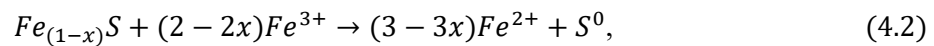
The integrated conceptual model of sulfidic mineral weathering presented by Wilson et al. (2018a) and Wilson et al. (2018b) is briefly summarized here. Oxidants $O_{2(aq)}$ and Fe^{3+} are recognized as dominant drivers of sulfide mineral oxidation (Nordstrom & Southam, 1997; Blowes et al., 2003). The following reaction stoichiometry for generic pyrrhotite describes the overall reactions (Nicholson and Scharer, 1998; Janzen et al., 2000; Belzile et al., 2004):

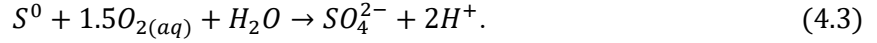


Mineral specific versions of equation 4.1 were developed to simulate oxidation of $Fe_{(1-x)}S$, $CuFeS_2$, ZnS , and $(Fe,Ni)_9S_8$ oxidation by $O_{2(aq)}$ (Table 4.1).

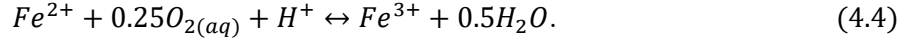
Three parallel reactions were used to represent the role of Fe^{3+} in sulfide mineral weathering. The three reactions follow the reaction mechanism described by Schippers and Sand (1999), in which the intermediary S species were represented by elemental S (S^0).

The reaction stoichiometry shown in equations 4.2 and 4.3 (Nicholson and Scharer, 1998) represent the introduction of S^0 (Table 4.1):





The oxidation of Fe^{2+} (equation 4.4) also represents an important component of the conceptual model in part because of its role in supplying Fe^{3+} . In this instance, the reaction was represented as kinetically controlled (Singer and Stumm, 1970; Schippers and Sand, 1999; Rohwerder et al., 2003):



Equations 4.5 and 4.6 describe rate expressions representing the shrinking core model (Levenspiel, 1972; Wunderly et al., 1996; Mayer et al., 2002) for oxidation of each of the sulfide minerals by $O_{2(aq)}$ and Fe^{3+} . The example rate expressions represent the oxidation of Diavik $Fe_{(1-x)}S$ by $O_{2(aq)}$ and Fe^{3+} respectively (after Mayer et al., 2002).

$$R_{Po\ ox} = -10^3 S_{Fe_{0.852}Ni_{0.004}Co_{0.001}S} \left[\frac{r_p}{(r_p - r_r)r_r} \right] D_{O_{2(aq)}} \left[\frac{O_{2(aq)}}{1.9285} \right], \quad (4.5)$$

$$R_{Po\ ox} = -10^3 S_{Fe_{0.852}Ni_{0.004}Co_{0.001}S} \left[\frac{r_p}{(r_p - r_r)r_r} \right] D_{Fe^{3+}} \left[\frac{Fe^{3+}}{1.714} \right], \quad (4.6)$$

where $R_{Po\ ox}$ represents the rate of pyrrhotite oxidation [$mol\ L^{-1}\ d^{-1}$] and $S_{Fe_{0.852}Ni_{0.004}Co_{0.001}S}$, r_p , r_r , and $D_{O_{2(aq)}}$ and $D_{Fe^{3+}}$ represent the reactive surface area [$m^2\ mineral\ L^{-1}\ porous\ medium$], average particle radius [m], unreacted particle radius [m], and effective diffusion coefficient [$m^2\ s^{-1}$] for $O_{2(aq)}$ and Fe^{3+} diffusion to the unreacted surface, respectively. The rate expressions for $O_{2(aq)}$ and Fe^{3+} acted simultaneously on the same mineral volume fraction.

Equation 4.7 describes the rate expression associated with Fe^{2+} oxidation (Equation 4.4) (after Singer and Stumm, 1970; Mayer et al., 2002; Roden, 2008):

$$R_{Fe^{2+} \rightarrow Fe^{3+}} = -S_1 k_{1_{Fe^{2+} \rightarrow Fe^{3+}}} [Fe^{2+}] [O_{2(aq)}] - S_2 k_{2_{Fe^{2+} \rightarrow Fe^{3+}}} [Fe^{2+}] [O_{2(aq)}] [OH^-]^2 - S_3 k_{3_{Fe^{2+} \rightarrow Fe^{3+}}} \left[\frac{[Fe^{2+}]}{K_S + [Fe^{2+}]} \right], \quad (4.7)$$

where $R_{Fe^{2+} \rightarrow Fe^{3+}}$ represents the rate of Fe^{2+} oxidation [$mol\ L^{-1}\ d^{-1}$]. The first two terms on the right side of Equation 4.7 represent the chemical oxidation of Fe^{2+} by $O_{2(aq)}$ with S , $k_{1_{Fe^{2+} \rightarrow Fe^{3+}}}$, and $k_{2_{Fe^{2+} \rightarrow Fe^{3+}}}$ representing a scaling factor [-], the reaction rate constant for $pH < \sim 3.5$ [$L\ mol^{-1}\ d^{-1}$] (Singer and Stumm, 1970), the reaction rate constant for $pH > \sim 4.5$ [$mol\ L^{-1}\ d^{-1}$] (Singer and Stumm, 1970), respectively. The third right hand term in Equation 4.7 represents the biotic oxidation

of Fe^{2+} where $k_{3_{\text{Fe}^{2+}-\text{Fe}^{3+}}}$ and K_s represent the reaction rate constant [$\text{mol L}^{-1} \text{d}^{-1}$] and half-saturation constant [mol L^{-1}], respectively.

Equation 4.8 describes the rate expression associated with the oxidation of S^0 to SO_4 by $\text{O}_{2(\text{aq})}$ (Equation 4.3) (after Roden, 2008):

$$R_{\text{S}^0-\text{SO}_4} = -k_{\text{S}^0-\text{SO}_4} \left[\frac{[\text{S}^0]}{K_s + [\text{S}^0]} \right], \quad (4.8)$$

where $R_{\text{S}^0-\text{SO}_4}$ represents the rate of biotic S^0 oxidation by O_2 [$\text{mol L}^{-1} \text{d}^{-1}$] and $k_{\text{S}^0-\text{SO}_4}$ and K_s represent the reaction rate constant [$\text{mol L}^{-1} \text{d}^{-1}$] and half-saturating constant [mol L^{-1}] respectively.

Site specific host minerals were represented in the conceptual model by reaction stoichiometry and rate expressions presented in Tables 4.1 and 4.2. Reaction stoichiometry and rate expressions represented irreversible surface weathering in all cases except for calcite and dolomite, those representative reactions were reversible. Secondary minerals included in the simulations were also based on site specific mineralogy and included minerals considered likely to be present based on the results of saturation index analysis of effluent geochemistry or reasonably likely to be present because of their association with the geochemical weathering of sulfidic waste rock. The secondary minerals considered in the simulation included: ferrihydrite [$\text{Fe}(\text{OH})_3$], jarosite [$\text{KFe}_3(\text{SO}_4)_2(\text{OH})_6$], gypsum [$\text{CaSO}_4 \cdot 2\text{H}_2\text{O}$], siderite [FeCO_3], gibbsite [$\text{Al}(\text{OH})_3$], and amorphous silica [SiO_2]. All secondary minerals precipitated or dissolved in accordance with reaction stoichiometry and equilibrium controlled expressions shown in Tables 4.1 and 4.2. The set of secondary minerals included in the test pile simulation was the same as described by Wilson et al. (2018a) and Wilson et al. (2018b); no calibration was conducted as part of this simulation with respect to secondary minerals. Wilson et al. (2018a) provides further detail on the selected set of included secondary minerals.

The interpolated temperatures within the test pile were used in conjunction with the results of the calibration conducted by Wilson et al. (2018a) and the Arrhenius expression to capture the temperature dependence of the waste-rock weathering at the test pile experiment. The temperature dependence of the diffusion coefficient used in calculation of sulfide-mineral weathering rates was adjusted to spatial and temporal temperature variation using the activation enthalpy calculated by Wilson et al. (2018a) using equation 4.9.

$$\Delta H = \frac{RT_1 T_2}{(T_1 - T_2)} \ln \frac{D_1^{eff}}{D_2^{eff}}. \quad (4.9)$$

90

Host mineral weathering rates were adjusted for temperature according to their respective activation energy calibrated as part of the development of the integrated conceptual model (Wilson et al., 2018a). No additional calibration for temperature was conducted as part of the test pile experiment simulations.

Table 4.1 Reaction stoichiometry and solubility products (K) for sulfide, host, and secondary minerals

Mineral	Sulfide Mineral Reaction	log K_i
pyrrhotite	$Fe_{0.852}Ni_{0.004}Co_{0.001}S + 0.143H_2O + 1.9285O_{2(aq)} \rightarrow$ $0.852Fe^{2+} + 0.004Ni^{2+} + 0.001Co^{2+} + SO_4^{2-} + 0.286H^+$ $Fe_{0.852}Ni_{0.004}Co_{0.001}S + 1.714Fe^{3+}$ $\rightarrow 2.566Fe^{2+} + 0.004Ni^{2+} + 0.001Co^{2+} + S^0$	134.66
sphalerite	$ZnS + 2O_{2(aq)} \rightarrow Zn^{2+} + SO_4^{2-}$ $ZnS + 2Fe^{3+} \rightarrow 2Fe^{2+} + Zn^{2+} + S^0$	--
chalcopyrite	$CuFeS_2 + 4O_{2(aq)} \rightarrow Cu^{2+} + Fe^{2+} + 2SO_4^{2-}$ $CuFeS_2 + 4Fe^{3+} \rightarrow 5Fe^{2+} + Cu^{2+} + 2S^0$	--
pentlandite	$Fe_{4.5}Ni_{3.6}Co_{0.9}S_8 + 16.5O_{2(aq)} + 2H^+ \rightarrow$ $4.5Fe^{2+} + 3.6Ni^{2+} + 0.9Co^{2+} + 8SO_4^{2-} + H_2O$ $Fe_{4.5}Ni_{3.6}Co_{0.9}S_8 + 18Fe^{3+}$ $\rightarrow 22.5Fe^{2+} + 3.6Ni^{2+} + 0.9Co^{2+} + 8S^0$	--
Host Mineral Reaction		
calcite	$CaCO_3 \rightarrow Ca^{2+} + CO_3^{2-}$	-8.48
dolomite	$MgCa(CO_3)_2 \rightarrow Mg^{2+} + Ca^{2+} + 2CO_3^{2-}$	-17.09
biotite	$KMg_2Fe(AlSi_3O_{10})(OH)_2 + 10H^+$ $\rightarrow K^+ + 2Mg^{2+} + Fe^{2+} + Al^{3+} + 3H_4SiO_4$	--
muscovite	$KAl_2(AlSi_3O_{10})(OH)_2 + 10H^+ \rightarrow K^+ + 3Al^{3+} + 3H_4SiO_4$	--
albite	$NaAlSi_3O_8 + 4H_2O + 4H^+ \rightarrow Na^+ + Al^{3+} + 3H_4SiO_4$	--
Secondary Mineral Reaction		
Fe(III) (oxy)hydroxide	$Fe(OH)_{3(am)} + 3H^+ \leftrightarrow Fe^{3+} + 3H_2O$	4.89
jarosite	$KFe_3(SO_4)_2(OH)_6 + 6H^+ \leftrightarrow K^+ + 3Fe^{3+} + 2SO_4^{2-} + 6H_2O$	-9.21
silica(am)	$SiO_2 + 2H_2O \leftrightarrow H_4SiO_4$	-2.71
gibbsite	$Al(OH)_{3(am)} + 3H^+ \leftrightarrow Al^{3+} + 3H_2O$	8.11
gypsum	$CaSO_4 \cdot 2H_2O \leftrightarrow Ca^{2+} + SO_4^{2-} + 2H_2O$	-4.58
siderite	$FeCO_3 \rightarrow Fe^{2+} + CO_3^{2-}$	-10.93

Table 4.2 Rate expressions for dissolution of host and secondary minerals

Host Minerals	Rate Expression
calcite	$R = -S_{CaCO_3} [10^{-0.05}[H^+] + 10^{-6.19} + 10^{-3.30}[H_2CO_3]] \left[1 - \frac{IAP}{10^{-8.48}} \right]$
dolomite	$R = -S_{MgCa(CO_3)_2} [10^{-2.59}[H^+]^{0.75} + 10^{-7.66} + 10^{-4.00}[H_2CO_3]^{0.75}] \left[1 - \frac{IAP}{10^{-17.09}} \right]$
biotite	$R = -S_{KMg_2Fe(AlSi_3O_{10})(OH)_2} k_1 [H^+]^{0.25}$
muscovite	$R = -S_{KAl_2(AlSi_3O_{10})(OH)_2} [k_1 [H^+]^{0.08} + k_2 [H^+]^{-0.1}]$
albite	$R = -S_{NaAlSi_3O_8} [k_1 [H^+]^{0.49} + k_2 [H^+]^{-0.3}]$
Secondary Minerals	
Fe(III) (oxy)hydroxide	$R = k_{Fe(OH)_3}^{eff} \left[1 - \frac{IAP}{10^{4.89}} \right]$
jarosite	$R = k_{KFe_3(SO_4)_2(OH)_6}^{eff} \left[1 - \frac{IAP}{10^{-9.21}} \right]$
silica(am)	$R = k_{SiO_2}^{eff} \left[1 - \frac{IAP}{10^{-2.71}} \right]$
gibbsite	$R = k_{Al(OH)_3}^{eff} \left[1 - \frac{IAP}{10^{-8.11}} \right]$
gypsum	$R = k_{CaSO_4 \cdot 2H_2O}^{eff} \left[1 - \frac{IAP}{10^{4.58}} \right]$
siderite	$R = k_{FeCO_3}^{eff} \left[1 - \frac{IAP}{10^{10.93}} \right]$

4.3 Model Parameters

The Type III test pile domain was constructed as a 1-D column with a depth of 12.5 m corresponding to the approximate depth from the test pile crest to the midpoint of the BCLs located at the base of the pile. The simulation domain was discretized in the z-direction as 125 10 cm control volumes. The simulation was run for 2555 days to correspond with the years 2006-2012 (construction of the Type III test pile was completed in 2006). Precipitation measured at the test pile research area were used to

estimate the infiltration with the FAO P-M method described by Neuner et al. (2013). Infiltration resulting from snow melt was insignificant because the majority of snowfall at the top of the test pile experiment is scoured from the crest by wind before the onset of the melting season (Neuner et al., 2013), and was therefore not considered. The partial pressure of $O_{2(g)}$ was set at atmospheric (0.21 atm) as a boundary condition at the top of the simulation domain and infiltrating water was assumed to be at equilibrium with atmospheric $O_{2(g)}$. Gas measurements conducted at the test pile experiment indicated the partial pressure of O_2 within the pile were at atmospheric concentration suggesting that O_2 ingress was not a limiting factor in the oxidation of sulfide minerals (Amos et al., 2009; Chi et al., 2011).

The temperature at each control volume in the simulation was calculated from an input file of measured temperatures (at 2 m intervals) by MIN3P using linear interpolation. Simulation temperature was made consistent with the internal temperature of the test pile experiments by interpolation of measured data as described in the previous section. Temperature data was collected throughout the test pile during the period of late 2006 to 2012 and the temperature of the simulations accurately represented the measured temperature at that time in the test pile (*e.g.*, the interpolated temperature at 5 m deep on December 31, 2007 was approximately the same as was measured in the Type III test pile for that date and depth). Simulation temperature changed on a daily basis and was typically the average of four values measured at a given location on a given day. Porosity, hydraulic conductivity, and soil hydraulic function parameters (Table 4.3) were based on the work of Neuner et al. (2013) and were not adjusted to calibrate the flow solution. The soil hydraulic function parameters were not adjusted to account for freezing conditions. A tracer simulation was conducted to assess the physical flow parameters used for the reactive transport simulations.

During construction of the Type III test pile Smith et al. (2013a) collected samples for S and C analyses providing the mineral volume fractions (ϕ_i) (Tables 4.4 and 4.5) for sulfide and carbonate minerals. Mineral volume fractions for less abundant sulfide minerals, $CuFeS_2$ and ZnS , were calculated using the ratios estimated by Wilson et al. (2018a) from bulk metal analysis conducted on humidity cell samples; $Fe_{4.5}Ni_{13.6}Co_{0.9}S_8$ ϕ_i was calibrated as part of the humidity cell simulations (Wilson et al., 2018a). Mineral volume fractions for host minerals were the same as those used by Wilson et al. (2018a) and Wilson et al. (2018b) (Table 4.5). Simulation ϕ_i were adjusted to 20% of their measured values to represent the portion of minerals in the matrix material and available to

geochemical processes. It was assumed that minerals contained in larger material fractions would not be exposed to O₂ and moisture and therefore would not significantly influence the waste rock geochemistry.

In order to conduct a multi-year simulation, the MIN3P code was modified to consider periods during the experiment when part or all of the test pile was frozen. During periods when the temperature less than 0 °C, hydraulic conductivity was reduced to $1 \times 10^{-10} \text{ m s}^{-1}$, effectively stopping water flow within the portion of the pile experiencing freezing conditions. Elberling (2005) measured O₂ depletion associated with frozen pyritic mine waste and concluded that oxidation reactions can proceed at temperatures below freezing. Using the oxygen depletion measurements, Elberling found that the Q₁₀ temperature coefficient (rate of change of chemical or biological process as a result of an increase of 10 °C in temperature) of the oxidation reaction rate increased significantly (*i.e.*, the reaction rate slowed significantly) at approximately -2 °C due to limited availability of aqueous and gaseous O₂. For this simulation, reaction rates for all minerals were assumed to be insignificant at temperatures below 0 °C. As a result, reaction rates for non-sulfide minerals and secondary minerals were set to zero for temperatures below 0 °C. The temperature dependence of sulfide mineral reaction rates were controlled by coefficients associated with the diffusion of oxidants through a rim of reacted material to the unreacted core of a given mineral; for temperatures below 0 °C, diffusion coefficients were set to zero.

Table 4.3 Physical parameters used in simulations

Parameter	Value
saturated hydraulic conductivity ¹	9.0×10^{-6}
van Genuchten soil hydraulic parameters ²	α 6.9
	n 1.5
flow rate ³	variable
porosity ⁴	0.05

¹Hydraulic conductivity based on experiments of Neuner et al. (2013) in m s^{-1} .

²Van Genuchten parameters based on work of Neuner et al. (2013); α in m^{-1} , n is unitless.

³Infiltration rate determined by FAO Penman-Monteith method.

⁴Porosity based on porosity of matrix material as a proportion to the total porosity of the test pile.

Table 4.4 Initial volume fraction and rate data for sulfide minerals in Type III test pile experiment simulations

Mineral	Type III $\phi_i^{1,2}$	D^{eff} (25 °C)
pyrrhotite – $O_{2(aq)}$	1.6×10^{-3}	2.6×10^{-13}
pyrrhotite – Fe^{3+}		1.2×10^{-9}
chalcopyrite - $O_{2(aq)}$	4.9×10^{-5}	3.5×10^{-13}
chalcopyrite - Fe^{3+}		1.2×10^{-9}
sphalerite - $O_{2(aq)}$	5.3×10^{-5}	4.6×10^{-14}
sphalerite - Fe^{3+}		1.2×10^{-9}
pentlandite - $O_{2(aq)}$	2.0×10^{-5}	4.6×10^{-13}
pentlandite - Fe^{3+}		1.2×10^{-9}

Reactions are transport controlled with $r^p = 0.0625$ mm (after Langman et al., 2014); effective diffusion coefficient (D^{eff}) from Wilson et al. (2018a) in $m^2 s^{-1}$; estimated surface area of $1 m^2 g^{-1}$ (Langman et al., 2014).

¹Total sulfide mineral content based on results of static testing after Smith et al. (2013); Bailey et al. (2015); chalcopyrite and sphalerite content based on Cu and Zn content from whole rock analysis; pentlandite content calibrated based on Ni and Co concentrations in humidity cell effluent.

²Calculated using density specific to each mineral in m^3 mineral m^{-3} porous medium.

Table 4.5 Initial volume fraction and rate data for host and secondary minerals in Type III test pile simulations

Mineral	Type III $\phi_i^{1,2}$	k/k^{eff}	E_a^3	S_i (calibrated)
calcite	1.6×10^{-4}	$k_1 = 10^{-0.05}$ $k_2 = 10^{-6.19}$ $k_3 = 10^{-3.30}$	21	--
dolomite	1.8×10^{-4}	$k_1 = 10^{-2.59}$ $k_2 = 10^{-7.66}$ $k_3 = 10^{-4.00}$	42	--
biotite ⁴	4.7×10^{-2}	$10^{-10.97}$	63	20
muscovite ⁴	1.6×10^{-2}	$k_1 = 10^{-12.60}$ $k_2 = 10^{-13.50}$	22	7
albite ⁴	1.5×10^{-1}	$k_1 = 10^{-9.69}$ $k_2 = 10^{-14.15}$	58	6
Fe(III) (oxy)hydroxide ⁵	--	10^{-8}	--	--
k-jarosite ⁵	--	10^{-8}	--	--
gibbsite ⁵	--	10^{-12}	--	--
silica (am) ⁵	--	10^{-6}	--	--
gypsum ⁵	--	10^{-6}	--	--
siderite ⁵	--	10^{-9}	--	--

¹Mineral content of carbonate minerals based on static testing (after Smith et al., 2013b; Bailey et al., 2015); mineral content of host minerals based on results presented in Jambor 1997.

²Calculated using $\rho_b = 1.62 \text{ g cm}^{-3}$ in m^3 mineral m^{-3} porous medium and adjusted during simulation calibration.

³Activation energy in kJ mol^{-1} .

⁴Calibrated surface area in m^2 mineral L^{-1} porous medium based on mineral volume fraction and bulk surface area after Langman et al. (2014) and adjusted to fit measured humidity cell effluent parameters (Wilson et al., 2018a). Calibrated activation energy (Wilson et al., 2018a).

⁵Calibrated effective rate constant in mol L^{-1} porous medium s^{-1} (Wilson et al., 2018a).

4.4 Results

One of the refinements of the test pile simulation relative to the previous DWRP reactive transport scale-up simulations (Wilson et al., 2018a; Wilson et al., 2018b) was the introduction of a spatially

dynamic temperature regime. The measured temperature data was compiled according to depth within the test pile and provided as input to the simulations through the use of a temperature field.

Temperature data was available at approximately 0.5 m intervals throughout the depth of the test pile except for the region between approximately 11.5 m depth and the base of the test pile (approximately 14.0 m). Six temperature regimes were constructed for the core of the test pile and included temperature fields which specified depth dependent temperature at one (homogeneous), three (6 m interval), five (3 m interval), seven (2 m interval), 13 (1 m interval), and 25 (0.5 m interval) nodes. Each temperature regime provided a daily temperature for each node. Flow simulations were conducted to determine the optimal temperature discretization by analysis of the error in the total annual simulation outflow compared to measured outflow and the error of interpolated simulation temperature compared to measured temperature at selected intervals. The results of the temperature regime optimization simulations indicated that including more than seven temperature nodes within the test pile did not improve the agreement between the interpolated and measured temperature profiles. The seven temperature node simulations captured the measured temperature variation at and between nodes (Figure 4.3). The simulations started on January 1, 2006; however, temperature data from the test pile was not available until August 2006. Temperature data from 2007 was substituted for the missing 2006 temperature data. Other than averaging up to four measurements per day to provide a daily average temperature for a given point, the input temperature was not modified or smoothed in any way. Additional processing of the temperature data did not improve the fit of the simulated outflow to the observed outflow.

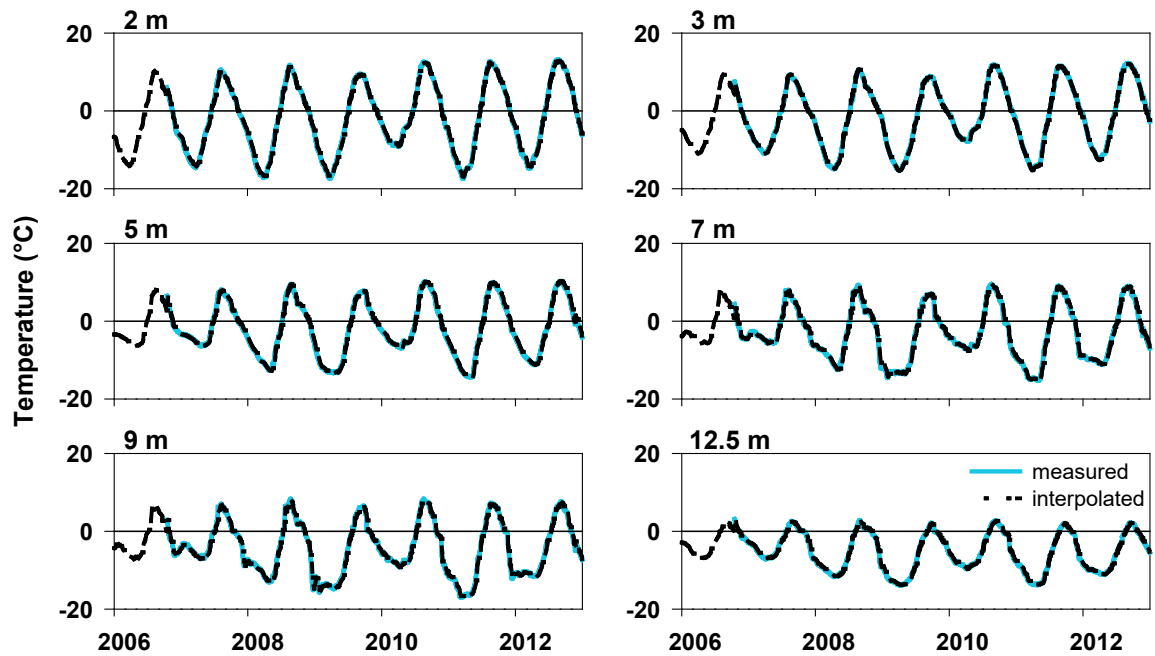


Figure 4.3 Interpolated simulation temperature and measured temperature [°C] at 2 m, 3 m, 5 m, 7 m, 9 m, and 12.5 m (measured from test pile crest) versus time [year]. Input temperatures for the simulations were provided for depths 0 m, 2.5 m, 4.5 m, 6.5 m, 8.5 m, 10.5 m, and 12.5 m (measured from test pile crest).

Water flow simulations were conducted in conjunction with the temperature regime interpolations. For comparison to the simulated outflow, the total daily measured outflow volume was divided by the total BCL area contributing to that outflow to calculate the daily volume of outflow from the Type III core per square meter. It was assumed that all flow to the BCLs was due to infiltration at the top of the test pile. Simulation of flow through the core of the Type III test pile indicated that measured outflow volume was captured by the simulated outflow (Figure 4.4) over the six year simulation period. A tracer test was simulated for the test pile domain to estimate water velocity through the test pile and residence time. The simulated water velocity of 0.01 m d^{-1} (averaged over the year) compared well with the velocity of 0.006 m d^{-1} calculated from the results of the 2007 tracer test

conducted at the Type III test pile experiment. The simulated residence time of approximately 5.3 years (Figure 4.5) is consistent with the measured peak tracer arrival (representing flow through the core of the test pile) of approximately 5 years reported by Krentz, 2014 and Zak, 2017. Error in the flow simulation was calculated by averaging the difference between the annual measured and simulated flow volumes. The error associated with the flow solution over the 6 year simulation was less than 7%. The simulation in some years under predicted the total flow (Figure 4.4 B) and over predicted in some years; however, the overall flow through the simulation period is consistent with the measured outflow.

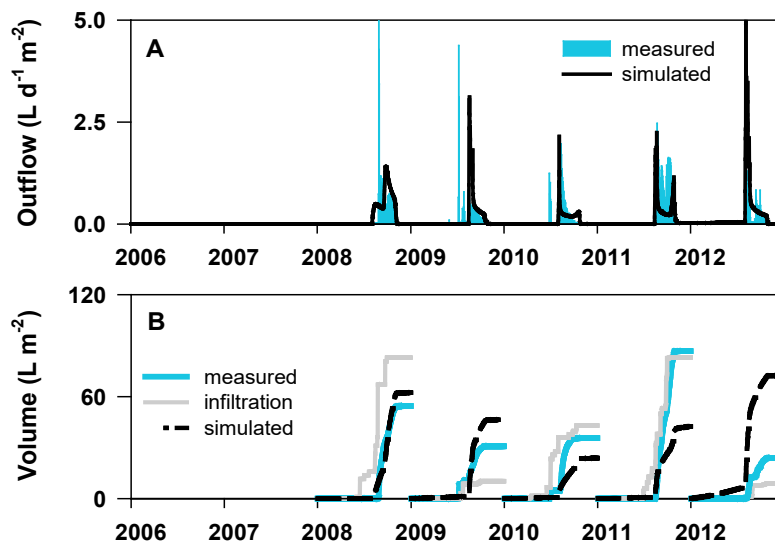


Figure 4.4 **A:** Daily outflow [L d⁻¹] versus time [year] measured and simulated for the Type III test pile experiment. **B:** Measured and simulated cumulative annual outflow [L] and cumulative annual estimated infiltration (using FAO-Penman Monteith method) versus time [year] for the Type III test pile.

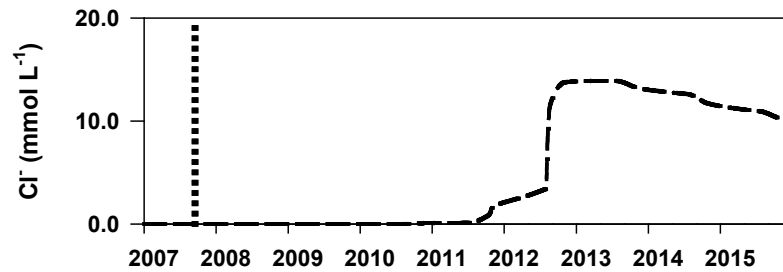


Figure 4.5 Simulated Cl^- concentration [mmol L^{-1}] (dashed line) from the Type III test pile core versus time [year] following injection on September 13, 2007 (vertical dotted line). Peak simulated tracer concentration occurred on December 31, 2012, approximately 5.3 years after tracer injection.

The simulated effluent geochemistry was compared to effluent geochemistry measured from samples collected at the BCL drains at the base of the Type III test pile. In this case, the measured effluent geochemistry was an average of all BCL samples collected during each sampling event. Compared parameters included SO_4 , Ni, Co, Cu, Zn, Fe, Al, Si, Ca, Mg, K, and Na in units of concentration (Figure 4.6) and units of mass flux (Figure 4.7); pH and alkalinity were also compared (Figure 4.6).

Sinclair et al. (2015) analyzed the effluent from the core of the Type III test pile and noted an early season flush of higher solute concentration was followed by a relatively steady decline in solute concentration for the duration of the flow season. Sporadic flow often occurred from the core of the test pile prior to the onset of the regular flow season; however, this early season flow was likely water frozen in the drain system the previous year and not representative of the geochemical condition of the core of the test pile (Sinclair et al., 2015). High solute loads observed at the start of each flow season was hypothesized to be a result of two related factors: i) water residence time and ii) extended sulfide oxidation occurring during periods of little or no flow near pile freeze-up (Sinclair et al., 2015). Briefly summarizing general trends, the average annual concentrations of solutes that are indicators of sulfide-weathering, including SO_4 , Ni, Co, Cu, and Zn, increased from 2008 to 2012. Average annual concentrations of solutes indicating host rock weathering, including Ca, K, Mg, Na, Al, and Si, remained relatively stable or increased slightly throughout the 2008 to 2012 period. Measured pH from the core of the Type III test pile declined slightly from an average annual value of

4.7 in 2008 to an average annual value of 4.3 in 2012. Over the same period, alkalinity declined from an annual average of approximately 9 mg L⁻¹ as CaCO₃ to an annual average of approximately 2 mg L⁻¹ as CaCO₃ (Sinclair et al., 2015).

The simulation captured the 2008-2012 general concentration trend and some annual variation well for some parameters (*e.g.*, SO₄, Ni, Co, Zn, Al, Si, Ca, and K); however, did not capture the concentrations of some metals associated with sulfide mineral oxidation (*e.g.*, Fe and Cu) or pH and alkalinity. Intra-annual concentration variations were not captured by the simulation; this was likely because the simplified implementation of freeze thaw dynamics did not fully represent the conceptual model proposed by Sinclair et al., 2015. The initially lower than observed simulated concentrations of Cu suggested variation in the adsorption parameters from the smaller scale experiments (humidity cells and AZLs) to the large-scale field experiment. The higher than observed simulated pH and alkalinity was consistent with the simulations of the geochemical evolution of the DWRP AZL (Wilson et al., 2018b). Wilson et al. (2018b) suggested that the higher than observed pH and alkalinity of the AZL simulations was consistent with limited carbonate mineral availability compared to the humidity cell simulations.

Similar to the concentration results, the annual mass flux trend from the system was reasonably captured for some parameters (*e.g.*, SO₄, Ni, Co, Al, Ca, and K); however, the simulations did not capture the mass load of some metals associated with sulfide mineral oxidation (Fe, Cu, and Zn). The mass flux for most parameters was not captured well in 2012 likely a result of the over-prediction of effluent volume for that year.

The pH of the system was simulated more accurately (Figure 4.8) by decreasing the calcite content to 20% of the measured value, consistent with the calibration of the AZL simulations required to accurately simulate the pH and alkalinity of the AZL experiment (Wilson et al., 2018b). Overall, following the modification of the calcite content, the simulated concentrations and mass flux compared well to the measured concentrations and mass flux with improved fit for Fe, pH, and alkalinity (Figure 4.8 and Figure 4.9). This result indicated that integrated conceptual model can be scaled from the medium field scale (AZL) to the large field scale to provide a reasonable characterization of the geochemical evolution of the Diavik waste rock. The medium sized field experiment provided an important link in the refinement of the conceptual model between laboratory and field experiments.

Sinclair et al. (2015) supplemented their characterization of the geochemical evolution of the Diavik waste rock with analysis of the samples collected from soil water solution samplers (SWSS) installed in the core of the Type III test pile. The SWSS were installed at depths of approximately 2, 3, 5, 7, and 9 m from the crest of the pile and samples were collected regularly (approximately bi-weekly) during periods when the test pile was not frozen. More details about the installation of the SWSS and sampling protocol can be found in Smith et al. (2013a) and Sinclair et al. (2015). Calibrated (for pH) simulation results for parameters indicative of sulfide mineral weathering (pH, Fe, SO₄, Ni, Cu, and Zn) and acid neutralization (alkalinity and Al) captured the general trends of most measured parameters through the years 2007 to 2012 (Figures 4.10 and 4.11) although some of the depth variation is not captured by the simulations. The alkalinity profile is the main exception; the simulated alkalinity profile did not capture the relatively well defined progression of alkalinity depletion within the test pile. The profiles of Ni, Cu, and Zn illustrate the difficulty of simulating adsorption while attempting to constrain the number of parameters used for calibration. Although the general profile was captured for all three metals, only the Ni profile matches the measured profile reasonably well; the simulated Cu profile overestimated the measured values and the simulated Zn profile only captures portions of the measured profile indicating differences in mineral surface processes from the humidity cell scale.

Simulation run times averaged approximately 3.5 hours on a single processor laptop machine.

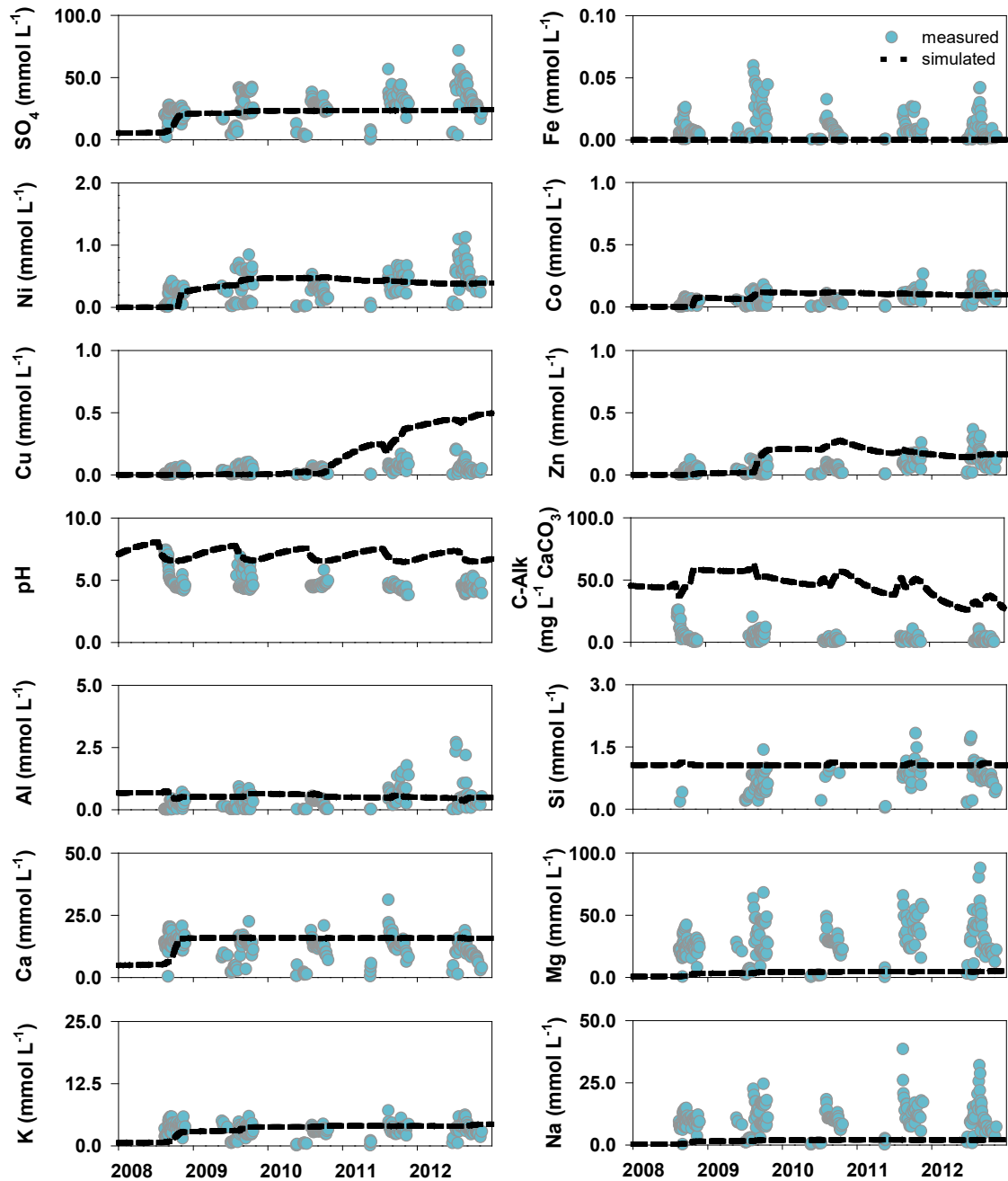


Figure 4.6 Concentrations of mineral weathering products SO₄, Fe, Ni, Co, Cu, Zn, Al, Si, Ca, Mg, K, and Na [mmol L⁻¹], pH [-], and alkalinity [as mg L⁻¹ CaCO₃] versus time [year] measured in Type III test pile effluent compared to aqueous concentration exiting the simulation domain. Measured concentrations are available only for periods of test pile core flow; simulated concentrations are

calculated by the model for all periods regardless of flow condition.

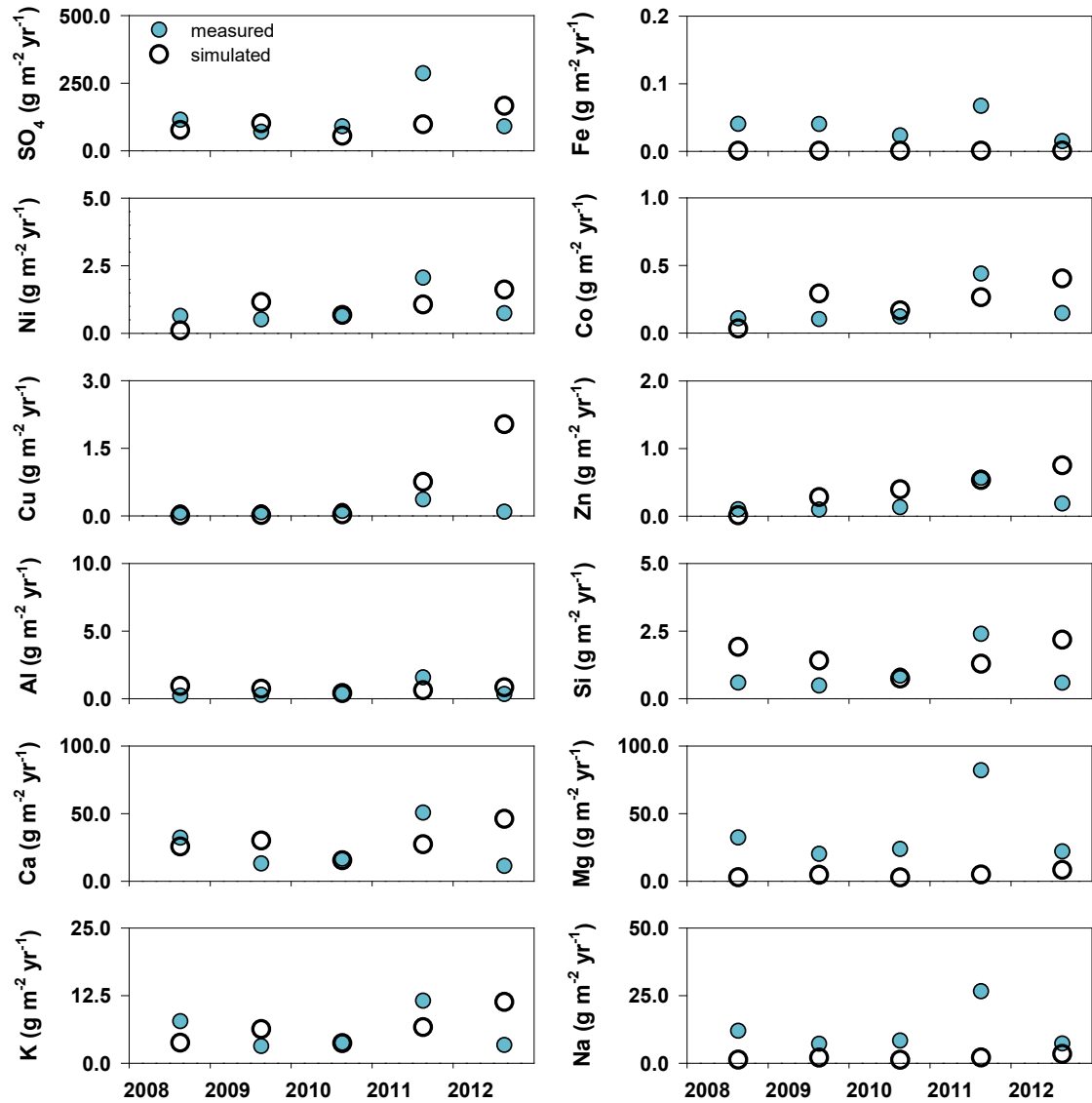


Figure 4.7 Total annual mass of mineral weathering products SO_4 , Fe, Ni, Co, Cu, Zn, Al, Si, Ca, Mg, K, and Na [$\text{g m}^{-2} \text{yr}^{-1}$] versus time [year] measured in Type III test pile effluent compared to total mass exiting the simulation domain.

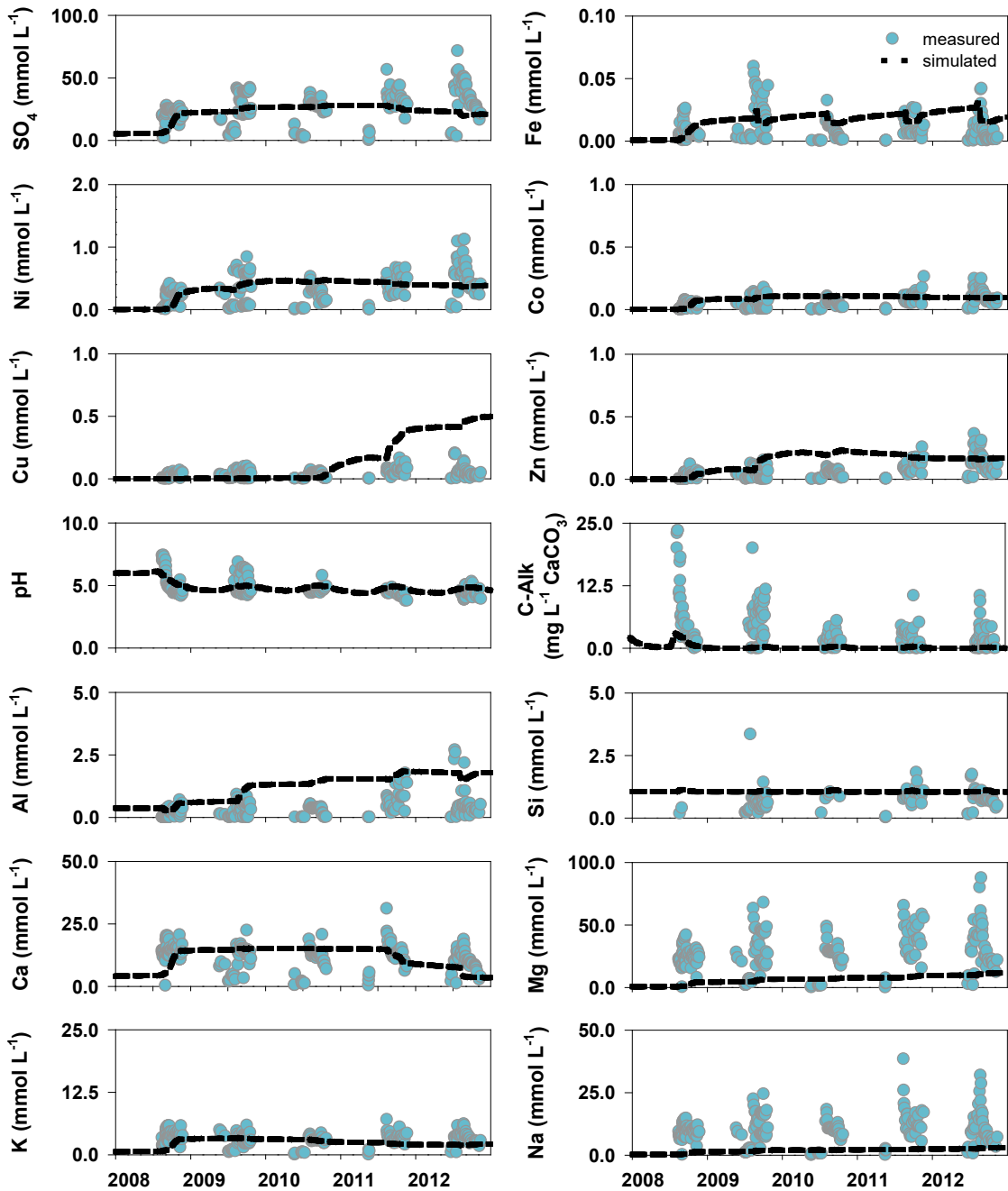


Figure 4.8 Concentrations of mineral weathering products SO₄, Fe, Ni, Co, Cu, Zn, Al, Si, Ca, Mg, K, and Na [mmol L⁻¹], pH [-], and alkalinity [as mg L⁻¹ CaCO₃] versus time [year] measured in Type III test pile effluent compared to aqueous concentration exiting the calibrated (calcite reduction to 20% of measured) simulation domain. Measured concentrations are available only for periods of test

pile core flow; simulated concentrations are calculated by the model for all periods regardless of flow condition.

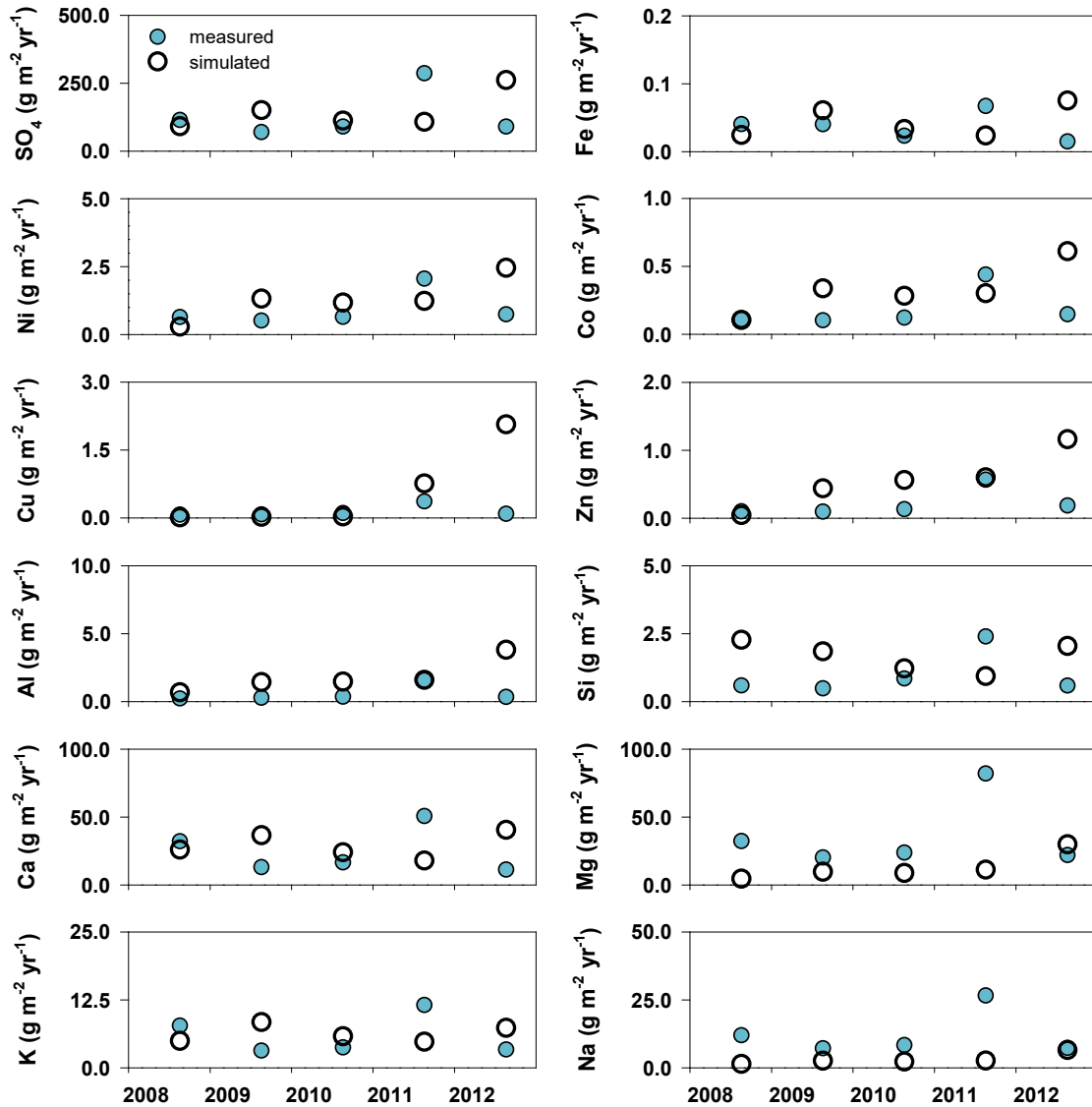


Figure 4.9 Total annual mass of mineral weathering products SO₄, Fe, Ni, Co, Cu, Zn, Al, Si, Ca, Mg, K, and Na [g m⁻² yr⁻¹] versus time [year] measured in Type III test pile effluent compared to total mass exiting the calibrated (calcite reduction to 20% of measured) simulation domain.

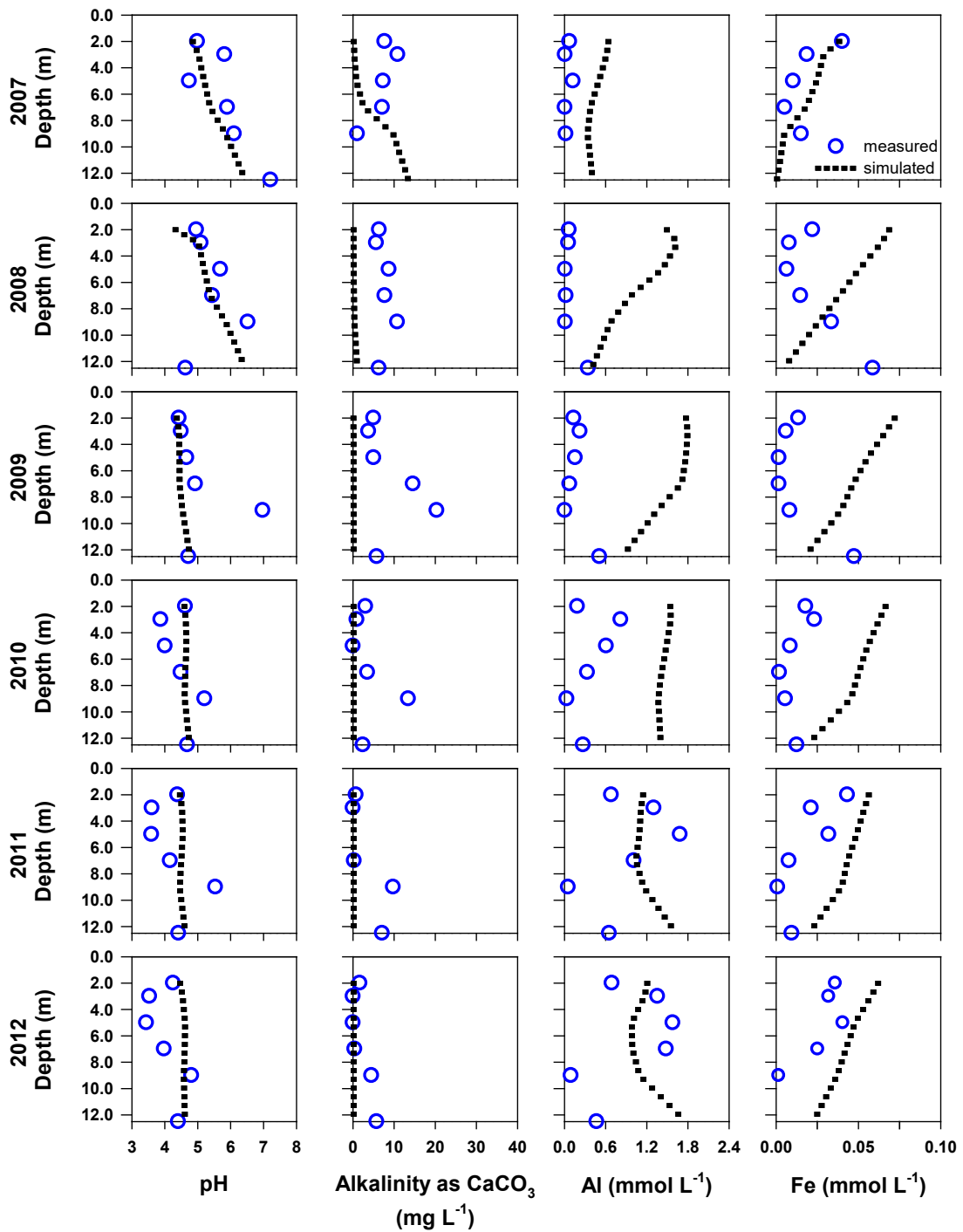


Figure 4.10 Average annual concentrations of mineral weathering products Al, Fe [mmol L⁻¹], pH [-], and alkalinity [as mg L⁻¹ CaCO₃] versus depth [m] measured from test pile crest, measured in

samples collected at soil water solution samplers installed in the Type III test pile compared to calibrated simulation aqueous concentration.

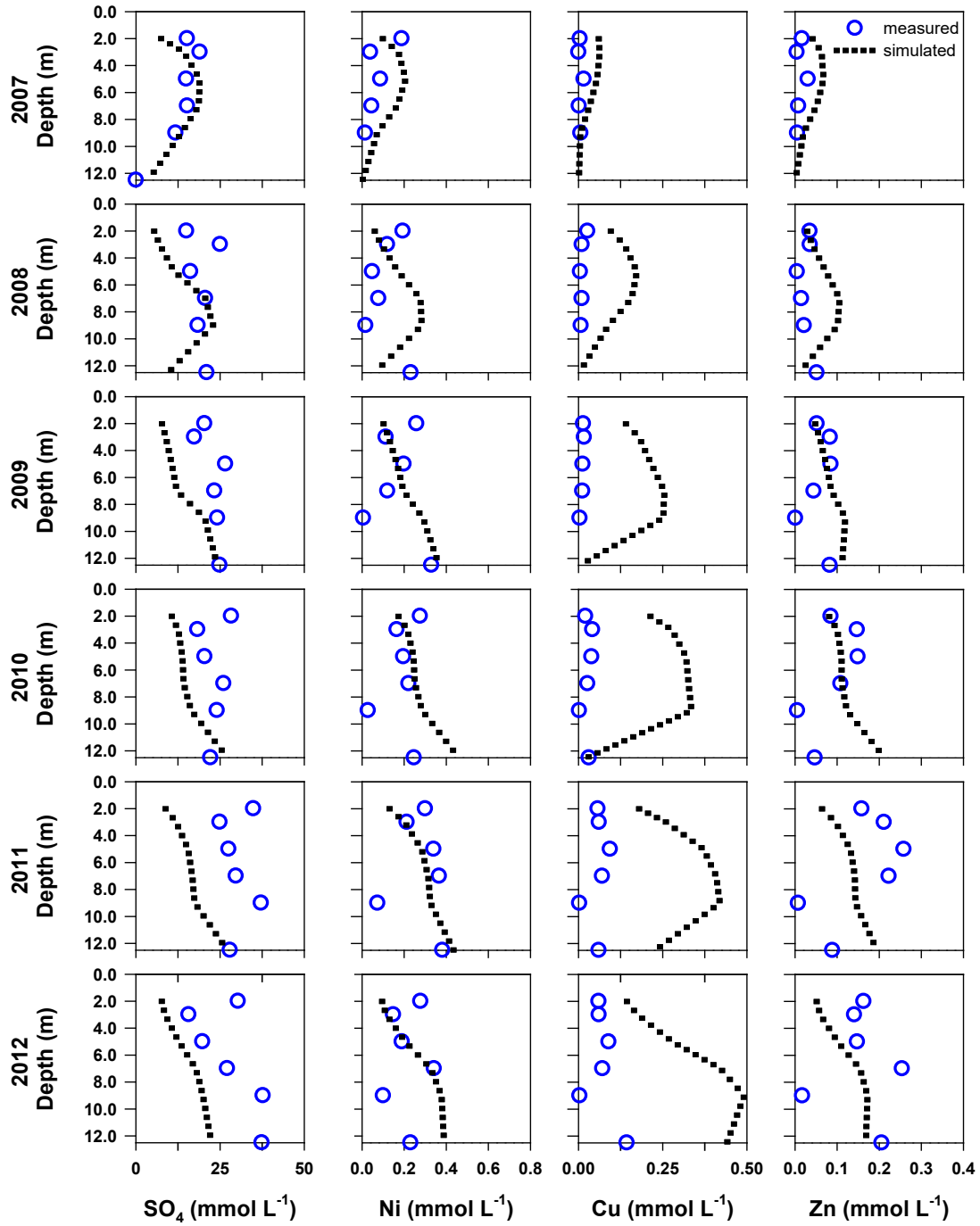


Figure 4.11 Average annual concentrations of mineral weathering products SO_4 , Ni, Cu, and Zn [mmol L^{-1}] versus depth [m], measured from test pile crest, measured in samples collected at soil water solution samplers installed in the Type III test pile compared to calibrated simulation aqueous concentration.

4.5 Discussion

The integrated conceptual model that was implemented for the DWRP test pile experiment was developed using widely applicable mechanisms (shrinking core model, adsorption model) such that when coupled with routinely measured, site specific physical parameters (mineral surface area, mineral volume fraction, hydraulic conductivity, temperature, and infiltration) can be used to simulate the geochemical evolution of waste rock under a variety of conditions. The version of the integrated conceptual model implemented for the DWRP experiments makes use of site specific mineralogy and physical parameters that will not necessarily be applicable to other sites. The simulations conducted for the test pile experiment were intended to test the integrated conceptual model under complex conditions closely replicating full size waste-rock piles and highlight any discrepancies that may occur when scaling a mechanistic method of geochemical simulation.

The uncalibrated integrated conceptual model captured the effluent concentrations of some parameters quite well over the course of the simulation. The concentrations of other parameters, including dissolved metals derived from sulfide-mineral oxidation, were not captured as well. The results illustrate some important differences between the experiment scales. Annual mass flux was captured reasonably well for some parameters, but was underestimated for metals derived from sulfide-mineral oxidation. The results of the uncalibrated simulation suggested an important difference in the geochemical evolution of the waste rock between the small laboratory scale and the large field scale that the availability of calcite was lower in the field experiments. It should be reiterated that the uncalibrated simulation was conducted using the same mineralogy as the uncalibrated AZL simulation (Wilson et al., 2018b). Supplemental simulation, based on similar behaviour for the AZL scale, indicated that decreased availability of calcite to 20% of the measured content resulted in a reasonable simulation of the geochemical evolution of the test pile waste rock.

To assess the quality of the scale-up approach, the root mean square error of the annual mass flux residual [mol m^{-2}] from the cold temperature humidity cells and core of the Type III test pile were compared (Table 4.6). Comparison was made to both the Type I and Type III humidity cell results to

provide a range of error values that encompassed the S content of the test pile experiment (the S content of the Type I and Type III humidity cells was 0.02 wt.% and 0.18 wt.% S, respectively). The cold humidity cells were used for the comparison because the average annual temperature in the core of the Type III test pile for days when the temperature was above 0 °C ranged from 3.8 to 5.2 °C (the cold temperature humidity cells were maintained at 5 °C); thus providing a comparable temperature regime. The number of above 0 °C days between 2008 and 2012 within the core of the Type III test pile ranged from 115 to 136. To account for periods of freezing within the test pile, the humidity cell ‘annual’ mass flux was calculated to correspond with the number of thawed days within the test pile (*e.g.*, year 1, 2008 in the test pile, corresponded to the first 129 days of the humidity cell experiment). The larger mass of matrix material in the test pile compared to the humidity cells was accounted for by multiplying the root mean square error for the humidity cell cases by a factor of 25 (*i.e.*, the test pile contained 25 times the matrix material per m²). The residual error of the mass flux for parameters at the test-pile scale is within the same order of magnitude or lower than the residual error of the mass flux at the humidity-cell scale. This residual analysis indicates that the scale-up approach provides a fit to the measured test pile data similar to the fit of the humidity cell simulations to the measured data at the laboratory scale.

Table 4.6 Summary of the root mean square error of annual mass flux residual [mol m^{-2}] from the Type I humidity cell, Type III humidity cell, and Type III test pile simulation cases

Parameter	Type I HC	Type III HC	Type III TP
Al	5.5×10^{-1}	9.5×10^{-1}	5.1×10^{-1}
Ca	1.1×10^0	2.8×10^0	3.8×10^{-1}
Co	4.6×10^{-3}	1.7×10^{-2}	2.7×10^{-2}
Cu	5.5×10^{-4}	5.8×10^{-2}	1.4×10^{-2}
Fe	9.8×10^{-3}	5.4×10^{-1}	7.4×10^{-4}
K	2.9×10^{-1}	4.8×10^{-1}	1.1×10^{-1}
Mg	4.0×10^{-1}	1.1×10^0	1.5×10^0
Na	3.6×10^{-1}	4.6×10^{-1}	5.4×10^{-1}
Ni	2.3×10^{-3}	7.7×10^{-2}	1.1×10^{-2}
Si	9.4×10^{-1}	2.3×10^0	3.4×10^{-2}
SO ₄	6.5×10^{-1}	5.1×10^0	9.2×10^{-1}
Zn	2.6×10^{-3}	4.5×10^{-2}	4.5×10^{-3}
pH	1.6×10^1	7.2×10^0	4.6×10^{-1}

One of the core outcomes of this investigation into mechanistic methods for scale-up was development of an integrated conceptual model capable of being implemented to simulate the geochemical evolution of waste rock exposed to atmospheric conditions. As a result, two significant additions to the integrated conceptual model, not considered for the AZL simulations (Wilson et al., 2018b), were i) spatially dynamic temperature, and ii) intermittent water flow and chemical reactions due to the development of freezing conditions.

4.5.1 Temperature

The interpolated temperature regime captured the measured temperature of the core of the test pile; however, the presence of heat trace within the test pile and the associated influence on temperature were not considered as part of the simulations. Heat trace within the pile is primarily located around drains and lysimeter installations but the influence of their temperature signal on the geochemical evolution of the waste rock was expected to be minimal. Additionally, temperature data was only

available to a depth of approximately 11.5 m (measured from the test pile crest) meaning that the temperature at depth 12.5 m (bottom of simulation) was linearly interpolated between deepest pile measurements and measurements from below the test pile at approximately 14 m depth. The interpolated temperature value likely underestimated the actual temperature due to the presence of heat trace at drains and lysimeters and may account for a portion of the difference in timing of measured outflow versus simulated outflow (*e.g.*, measured outflow occurs in 2009, 2010, and 2012 prior to simulated outflow).

4.5.2 Infiltration

The temporally dynamic infiltration regime along with a temporally and spatially dynamic temperature regime included in the simulations captured the general outflow from the core of the test pile. The infiltration regime was based on the estimates of infiltration calculated using the same FAO-PM method used for the AZL simulations (Neuner et al., 2013). Infiltration events initiated water flow through the test pile core by pressure wave propagation and displacement of resident pore water (Neuner et al., 2013). The simulation of water flow from the core of the test pile agreed well with the timing of flow measured in each of the five flow seasons (2008-2012). No flow occurred from the simulation domain in 2006 and 2007 as was the case at the test pile. The matrix material saturated hydraulic conductivity of $9 \times 10^{-6} \text{ m s}^{-1}$ measured by Neuner et al. (2013) was used to simulate the flow system, no calibration of the hydraulic conductivity was conducted as part of the scale-up from medium- to large-scale field experiments.

Water freezing was considered for the test-pile experiment simulations. The MIN3P code was developed such that the saturated hydraulic conductivity of the frozen material was reduced to $1 \times 10^{-10} \text{ m s}^{-1}$ when temperatures were less than $0 \text{ }^{\circ}\text{C}$. This refinement in the implementation of the integrated conceptual model meant flow occurred in some parts of the test pile and not in other parts of the pile according to the temperature regime; this modification provided reasonable agreement between timing of measured and simulated outflow.

4.5.3 Mineral Volume Fraction

For the Type III test pile simulations, the sulfide mineral volume fraction was identical to that used for the AZL simulations (Wilson et al., 2018b). The test pile simulations were conducted assuming the significant geochemical weathering occurred in the fine grained component of the pile, consistent

with the AZL simulations and the calibration of the conceptual model at the humidity cell scale. The reliance of the test pile simulations on mineral surface area lends confidence to the suggestion of Amos et al. (2015) that a primary parameter of consideration when assessing the geochemical evolution of waste rock at various scales is mineral surface area and provides further indication that reactions within the high surface area matrix material exert significant influence on the geochemical evolution of waste rock (Amos et al., 2011).

4.5.4 Secondary Mineral Control

The geochemical characterization of the Type III test pile conducted by Sinclair et al. (2015) included analysis of the influences of secondary minerals on pore water concentrations of Fe, Al, Ca, and SO₄. The results of the reactive transport simulation indicate secondary-mineral precipitation did exert control on solute concentrations confirming the importance of including secondary minerals when characterizing the geochemical evolution of waste rock using scale-up approaches.

The precipitation of secondary Fe minerals Fe(OH)₃ and KFe₃(SO₄)₂(OH)₆ occurred throughout the test pile for the duration of the simulation with KFe₃(SO₄)₂(OH)₆ lagging one year behind Fe(OH)₃. Simulated Fe(III) (oxy)hydroxide started precipitating in 2006; KFe₃(SO₄)₂(OH)₆ did not precipitate until part way through 2007. Fe(III) (oxy)hydroxide precipitation generally occurred throughout the flow season in the deeper portions of the test pile; in the upper portion of the test pile dissolution occurred mid-season approximately corresponding with periods of higher temperature and higher rates of sulfide oxidation, which was consistent with the Sinclair et al. (2015) hypothesis that Fe(OH)₃ could be acting as a pH control within the system. The dominance of Fe(OH)₃ precipitation over dissolution in the simulations indicated Fe(OH)₃ was in general acting as a control on Fe concentrations in pore water. Jarosite precipitation in the simulations occurred during 2007 and 2008 then followed a pattern of early season precipitation followed by later season dissolution indicating its influence as a temporary delay mechanism in release of Fe and SO₄ and its bimodal influence in pH moderation. The precipitation/dissolution cycle of KFe₃(SO₄)₂(OH)₆ in the test pile simulations was consistent with the behaviour of KFe₃(SO₄)₂(OH)₆ in the AZL simulations.

Simulation results indicated that CaSO₄·2H₂O precipitation occurred within the test pile exerting only temporary control on Ca concentrations as proposed by Sinclair et al. (2015). Gypsum precipitation occurred in the simulations, primarily in the lower portion of the test pile (>9 m depth)

during the later years of the simulation (2009-2012) and was followed by dissolution to complete depletion in the same year.

Sinclair et al. (2015) proposed the precipitation of Al secondary minerals, including $\text{Al}(\text{OH})_3$, as an initial control on Al concentrations in pore water, becoming a secondary source of Al as the capacity of calcite to consume H^+ was exhausted. The results of the simulations indicated that $\text{Al}(\text{OH})_3$ precipitated throughout the pile during all years of the simulation. Limited dissolution of $\text{Al}(\text{OH})_3$ occurred, primarily in the upper portion of the test pile during later years of the simulation, consistent with the hypothesis put forth by Sinclair et al. (2015). The simulation indicated the primary influence of $\text{Al}(\text{OH})_3$ on the test pile system during the period 2008-2012 was as a control on the release of Al to pore water.

Amorphous Si precipitated in the simulated test-pile domain for the duration of the simulation period exerting a control on the Si effluent concentrations.

4.5.5 Acid Neutralization

The trend of decreasing pH and alkalinity at the Type III test pile experiment during the 2008-2012 period is indicative of decreased calcite availability and complete depletion of calcite by 2010 (Sinclair et al., 2015). The uncalibrated simulation results indicated that calcite was capable of consuming the H^+ produced by sulfide oxidation resulting in a pH that did not decrease during the simulation. This result was consistent with the uncalibrated AZL simulations suggesting not all of the measured carbonate mineral content was available for H^+ consumption. Decreasing the calcite content to 20% of the measured resulted in accurately simulated pH, which is consistent with the method used to accurately simulate the pH of the medium-scale field experiment and lends strength to the argument that there was a lowered calcite availability from the small-scale laboratory experiment to the medium- and large-scale field experiments.

The simulation of the geochemical evolution of the test pile illustrated the acid neutralization sequence within the pile (Figure 4.12). Sinclair et al. (2015) proposed an acid neutralization sequence that started with calcite dissolution. Following calcite exhaustion, Sinclair et al. (2015) proposed a sequence of limited $\text{Al}(\text{OH})_3$ dissolution that progressed to $\text{Fe}(\text{OH})_3$ dissolution as the primary acid neutralization phase. Review of the simulation results indicates the model neutralization sequence is consistent with the Sinclair et al. (2015) hypothesis. Matrix material calcite content was exhausted

within the simulation by mid-2009. Subsequent acid neutralization was dominated by $\text{Fe}(\text{OH})_3$ dissolution particularly when sulfide mineral oxidation rates are at their peak in the mid flow season. Limited $\text{Al}(\text{OH})_3$ dissolution occurred, and was restricted to the upper portion of the simulation domain. The carbonate mineral dolomite was present within the simulated system and contributed to acid neutralization throughout the simulation period at all depths of the test pile domain; however, because the rate of dolomite dissolution was an order of magnitude lower than calcite the influence of dolomite in the acid neutralization sequence may be of secondary importance.

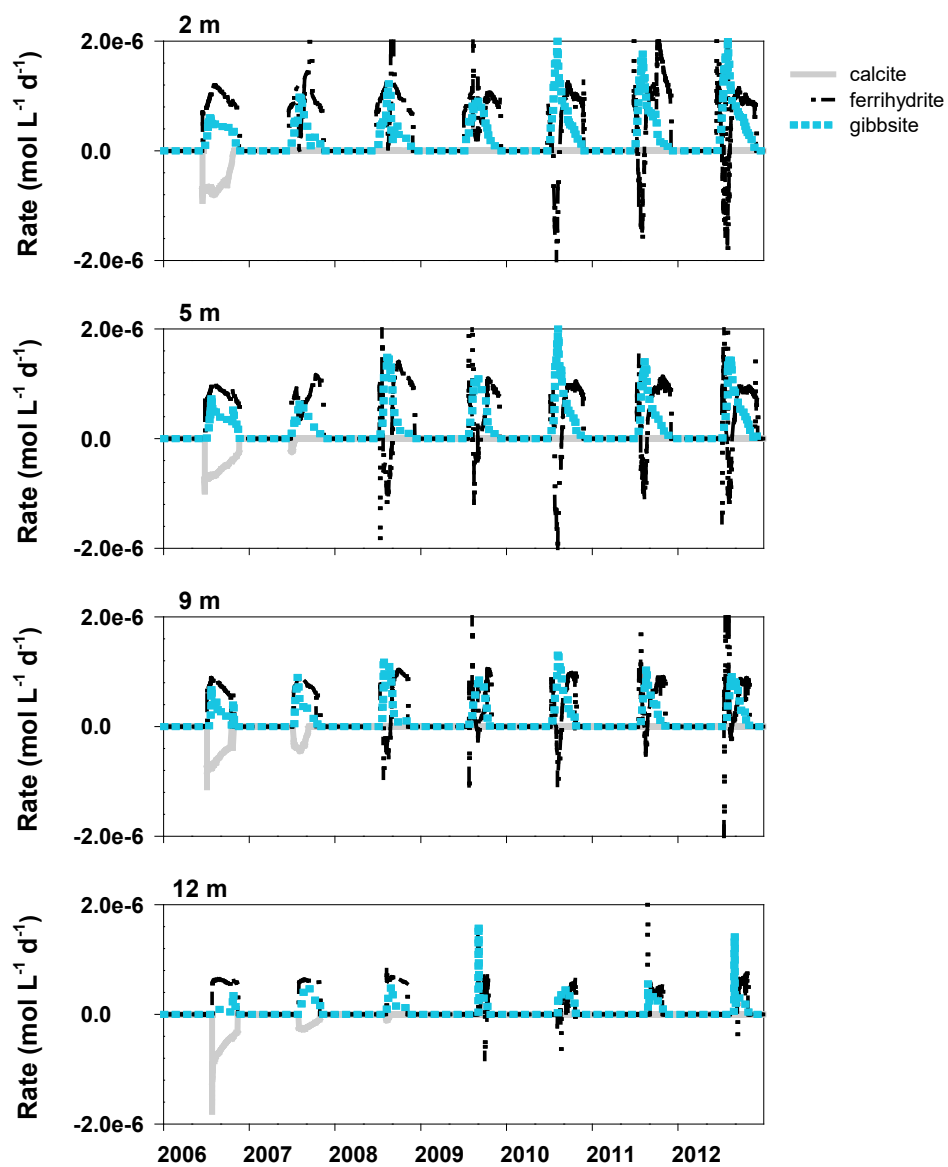


Figure 4.12 Simulated rates of calcite, gibbsite, and ferrihydrite dissolution and/or precipitation [$\text{mol L}^{-1} \text{bulk d}^{-1}$] versus time [year] in the Type III test pile. Rates greater than zero indicate mineral precipitation; rates less than zero indicate mineral dissolution. Rates of zero indicate that the test pile is frozen and reactions have stopped or that a mineral has been exhausted.

4.6 Conclusions

Simulation of the geochemical evolution of the Diavik waste rock through implementation of the integrated conceptual model provided an excellent opportunity to evaluate the efficacy of mechanistic scaling techniques. Analysis of the flow portion of the simulation indicated that some of the divergence in the simulation mass flux results from the measured values can be attributed to simulated flow volume, illustrating the importance of adequately representing the flow regime at the more complex larger scales.

Scaling the integrated conceptual model resulted in good agreement between measured and simulated concentrations and mass flux of most parameters. The integrated conceptual model was capable of producing a reasonable assessment of waste rock characterization under the temporally and spatially dynamic temperature regime of the Type III test pile.

The test pile simulations suggested calcite availability as a primary mechanism that contributed to differences between the small-scale and large-scale simulations. The results of the calibrated simulation indicated that calcite availability was approximately 20% of the measured content; this result is consistent with simulation of the DWRP medium scale field experiment using the integrated conceptual model (Wilson et al., 2018b).

The mechanistic approach to scale-up documented here highlighted that a detailed conceptual model coupled with a reactive transport model is capable of providing a reasonable characterization of the geochemical evolution of a waste rock. The central parameters of the integrated conceptual model, including mineral surface area, mineral content, temperature, and infiltration, have been shown here to provide appropriate scale-up factors in the mechanistic simulation of the geochemical evolution of waste rock. The reliance on a relatively limited number of easily measurable parameters suggests that this approach could be implemented at other sites using the appropriate site specific parameters.

Chapter 5

Geostatistical analysis of sulfur, carbon, and hydraulic conductivity distribution in a mine waste-rock test pile

Mine-waste rock stockpiled at surface and exposed to O₂ and moisture can lead to high concentrations of sulfate and transition metals and acidic effluent. This effluent requires management to mitigate impacts to receiving environments. To assess the quality of mine-waste effluent, empirical (*e.g.*, scale factors) and mechanistic (*e.g.*, reactive transport models) methods have been used (*e.g.*, Wunderly et al., 1996; Bain et al., 2001; Jurjovec et al., 2004; Andrina et al., 2006; Brookfield et al., 2006; Demers et al., 2013). Most methods of effluent assessment or prediction are dependent on the mine-waste characteristics that contribute to the geochemical evolution of mine-waste rock including the mineralogy of the waste and the physical characteristics controlling water flow and O₂ transport. Investigations of waste-rock weathering often rely on global parameters such as mean S and C mineral content and saturated hydraulic conductivity (K_S). Limited investigations have been conducted regarding the heterogeneity of these critical parameters. Fala et al. (2013) investigated the role of K_S heterogeneity on water flow through a hypothetical waste-rock pile and found that flow patterns generally followed the distribution of K_S within a waste-rock pile. The Fala et al. (2013) study included the role of heterogeneous S distribution within a hypothetical waste-rock pile and found that lower pH and higher S oxidation rates were associated with areas of the pile with higher S fraction and smaller particle size. Coupling a heterogeneous K_S distribution with a heterogeneous S and/or C distribution in a mechanistic implementation could define further the role of mineralogical and K_S heterogeneity in the geochemical evolution of mine-waste rock.

The Diavik Waste Rock Project (DWRP) experiments included two large-scale test piles that were constructed, starting in 2005, at the Diavik Diamond Mine, NT, Canada (Diavik) to investigate the geochemical evolution of sulfidic waste rock exposed to atmospheric conditions. The densely instrumented test piles were approximately 50 m x 60 m x 15 m and were constructed with sulfidic waste rock according to the Diavik separation protocol. Waste rock at the mine was separated according to S content: Type I (wt.% S < 0.04), Type II (0.04-0.08 wt.% S), and Type III (wt.% S > 0.08). One of the test piles was constructed entirely of Type I material (average 0.035 wt.% S), a

second test pile was constructed entirely of Type III material (mean 0.053 wt.% S) (Smith et al., 2013b).

The Type I test pile was deconstructed in 2014 to investigate the progress of mineral weathering within the test pile. The test pile was excavated in a series of benches that allowed sample collection for parameters including mineralogy and grain size throughout the pile (Atherton, 2017). The mineralogy of the waste rock used to construct the test pile experiments has been documented by Jambor (1997) and Smith et al. (2013a).

The purpose of this work was to characterize the spatial distribution of S, C, and K_S based on samples collected during the construction of the Type I and Type III test piles and the deconstruction of the Type I test pile. The analysis will be used to investigate the use of geostatistics in the characterization of mineralogical and physical heterogeneity of a waste-rock pile.

5.1 Methodology

The geostatistical calculations for S, C, and K_S were conducted on samples collected for mineralogical and particle-size distribution (PSD) analyses as part of the construction (Type I and Type III) and deconstruction (Type I) of the test pile experiments. The data sets will be referred to herein as ‘construction’ when referencing samples collected during the construction of the Type I and/or Type III test piles, and ‘deconstruction’ when referencing samples collected during the deconstruction of the Type I test pile. Samples collected during the construction phase of the experiment generally have limited associated spatial information; samples collected during the Type I deconstruction were spatially located using a Real Time Kinetic Global Positioning System with +/- 2 cm accuracy (Atherton, 2017).

During construction of the test-pile experiments, samples for analyses of S, C, and PSD were collected from the truck loads prior to being bulldozed over the tip face of a test pile (Smith et al., 2013a). The majority of the construction mineralogy samples were analyzed for S only. A total of 434 samples were collected for analysis of S during the construction of the test piles (247 samples from the Type I test pile and 187 from the Type III test pile). A relatively small number of samples (30) were collected for C analysis using the same method as S sample collection. A total of 292 samples were collected for PSD analysis during the construction program (165 samples from the Type I test pile and 127 from the Type III test pile).

Samples ranging in size from 5-10 kg facilitated assessment the PSD of the <50 mm fraction of the waste rock used to construct the test-pile experiments (Smith et al., 2013b). The geostatistical analysis documented here focusses on the PSD of the matrix material (<5 mm fraction) because flow through matrix material was found to dominate infiltration of water through the test pile (Neuner et al., 2013). Particle-size distribution samples from the interior of the pile only were included in the calculations and statistical analyses of K_s . Further detail regarding the collection of mineralogical and PSD samples during the construction of the test piles was documented by Smith et al. (2013a) and Smith et al. (2013b).

The test-pile experiments were constructed in phases to allow installation of instrumentation along tip faces of the pile at consistent intervals. Tip faces where instruments were installed are referred to as instrumentation faces. The limited spatial information retained for construction samples was a sample identifier that specified the instrumentation face of the test pile the sampled load was used during construction. As a result, approximate horizontal spatial location was retained, but no vertical spatial information was retained.

During deconstruction of the Type I test pile, spatially located samples were collected for mineralogical and PSD analysis. The Type I test pile was excavated in benches approximately 3 m thick; subsequently, inclined trenches, of width approximately 10 m, were excavated to facilitate sample collection. Sample locations were selected to allow construction of vertical and horizontal profiles of mineralogical, physical, and geochemical parameters throughout the test pile experiment. Samples for analysis of mineralogy and PSD were collected from approximately the same locations. A total of 562 samples for mineralogy analysis and 244 samples for PSD analysis were collected as part of the deconstruction program. A subset of 118 deconstruction mineralogy samples was selected for the S and C portion of the geostatistical analysis. Particle-size distribution analysis was conducted for 141 spatially located samples from the Type I test pile deconstruction experiment.

Samples of approximately 70 kg were collected to assess the PSD of the <75 mm fraction of the waste rock in the Type I test pile after 8 years of operation (Barsi, 2017). Only the PSD of the matrix material (<5 mm fraction) was used for the geostatistical analysis for the same reason noted previously (*i.e.*, water flow through the pile was dominated by matrix material flow). More detail regarding the deconstruction program in general and specifics about the sampling procedures was documented by Atherton (2017) and Barsi (2017).

Neuner et al. (2013) conducted constant-head permeameter tests on samples of matrix material, collected at the test pile experiments, to measure saturated K. The results of the laboratory testing indicated a geometric mean saturated K of $9 \times 10^{-6} \text{ m s}^{-1}$ with values ranging from $2 \times 10^{-6} \text{ m s}^{-1}$ to $3 \times 10^{-5} \text{ m s}^{-1}$ (Neuner et al., 2013). Four methods of calculating saturated K from the results of the PSD analysis were evaluated as part of this investigation. The methods of Hazen (1892), Schlichter (1905), Terzaghi (1925), and Chapuis (2004) (Equation 5.1) were used to calculate saturated K and compared to the results of the Neuner et al. (2013) experiments.

$$K_S = 2.4622 \left[\frac{d_{10}^2 e^3}{(1+e)} \right]^{0.7825}, \quad (5.1)$$

where K_S is saturated hydraulic conductivity [cm s^{-1}], d_{10} is the representative grain size [mm], and e is the void ratio [$\text{m}^3 \text{ m}^{-3}$]. The use of the Kozeny-Carman equation (Carman, 1937) was considered, however, the method was rejected due to the requirement for a soil specific surface value.

The data analysis followed a standard geostatistical approach for characterization of parameters to quantify the spatial distribution of the S, C, and K_S within the Type I test pile. The approach included:

1. Calculation of sample statistics of S, C, and K_S .
2. Assessment of stationarity S, C, and K_S .
3. Estimation of semi-variograms for S, C, and K_S .
4. Fitting of theoretical semi-variograms to estimated semi-variograms.

5.2 Results

The distribution of material in the test-pile experiments was the result of anthropogenic activities. Geostatistical analyses is traditionally applied to materials that were deposited as a result of natural processes; however, it was assumed that these techniques could be applied to waste rock to provide a meaningful characterization of the distribution of physical, geochemical and mineralogical properties.

5.2.1 Calculation of Hydraulic Conductivity

The results of the estimation of K_S values using the methods of Hazen (1892), Schlichter (1905), Terzaghi (1925), and Chapuis (2004) indicated that the method of Chapuis (2004) provided the best fit to the measured K_S values, with a geometric mean of $4 \times 10^{-5} \text{ m s}^{-1}$. The Hazen (1892) method was

rejected because of the requirement for a uniformity coefficient of less than five; most calculated uniformity coefficients for the matrix material portion of the waste rock were greater than 50 indicating the sampled material was poorly sorted. The results of the Terzaghi (1925) estimates were rejected because the geometric mean was two orders of magnitude higher than the geometric mean measured by Neuner et al. (2013). Saturated K_s estimates resulting from the Schlichter (1905) method were reasonable but slightly low (geometric mean of $5 \times 10^{-6} \text{ m s}^{-1}$). The Chapuis (2004) equation was selected as the preferred method for estimation of K_s for the remainder of this geostatistical analysis.

5.2.2 Statistical Distribution

Preliminary analysis included visual inspection of the S, C, and estimated K_s profiles and calculation of sample statistics including mean and standard deviation for each of the construction and deconstruction S, C, and K_s data sets (Tables 5.1 and 5.2). Visual inspection of the profiles did not reveal any significant trends in the spatial distribution of the parameters (Figure 5.1). Frequency density histograms of the statistical distribution of the Type I construction, Type I deconstruction, and Type III construction data sets for S, C, and K_s were assembled and observed to have skewness to the right indicating non-normal distribution (Figure 5.2); however, chi-square goodness-of-fit tests and quantile-quantile plots for each of the log normally transformed data sets (*i.e.*, $Y = \ln(K_s)$) indicated acceptance of the normal distribution hypothesis in each case (Figure 5.2). The assumption of log normal distribution was further analyzed using subsets of 50 randomly selected values from the Type I deconstruction $\ln(K_s)$ and the combined Type I construction and deconstruction $\ln(S)$ data sets. Chi-square goodness-of-fit tests conducted on these subsets indicated most passed the additional chi-square testing lending strength to the assumption of log normal distribution for the data sets was reasonable. The data set for Type I C contained less than 10 values, therefore the distribution analysis was not conducted for this data set.

The correlation of S, C and K_s at collocated sampling points was calculated. The S and C data exhibited a low degree of correlation with a correlation coefficient of -0.15 based on 120 collocated samples. The S and K_s and C and K_s data sets exhibited low degrees of correlation with correlation coefficients of -0.11 and -0.21 respectively, based on 85 collocated samples for each set.

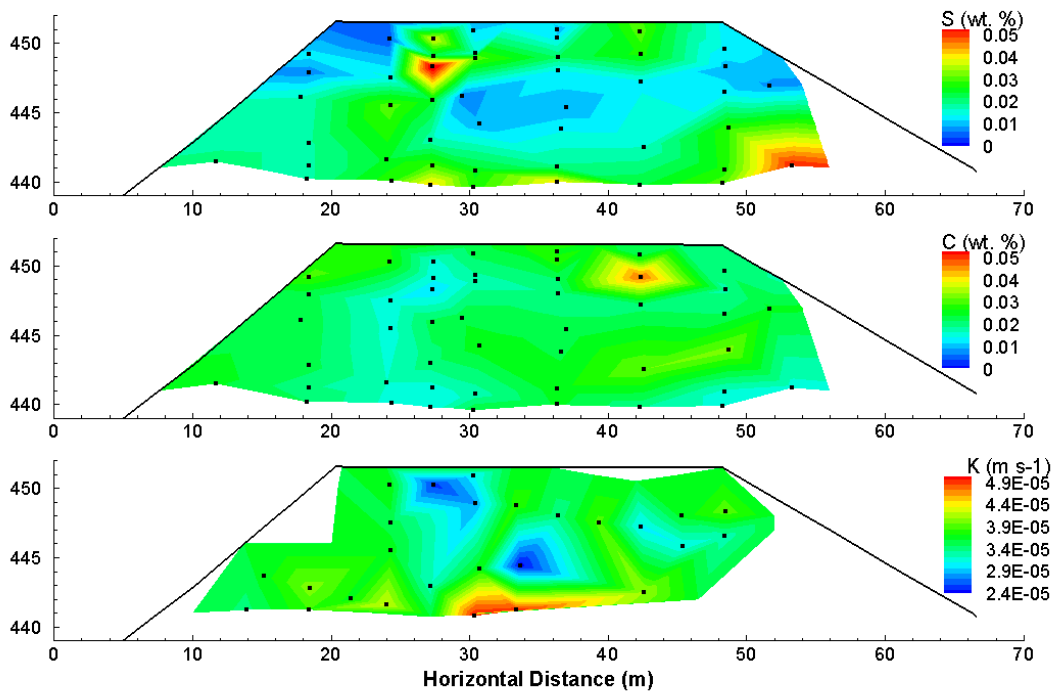


Figure 5.1 Location and spatial distribution of S and C measurements and saturated K estimates at the 15 m profile of the Type I test pile. (•) indicates a sample location and the black line indicates the outline of the test pile. The linear interpolation method was used to present the data.

Table 5.1 Summary of mean, standard deviation, and number of data points for $Ln(S)$ and $Ln(C)$ at Type I and Type III test pile

Data set	$\bar{x} Ln(S)$	$s Ln(S)$	$\bar{x} Ln(C)$	$s Ln(C)$	n
Type I construction ¹	-3.82	0.69	-3.36	0.27	186
Type I deconstruction	-4.01	0.56	-3.94	0.23	118
Type III construction ²	-3.08	0.64	-3.66	0.22	187 ¹

¹The Type I construction data set for $Ln(C)$ consisted of 5 samples.

²The Type III construction data set for $Ln(C)$ consisted of 26 samples.

Table 5.2 Summary of mean, standard deviation, and number of data points for $Ln(K_S)$ at Type I and Type III test pile

Data set	$\bar{x} Ln(K_S)$	$s Ln(K_S)$	n
Type I construction	-10.29	0.27	84
Type I deconstruction	-10.16	0.20	139
Type III construction	-10.26	0.17	50

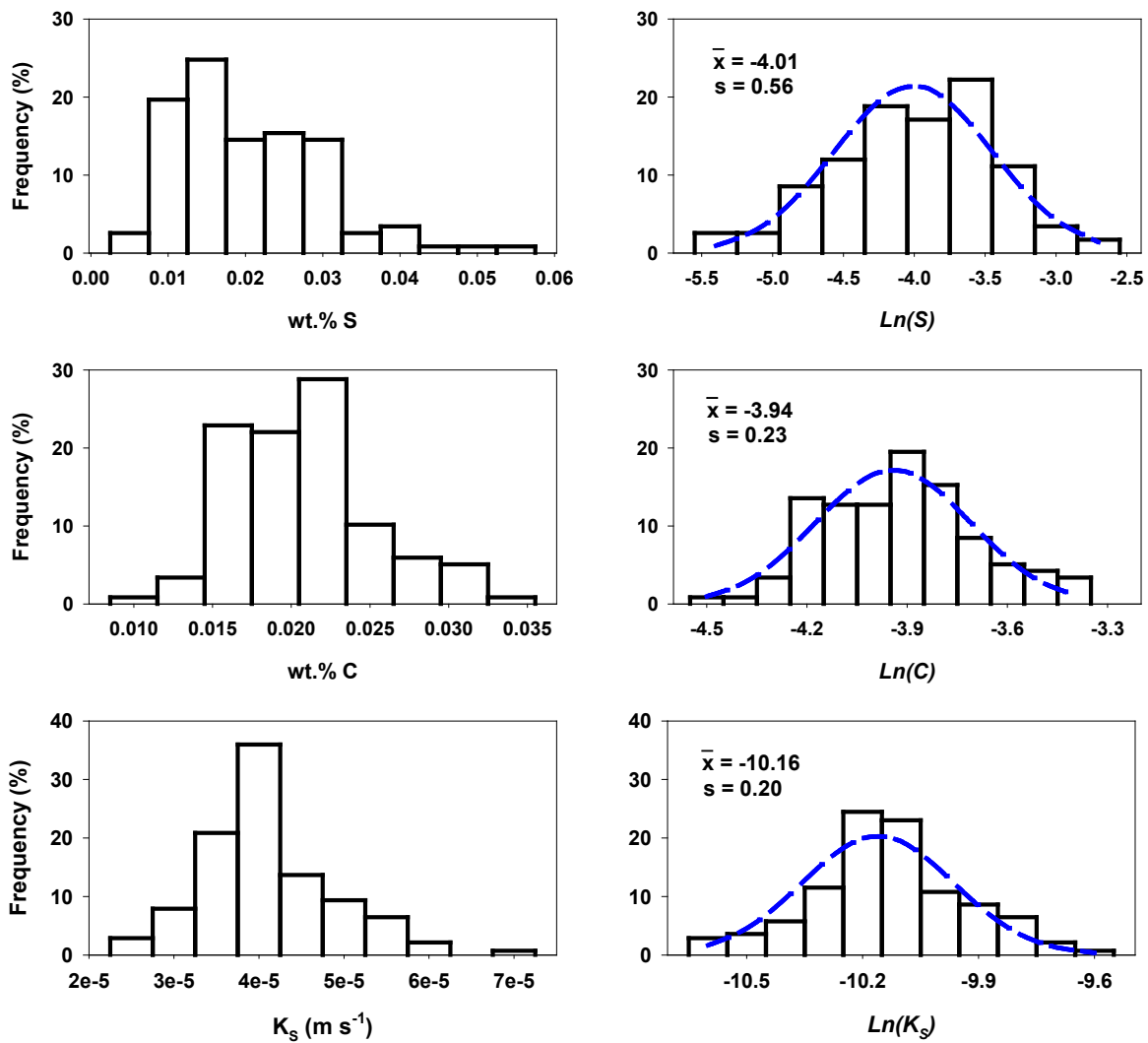


Figure 5.2 Frequency histograms for Type I deconstruction wt.% S, wt.% C, K (m s^{-1}), $\text{Ln}(S)$, $\text{Ln}(C)$, and $\text{Ln}(K)$.

5.2.3 Stationarity

To characterize the spatial dependence of the Type I deconstruction data set, the assumption of stationarity in the first two moments (mean and variance) for $\text{Ln}(S)$, $\text{Ln}(C)$, and $\text{Ln}(K_S)$ was considered. Stationarity is defined in this context as the absence of significant trends in mean and variance of the analyzed parameters with depth in the test-pile experiment. The stationarity of the $\text{Ln}(S)$, $\text{Ln}(C)$, and $\text{Ln}(K_S)$ was tested by calculating the mean and variance at each bench for the Type I deconstruction data and compared to the overall mean and variance of the deconstruction data set (Figure 5.3). There was some fluctuation in the mean and variance about the average in each case. Stationarity in the $\text{Ln}(S)$, $\text{Ln}(C)$, and $\text{Ln}(K_S)$ was a reasonable assumption for the Type I test pile. The spatial information for the Type I and Type III construction data sets was limited to the instrumentation face the samples were associated with; however, analysis of the mean and variance of the samples by face compared to the overall mean and variance indicated that the assumption of stationarity of the construction samples for $\text{Ln}(S)$ and $\text{Ln}(K_S)$ appeared reasonable. The stationarity of $\text{Ln}(C)$ was not investigated using construction samples due to the low number of samples analyzed for this parameter during construction of the test piles.

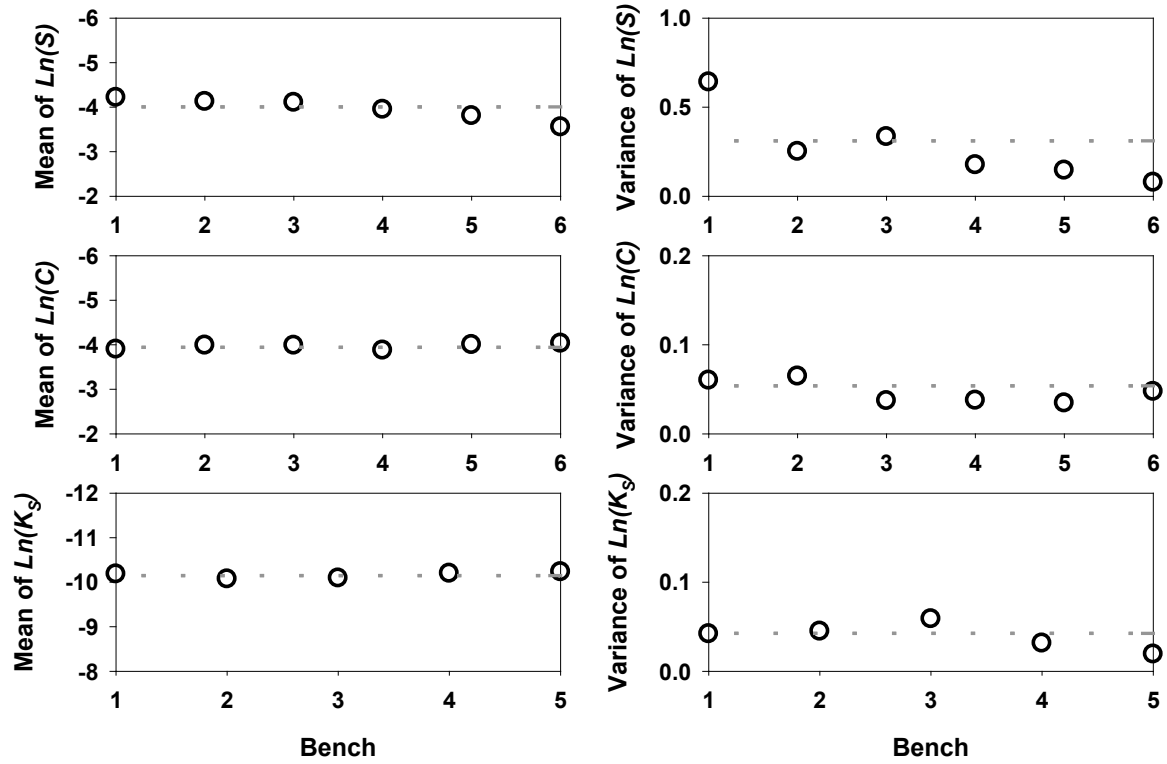


Figure 5.3 Mean and variance of $Ln(S)$, $Ln(C)$, and $Ln(K_s)$ from the deconstruction samples calculated by deconstruction bench. PSD analysis was conducted for samples from benches 1 to 5 only.

5.2.4 Experimental Semi-variogram Estimation

Experimental semi-variograms were estimated for the $Ln(S)$, $Ln(C)$, and $Ln(K_s)$ data from the deconstruction of the Type I test pile. Three common variogram estimation methods were applied in an attempt to assess the capability of the estimators to describe the distribution of anthropogenically deposited materials. The classical variogram estimator (Matheron, 1963) is:

$$\gamma(s) = \frac{1}{2N(s)} \sum_{i=1}^{N(s)} (y_i - y_{i+s})^2, \quad (5.2)$$

where $N(s)$ is the number of data pairs separated by lag distance s , y_i is the log normally transformed parameter at a given location, and y_{i+s} is the log normally transformed parameter at a second location distance s from y_i .

Two estimators generally considered to be more robust include the Cressie-Hawkins estimator (Cressie and Hawkins, 1980) and the squared median of the absolute deviations (SMAD) estimator (Dowd, 1984) are:

$$\gamma(s) = \frac{1}{2} \left[\frac{1}{N(s)} \sum_{i=1}^{N(s)} (y_i - y_{i+s})^{0.5} \right]^4 / \left(0.457 + \frac{0.49}{N(s)} \right), \quad (5.3)$$

$$\gamma(s) = 2.198(\text{median}|y_i - y_{i+s}|)^2. \quad (5.4)$$

Horizontal and vertical semi-variograms were estimated for $Ln(S)$, $Ln(C)$, and $Ln(K_S)$ using each of the methods (Figure 5.4). Horizontal semi-variograms were estimated from parameter pairs that were separated by bench. The maximum vertical separation of horizontal $Ln(S)$ and $Ln(C)$ pairs was 2.6 m; the maximum vertical separation of horizontal $Ln(K_S)$ pairs was 3.7 m. Vertical semi-variograms were estimated from pairs that were horizontally separated by a maximum of 3 m. Lag intervals were selected based on number of pairs available to provide a reasonable estimate. The horizontal lag interval selected for $Ln(S)$ and $Ln(C)$ was 4 m; the vertical lag interval selected for $Ln(S)$ and $Ln(C)$ was 1.5 m. The lag intervals selected for $Ln(K_S)$ were 3 m and 1 m for horizontal and vertical lags respectively.

Visual inspection of the experimental semi-variograms indicated that the estimates calculated by the classical method provided the most stable trends in each of the $Ln(S)$, $Ln(C)$, and $Ln(K_S)$ cases and as such was selected as the estimator for fitting of the theoretical variograms.. The semi-variograms included in Figure 5.4 were all estimated with outliers included in the data sets. Outliers were removed from the $Ln(C)$ and $Ln(K_S)$ data sets using the outlier labeling rule (Hoaglin et al., 1986) and supplemental experimental semi-variograms were estimated. Outlier removal from the $Ln(C)$ and $Ln(K_S)$ data sets did not significantly decrease the fluctuation of the estimated $Ln(C)$ and $Ln(K_S)$ horizontal and vertical semi-variograms.

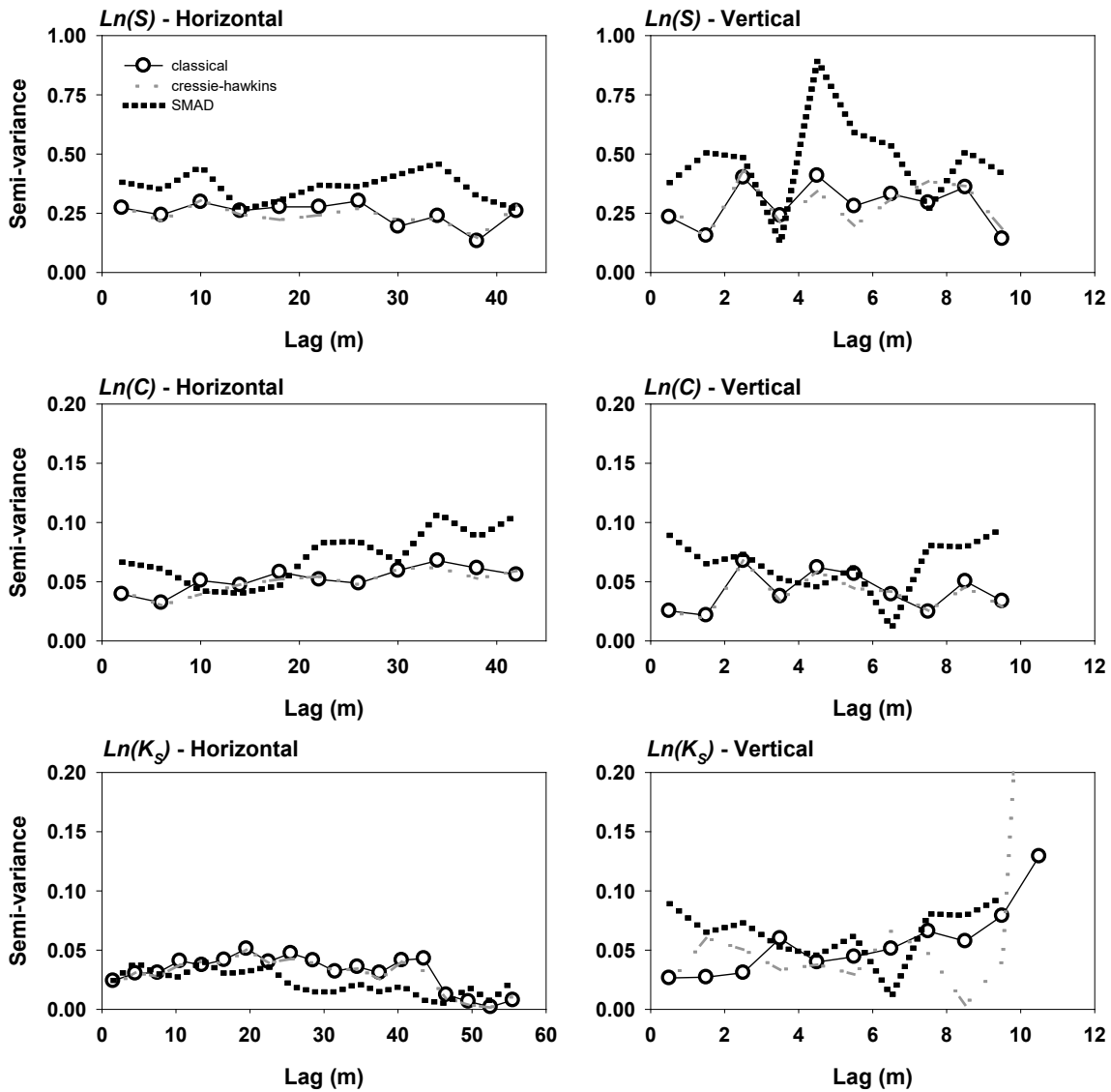


Figure 5.4 Horizontal and vertical experimental semi-variograms for $Ln(S)$, $Ln(C)$, and $Ln(K_S)$ using classical, Cressie-Hawkins, and SMAD estimators.

5.2.5 Theoretical Semi-variogram Fitting

Visual inspection of the experimental semi-variogram estimates indicated little evidence of spatial dependence in $Ln(S)$, $Ln(C)$, or $Ln(K_S)$ in the horizontal or vertical directions; however, attempts were made to fit three common theoretical semi-variogram models to the estimates to confirm this initial hypothesis. The theoretical semi-variogram models evaluated included linear (pure nugget),

exponential, and Gaussian (Webster and Oliver, 2001) and were fitted to the experimental semi-variograms using spreadsheet calculations. Models were evaluated for fit by calculating the standard error of the regression (sum of squares). The pure nugget model (Equation 5.5) was selected for analysis because visual inspection of the semi-variograms for $Ln(S)$ and $Ln(C)$ indicated no spatial dependence at the selected lag intervals. The exponential model (Equation 5.6) was selected based on the success of other researchers in fitting the model to semi-variograms of $Ln(K_S)$ under naturally deposited conditions (e.g., Woodbury and Sudicky, 1991; Turcke and Kueper, 1996; Sudicky et al., 2010). The Gaussian model (Equation 5.7) was selected based on visual inspection of the experimental $Ln(K_S)$ semi-variograms.

$$\gamma(s) = \sigma_Y^2 \{1 - \delta(s)\}, \quad (5.5)$$

where σ_Y^2 is the global variance $\delta(s)$ and is the Kronecker delta equaling 1 when lag distance $s = 0$ and 0 when $s > 0$.

$$\gamma(s) = \sigma_0^2 + \sigma_Y^2 \left\{1 - \exp\left(-s/\lambda\right)\right\}, \quad (5.6)$$

where σ_0^2 is the nugget and λ [m] is the correlation length.

$$\gamma(s) = \sigma_0^2 + \sigma_Y^2 \left\{1 - \exp\left(-s^2/\lambda^2\right)\right\}. \quad (5.7)$$

Fitting of the estimated semi-variogram for $Ln(S)$ and $Ln(C)$ indicated that in all cases there was very little to no evidence of spatial dependence at scales of 4 m (horizontal) and 1.5 m (vertical) with negligible difference in standard error for the three theoretical models. As a result, the pure nugget model was selected to represent the spatial dependence of $Ln(S)$ and $Ln(C)$ (Figure 5.5). The pure nugget model fitting parameter (σ_Y^2) was 0.28 for horizontal $Ln(S)$, 0.32 for vertical $Ln(S)$, 0.05 for horizontal $Ln(C)$, and 0.06 for vertical $Ln(C)$. The horizontal and vertical semi-variograms for $Ln(K_S)$ indicated limited spatial dependence with the Gaussian model providing the best fit with σ_Y^2 of 0.043, λ of 5 m, and σ_0^2 of 0.025 (Figure 5.5).

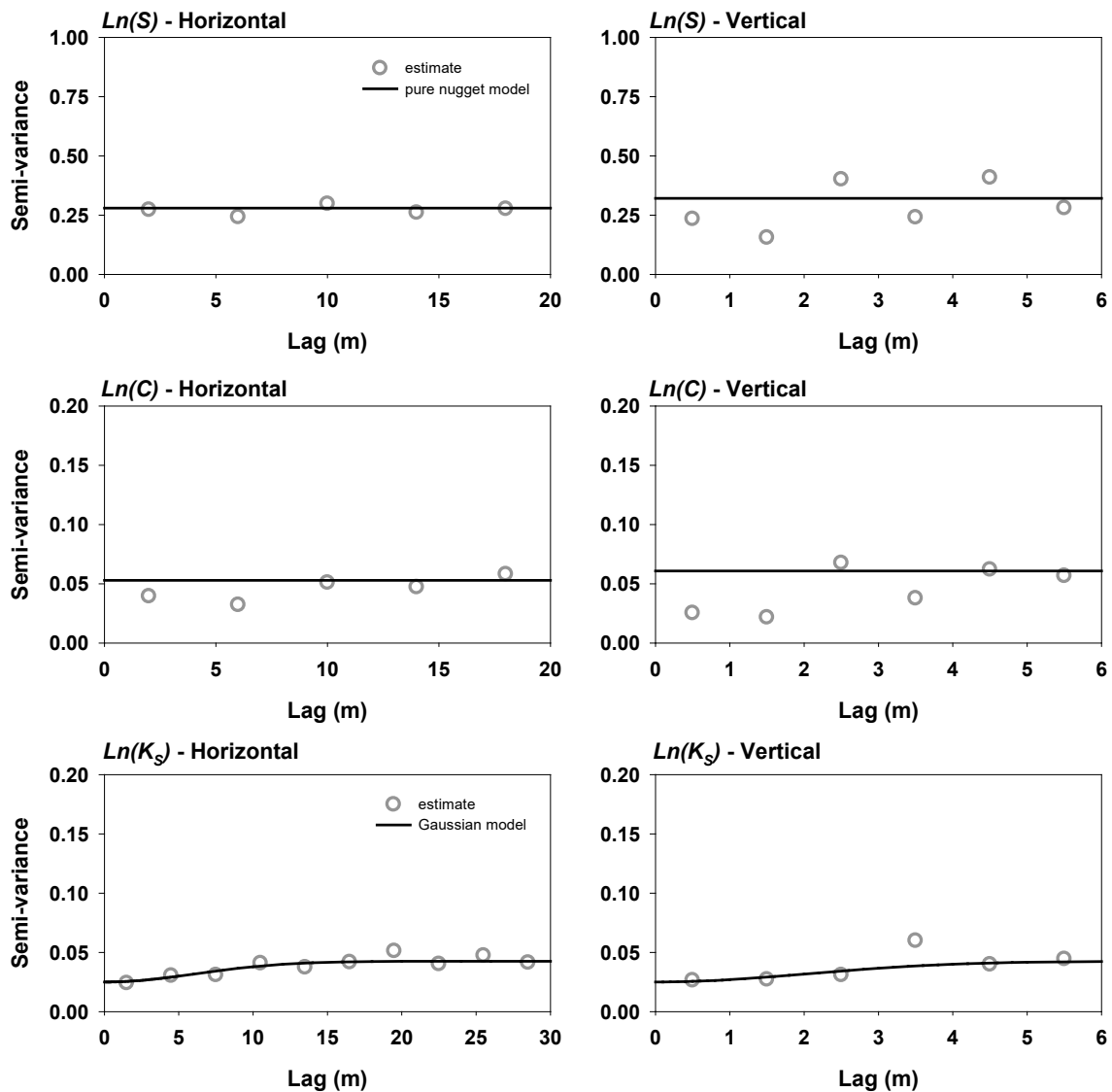


Figure 5.5 Theoretical semi-variogram fits to classical horizontal and vertical semi-variogram estimates for $Ln(S)$, $Ln(C)$, and $Ln(K_s)$. The pure nugget model is fit to $Ln(S)$ and $Ln(C)$ experimental semi-variograms; the Gaussian model is fit to $Ln(K_s)$ experimental semi-variograms.

5.3 Discussion

The geostatistical characterization of S, C, and K_s was intended to investigate the spatial distribution of these parameters critical to the assessment of the geochemical evolution of waste rock. The statistical distributions of S, C, and K_s was determined to be log normal, which is often the case with

natural systems (Sudicky et al., 1986; Sudicky et al., 2010; Limpert et al., 2001). A log normal distribution has sometimes been used to fit the spatial distribution of groundwater contaminant plume concentrations (USEPA, 1997). There has been very little research on waste-rock piles to indicate the spatial distribution of mineralogical and physical parameters. Khalil et al. (2013) suggested a normal distribution was appropriate for solid sample metal concentrations at their study site. The soil sample locations were widely distributed and collected from near the waste rock pile surface, therefore may not be indicative of distribution through the depth of the pile. Marescotti et al. (2010) used geostatistics to quantify the distribution of metals at a sulfidic waste-rock pile. Their semi-variogram work indicated spatial relationships for most of the assessed parameters but, similar to the work of Khalil et al. (2013), samples were collected close to the surface of the waste-rock pile.

5.3.1 Statistical Comparison of Construction Samples

Comparison of $Ln(S)$, $Ln(C)$, and $Ln(K_S)$ for the Type I and Type III construction sample results indicated that the assumption of log normally distributed data and stationarity in the first two moments was reasonable at each test pile. The variances of $Ln(S)$ and $Ln(C)$ were consistent between the Type I and Type III test piles. The means of $Ln(S)$ and $Ln(C)$ were not consistent between the test piles, reflecting the slightly differing S and C mineralogy of the two piles. The mean and variance of $Ln(K_S)$ was consistent between the two test piles. The similarity in parameter distribution, mean variance and stationarity suggested that the K_S of the two test piles are statistically very similar and that PSD of the matrix material collected at the Type I pile could be used to describe the heterogeneity in K_S of the Type III pile despite difference in S mineralogy between the two piles. This is expected given the similar construction methods used and the similar mineralogy of host material in the two piles and this result could likely be applied to other waste-rock piles where host rock mineralogy is relatively homogeneous.

5.3.2 Theoretical Semi-variogram Fitting

The pure nugget theoretical semi-variogram model (Equation 5.5) that provided the best fit to the $Ln(S)$ and $Ln(C)$ semi-variogram estimates was somewhat expected in view of the sampling density of the Type I deconstruction program and the construction techniques used to build the test piles. The use of the pure nugget model indicates that the discernable variations in the S and C were at a scale smaller than the sampling density. Following blasting and transport to the test-pile construction site,

loads of Type I or Type III material were deposited at the crest of the test piles and push dumped over the edge of the pile suggesting any spatial dependence in S and C in intact rock at a scale of >2 m scale would likely be lost. The test pile experiments were constructed using the push dumping method in a single lift.

The geostatistical analysis result of no spatial dependence in S and C could be influenced by factors including: i) sampling density used to determine the spatial dependence of S and/or C was too low, and/or ii) the estimated semi-variograms for S and C considered the spatial dependence in the pile as a whole, which may have eliminated smaller scale detail. The results of the spatial analyses highlighted the importance of considering sampling density that is based on the physical characteristics of the material being investigated. This geostatistical analysis indicated that higher sampling density would be required to investigate small-scale variability of mineralogy and physical parameters within waste rock; however, given the size of waste rock piles, a sampling density on the order of meters is likely sufficient to characterize the heterogeneity of these parameters.

The Gaussian theoretical model provided the best fit to the $Ln(K_S)$ horizontal and vertical semi-variograms with the spatial dependence being more prominent in the horizontal direction. Both directions were fit using a relatively large nugget value (59% of the underlying variance) suggesting limited spatial dependence.

Research of the internal structure of waste-rock piles has indicated the presence of low K_S lenses associated with traffic surfaces created during pile construction (Anterrieu et al., 2010). Internal traffic surfaces were not created as part of the construction of the test piles due to their relatively small size; however, some PSD samples were collected at the Type I and Type III crests following construction. Analysis of these samples indicated mean $Ln(K_S)$ values of -11.2 and -10.9 for samples collected at the crest of the Type I and Type III piles respectively. These results are significantly lower than the mean $Ln(K_S)$ values for samples collected from Type I and Type III test pile core material (-10.3 in both piles) and fall outside the log normal distribution of the core samples from both piles suggesting that the presence of traffic surfaces within a waste-rock pile could significantly alter the hydrogeologic regime within a pile. The PSD samples collected from the top of the test piles were not included in this geostatistical investigation. Analysis of the stationarity of the mean and variance of $Ln(K_S)$ indicated that K_S did not vary significantly with depth within the core of the Type I test pile experiment. The lack of depth dependence in K_S likely results from using only the PSD of

the matrix material within the pile. The bulk K_S increased with depth in the Type I test pile experiment (Barsi, 2017), but the matrix material K_S was not depth dependent. This observation is significant, because of the important role of the matrix material in controlling the hydrology; most of the water flow is conveyed through the fine-grained matrix of the waste-rock pile. Furthermore, due to the large surface area of the fine fraction, the geochemical evolution of the pore water is dominantly controlled by the matrix material. The uniformity of the matrix throughout the pile suggests that the entire thickness of the waste rock will contribute to the solute loading from the pile.

Experimental semi-variogram estimations are typically used to conduct analysis of the spatial dependence of physical characteristics (*e.g.*, K_S) resulting from natural deposition. The results of these geostatistical analyses indicated that these tools can be applied to anthropogenic material deposits. Although no spatial dependence of the selected parameters was observed in the test-pile experiments, larger waste-rock piles may exhibit different spatial characteristics due to a variety of factors including construction methods and material type.

5.4 Conclusions

Geostatistical analyses were conducted for measured S and C and estimated K_S from samples collected as part of the Type I and Type III test pile construction and Type I test pile deconstruction. Sulfur and C content were measured from mineralogical samples and matrix material K_S was estimated from samples collected for PSD analysis. Analysis of the population statistics indicated that S, C, and K_S were log normally distributed with consistent mean and variance among sub-populations of the same parameter.

Geostatistical analysis of the spatially located Type I deconstruction samples indicated limited spatial dependence of the K_S field within the matrix material of the test pile at a scale of 3 m horizontal and 1 m vertical. The saturated hydraulic conductivity of the matrix material was not depth dependent indicating that the matrix material throughout the pile was relatively homogeneous. It was determined that there was no spatial dependence in the structures of the S and C distribution in the Type I test pile at a scale of 4 m horizontal and 1.5 m vertical. This result was expected given the methods used to construct the test-pile experiments. Sampling density during the deconstruction of the Type I test pile likely contributed to the results of the geostatistical characterization; however given the extremely large size of typical waste rock piles, a denser characterization of the spatial

distribution of S, C, and K_S may not contribute significantly to an overall assessment of the geochemical evolution of waste rock. The sampling density required to support simulations for larger piles should take into consideration the lower spatial resolution of a model using the spatial data to simulate larger systems.

The results of the geostatistical characterization suggest that the spatial distribution of S, C, and K_S in waste rock piles, likely due to construction methods, can be characterized as randomly heterogeneous. The heterogeneity of S, C, and K_S in waste rock at Diavik can be approximated using a log normal distribution with mean and standard deviation calculated from samples collected during construction. Waste-rock piles that are portioned according to S content would require separate spatial distributions for S content. Additional internal structures not present in the test pile experiments (e.g., traffic surfaces) may require specific statistical description. The lack of spatial dependence in matrix K_S is significant, because of the importance of the matrix material in the control of water flow through the test-pile experiments. Due to the large surface area of the matrix material, the geochemical evolution of pore water is dominantly controlled by this finer fraction. The uniformity of the matrix material throughout the pile suggests that contributions to the solute loading from the pile would be somewhat dependent on matrix material distribution in the waste-rock pile and that the proportion of matrix to coarse material and their distributions within a pile are important factors to consider when assessing the geochemical evolution of a waste-rock pile.

Chapter 6

Influence of heterogeneity in S, C, and hydraulic conductivity on the geochemical evolution of large-scale test piles using reactive transport simulations

Piles of mine waste rock are typically very large and can contain rock from many stages of mine development. These structures can exhibit large variability in mineralogy and physical parameters that could affect the geochemical evolution of the waste rock. Many studies have investigated the role of heterogeneity of physical parameters in the migration of contaminants through porous media (*e.g.*, Gelhar, 1986; Sudicky, 1986; Malmström et al., 2008; Sudicky et al., 2010; Fala et al., 2013; Pedretti et al., 2017). Studies of waste-rock dumps indicate heterogeneity in physical characteristics such as porosity and moisture content can affect the flow regime within piles (Anterrieu et al., 2010; Lahmira et al., 2017) and can influence the resulting geochemical evolution (Fala et al., 2013). Larger-scale waste-rock piles are rarely used to characterize mine wastes; however, several studies using larger field experiments (*e.g.*, Smith et al., 2013a; Corazao et al., 2007; Andrina et al., 2006; Stockwell et al., 2006; Nichol et al., 2005) have shown that heterogeneity within waste-rock piles occurs and should be considered in the characterization of waste-rock piles.

Due to a paucity of data related to the spatial distribution of mineralogy and physical parameters in waste-rock piles, mechanistic investigations of waste rock weathering typically rely on globally averaged parameters to describe the mineralogical and physical characteristics of a simulation domain. Fala et al. (2013) used heterogeneity in physical and mineralogical characteristics of a hypothetical waste-rock pile to assess the geochemical evolution of waste rock and found that flow patterns generally followed the distribution of hydraulic conductivity, and regions of higher S fraction and smaller particle size contributed to locally reduced pH. Fala et al. (2013) focused on a single realization of the parameter distribution and noted that many realizations would be required to gain a deeper understanding of the role of heterogeneity within a waste-rock pile. Pedretti et al. (2017) used stochastic analysis to show that heterogeneity in pyrite and calcite distribution within a hypothetical waste rock pile can have a strong influence on the bulk neutralization potential and suggested that consideration of mineralogical heterogeneity could lead to an improvement in scale-up results.

As part of the Diavik Waste Rock Project (DWRP) two large-scale test piles were constructed in 2006 at the Diavik Diamond Mine, NT, Canada (Diavik) to investigate the geochemical evolution of a low-sulfide waste rock. The test piles measured approximately 50 m x 60 m x 15 m high and consisted of waste rock separated according to wt.% S. Sample collection and analysis during the construction of the test piles indicated that the mean wt.% S of the Type III test pile was 0.053 and the mean wt.% S of the Type I test pile was 0.035 (Smith et al., 2013b).

The test pile experiments (Type I and Type III) consisted of approximately 8.2×10^7 kg of waste rock with flow from each pile core measured and collected by a drainage network leading from basal collection lysimeters (BCLs) constructed at the test pile bases (Figure 6.1). The BCLs and associated drainage network facilitated the collection of effluent quality and quantity data from the cores of the pile experiments (*i.e.*, water that infiltrated from the crest of the test pile) (Smith et al., 2013a). Rain gauge tipping buckets were used to measure flow volume from each of the BCLs (Smith et al., 2013a). Effluent samples were collected every two to three days during the flow seasons from 2008 to 2012 and analyzed for parameters including Fe, Ni, Co, Cu, Zn, Al, Si, Ca, Mg, K, Na, SO₄, pH, and alkalinity to assess the geochemical characteristics of the test pile effluent (Smith et al., 2013b). More detailed descriptions of the test pile experiments and the geochemical evolution of the test piles are provided by Smith et al. (2013a) and Sinclair et al. (2015).

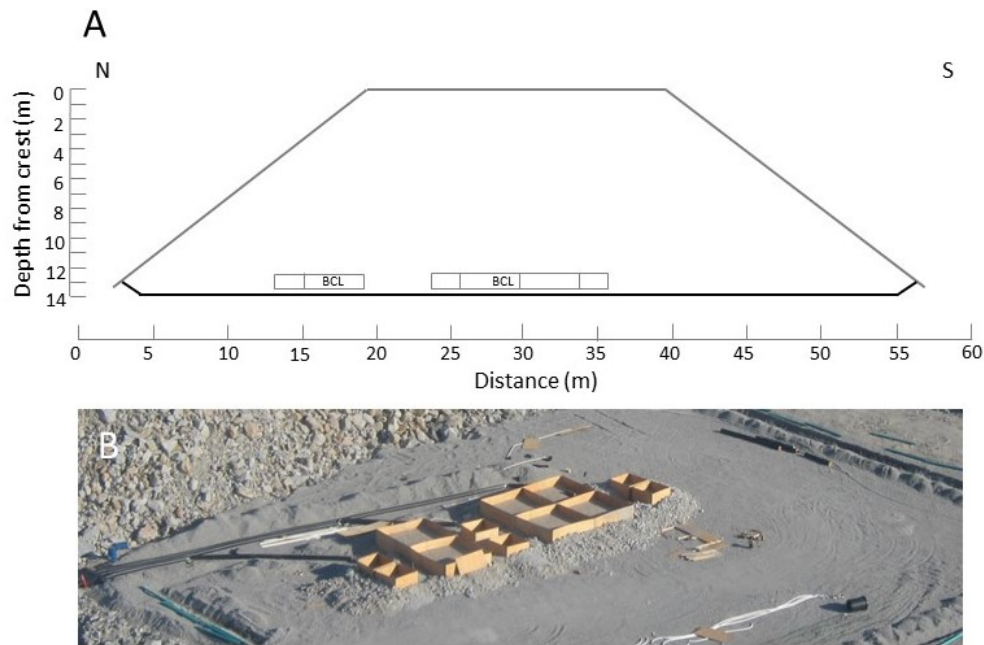


Figure 6.1 (A): Conceptual cross-section of DWRP Type III test pile experiment indicating approximate location of basal collection lysimeters (BCL). (B): Construction of basal collection lysimeters prior to run-of-mine material placement at Type III test pile.

One of the test piles (Type I) was dismantled in 2014 to investigate the spatial distribution of mineralogical and physical parameters and how the mineralogical and physical characteristics of the pile had been altered during 8 years of weathering. Spatially located samples facilitated geostatistical analysis that informed this modelling study of the heterogeneity in the geochemical evolution of waste-rock piles (Chapter 5).

The integrated conceptual model documented by Wilson et al. (2018a) was implemented using reactive transport model MIN3P-THCm (version: 1.0.591.0) (Mayer et al., 2002; Su et al., 2017) to simulate 1-D and 2-D flow and geochemical evolution through the core of the Type III test pile. Geostatistical analysis of mineralogy and particle size spatial distribution data, collected during the construction and deconstruction of the test piles experiment, was used to generate realizations of spatial distribution for S and C mineralogy and hydraulic conductivity. The objective of the simulations was to investigate the influence of heterogeneity in mineralogy (specifically S and C

content) and physical parameters (specifically hydraulic conductivity) on the geochemical evolution of waste rock and the test-pile field experiments.

6.1 Simulation Methodology

To assess the influence of heterogeneity in S, C, and saturated hydraulic conductivity on the geochemical evolution of Diavik waste rock, two sets of conditions were simulated. Each set consisted of 80 simulations resulting in 160 total 2-D simulations representing the geochemical evolution within the core of the Type III test pile.

The first set of 80 simulations (referred to as the SC_i case) used heterogeneous mineralogy fields to evaluate the influence of heterogeneity in S and C mineralogy on the effluent geochemistry. Eighty spatially heterogeneous realizations of S and C mineralogy were generated based on geostatistics shown in Chapter 5. Specific minerals included were pyrrhotite, chalcopyrite, sphalerite, pentlandite, calcite, and dolomite. The results of the geostatistics study indicated that S and C lacked spatial dependence (*i.e.*, adjacent samples of S or C were not related to each other with regards to wt.%) and exhibited a low degree of correlation (*i.e.*, the S content at any given location was not related to the C content at that same location). The S and C realizations were generated with a spreadsheet random number generator using a log normal distribution (based on the statistical distribution of the spatially located samples collected from the Type I pile deconstruction), and the mean and standard deviation of the un-weathered samples collected during the construction of the Type III test pile (Figures 6.2 and 6.4). Following the results of the semi-variance analysis from Chapter 5, the S and C realizations were generated without spatial dependence constraints. A homogeneous hydraulic conductivity distribution using an average hydraulic conductivity of $9 \times 10^{-6} \text{ m s}^{-1}$ was used to simulate flow for the SC_i case.

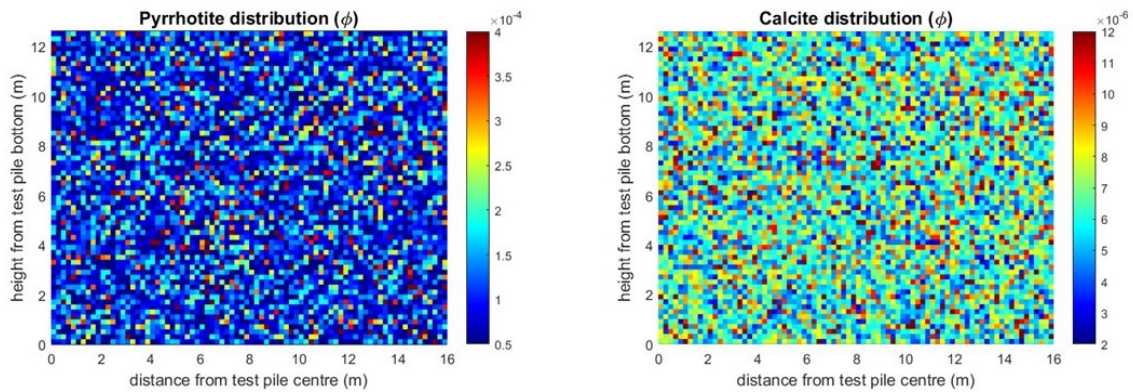


Figure 6.2 A single realization of the spatial distribution of pyrrhotite and calcite volume fractions for the Type III test pile simulation domain based on mean and standard deviation of samples collected as part of test pile construction and log normal distribution of samples collected as part of the Type I test pile deconstruction.

The second set of simulations (referred to as set ‘SC- K_{Si} ’) used the same heterogeneous mineralogy fields used for the SC_i case in conjunction with heterogeneous hydraulic conductivity fields. Eighty spatially heterogeneous realizations of hydraulic conductivity were generated based on geostatistics calculated in Chapter 5 for the Type I test pile experiment. The results of that study indicated there was possibly a very slight spatial dependence (*i.e.*, adjacent samples of hydraulic conductivity had little to no dependence to each other). The values of hydraulic conductivity in the realizations were not related to S and C mineralogy of the mineralogical realizations because the geostatistical analysis indicated that values of hydraulic conductivity, S, and C expressed a low degree of correlation (Chapter 5). The hydraulic conductivity realizations were generated with a spreadsheet random number generator using a log normal distribution (based on the statistical distribution of the spatially located samples from the Type I pile), and the mean and standard deviation of saturated hydraulic conductivity measurements conducted by Neuner et al., 2013 (Figures 6.3 and 6.4). The slight spatial dependence constraint on K_S shown in Chapter 5 was not considered in the generated realizations.

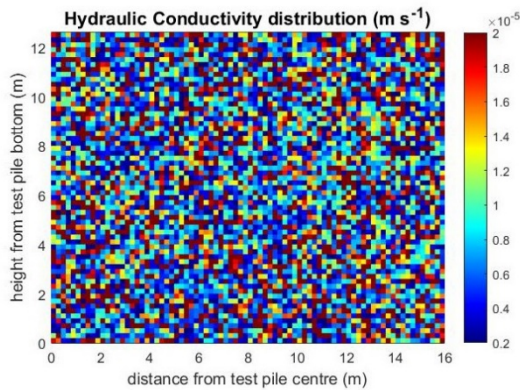


Figure 6.3 A single realization of spatial distribution of hydraulic conductivity for the Type III test pile simulation domain based on mean and standard deviation of samples collected as part of test pile construction and log normal distribution of samples collected as part of the Type I test pile deconstruction.

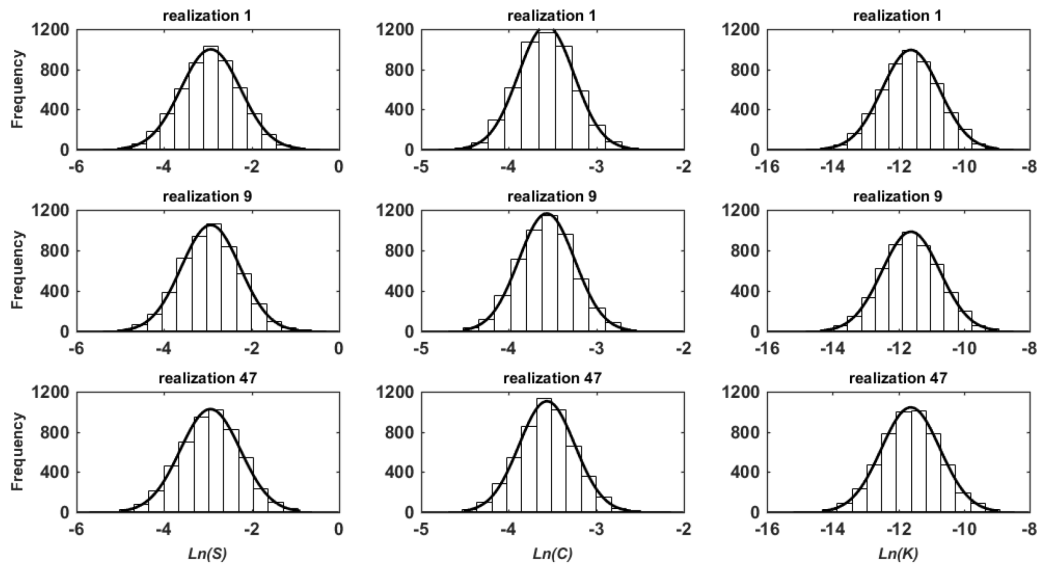


Figure 6.4 Example statistical distributions for three generated S, C, and K_S realizations (realization 1, realization 9, and realization 47) showing log normal distribution. Mean and standard deviation of measured log transformed S [wt. %], C [wt. %], and K_S ($m s^{-1}$) are -2.94 and 0.68, -3.56 and 0.32, and -11.62 and 0.88 respectively.

The Type III test pile host mineralogy was assumed to be similar to that of the DWRP Type III humidity cells (Langman et al., 2014) comprising approximately 75% granite (primarily quartz [SiO₂], K-feldspar [KAlSi₃O₈], and albite [NaAlSi₃O₈]), 14% pegmatitic granite, 10% biotite schist, and 1% diabase (Blowes & Logsdon, 1998; Langman et al., 2014). Sulfidic minerals were primarily contained in the biotite schist component, which is comprised of albite (35–55%), quartz (20–50%), and biotite [KMg_{1.6}Fe_{1.4}AlSi₃O₁₀(OH)₂] (10–25%) (Langman et al. 2014). The primary sulfide mineral was pyrrhotite [Fe_(1-x)S], with minor substitution of Ni and Co for Fe in the following approximate ratio: Fe_{0.852}Ni_{0.004}Co_{0.001}S (Jambor, 1997). Smaller contributions of chalcopyrite [CuFeS₂], sphalerite [ZnS], and pentlandite [(Fe,Ni)₉S₈] were found to be present (Langman et al., 2014).

The parallelized version of MIN3P-THCm (ParMIN3P-THCm, Su et al., 2017) was used in conjunction with the high performance Compute Canada cluster Graham to conduct the reactive transport simulations discussed in this study. Each simulation was run on 32 processors with an average run time of 12.6 hours.

6.2 Conceptual Model

The simulations in this study are based on the integrated conceptual model developed by Wilson et al. (2018a) and include the same host mineralogy and physical characteristics (with the exception of K_s in the heterogeneous K_s simulation set) documented in Chapter 4. A conceptual model of the annual temperature fluctuations at the Type III test pile was presented by Sinclair et al. (2015) where the pile was fully frozen from December to May and fully thawed from August to October. Transitional periods typically consisted of relatively uniform warming from top to bottom (early summer) and relatively uniform cooling from top to bottom with slight cooling from bottom to top (late fall).

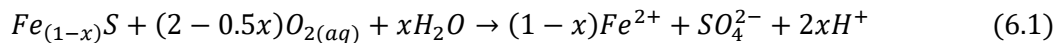
To account for temperature variation within the Type III test pile experiment, a spatially and temporally variable temperature regime was implemented in the simulations. Temperatures measured in the test pile experiment, with a regularly spaced thermistor network (approximately 0.5 m interval vertically within the core of the test pile), were used to define the distribution along with additional thermistors installed prior to test pile in boreholes beneath the test pile. Temperature within the test pile, measured approximately every 6 hours from 0.5 m to 11 m below the crest, was combined with the deeper measurements to provide an average daily, spatially variable temperature within the

simulation domain. The temperature was assumed to vary only with depth and was held constant laterally within the 2-D simulation domain. The simulation temperature at each node was consistent with the temperatures measured within the Type III test pile. The temperature profile within the pile was treated the same way for both sets of heterogeneous simulations. Additional detail regarding the installation and operation of the thermal measurement network was documented by Smith et al. (2013a) and Pham et al. (2013).

The interpolated temperatures of the Type III test pile simulation domain were used in conjunction with the activation energy (E_a) values calibrated as part of the Diavik humidity cell simulations (Wilson et al., 2018a) to account for the temperature dependence of reactions involving host minerals. The temperature dependence of the sulfide mineral oxidation reactions was controlled using activation enthalpy values calibrated as part of the simulations conducted on smaller DWRP waste-rock experiments (Wilson et al., 2018b).

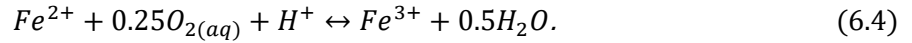
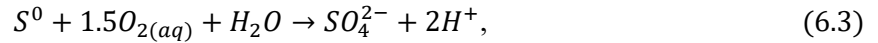
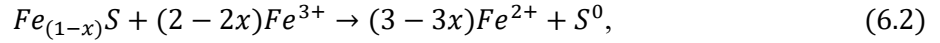
The flow regime used in the simulations was based on the experimental conditions measured at the DWRP test piles as described by Smith et al. (2013a) and Neuner et al. (2013). Infiltration to the simulation domain was based on discrete infiltration events to the test-pile experiment estimated using the FAO Penman-Monteith (FAO P-M) method described by Neuner et al. (2013) and measured precipitation at the experiment site. Tracer tests conducted by Neuner et al. (2013) at the test pile experiments indicated that water flow was dominated by flow through the matrix portion of the waste-rock pile (particle size diameter <5 mm) as a result the flow simulation only considers flow through the matrix material portion of the test pile.

The geochemical portion of the simulations was based on the integrated conceptual model of sulfidic mineral weathering presented by Wilson et al. (2018a) and in Chapter 4. The integrated conceptual model includes $O_{2(aq)}$ and Fe^{3+} as the primary oxidants controlling sulfide-mineral oxidation (Nordstrom & Southam, 1997; Blowes et al., 2003). Using pyrrhotite as an example, the following reaction stoichiometry presents the overall reaction (Nicholson and Scharer, 1998; Janzen et al., 2000; Belzile et al., 2004):



The general form of reaction 6.1 was used to define similar reactions for the oxidation of the other main sulfide minerals present in Diavik waste rock including CuFeS_2 , ZnS , and $(\text{Fe,Ni})_9\text{S}_8$ (Table 6.1).

The influence of Fe^{3+} on the oxidation of sulfidic waste rock was represented by the reaction sequence described by Schippers and Sand (1999) in addition to the kinetically controlled oxidation of Fe^{2+} by $\text{O}_{2(\text{aq})}$ (Singer and Stumm, 1970; Schippers and Sand, 1999; Rohwerder et al., 2003):



The shrinking core model was used to formulate rate expressions for sulfide mineral oxidation by $\text{O}_{2(\text{aq})}$ and Fe^{3+} (Levenspiel, 1972; Wunderly et al., 1996; Mayer et al., 2002). The rate expressions for oxidation of Diavik $\text{Fe}_{(1-x)}\text{S}$ (after Mayer et al., 2002) were as follows:

$$R_{Po\text{ ox}} = -10^3 S_{\text{Fe}_{0.852}\text{Ni}_{0.004}\text{Co}_{0.001}\text{S}} \left[\frac{r^p}{(r^p - r^r)r^r} \right] D_{\text{O}_{2(\text{aq})}} \left[\frac{\text{O}_{2(\text{aq})}}{1.9285} \right], \quad (6.5)$$

$$R_{Po\text{ ox}} = -10^3 S_{\text{Fe}_{0.852}\text{Ni}_{0.004}\text{Co}_{0.001}\text{S}} \left[\frac{r^p}{(r^p - r^r)r^r} \right] D_{\text{Fe}^{3+}} \left[\frac{\text{Fe}^{3+}}{1.714} \right]. \quad (6.6)$$

where $R_{Po\text{ ox}}$ represents the rate of pyrrhotite oxidation [$\text{mol L}^{-1} \text{d}^{-1}$] and $S_{\text{Fe}_{0.852}\text{Ni}_{0.004}\text{Co}_{0.001}\text{S}}$, r^p , r^r , and $D_{\text{O}_{2(\text{aq})}}$ and $D_{\text{Fe}^{3+}}$ represent the reactive surface area [$\text{m}^2 \text{mineral L}^{-1} \text{porous medium}$], average particle radius [m], unreacted particle radius [m], and effective diffusion coefficient [$\text{m}^2 \text{s}^{-1}$] for $\text{O}_{2(\text{aq})}$ and Fe^{3+} diffusion to the unreacted surface, respectively. The oxidation of each sulfide mineral by $\text{O}_{2(\text{aq})}$ and Fe^{3+} occurred in parallel on the same mineral volume fraction.

The rate expression to represent the oxidation of Fe^{2+} (after Singer and Stumm, 1970; Mayer et al., 2002; Roden, 2008) is as follows:

$$\begin{aligned} R_{\text{Fe}^{2+} - \text{Fe}^{3+}} = & -S_1 k_{\text{Fe}^{2+} - \text{Fe}^{3+}}^1 [\text{Fe}^{2+}] [\text{O}_{2(\text{aq})}] \\ & - S_2 k_{\text{Fe}^{2+} - \text{Fe}^{3+}}^2 [\text{Fe}^{2+}] [\text{O}_{2(\text{aq})}] [\text{OH}^-]^2 - S_3 k_{\text{Fe}^{2+} - \text{Fe}^{3+}}^3 \left[\frac{[\text{Fe}^{2+}]}{K_s + [\text{Fe}^{2+}]} \right]. \end{aligned} \quad (6.7)$$

where $R_{\text{Fe}^{2+} - \text{Fe}^{3+}}$ represents the rate of Fe^{2+} oxidation [$\text{mol L}^{-1} \text{d}^{-1}$]. The first two terms on the right side of equation 6.7 represent the chemical oxidation of Fe^{2+} by $\text{O}_{2(\text{aq})}$ with S , $k_{\text{Fe}^{2+} - \text{Fe}^{3+}}^1$,

and $k_{\text{Fe}^{2+}-\text{Fe}^{3+}}^2$ representing scaling factor [-], the reaction rate constant for $\text{pH} < \sim 3.5$ [$\text{L mol}^{-1} \text{d}^{-1}$] (Singer and Stumm, 1970), the reaction rate constant for $\text{pH} > \sim 4.5$ [$\text{mol L}^{-1} \text{d}^{-1}$] (Singer and Stumm, 1970), respectively. The final right hand side term in equation 6.7 represents the biotic oxidation of Fe^{2+} where $k_{\text{Fe}^{2+}-\text{Fe}^{3+}}^3$ and K_s represent the reaction rate constant [$\text{mol L}^{-1} \text{d}^{-1}$] and half-saturation constant [mol L^{-1}], respectively.

The oxidation of S^0 by $\text{O}_{2(\text{aq})}$ (equation 6.4) (after Roden, 2008) is represented by the following rate expression:

$$R_{\text{S}^0-\text{SO}_4} = -k_{\text{S}^0-\text{SO}_4} \left[\frac{[\text{S}^0]}{K_s + [\text{S}^0]} \right] \quad (6.8)$$

where $R_{\text{S}^0-\text{SO}_4}$ represents the rate of biotic S^0 oxidation by oxygen [$\text{mol L}^{-1} \text{d}^{-1}$] and $k_{\text{S}^0-\text{SO}_4}$ and K_s represent the reaction rate constant [$\text{mol L}^{-1} \text{d}^{-1}$] and half-saturation constant [mol L^{-1}] respectively.

Host minerals specific to the Diavik site were represented in the conceptual model by the reactions stoichiometry and rate expressions presented in Tables 6.2 and 6.3. In the cases of calcite and dolomite, the reactions are reversible; for biotite, muscovite, and albite the reactions are irreversible dissolution. The included secondary minerals were based on site specific mineralogy and saturation index analysis conducted on effluent geochemistry. The secondary minerals included in the simulations were: Fe(III)(oxy)hydroxide [$\text{Fe}(\text{OH})_3$], jarosite [$\text{KFe}_3(\text{SO}_4)_2(\text{OH})_6$], gypsum [$\text{CaSO}_4 \cdot 2\text{H}_2\text{O}$], siderite [FeCO_3], gibbsite [$\text{Al}(\text{OH})_3$], and amorphous silica [SiO_2]. The secondary minerals were allowed to precipitate or dissolve in relation to their reaction stoichiometry and associated equilibrium-controlled rate expression (Tables 6.2 and 6.3). Wilson et al. (2018a) provides further detail on the selected set of included secondary minerals.

Table 6.1 Reaction stoichiometry and solubility products (K) for sulfide minerals

Mineral	Sulfide Mineral Reaction	log K_i
pyrrhotite	$Fe_{0.852}Ni_{0.004}Co_{0.001}S + 0.143H_2O + 1.9285O_{2(aq)} \rightarrow$ $0.852Fe^{2+} + 0.004Ni^{2+} + 0.001Co^{2+} + SO_4^{2-} + 0.286H^+$	134.66
	$Fe_{0.852}Ni_{0.004}Co_{0.001}S + 1.714Fe^{3+}$ $\rightarrow 2.566Fe^{2+} + 0.004Ni^{2+} + 0.001Co^{2+} + S^0$	
sphalerite	$ZnS + 2O_{2(aq)} \rightarrow Zn^{2+} + SO_4^{2-}$	--
	$ZnS + 2Fe^{3+} \rightarrow 2Fe^{2+} + Zn^{2+} + S^0$	
chalcopyrite	$CuFeS_2 + 4O_{2(aq)} \rightarrow Cu^{2+} + Fe^{2+} + 2SO_4^{2-}$	--
	$CuFeS_2 + 4Fe^{3+} \rightarrow 5Fe^{2+} + Cu^{2+} + 2S^0$	
pentlandite	$Fe_{4.5}Ni_{3.6}Co_{0.9}S_8 + 16.5O_{2(aq)} + 2H^+ \rightarrow$ $4.5Fe^{2+} + 3.6Ni^{2+} + 0.9Co^{2+} + 8SO_4^{2-} + H_2O$	--
	$Fe_{4.5}Ni_{3.6}Co_{0.9}S_8 + 18Fe^{3+} \rightarrow 22.5Fe^{2+} + 3.6Ni^{2+} + 0.9Co^{2+} + 8S^0$	

Table 6.2 Reaction stoichiometry and solubility products (K) for host and secondary minerals

Mineral	Host Mineral Reaction	log K_i
calcite	$CaCO_3 \rightarrow Ca^{2+} + CO_3^{2-}$	-8.48
dolomite	$MgCa(CO_3)_2 \rightarrow Mg^{2+} + Ca^{2+} + 2CO_3^{2-}$	-17.09
biotite	$KMg_2Fe(AlSi_3O_{10})(OH)_2 + 10H^+ \rightarrow K^+ + 2Mg^{2+} + Fe^{2+} + Al^{3+} + 3H_4SiO_4$	--
muscovite	$KAl_2(AlSi_3O_{10})(OH)_2 + 10H^+ \rightarrow K^+ + 3Al^{3+} + 3H_4SiO_4$	--
albite	$NaAlSi_3O_8 + 4H_2O + 4H^+ \rightarrow Na^+ + Al^{3+} + 3H_4SiO_4$	--
Secondary Mineral Reaction		
Fe(III) (oxy)hydroxide	$Fe(OH)_{3(am)} + 3H^+ \leftrightarrow Fe^{3+} + 3H_2O$	4.89
jarosite	$KFe_3(SO_4)_2(OH)_6 + 6H^+ \leftrightarrow K^+ + 3Fe^{3+} + 2SO_4^{2-} + 6H_2O$	-9.21
silica(am)	$SiO_2 + 2H_2O \leftrightarrow H_4SiO_4$	-2.71
gibbsite	$Al(OH)_{3(am)} + 3H^+ \leftrightarrow Al^{3+} + 3H_2O$	8.11
gypsum	$CaSO_4 \cdot 2H_2O \leftrightarrow Ca^{2+} + SO_4^{2-} + 2H_2O$	-4.58
siderite	$FeCO_3 \rightarrow Fe^{2+} + CO_3^{2-}$	-10.93

Table 6.3 Rate expressions for dissolution of host and secondary minerals

Host Mineral	Rate Expression
calcite	$R = -S_{CaCO_3} [10^{-0.05} [H^+] + 10^{-6.19} + 10^{-3.30} [H_2CO_3]] \left[1 - \frac{IAP}{10^{-8.48}} \right]$
dolomite	$R = -S_{MgCa(CO_3)_2} [10^{-2.59} [H^+]^{0.75} + 10^{-7.66} + 10^{-4.00} [H_2CO_3]^{0.75}] \left[1 - \frac{IAP}{10^{-17.09}} \right]$
biotite	$R = -S_{KMg_2Fe(AlSi_3O_{10})(OH)_2} k_1 [H^+]^{0.25}$
muscovite	$R = -S_{KAl_2(AlSi_3O_{10})(OH)_2} [k_1 [H^+]^{0.08} + k_2 [H^+]^{-0.1}]$
albite	$R = -S_{NaAlSi_3O_8} [k_1 [H^+]^{0.49} + k_2 [H^+]^{-0.3}]$
Secondary Mineral	
Fe(III) (oxy)hydroxide	$R = k_{Fe(OH)_3}^{eff} \left[1 - \frac{IAP}{10^{4.89}} \right]$
jarosite	$R = k_{KFe_3(SO_4)_2(OH)_6}^{eff} \left[1 - \frac{IAP}{10^{-9.21}} \right]$
silica(am)	$R = k_{SiO_2}^{eff} \left[1 - \frac{IAP}{10^{-2.71}} \right]$
gibbsite	$R = k_{Al(OH)_3}^{eff} \left[1 - \frac{IAP}{10^{-8.11}} \right]$
gypsum	$R = k_{CaSO_4 \cdot 2H_2O}^{eff} \left[1 - \frac{IAP}{10^{4.58}} \right]$
siderite	$R = k_{FeCO_3}^{eff} \left[1 - \frac{IAP}{10^{10.93}} \right]$

6.3 Model Parameters

The Type III test pile 2-D rectangular domain had a depth (z-axis) of 12.6 m and width (x-axis) of 16.0 m corresponding to the approximate depth from the test pile crest to the midpoint of the BCLs and half the width of the test pile crest respectively. The simulation domain was discretized in the x-

direction as 81 0.2 m control volumes and in the z-direction as 64 0.2 m control volumes. Simulation run times were 2555 days corresponding with the years 2006-2012 (Type III test pile construction was completed in 2006).

Simulation temperature was based on measured internal temperatures of the Type III test pile experiment. Control volume temperature was calculated (at 2 m intervals) by MIN3P-THCm using linear interpolation. The E_a or diffusion coefficient values were not calibrated during the Type III heterogeneous simulations.

Physical parameters including porosity and soil hydraulic function parameters (Table 6.4) were obtained from Neuner et al. (2013); soil hydraulic function parameters were constant for the heterogeneous K_S simulations. No calibration of the physical parameters was conducted as part of the 2-D simulations. A value of $9 \times 10^{-6} \text{ m s}^{-1}$ (Neuner et al., 2013) was used for the homogeneous hydraulic conductivity cases. Hydraulic conductivity realizations for the heterogeneous hydraulic conductivity cases were generated using a mean of $9 \times 10^{-6} \text{ m s}^{-1}$ and standard deviation of 9×10^{-6} assuming a log normal distribution of values within the model domain.

As part of the Type III test-pile experiment, construction samples were collected for analysis of S and C analyses providing the mineral volume fractions (ϕ_i) (Tables 6.5 and 6.6) for sulfide and carbonate minerals. Mineral volume fractions for the secondary sulfide minerals, CuFeS_2 and ZnS , were calculated using the results of bulk metal analysis conducted on samples collected from the DWRP humidity cell experiments (Wilson et al., 2018a) and the $\text{Fe}_{4.5}\text{Ni}_{3.6}\text{Co}_{0.9}\text{S}_8$ ϕ_i was calibrated as part of the humidity cell simulations (Wilson et al., 2018a). Mineral volume fractions for host minerals biotite, muscovite, and albite were the same as used in Chapter 4 (Table 6.6).

Modifications to the MIN3P-THCm code to facilitate multi-year continuous simulations including minimization of water flow and reaction rates during freezing conditions. These conditions on flow and reaction rates were included as part of the 1-D simulations of the Type III test pile experiment (Chapter 5). The code was formulated such that when the temperature of a control volume is less than 0°C , hydraulic conductivity was reduced to $1 \times 10^{-10} \text{ m s}^{-1}$, effectively stopping water flow, and reaction rates were set to zero, stopping geochemical reactions. Further details regarding these modifications are provided in Chapter 4.

Table 6.4 Physical parameters used in the Type III test pile experiment 2-D heterogeneous simulations

Parameter		Value
homogeneous hydraulic conductivity ¹		9×10^{-6}
heterogeneous hydraulic conductivity ²	\bar{x}	-11.6
	s	0.9
	α	6.9
van Genuchten hydraulic parameters ³	n	1.5
infiltration rate ⁴		Variable
porosity ⁵		0.05

¹Homogeneous hydraulic conductivity based on experiments of Neuner et al. (2013) in $m s^{-1}$.

²Heterogenous log transformed mean hydraulic conductivity and standard deviation based on experiments of Neuner et al. (2013).

³Van Genuchten parameters based on work of Neuner et al. (2013); α in m^{-1} , n is unitless.

⁴Infiltration rate determined by FAO Penman-Monteith method.

⁵Porosity based on porosity of matrix material as a portion to the bulk porosity of the test pile.

Table 6.5 Initial volume fraction generation statistics and diffusion coefficient data for sulfide and carbonate minerals in Type III test pile experiment 2-D heterogeneous simulations

Mineral	μ_{ϕ_i}	σ_{ϕ_i}	D^{eff} (25 °C)
pyrrhotite – O _{2(aq)}	1.0 x 10 ⁻⁴	7.3 x 10 ⁻⁵	2.6 x 10 ⁻¹³
pyrrhotite – Fe ³⁺			1.2 x 10 ⁻⁹
chalcopyrite - O _{2(aq)}	3.1 x 10 ⁻⁶	2.2 x 10 ⁻⁶	3.5 x 10 ⁻¹³
chalcopyrite - Fe ³⁺			1.2 x 10 ⁻⁹
sphalerite - O _{2(aq)}	3.6 x 10 ⁻⁶	2.5 x 10 ⁻⁶	4.6 x 10 ⁻¹⁴
sphalerite - Fe ³⁺			1.2 x 10 ⁻⁹
pentlandite - O _{2(aq)}	1.3 x 10 ⁻⁶	8.9 x 10 ⁻⁷	4.6 x 10 ⁻¹³
pentlandite - Fe ³⁺			1.2 x 10 ⁻⁹
calcite	2.8 x 10 ⁻⁵	1.2 x 10 ⁻⁵	--
dolomite	3.2 x 10 ⁻⁵	1.4 x 10 ⁻⁵	--

Sulfide reactions are transport controlled with $r^p = 0.0625$ mm (after Langman et al., 2014); effective diffusion coefficient (D^{eff}) from Wilson et al. (2018a) in $m^2 s^{-1}$; estimated surface area of $1 m^2 g^{-1}$ (Langman et al., 2014).

¹Total sulfide and carbonate mineral content based on results of static testing after Smith et al. (2013c); Bailey et al. (2015); chalcopyrite and sphalerite content based on Cu and Zn content from whole rock analysis; pentlandite content calibrated based on Ni and Co concentrations in humidity cell effluent.

²Calculated using density specific to each mineral in m^3 mineral m^{-3} porous medium.

Table 6.6 Initial volume fraction and rate data for host and secondary minerals in Type III simulations

Mineral	Type III $\phi_i^{1,2}$	k/k^{eff}	E_a^3	S_i (calibrated)
calcite	1.6×10^{-4}	$k_1 = 10^{-0.05}$ $k_2 = 10^{-6.19}$ $k_3 = 10^{-3.30}$	21	--
dolomite	1.8×10^{-4}	$k_1 = 10^{-2.59}$ $k_2 = 10^{-7.66}$ $k_3 = 10^{-4.00}$	42	--
biotite ⁴	4.7×10^{-2}	$10^{-10.97}$	63	20
muscovite ⁴	1.6×10^{-2}	$k_1 = 10^{-12.60}$ $k_2 = 10^{-13.50}$	22	7
albite ⁴	1.5×10^{-1}	$k_1 = 10^{-9.69}$ $k_2 = 10^{-14.15}$	58	6
Fe(III) (oxy)hydroxide ⁵	--	10^{-8}	--	--
k-jarosite ⁵	--	10^{-8}	--	--
gibbsite ⁵	--	10^{-12}	--	--
silica (am) ⁵	--	10^{-6}	--	--
gypsum ⁵	--	10^{-6}	--	--
siderite ⁵	--	10^{-9}	--	--

¹Mineral content of carbonate minerals based on static testing (after Smith et al., 2013b; Bailey et al., 2015); mineral content of host minerals based on results presented in Jambor 1997.

²Calculated using $\rho_b = 1.62 \text{ g cm}^{-3}$ in m^3 mineral m^{-3} porous medium and adjusted during simulation calibration.

³Activation energy in kJ mol^{-1} .

⁴Calibrated surface area in m^2 mineral L^{-1} porous medium based on mineral volume fraction and bulk surface area after Langman et al. (2014) and adjusted to fit measured humidity cell effluent parameters (Wilson et al., 2018a). Calibrated activation energy (Wilson et al., 2018a).

⁵Calibrated effective rate constant in mol L^{-1} porous medium s^{-1} (Wilson et al., 2018a).

6.4 Results

Simulated water flow through the 2-D domain for the homogeneous and heterogeneous hydraulic conductivity cases was assessed to evaluate the influence of the hydraulic conductivity distribution on effluent volume. The simulated outflow was compared to flow from the Type III test pile experiment, which was measured using tipping bucket rain gauges connected to the BCL drain lines. Further

details regarding the flow system at the Type III test pile was documented by Smith et al. (2013a), Neuner et al. (2013), and Sinclair et al. (2015). For comparison to simulated flow, measured flow from the pile interior was calculated as the total flow measured at the BCL tipping buckets divided by the area of the test pile contributing flow to the BCL. The simulations for the homogeneous and heterogeneous hydraulic conductivity cases captured the core outflow consistent with the 1-D flow simulation conducted in Chapter 4. The total flow over the course of the simulation period (6 years) was consistent with the total measured outflow for each of the 160 simulations (Figures 6.5 and 6.6).

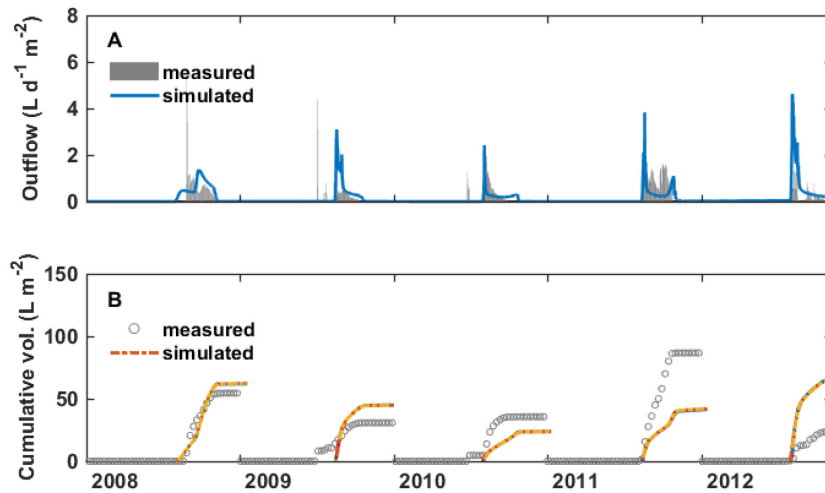


Figure 6.5 A: Measured and simulated (80 2-D simulations, homogeneous K_s) daily outflow [$L d^{-1}$] versus time [year] for the Type III test pile experiment. B: Measured and simulated (80 2-D simulations, homogeneous K_s) cumulative annual outflow [L] versus time [year] for the Type III test pile.

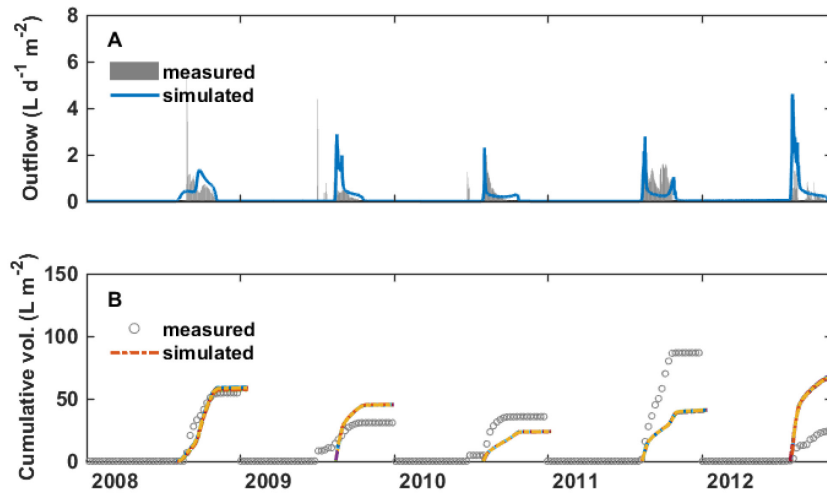


Figure 6.6 A: Measured and simulated (80 2-D simulations, heterogeneous K_S) daily outflow [$L d^{-1}$] versus time [year] for the Type III test pile experiment. B: Measured and simulated (80 2-D simulations, heterogeneous K_S) cumulative annual outflow [L] versus time [year] for the Type III test pile.

To assess the influence of spatial heterogeneity in hydraulic conductivity on the geochemical evolution of the Diavik waste rock, the 2-D simulation results were compared to the measured effluent concentrations from the core of the Type III test pile. Measured concentrations were calculated as the average of all samples collected from the BCL drains at a given sampling event. The simulated effluent concentrations were compared to measured concentrations at 1 m intervals across each of the SC_i (heterogeneous S and C mineralogy and homogeneous K_S) and $SC-K_{Si}$ (heterogeneous S and C mineralogy and heterogeneous K_S field) simulation domains to assess variability within a given simulation and consistency with measured values. Figure 6.7 provides an example of the variability across a single domain (simulation SC_1 or $SC-K_{S1}$) and is representative of the variability exhibited by each of the 160 simulations. Review of these plots indicated that effluent concentration variability for parameters SO_4 , Ni, Co, Cu, Zn, Mg, Na, Ca, and K along the x-axis of the domain was limited; parameters including Fe, Al, and pH were more sensitive to heterogeneity in S and C. The sensitivity of Fe and pH was restricted to early in the simulations (2008); the sensitivity of Al was consistent for the duration of the simulations. The variability of parameter effluent concentration did not appear to be influenced by the hydraulic conductivity field (*i.e.*, homogeneous or heterogeneous).

The simulated concentrations for parameters SO₄, Fe, Ni, Co, Cu, Zn, Mg, Na, Ca, and K were similar to the measured concentrations throughout the period; the simulated pH values and the measured values agree well for the modelled period. Measured concentrations of Al were over-predicted for most of the simulation period. Over-prediction of Al concentrations occurred in the pH calibrated 1-D simulations, although the 1-D simulated concentrations were closer to the measured values compared to the 2-D values.

To assess the variability in effluent concentrations between simulations, the mean effluent concentrations across all SC_i and SC-K_{Si} simulation domains (average of 16 effluent concentrations at 1 m intervals) were compared and plotted with measured effluent concentrations. Review of the plots (Figure 6.8) indicates less variability between simulations than within a given simulation with the exception of Fe which displayed a greater sensitivity to variations in S and C distribution. The variability of parameter effluent concentrations did not appear to be influenced by the hydraulic conductivity field (*i.e.*, homogeneous or heterogeneous).

Mass flux calculations were conducted to assess the variability in annual solute mass flux from the simulation domains compared to the measured mass flux (Figure 6.9). Mass flux of solutes from a 1-D simulation were also plotted to assess the influence of heterogeneity on the simulations. The variability in mass flux was modest for parameters SO₄, Fe, Ni, Co, Cu, Zn, Mg, Na, Ca, and K in all years with the exception of Fe which exhibited elevated variability in 2008. The annual mass flux of Fe exhibited greater sensitivity to heterogeneities in the S and C contents, in a manner similar to that observed in the analysis of Al and Fe effluent concentration. The mass flux of solutes from the simulation domains compared well with measured mass flux for years 2008, 2009, 2010, and 2012 but deviated from the measured values in 2011 similar to the 1-D simulation values. The variability of mass solute flux was not influenced significantly by the hydraulic conductivity field (*i.e.*, homogeneous or heterogeneous).

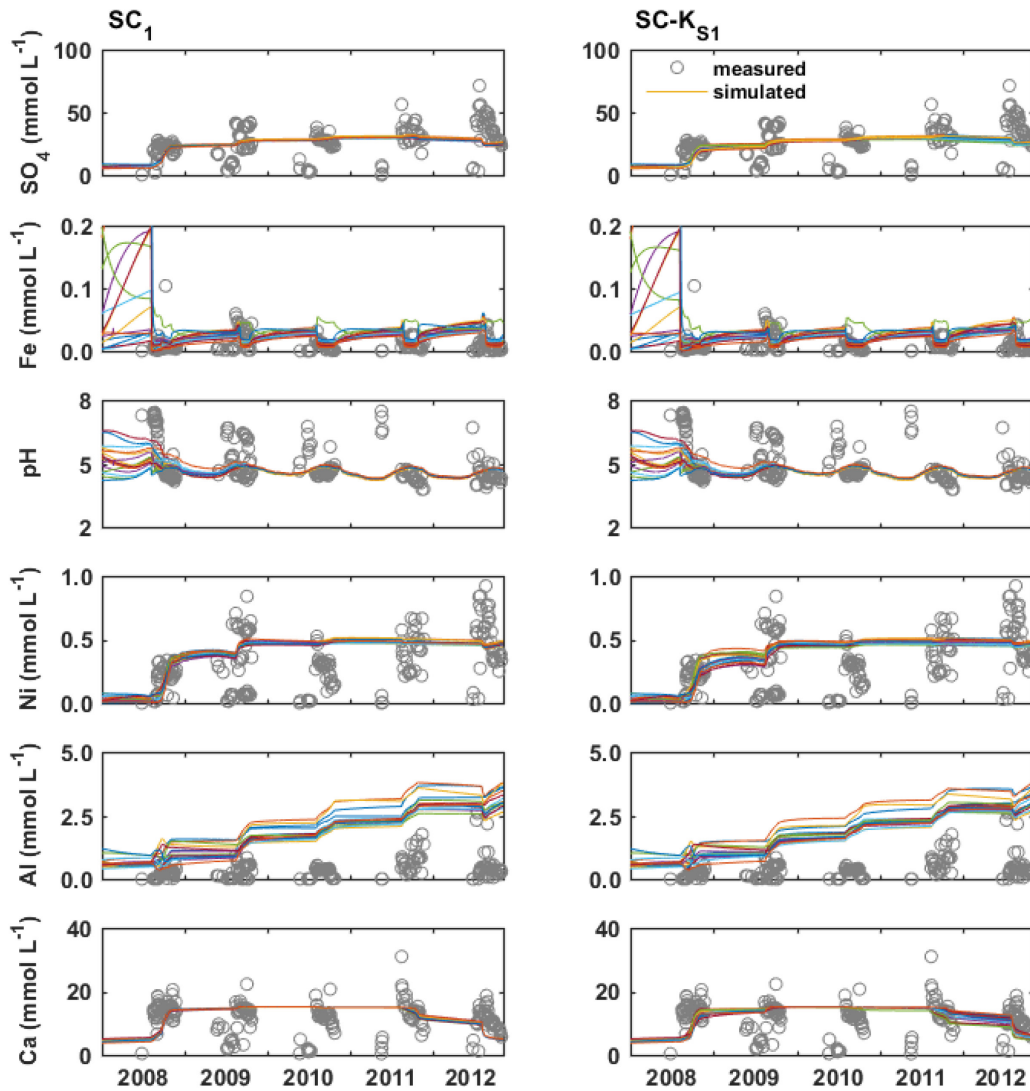


Figure 6.7 Concentrations of mineral weathering products SO_4 , Fe, Ni, Al, Ca [mmol L^{-1}] and pH [-] versus time [year] measured in Type III test pile effluent compared to aqueous concentration exiting the simulation domain. Simulated concentrations are from 1 2-D simulations (16 points along x-axis) with homogeneous hydraulic conductivity (SC_1) and heterogeneous hydraulic conductivity ($\text{SC-K}_{\text{S}1}$). Measured concentrations are available only for periods of test pile core flow; simulated concentrations are calculated by the model for all periods regardless of flow condition.

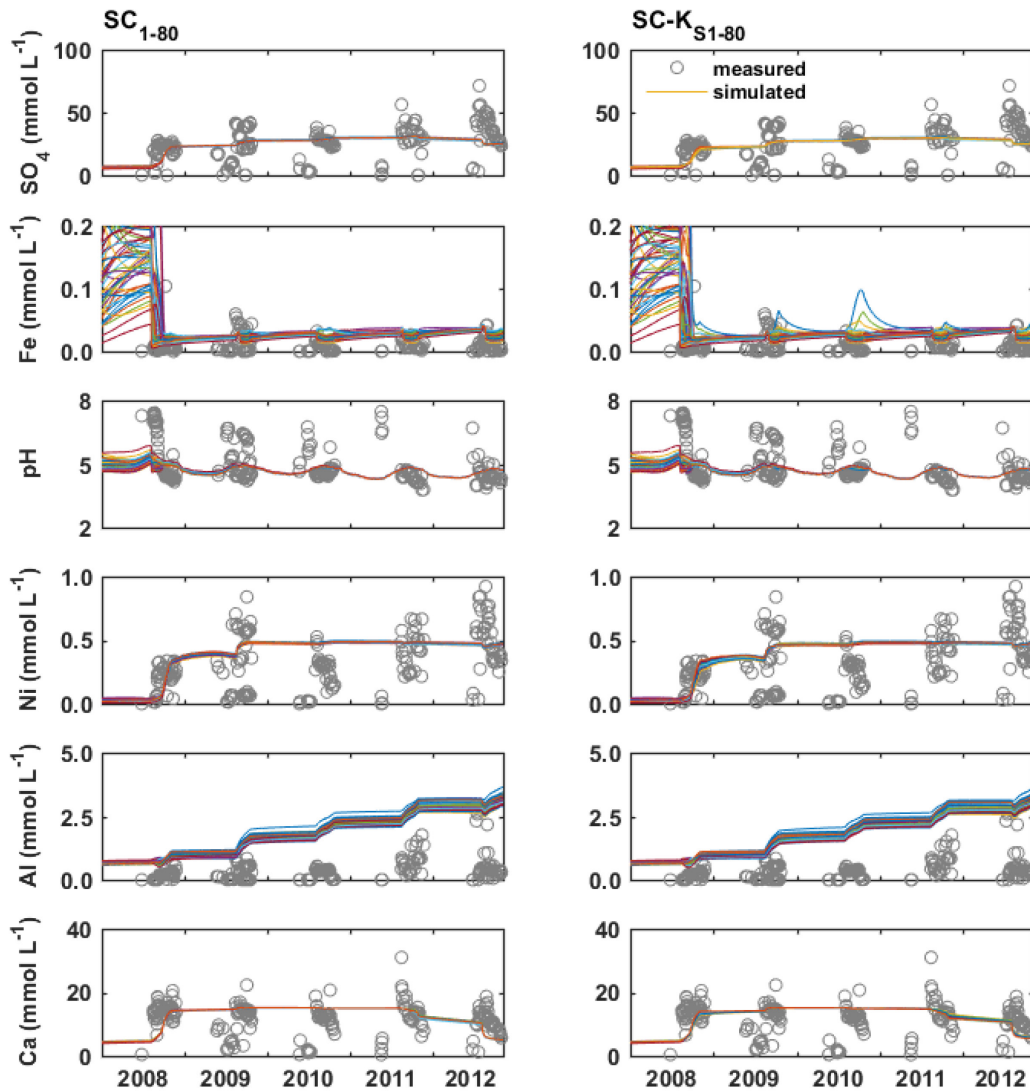


Figure 6.8 Concentrations of mineral weathering products SO_4 , Fe, Ni, Al, Ca [mmol L^{-1}] and pH [-] versus time [year] measured in Type III test pile effluent compared to aqueous concentration exiting the simulation domain. Simulated concentrations are from 80 2-D simulations (16 points along x-axis) with homogeneous hydraulic conductivity (SC_{1-80}) and heterogeneous hydraulic conductivity (SC-K_{S1-80}). Measured concentrations are available only for periods of test pile core flow; simulated concentrations are calculated by the model for all periods regardless of flow condition.

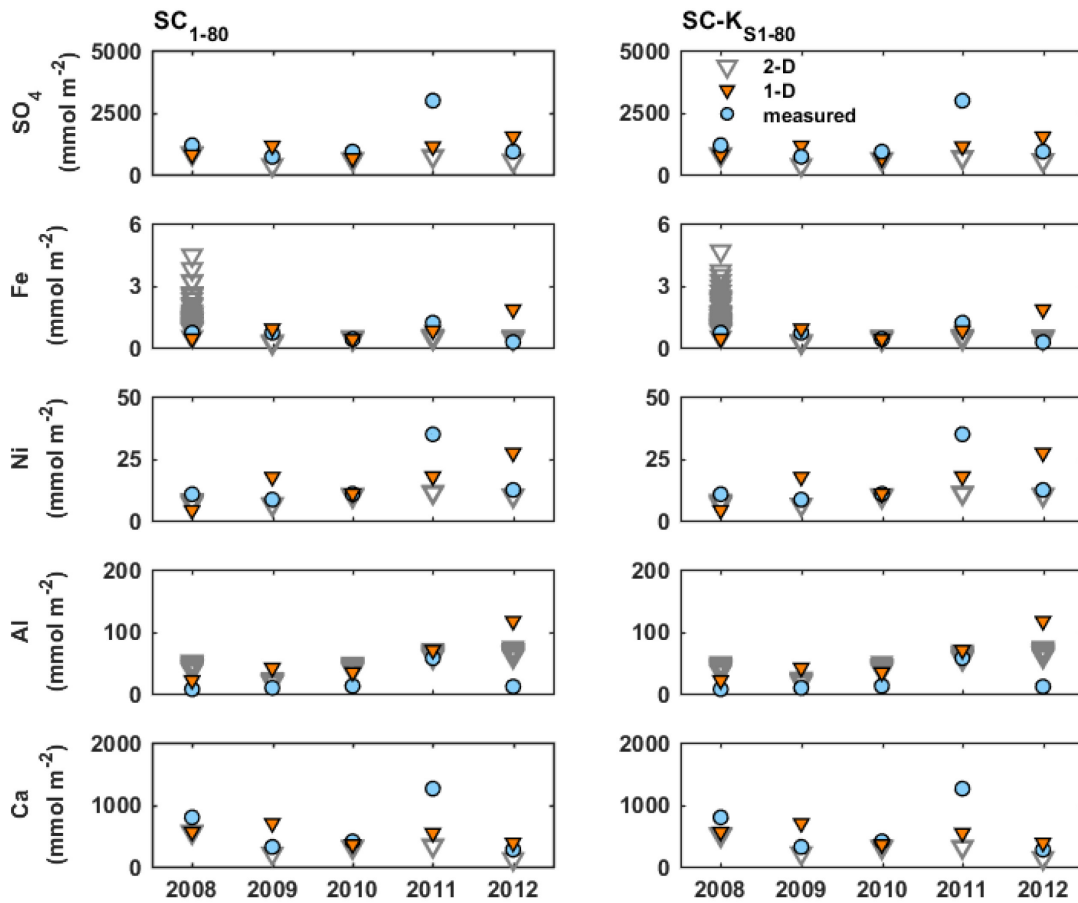


Figure 6.9 Total annual mass of mineral weathering products SO₄, Fe, Ni, Al, and Ca [mmol m⁻² yr⁻¹] versus time [year] measured in Type III test pile effluent compared to simulated total mass exiting the 2-D homogeneous hydraulic conductivity (SC₁₋₈₀), 2-D heterogeneous hydraulic conductivity (SC-K_{S1-80}) and 1-D simulation domains. Circles represent the measured values from the core of the test pile, empty triangles represent 80 2-D simulation results, solid triangles represent the 1-D simulation results (Chapter 4).

6.5 Discussion

The integrated conceptual model used for these heterogeneous simulations was the same used for the 1-D simulation of the Type III test pile experiment including calibration for pH. The calibration of pH involved the reduction of calcite mineral volume fraction to 20% of the measured content (Wilson et al., 2018b) and was included to better reflect the measured pH conditions of the test pile effluent, and

may reflect the availability of carbonate minerals within the Diavik rock. The simulations for the homogeneous (SC_i) and heterogeneous hydraulic conductivity (SC-K_{Si}) cases are generally consistent and described the effluent concentrations of many key parameters well (*e.g.*, SO₄, Ni, Co, Ca, pH), whereas the concentrations of other parameters were not captured as closely (*e.g.*, Al, Cu, Zn). Annual mass flux in both cases was represented well (especially in years 2008-2010 and 2012) for parameters related to sulfide oxidation (*e.g.*, SO₄, Ni, Co, Cu, Zn), but the mass load was underestimated for most parameters in 2011. In many cases the heterogeneous simulations provided results that were very similar to the 1-D homogeneous results. In cases where the simulation results differed (*e.g.*, SO₄, Ni, Ca), the heterogeneous simulations provided values more similar to the measured mass loadings.

6.5.1 Temperature

In all cases, simulations used the same spatially- and temporally-variable temperature distribution to represent the thermal conditions within profile during the Type III test pile experiment. The simulated temperature may not fully represent the temperature variations with the test pile experiment because of heat trace located at the BCLs and associated drains, which was installed to prevent damage due to freezing. The heat trace probably did not affect the geochemical evolution of the waste rock, but it may have influenced the timing of flow at the drains (*e.g.*, measured outflow occurs in 2009, 2010, and 2012 prior to simulated outflow). The influence of the heat trace was not considered in the simulations.

6.5.2 Influence of Heterogeneous S and C Distribution

The distribution of daily mass-flux values (mean mass flux across simulation domain) for parameters SO₄, Fe, Ni, Co, Cu, Zn, Al, Si, Ca, Mg, K, and Na was compared to normal and log normal distributions (Figure 6.10 shows examples of the generated histograms for SO₄, Fe, and Ni on September 9, 2008-2012). The chi-squared goodness-of-fit parameter was calculated for each of the SC_i and SC-K_{Si} cases for days when water flowed from the simulation domains. For the daily mass flux in the SC_i case, the log normal distribution resulted in the best fit for all evaluated parameters with the distribution fitting > 80% of the flow days for all parameters except Si, K, and Na (57%, 73%, and 77% respectively). For the daily mass flux in the SC-K_{Si} case, the log normal distribution resulted in the best fit for all evaluated parameters with the distribution fitting > 80% of the flow days

for all parameters except Cu (75%). The distribution of annual mass-flux values (mean annual mass flux across simulation domain) was also calculated to provide a probability density function for the annual mass flux of the evaluated parameters (Figure 6.11). The distribution of the annual mass flux for the SC_i case for years where flow occurred (2008-2012) compared well with the log normal distribution generated using the mean annual mass flux for most parameters (shown for SO₄, Fe, and Ni in Figure 6.11). The results of chi-square goodness-of-fit analysis for all evaluated parameters in each of the hydraulic conductivity cases indicated that the log normal probability density function provides the best approximation to the annual mass flux from the simulation domain.

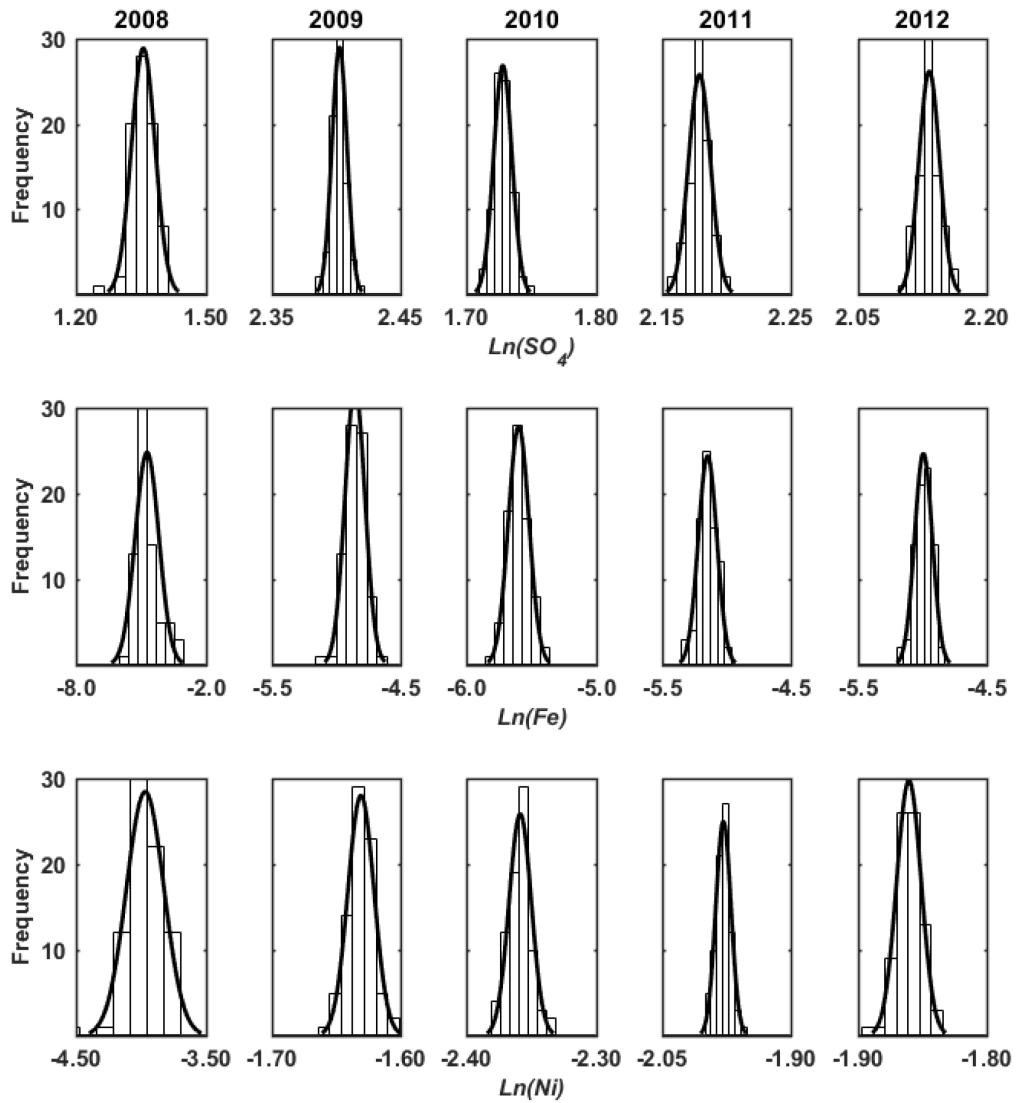


Figure 6.10 Histograms indicating the distribution of the log-transformed daily mass flux [mmol m^{-2}] from the 2-D homogeneous hydraulic conductivity simulation domain compared to the fitted normal distribution for parameters SO_4 , Fe, and Ni on September 9 of each year.

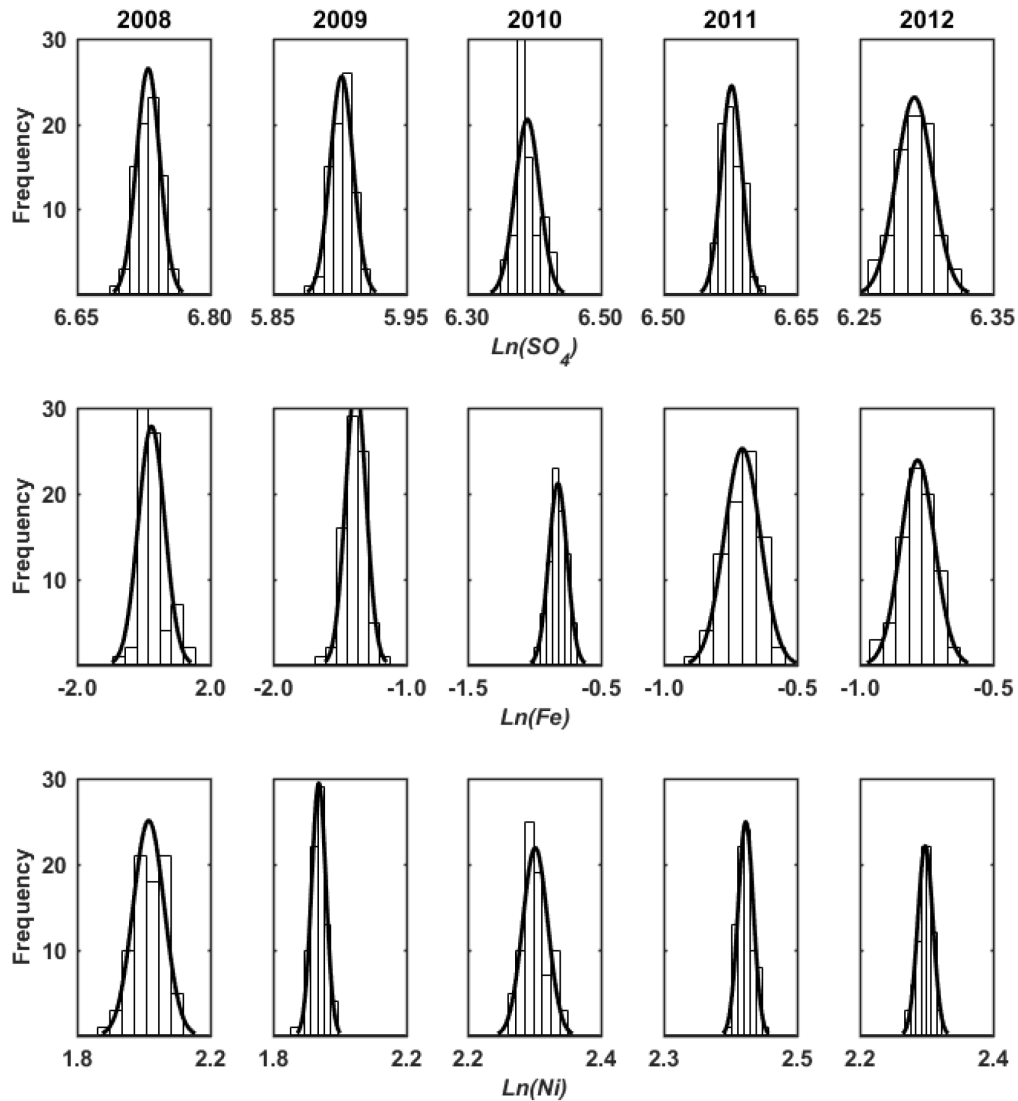


Figure 6.11 Histograms indicating the distribution of the log-transformed annual mass flux [mmol m^{-2}] from the 2-D homogeneous hydraulic conductivity simulation domain compared to the fitted normal distribution for the parameters SO_4 , Fe, and Ni.

The annual mass flux for each of the SC_i and SC-K_{Si} cases was compared to the annual mass flux from a 1-D simulation of the Type III test-pile experiment. The 1-D simulation was run with

homogeneous S, C, and hydraulic conductivity distributions for a 1 m x 1 m x 12.5 m column within the core of the test pile. Further details on the results of the 1-D simulation were documented in Chapter 4.

Annual mass flux for the 1-D simulation was similar to the annual mass flux for the heterogeneous simulations for some parameters (*e.g.*, SO₄, Ca) and diverged slightly from the heterogeneous cases for other parameters (*e.g.*, Ni, Al) (Figure 6.9). The root mean square error calculations for the 2-D heterogeneous cases (relative to measured values) indicated that mean residual mass fluxes from the 2-D simulations were very similar to the residual mass values calculated from 1-D simulations for most of the parameters evaluated (Figure 6.12), but were significantly lower for some parameters in some years (*e.g.*, 2009 and 2012). Over the entire simulation period the root mean square error from the heterogeneous simulations was lower than for the 1-D simulation for all parameters except Ca, K, Mg, Na, and SO₄ (Table 6.7).

Table 6.7 Summary of the root mean square error of mean total mass flux residual [mmol m⁻²] from the heterogeneous 2-D and homogeneous 1-D simulation cases for selected parameters

Simulation	Al	Ca	Cu	Fe	K	Mg	Na	Ni	SO ₄	Zn
SC _i	32.8	435.1	5.7	0.5	141.0	1589.4	568.3	10.7	1052.4	2.9
SC-K _{Si}	32.2	446.9	5.5	0.5	141.6	1593.9	569.6	10.8	1069.2	2.8
1-D	51.1	381.5	14.2	0.7	106.6	1502.6	542.5	11.3	915.1	4.5

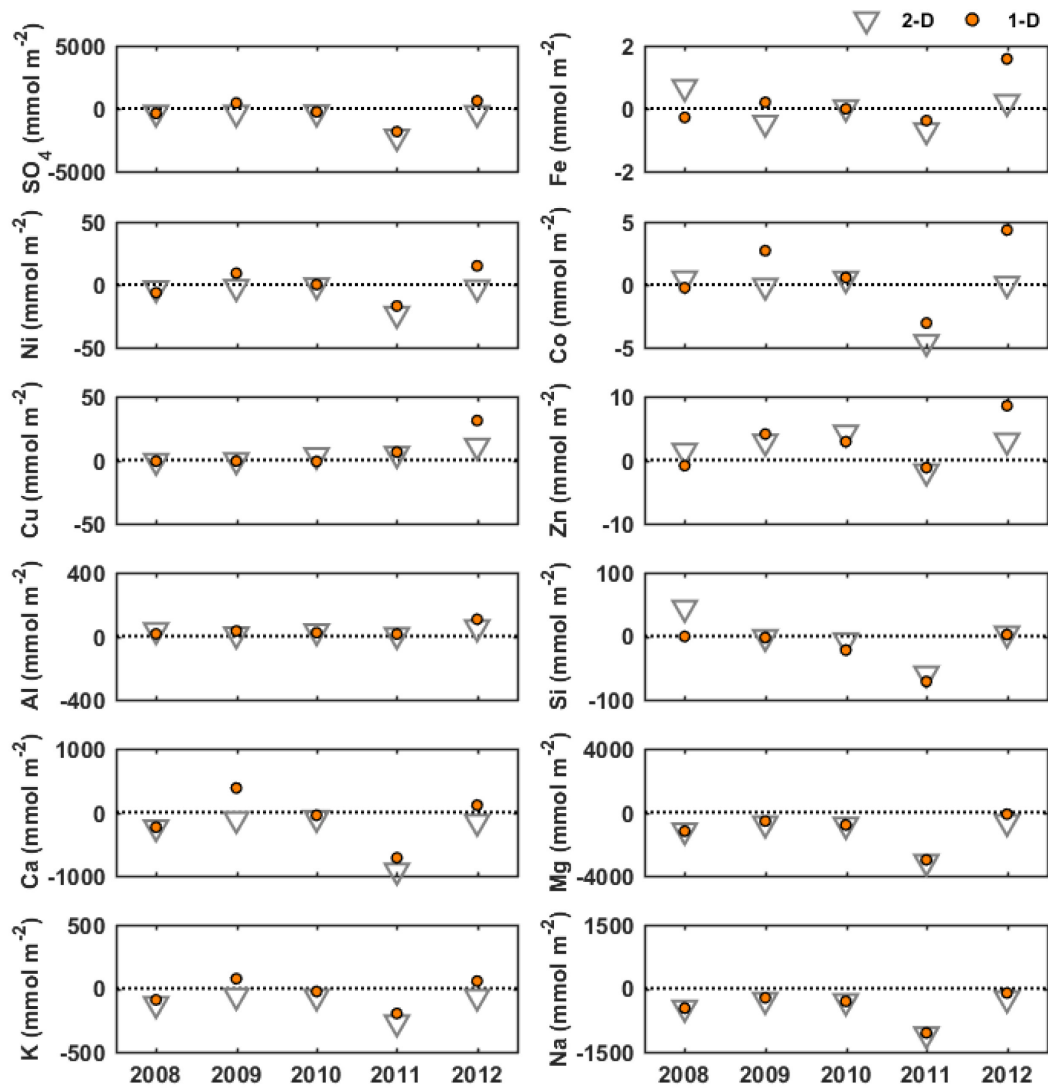


Figure 6.12 Residual of mean annual mass flux of mineral weathering products SO_4 , Fe, Ni, Co, Cu, Zn, Al, Si, Ca, Mg, K, and Na [$\text{mmol m}^{-2} \text{yr}^{-1}$] versus time [year] exiting the SC_{1-80} and $\text{SC-K}_{\text{S}1-80}$ simulation domains and exiting the 1-D simulation domain.

6.5.3 Influence of Heterogeneous Hydraulic Conductivity Distribution

The use of measured precipitation data and estimated infiltration along with a measured temperature distribution resulted in simulated flow that captured the measured flow from the core of the test-pile experiment. Simulated flow from the test pile core matched the measured flow with no flow occurring from the simulation domain in 2006 and 2007, and flow timing for years 2008-2012 matching the measured flow seasons well. Infiltration resulting from snow melt was not considered in the simulations because snowfall was typically removed from the top of the test pile experiment by wind prior to melting (Neuner et al., 2013). To incorporate no flow under water-freezing conditions, the integrated conceptual model included reducing the saturated hydraulic conductivity to stop flow for temperatures less than 0 °C.

The results of the SC_i and SC-K_{Si} simulations were analyzed separately to assess the influence of a heterogeneous hydraulic conductivity field on the geochemical evolution of test-pile effluent. Review of the simulated flow from the core of the test pile experiment indicated that mean total flow from the homogeneous hydraulic conductivity simulations was higher than mean total flow from the heterogeneous hydraulic conductivity simulations (Table 6.8). Variance in total flow volume was larger for the heterogeneous K_S case and was consistent with the daily variability in measured flow from the BCLs. A normal probability distribution function provided the best fit to the distribution of flow volumes for the heterogeneous K_S case. Direct comparison of mean total flow indicated that the heterogeneous cases provided a simulation of flow through the test-pile experiment that was closer to the measured volume (232 L m⁻²).

The daily variability of the flow simulations was compared to daily variability in measured flow from BCLs. The variance in daily flow from the BCLs was calculated only for days when flow was observed in three or more BCLs at the Type III test pile during the 2008-2012 period. The variance in simulated daily flow was calculated for all flow days during the simulated period. The daily variance in simulated flow ranged from 10⁻¹ to 10⁻¹¹; higher variance values typically occurred earlier in a flow season and declined to lower values near the end of a flow season. The minimum, maximum, and mean daily variance for homogeneous K_S cases were less than for the heterogeneous K_S cases. The daily variance in measured flow ranged from 10⁻⁶ to 10⁰ with a mean daily variance (10⁻¹) two orders of magnitude higher than the simulated flow cases. The simulated daily flow variance was within the range of measured daily variances for portions of 2009, 2011, and 2012. The higher variance of the

measured flow was likely a result, in part, of the much lower sample size (average of 3 samples compared to 80 for the each of simulated cases) but also suggested that a portion of the flow measured at the BCLs was non-matrix and/or macro-pore related. The simulated flow only considered matrix flow and therefore would be expected to exhibit lower variance in daily flow.

Table 6.8 Flow simulation statistic comparison for homogeneous and heterogeneous hydraulic conductivity distributions

Total flow	Homogeneous	Heterogeneous
mean (L m ⁻²)	247.2	244.0
variance	0.02	0.16

The differing hydraulic conductivity distributions (homogeneous versus heterogeneous) did not significantly influence simulation of the geochemical evolution of the waste rock. The variance in daily mass-flux values for parameters SO₄, Fe, Ni, Co, Cu, Zn, Al, Si, Ca, Mg, K, and Na was calculated for each set of simulations then compared using an F-test to assess the influence of heterogeneous hydraulic conductivity on the mass flux of evaluated solutes. The probability density function that best fit the daily mass flux for the SC_i and SC-K_{Si} cases was determined to be the log normal distribution. As a result, the mass flux data was log-transformed to facilitate completion of the F-test analysis of variance. The results of the F-tests (one test for each day of flow for a total of 342 tests for each of 12 parameters) indicated that the null hypothesis (that the variances were not statistically different) was rejected < 20% of the days for parameters Al, Co, Cu, Fe, K, Mg, Ni, and Zn. The null hypothesis was rejected ranging from 12% (Si) to 80% (SO₄) of the days for parameters Ca, Si, Na, and SO₄. Review of the p-values associated with the F-tests for all parameters confirmed that the variance in daily mass flux between the SC_i and SC-K_{Si} cases was not statistically different for the majority of the evaluated parameters. The standard error of the estimate calculations indicated that the residual annual mass flux from each of the hydraulic conductivity cases was very similar (but not the same) for all evaluated parameters (Figure 6.13).

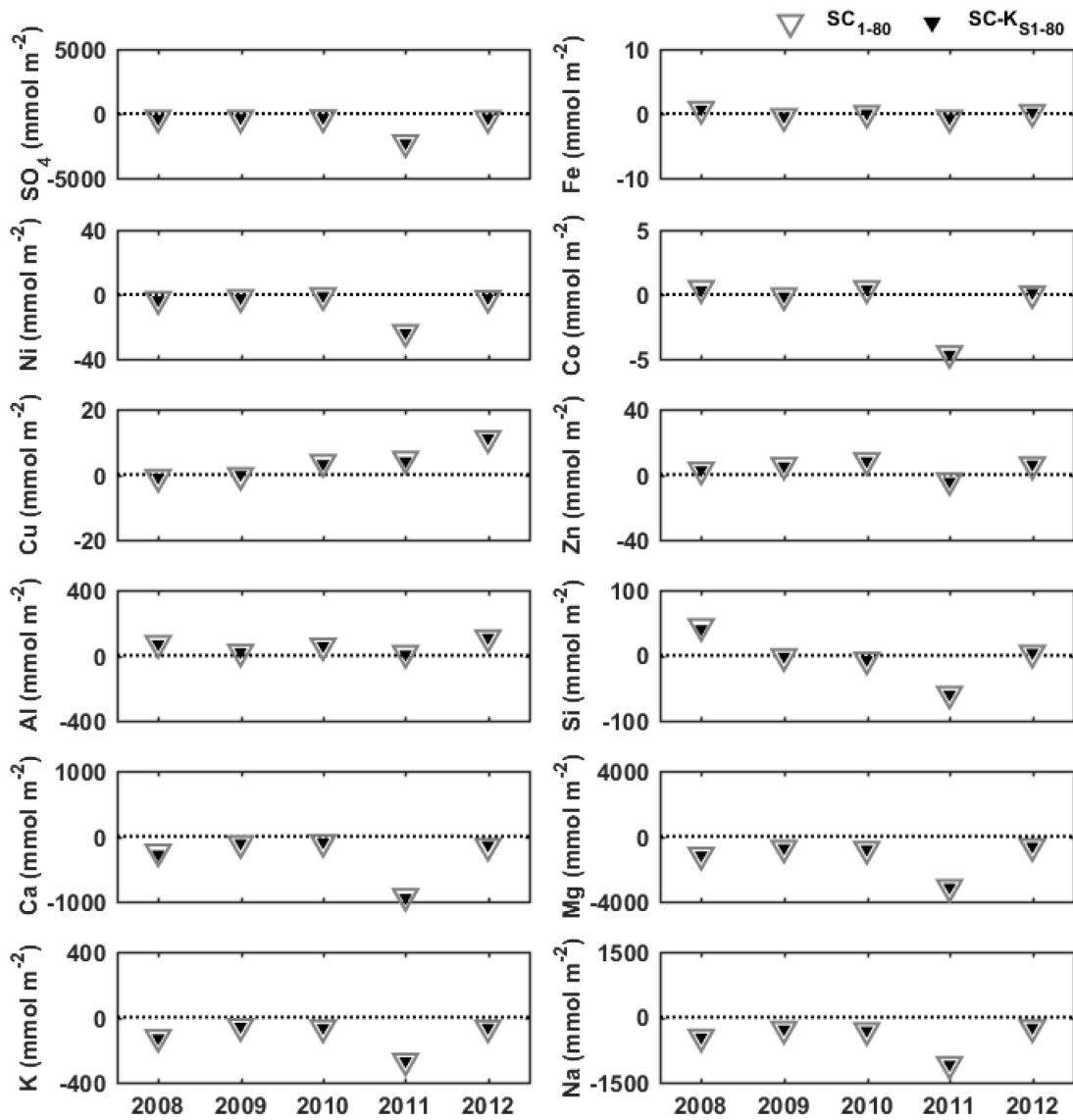


Figure 6.13 Residuals of mean annual mass flux of mineral weathering products SO₄, Fe, Ni, Co, Cu, Zn, Al, Si, Ca, Mg, K, and Na [mmol m⁻² yr⁻¹] versus time [year] exiting the homogeneous (SC₁₋₈₀) and heterogeneous hydraulic conductivity (SC-K_{S1-80}) simulation domains.

The results of the statistical analysis suggests that the influence of heterogeneity in the distribution of hydraulic conductivity in the core of the Type III test pile on the geochemical mass flux was not significant with respect to geochemistry. The root mean square error calculations for mass flux indicates that the residual mass fluxes for SC-K_{Si} cases were within $\pm 2\%$ of the residual mass fluxes for the SC_i cases over the 5 year simulation period for all evaluated parameters.

6.5.4 Variability of Effluent Geochemistry

Significant variability in measured effluent concentrations of some parameters has been observed at the DWRP experiments by previous researchers. For example, Bailey et al., (2015) reported maximum SO₄ concentrations from the medium-size field experiments (active zone lysimeters) in July 2010 were 8,600 mg L⁻¹ and 13,300 mg L⁻¹ in the two Type III effluent drains respectively and suggested this discrepancy was due to differing volumes of matrix material contributing to solute release in the experiments (*i.e.*, heterogeneity between the experiments). Mean annual concentrations of parameters including Al, Ni, and Cu were also reported by Bailey et al. (2015) to vary significantly between the two Type III active zone lysimeters (*e.g.*, 2010 values for Al: 30 and 66 mg L⁻¹, Ni: 17 and 30 mg L⁻¹, and Cu: 1.9 and 3.9 mg L⁻¹) indicating that deviation of simulated concentrations from the measured concentrations was expected. Review of SO₄ concentrations from the interior of the test pile experiment indicated similar variation. For example, in July 2012 maximum and minimum SO₄ concentrations of 8,500 mg L⁻¹ and 300 mg L⁻¹ were recorded in samples collected from the same test pile BCL less than 10 days apart indicating substantial variability within individual DWRP experiments.

The intra-variability (variance within a single simulation) and inter-variability (variance between all simulations) of the effluent solute concentrations was calculated and compared to the variability of measured samples to assess whether the heterogeneous simulations captured the heterogeneity of the test pile experiment with respect to geochemistry. The assessment was conducted for parameters SO₄, Fe, Ni, Co, Cu, Zn, Al, Si, Ca, Mg, K, Na, and pH. Intra-variability was assessed by calculating the daily variance in solute concentrations at 1 m intervals along the effluent boundary for each simulation in the SC_i and SC-K_{Si} cases. Inter-variability was assessed by calculating the daily variance in solute concentrations from all simulations. The variability in measured solute concentrations was calculated for days where three or more samples were collected from the BCLs in a single sampling event.

Intra-variability and inter-variability values were lower (typically by one to two orders of magnitude) than the variance measured for all parameters except Fe for both the SC_i and SC-K_{S_i} cases. The variance of simulated Fe concentrations was higher than the variance in measured samples for the inter-variance case. For parameters Al, Ca, Cu, Fe, Zn, and pH, the variance in the simulated concentrations was within the range of variances for all measured samples, indicating that the simulations captured a portion of the variability in the test pile experiment. Confidence intervals (95th percentile) were calculated for individual SC-K_{S_i} simulations and for the SC-K_{S_i} simulation set as a whole and indicated that the range of expected (simulated) concentrations were within the measured concentrations for most parameters (except Al) and that the 95th percentile confidence interval was relatively narrow for most parameters (Figure 6.14). In general, inter-variability was slightly higher than intra-variability and variance for the SC-K_{S_i} cases was higher than for the SC_i cases suggesting a multi-realization, heterogeneous S and C, heterogeneous K_S simulation approach best represents the heterogeneity within the test pile experiment.

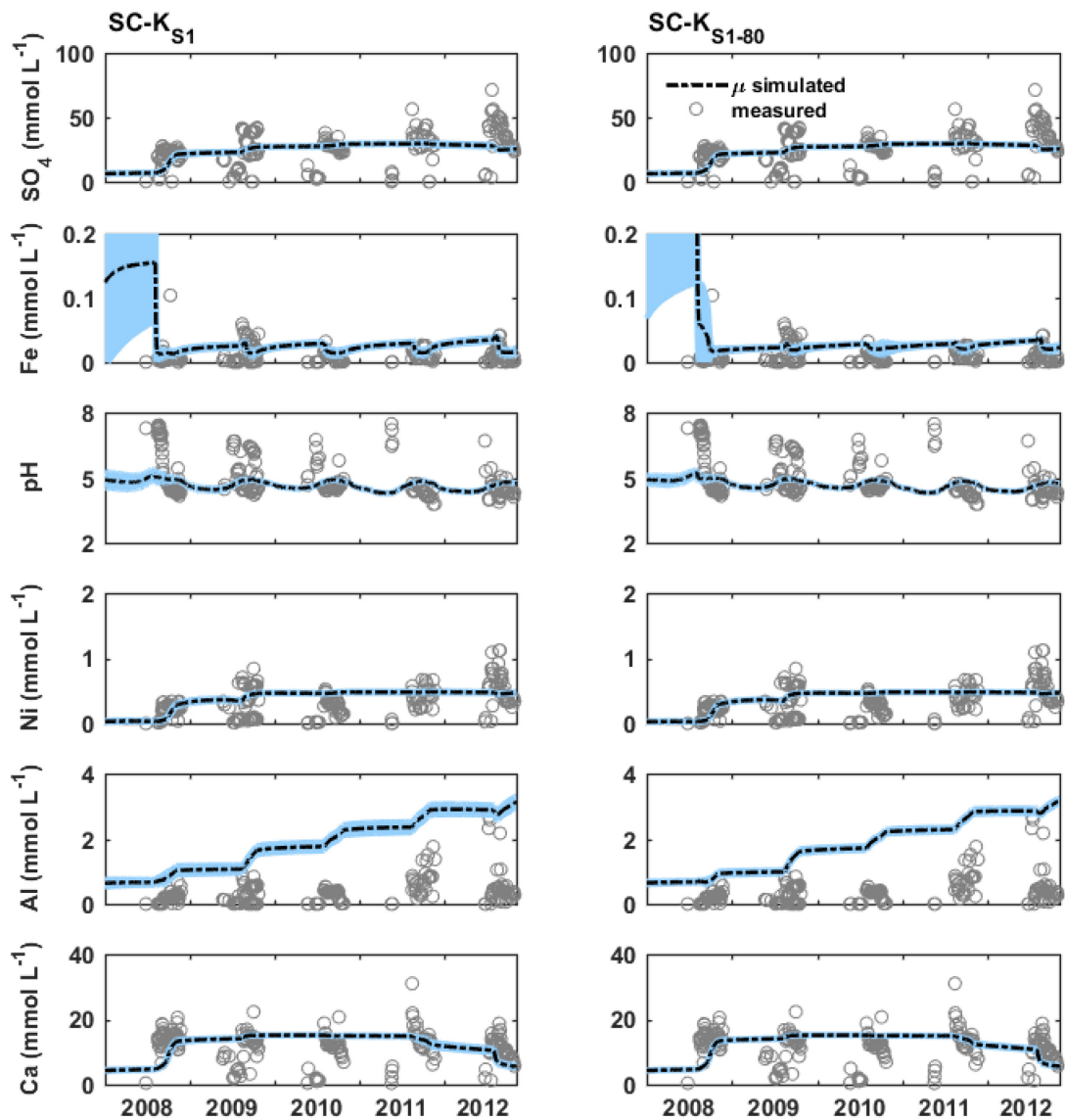


Figure 6.14 Concentrations of mineral weathering products SO_4 , Fe, Ni, Al, Ca [mmol L^{-1}], and pH [-] versus time [year] measured in Type III test pile effluent compared to the mean aqueous concentration exiting the simulation domain. Simulated concentrations are from a single 2-D heterogeneous simulation (SC-K_{S1}) and the entire set of 2-D heterogeneous simulations ($\text{SC-K}_{\text{S1-80}}$). Confidence intervals (95th percentile) are shown in blue shading around the daily mean values. Measured concentrations are available only for periods of test pile core flow; simulated

concentrations are calculated by the model for all periods regardless of flow condition.

6.6 Conclusions

Multiple 2-D simulations of the geochemical evolution of the core of a test-pile experiment facilitated an analysis of the influence of heterogeneity in S and C mineralogy and hydraulic conductivity on the geochemical evolution of a waste-rock pile. The simulations also allowed calculation of probability density functions to approximate the distribution of the solute mass-flux values from heterogeneous S and C distributions.

The SC_i (heterogeneous S and C and homogeneous K_S) and $SC-K_{Si}$ (heterogeneous S, C, and K_S) cases resulted in very similar solute-concentration, and solute mass-flux values, suggesting that using a heterogeneous hydraulic conductivity distribution did not significantly influence the solute flux. This result affirms the significant control that sulfide oxidation (a diffusion controlled process) exerts on the geochemistry of the test pile effluent. The similarity in geochemistry between the SC_i and $SC-K_{Si}$ cases may have been influenced by the relatively simple physical characteristics of the test-pile experiment, in which internal structures common to full-scale waste-rock piles, such as traffic surfaces, were not present. The heterogeneous simulations provided mass flux values that were usually within one order of magnitude of the measured results. Analysis of the solute mass-flux values for parameters indicative of sulfide and host mineral weathering from the heterogeneous simulations indicated that the distribution of solute mass fluxes from the test-pile experiment could be best approximated with a log normal probability density function.

Despite the apparent lack of influence of the heterogeneous K_S field over the geochemical evolution within the test pile core, the heterogeneous K_S simulations provided value in the understanding of flow and geochemical dynamics within waste rock piles. The variability in total flow volume from the heterogeneous K_S simulations was an order of magnitude higher than for the homogeneous K_S simulations and was consistent with the variability of measured daily flow at the BCLs. Although not directly comparable (total flow versus daily flow), the consistency between the total simulated flow variance and daily measured flow variance indicated that the heterogeneous K_S simulations were able to capture some of the variability with respect to flow within the test pile that the homogeneous K_S simulations did not, thereby providing an assessment that better represented the actual conditions with respect to flow through the core of the test pile.

A comparison of the solute mass flux from the 2-D simulations with the 1-D homogeneous case suggested that introducing more complex distributions of mineralogy (S and C) and physical parameters (hydraulic conductivity) do not necessarily produce a significantly improved approximation of the measured geochemical conditions at the test-pile experiment. Modifying the domain structure to 2-D following model calibration as a 1-D domain may have introduced complexities that required supplemental calibration in order to extract maximum benefit.

In the context of a mechanistic approach to scale-up, the influence of heterogeneity in mineralogy and hydraulic conductivity can also be assessed. Standard error analysis of the 2-D heterogeneous simulation results suggested some improvement over 1-D homogeneous simulations; and showed that simulated effluent concentrations of some parameters (*e.g.*, Fe, pH, Al) varied significantly across a single 2-D domain. The significant variation observed for some parameters (order of magnitude for Fe, pH ranging from 4 to 6, and doubling of Al concentrations) across the domain for a relatively homogeneous low-sulfide waste rock suggests simulations of heterogeneous S and C mineralogy would be necessary to capture variability in concentrations exhibited by measured values and to assess maximum effluent solute concentrations and mass flux that could be released from a waste-rock pile. This result is consistent with the results of Pedretti et al. (2017) and Fala et al. (2013) which also showed significant parameter variation resulting from heterogeneous distributions of mineralogy. Although similarly homogeneous waste rock may exhibit similarly low variability in effluent concentrations of sulfide related parameters including SO₄ and metals (Ni in this case), it is expected that increased mineralogical complexity would result in increased variability in effluent concentration and mass flux, thereby increasing the necessity of considering heterogeneity within reactive transport simulations. Analysis of intra- and inter-variability suggests that including the mineralogical and physical heterogeneity of waste rock in multiple realizations provides the best representation of the test pile heterogeneity but, in the case of the Diavik test-pile experiments, a significant portion of the heterogeneity can be represented even by a single realization.

Chapter 7

Conclusions

7.1 Overview of Research

The primary focus of the research documented in this thesis was to develop a mechanistic method for characterization of the geochemical evolution of sulfidic mine-waste rock by scaling the results of laboratory experiments to make assessments at the large field scale. The goal was to develop a method that was scientifically defensible but also flexible in a manner that would facilitate implementation at locations other than the research site. Using the reactive transport code MIN3P-THCm (Mayer et al., 2002; Su et al., 2017) a conceptual model for the simulations was developed based on the results of small-scale column experiments (humidity cells). Humidity cell experiments are routinely used to make long-term predictions about the effluent geochemistry from mine wastes and are thus a common starting point for the characterization of the geochemical evolution of mine-waste rock. The model was calibrated at the humidity-cell scale to provide the best visual fit to humidity cell effluent data for four scenarios (Type I room and cold temperature and Type III room and cold temperature). This method of calibration allowed consideration of different S and C contents and of the temperature dependence of the simulated geochemical processes.

The calibrated model was then used to simulate the geochemical evolution of waste rock contained in the Diavik field experiments (Type I and Type III active zone lysimeters (AZLs) and Type III test pile). Scaling, in the case of the AZL experiments, consisted of considering only the matrix material (< 5 mm diameter) as significantly reactive, because the surface area of the coarse (> 5 mm diameter) fraction of the waste rock is much less than the surface area associated with the matrix material. The simulation domain was increased to represent the size of the experiment, and adjusting the S and C mineral content to be consistent with the Type I and Type III AZL experiments. Infiltration and temperature were adjusted for the AZL simulations to represent the measured conditions of the field experiments. No model calibration was required to obtain the preliminary results shown in Figure 3.5. Scaling, in the case of the Type III test-pile experiment, included the same process as for the AZL simulations with three important additions: i) the temperature of the test pile experiment varied spatially and temporally (AZL temperature only varied temporally), ii) flow in the test pile simulation was effectively stopped when test pile temperature was less than 0 °C, and iii) geochemical reactions

were stopped when test pile temperature was less than 0 °C. No calibration was conducted to obtain the preliminary results shown in Figure 4.4. To optimize the pH for simulations of the Type III field experiments, calibration of the CaCO₃ content was conducted.

A second focus of this research was to investigate the influence of heterogeneity in mineralogical and physical parameters on the geochemical evolution of the Diavik waste rock. Three important parameters to consider when assessing the geochemical evolution of a waste rock are S and C content and saturated hydraulic conductivity (K_s). An assessment of the role of heterogeneity in S and C content and hydraulic conductivity was conducted for the large-scale field experiments (Type I and Type III test piles). Geostatistical analysis of S and C content and pore-size distribution samples collected during deconstruction Type I test pile was conducted to assess the distribution and spatial dependence of these parameters. Subsequently, 80 realizations of S and C distribution and 80 realizations of K_s distribution were generated and used to conduct 160 2-D simulations of the geochemical evolution of the Type III test pile to assess the influence of heterogeneity in S and C content and K_s on the geochemical evolution of Diavik waste rock. The heterogeneous simulations were conducted using the reactive transport model developed as part of the scale-up investigation.

7.2 Summary of Major Findings

The integrated conceptual model developed to simulate the geochemical evolution of low-sulfide waste rock was implemented and calibrated at the laboratory scale using the reactive transport model MIN3P-THCm. The results indicated that measured solute concentrations were generally captured by the simulations, suggesting that the conceptual model, which considered the differing temperature and sulfide mineral contents of the humidity cell experiments, represented the primary geochemical processes occurring within the experiments. The simulations facilitated identification of parameters including mineral surface area, temperature, and pH as significant factors controlling the geochemical evolution of Diavik waste rock (i.e. lower quality effluent in the shorter term due to sulfide-mineral oxidation and improved quality effluent in the longer term due to depletion of the available sulfide minerals). The humidity cell simulation results suggest the integrated conceptual model could be used to simulate the geochemical evolution of the DWRP field experiments, provided that dynamic temperature and infiltration regimes representing field conditions are considered.

Implementation of the integrated conceptual model to simulate waste-rock weathering at the medium-scale field experiments (AZLs) resulted in good agreement of concentrations and mass flux with measured values from the AZL experiments. The results of the AZL simulations indicated that the integrated conceptual model could produce a reliable assessment of Diavik waste-rock weathering when dynamic temperature and infiltration regimes, representing measured field conditions, were included. Use of the calibrated model to simulate the geochemical evolution at the large-scale experiment (test pile) also resulted in good agreement between measured and simulated concentrations and mass flux of most parameters. Supplemental calibration of the field-scale simulations indicated that calcite (CaCO_3) availability was lower for the field experiments (approximately 20% of measured content) compared to the laboratory experiments. The field-scale simulation results indicated that the integrated conceptual model, based on the results of laboratory experiments, was sufficiently versatile to provide representative multi-year simulations of field experiments.

Although simulations of the field experiments did not rely on geochemical data for calibration, the model did rely on site specific physical data, including mineralogy-related parameters such as surface area and volume fraction; hydrology-related parameters such as hydraulic conductivity, grain-size distribution, porosity, and water-retention curve values; and environmental parameters such as temperature and precipitation; to facilitate reasonable assessment of the geochemical evolution of waste rock. The reactive transport simulations documented in Chapters 2 to 4 demonstrated that a comprehensive, integrated conceptual model of sulfide weathering and geochemical evolution of sulfidic waste rock developed from humidity cell experiments can be applied to field-scale experiments using a limited number of measurable parameters to scale the simulations. The reliance on a limited number of easily measurable parameters suggested that this approach could be implemented at other sites using the appropriate site-specific parameters. This mechanistic approach provides the basis for predictive geochemical characterization of waste rock.

One of the major factors facilitating the scale-up of the humidity cell experiments was the consideration of temperature variations on the geochemical evolution of the waste rock in the humidity cells. Conducting replicate sets of humidity cell experiments at two temperatures (5 °C and 22 °C) allowed for the calibration of the small-scale simulations to account for the influence of temperature on the solid-, aqueous-, and gas-phase reactions of the experiments. Calibration to

account for the influence of temperature at the laboratory scale was a critical component in the scale-up process because of the dynamic temperature regime surface-stored waste rock is exposed to and the lack of geochemical data at many field scales. Measurement of temperature at the field scale would be a critical component of any scale-up program and calibration of a reactive transport model at the laboratory scale would facilitate use of the field temperature data in a meaningful way to assess the geochemical evolution of a waste rock.

Review of the scale-up simulation results as a whole provided some observations from which conclusions regarding the performance of the initial model calibration can be made. The concentration of Cu in the Type I warm and cold temperature humidity cells and Type III warm temperature cells indicated a slight delay (Type III warm) to extended delay (Type I warm and cold) in release of peak Cu concentrations when compared to measured Cu concentrations. Review of the Type I and Type III AZL and Type III test pile simulation results indicated a similar trend where a larger than measured release of Cu occurred in 2010 and 2011 from the AZLs and in 2011 and 2012 from the test pile. This trend suggests that the mechanism for Cu attenuation may not be fully captured by the simulations. For example, at many mine sites Cu attenuation results from formation of secondary copper sulfides, covellite or chalcocite, on pyrrhotite and sphalerite surfaces. Secondary copper sulfide formation was not included in the DWRP simulations. In addition, calibration of the adsorption parameters was not conducted as part of this research for any of the sulfide derived elements. The measured concentration of Al in the Type I and Type III warm humidity cells was captured well by the humidity cell simulations but over-predicted in the Type I and Type III cold humidity cell simulations. Review of the simulated Al concentrations in the AZL simulations indicates under-prediction for the Type III experiment and over-prediction for the Type I experiment and the Al concentration is well represented by the Type III test pile simulation. The results for Al indicated that the retention mechanisms or the influence of temperature on reactions involving Al are not fully captured by the simulations. Al was associated with four different minerals (primary and secondary) making Al a difficult parameter to simulate accurately. Concentrations of SO₄ and Ni were captured very well in the Type III simulations at each scale indicating that primary sulfide oxidation processes were well represented by the models. Early time Ca concentrations were generally over-predicted in the humidity cell simulations but Ca concentrations were well represented by the simulations of the field experiments suggesting that differences in CaCO₃ dissolution between laboratory and field experiments were not fully captured by the simulations.

This use of primarily site specific Diavik Waste Rock Project data also indicated that thorough characterization of mineralogical and physical parameters was required to support mechanistic approaches to scale-up. Characterization should include measurement of the mean and range of S, C, and host mineral content, bulk mineral surface area and particle-size distribution, water flow and infiltration characteristics as well as general climatic conditions (temperature and precipitation) are also important considerations when applying reactive transport models to geochemical evolution and scale-up problems.

The results of the geostatistical characterization suggest that the spatial distribution of S, C, and K_S in the Diavik test-pile experiments can be characterized as randomly heterogeneous. The heterogeneity of these parameters can be approximated using a log normal distribution with mean and standard deviation calculated from samples collected during test pile construction. The lack of spatial dependence in matrix K_S was a significant observation because of the control that the matrix material (< 5 mm) exerted over the flow of water through the test-pile experiments. Also, the geochemical evolution of pore water was dominantly controlled by this fine-grained fraction due to the much larger surface area of matrix material when compared to the coarser fraction. This result suggests that solute loading from the pile would be somewhat dependent on matrix material distribution and the proportion of matrix to coarse material is an important parameter when assessing the geochemical evolution of a waste-rock pile.

Analysis of the influence of mineralogical (S and C content) and physical (K_S) heterogeneity on the geochemical evolution of the Diavik waste rock in the Type III test-pile experiment was facilitated by completion of 160 2-D simulations. Comparison of the mass solute flux and solute concentrations from the two cases, heterogeneous S and C with homogeneous K_S (SC_i case) and heterogeneous S, C and K_S ($SC-K_{Si}$ case), indicated that the influence of a heterogeneous K_S field on the geochemical evolution of the Type III test pile waste rock was not significant. Construction of the test pile in a single lift very likely influenced these results because internal structures typically present in waste-rock piles, such as traffic surfaces, were not present in the test-pile experiment and therefore not considered as part of this research. The $SC-K_{Si}$ simulations resulted in total flow volumes that were closer to the measured value and the variability in total flow volume compared well with daily flow variations measured in the field, indicating that the heterogeneous K_S field provided a better overall representation of the flow from the core of the test pile.

Comparison of the mass flux of solutes from the heterogeneous simulations with measured values indicated that simulated values were typically within one order of magnitude of the measured results. Analysis of the results of the two sets of simulations indicated that the distribution of solute mass fluxes from the test-pile experiment for most parameters could be best approximated with a log normal probability density function. The influence of the heterogeneous mineralogy field on the geochemical evolution of the waste rock was observed in significant variation in effluent concentrations across the simulation domains.

In the context of a mechanistic approach to scale-up, the influence of heterogeneity on mass flux was not significant when viewed as a bulk parameter (2-D heterogeneous results were not significantly different from 1-D homogeneous results); however, review of effluent concentrations indicated significant variation across a single domain. Effluent concentrations from the heterogeneous simulations (specifically the SC-K_{Si} case) exhibited variability for some parameters that was in the range of the variability for observed during the experiment suggesting that the heterogeneous simulations captured a portion of the heterogeneity within the test pile experiment. The use of heterogeneous mineralogy and hydraulic conductivity therefore best represents the conditions of the waste rock and is important for identification of worst-case scenarios and thus more appropriate, compared to the use of homogeneous mineral distribution, for assessment of the long-term geochemical evolution of waste rock.

7.3 Future Work

Future work to extend the research documented can be encompassed in three major themes.

1. The influence of temperature on the geochemical evolution of minerals.
2. The influence of heterogeneity in mineralogy and physical parameters on the effluent quality.
3. Use of the integrated conceptual model and implemented reactive transport model at different mine sites that stockpile sulfidic waste rock.

7.3.1 Temperature

The influence of temperature on geochemical reactions in the systems discussed in this thesis would be difficult to overstate. Significant effort was made in this research to integrate the influence of temperature on geochemical reactions and flow regime of the field-scale experiments (test piles and

active zone lysimeters). Future work should include calibration of the AZL and test pile simulations to further assess the influence of temperature on the primary/secondary Fe and Al mineral dependence.

7.3.2 Heterogeneity

The influence of heterogeneity in K_S on the geochemical evolution of the DWRP experiments was found to be minor, possibly reflecting the relatively homogeneity of the matrix material.

Heterogeneity is difficult to characterize in most systems and the role of heterogeneity in this system was likely influenced by the simplified flow geometry of the pile. The construction of the test-pile experiment did not reproduce some of the internal structures typically associated with waste rock pile (such as traffic surfaces). Furthermore, only the core of the test pile was investigated. Further work in this area should involve inclusion of a more realistic approach to physical heterogeneity that includes lower hydraulic conductivity of features such as traffic surfaces and higher hydraulic conductivity features such as pile batters and rubble zones.

7.3.3 Other sites

The results of the implementation of the integrated conceptual model at the three DWRP experimental scales indicated that reactive transport models can be used to scale the results of laboratory experiments to assess the geochemical evolution of waste rock at field scales. This is a promising result; however, requires the qualification that this work was conducted for a single site.

To implement this method at another site would not necessarily require the level of detail obtained as part of the DWRP; however, there are a number of essential processes that should be included in a mechanistic scale-up approach. Internal geochemical processes that should be considered when using a mechanistic approach include sulfide mineral oxidation, host mineral dissolution, secondary mineral precipitation and dissolution, adsorption, and gas transport. The primary internal physical process that requires consideration is the flow of water through the system (*i.e.*, does flow through the matrix material dominate the system or are macropore/preferential flow processes a significant contributor to the flow system). External processes include the influence of precipitation and temperature on the waste rock pile; the influence of temperature on the geochemical and physical processes both externally and internally is a major component of the mechanistic scale-up process. An excellent test

of the integrated scale-up approach would include implementation of the approach at other sites with different mineralogy and physical characteristics.

Bibliography

- American Society for Testing and Materials. Test Method for Laboratory Weathering of Solid Materials Using a Humidity Cell; ASTM International, 1996; 19 p.
- Amos, R.T., Bailey, B.L., Chi, X., Stanton, A.L., Smith, L.D.J., Blowes, D.W., Segó, D.C., Smith, L., Stasna, M., 2011. The Diavik waste rock research project: geochemistry, scale-up and gas transport. In: Symposium 2011 on Mines and the Environment. November 6-9, Rouyn-Noranda, QC.
- Amos, R.T., Blowes, D.W., Bailey, B.L., Segó, D.C., Smith, L., Ritchie, A.I.M., 2015. Waste-rock hydrogeology and geochemistry. *Appl. Geochem.* 57, 140-156.
- Amos, R.T., Blowes, D.W., Smith, L., Segó, D.C., 2009. Measurement of wind-induced pressure gradients in a waste rock pile. *Vadose Zone J.* 8, 953-962.
- Amos, R.T., Mayer, K.U., Blowes, D.W., Ptacek, C.J., 2004. Reactive transport modeling of column experiments for the remediation of acid mine drainage. *Environ. Sci. Technol.* 38, 3131-3138.
- Andrina J., Wilson, G.W., Miller, S.D., 2012. Waste rock kinetic testing program: assessment of the scale up factor for sulphate and metal release rates. In: *Proceedings of Ninth International Conference on Acid Rock Drainage*; Ottawa, Ontario, 2012.
- Andrina, J., Wilson, G.W., Miller, S., Neale, A., 2006. Performance of the acid rock drainage mitigation waste rock trial dump at Grasberg mine. In: *Proceedings of Seventh International Conference on Acid Rock Drainage*; St. Louis, Missouri, 2006.
- Anterrieu, O., Chouteau, M., Aubertin, M., 2010. Geophysical characterization of the large-scale internal structure of a waste rock pile from a hard rock mine. *Bull. Eng. Geol. Environ.* 69, 533-548.

- Ardau, C., Blowes, D.W., Ptacek, C.J., 2009. Comparison of laboratory testing protocols to field observations of the weathering of sulfide-bearing mine tailings. *J. Geochem. Explor.* 100, 182-191.
- Atherton, C., 2017. *An investigation of heterogeneity and the impact of acidic regions on bulk effluent from a deconstructed low sulfide waste-rock pile*. M.Sc. thesis, University of Waterloo, 123 p.
- Bailey, B.L., 2013. *Geochemical and microbiological characterization of effluent and pore water from low-sulfide content waste rock*. Ph.D. thesis, University of Waterloo, 399 p.
- Bailey, B.L., Blowes, D.W., Smith, L., Segó, D.C., 2015. The Diavik Waste Rock Project: geochemical and microbiological characterization of drainage from low-sulfide waste rock: active zone field experiments. *Appl. Geochem.* 62, 18-34.
- Bain, J.G., Mayer, K.U., Blowes, D.W., Frind E.O., Molson, J.W.H., Kahnt, R., Jenk, U., 2001. Modelling the closure-related geochemical evolution of groundwater at a former uranium mine. *J. Contam. Hydrol.* 52, 109-135.
- Balistrieri, L.S., Box, S.E., Tonkin J.W., 2003. Modeling precipitation and adsorption of elements during mixing of river water and porewater in the Coeur d'Alene river basin. *Environ. Sci. Technol.* 37, 4694-4701.
- Barsi, D., 2017. *Spatial variability of particles in waste rock piles*. M.Sc. thesis, University of Alberta, 195 p.
- Belzile, N., Chen, Y.W., Cai, M.F., Li, Y., 2004. A review on pyrrhotite oxidation. *J. Geochem. Explor.*, 84, 65–76.
- Blackmore, S., Smith, L., Mayer, K.U., Beckie, R.D., 2014. Comparison of unsaturated flow and solute transport through waste rock at two experimental scales using temporal moments and numerical modeling. *J. Contam. Hydrol.* 171, 49-65.

- Blowes, D.W., Logsdon, M.J., 1998. Diavik Geochemistry Baseline Report. Prepared by Sala Groundwater, Inc. and Geochimica, Inc. for Diavik Diamond Mines and submitted to Canadian Environmental Assessment Agency, 121 p.
- Blowes, D.W., Ptacek, C.J., Jambor, J.L., Weisener, C.G., 2003. The geochemistry of acid mine drainage. In: Lollar, B.S. (Ed.), *Environmental Geochemistry*, 9, Treatise on Geochemistry, Elsevier-Pergamon, pp. 149–204.
- Blum, A.E., Stillings, L.L., 1995. Feldspar dissolution kinetics. In: White, A.F. and Brantley, S.L. (Eds.), *Chemical Weathering Rates of Silicate Minerals*, Rev. Mineral., 31, 291-351.
- Borg, R.J., Dienes, G.J., 1988. *An Introduction to Solid State Diffusion*. Academic Press Inc., San Diego, 1988, pp 60-66.
- Brookfield, A.E., Blowes, D.W., Mayer, K.U., 2006. Integration of field measurements and reactive transport modelling to evaluate contaminant transport at a sulfide mine tailings impoundment. *J. Contam. Hydrol.* 88, 1-22.
- Burr, D.T., Sudicky, E.A., Naff, R.L., 1994. Nonreactive and reactive solute transport in three-dimensional heterogeneous porous media: mean displacement, plume spreading, and uncertainty. *Water Resour. Res.* 30(3), 791-815.
- Carman, P.C., 1937. Fluid flow through granular beds. *Transactions, Institution of Chemical Engineers, London.* 15, 168-188.
- Chapuis, R. P., 2004. Predicting the saturated hydraulic conductivity of sand and gravel using effective diameter and void ratio. *Can. Geotech. J.* 41, 787-795.
- Chi, Xiaotong, 2010. *Characterizing low-sulfide instrumented waste-rock piles: image grain-size analysis and wind-induced gas transport*. M.Sc. thesis, University of Waterloo, 139 p.

- Chi, X., Amos, R.T., Stastna, M., Blowes, D.W., Segó, D.C., Smith, L., 2011. The Diavik Waste Rock Project: Implications of wind-induced gas transport. *Appl. Geochem.*, 36 246-255.
- Corazao, J.C., Bay, D., Beckie, R., Klein, B., Mayer, K.U., Smith, J.L., Wilson, G.W., Brienne, S. and Letient, H., 2007. Design and construction of field-scale waste rock test piles at the Antamina Mine, Peru. *Geotechnical News*, 25(1): 49-53.
- Cressie, N., Hawkins, D., 1980. Robust estimation of the variogram. *Math. Geol.* 12(2), 115-125.
- Dagan, G., 1982. Stochastic modeling of groundwater flow by unconditional and conditional probabilities, 2, the solute transport. *Water Resour. Res.* 18(4), 835-848.
- Davis, G.B., Ritchie, A.I.M., 1986. A model of oxidation in pyritic mine wastes, part 1, equations and approximate solution. *Appl. Math. Model.* 10, 314-322.
- Demers, I., Molson, J., Bussiere, B., Laflamme, D., 2013. Numerical modeling of contaminated neutral drainage from a waste-rock field test cell. *Appl. Geochem.* 33, 346-356.
- Dowd, P.A., 1984. The variogram and kriging: robust and resistant estimators. In: *Geostatistics for Natural Resources Characterization, Part 1*, NATO ASI Series, Ser. C: 122, 91-107.
- Dzombak, D.A., Morel, F.M.M., 1990. *Surface Complexation Modelling, Hydrous Ferric Oxide*. John Wiley & Sons, 393 p.
- Elberling, B., 2005. Temperature and oxygen control on pyrite oxidation in frozen mine tailings. *Cold Reg. Sci. Technol.* 41, 121-133.
- Fala, O., Molson, J., Aubertin, M., Dawood, I., Bussiere, B., Chapuis, R.P., 2013. A numerical modelling approach to assess long-term unsaturated flow and geochemical transport in a waste rock pile. *Int. J. Min. Reclam. Env.* 27(1), 38-55.

- Gautelier, M., Oelkers, E.H., Schott, J., 1999. An experimental study of dolomite dissolution rates as a function of pH from -0.5 to 5 and temperature from 25 to 80°C. *Chem. Geol.* 157, 13-26.
- Gelhar, L.W., 1986. Stochastic subsurface hydrology from theory to applications. *Water Resour. Res.* 22(9), 135S-145S.
- Gelhar, L.W., Axness, C.L., 1983. Three-dimensional stochastic analysis of macrodispersion in aquifers. *Water Resour. Res.* 19(1), 161-180.
- Gorski, C.A., Handler, R.M., Beard, B.L., Pasakarnis, T., Johnson, C.M., Scherer, M.M., 2012. Fe atom exchange between aqueous Fe²⁺ and magnetite. *Environ. Sci. Technol.* 46, 12399-12407.
- Handler, R.M., Beard, B.L., Johnson, C.M., Scherer, M.M., 2009. Atom exchange between aqueous Fe(II) and goethite: an Fe isotope tracer study. *Environ. Sci. Technol.* 43, 1102-1107.
- Hazen, A., 1892. Some physical properties of sand and gravel: with special reference to their use in filtration. In: Massachusetts State Board of Health 24th Annual Report, Publication No. 34, pp 539-556.
- Hoaglin, D.C., Iglewicz, B., Tukey, J.W., 1986. Performance of some resistant rules for outlier labeling. *J. Am. Stat. Assoc.* 81(396), 991-999.
- Jambor, J.L., 1997. *Mineralogy of the Diavik Lac de Gras kimberlites and host rocks*. Prepared by Leslie Investment, Ltd. for Diavik Diamond Mines and submitted to the Canadian Environmental Assessment Agency, 1997, 187 p.
- Jambor, J.L., 2003. Mine-waste mineralogy and mineralogical perspectives of acid-base accounting. In: Jambor, J.L., Blowes, D.W., Ritchie, A.I.M. (Eds.), *Environmental Aspects of Mine Wastes: Mineralogical Association of Canada Short Course Series*. Economic Geology Publishing Company, pp. 117-145.

- Janzen, M.P., Nicholson, R.V., Scharer, J.M., 2000. Pyrrhotite reaction kinetics: reaction rates for oxidation by oxygen, ferric iron, and for nonoxidative dissolution, *Geochim. Cosmochim. Acta* 64(9), 1511–1522.
- Jurjovec, J., Blowes, D.W., Ptacek, C.J., Mayer, K.U., 2004. Multicomponent reactive transport modeling of acid neutralization reactions in mine tailings. *Water Resour. Res.* 40, W11202-1-17.
- Jurjovec, J., Ptacek, C.J., Blowes, D.W., 2002. Acid neutralization mechanisms and metal release in mine tailings: A laboratory column experiment. *Geochim. Cosmochim. Acta* 66(9), 1511-1523.
- Kempton, H., 2012, A review of scale factors for estimating waste rock weathering from laboratory tests. In: *Proceedings of Ninth International Conference on Acid Rock Drainage*; Ottawa, Ontario, 2012.
- Khalil, A., Hanich, L., Bannari, A., Zouhri, L., Pourret, O., Hakkou, R., 2013. Assessment of soil contamination around an abandoned mine in a semi-arid environment using geochemistry and geostatistics: Pre-work of geochemical process modeling with numerical models. *J. Geochem. Explor.* 125, 117-129.
- Krentz, A., 2014. *The hydrogeologic behaviour of waste rock piles in the Canadian arctic: snowmelt infiltration and the onset of long term freezing in test piles*. M.Sc. thesis, University of British Columbia, 282 p.
- Lahmira, B., Lefebvre, R., Aubertin, M., Bussière, B., 2017. Effect of material variability and compacted layers on transfer processes in heterogeneous waste rock piles. *J. Contam. Hydrol.* 204, 66-78.
- Langman, J.B., Blowes, D.W., Veeramani, H., Wilson, D., Smith, L., Segó, D.C., Paktunc, D., 2015. The mineral and aqueous phase evolution of sulfur and nickel with weathering of pyrrhotite in a low sulfide, granitic waste rock. *Chem. Geol.* 401, 169-179.

- Langman, J.B., Moore, M.L., Ptacek, C.J., Smith, L., Sego, D., Blowes, D.W., 2014. Diavik Waste Rock Project: evolution of mineral weathering, element release, and acid generation and neutralization during a 5-year humidity cell experiment. *Minerals* 4(2), 257–278.
- Lapakko, K.A., 2003. Developments in humidity-cell tests and their application. In: Jambor, J.L., Blowes, D.W., Ritchie, A.I.M. (Eds.), *Environmental Aspects of Mine Wastes: Mineralogical Association of Canada Short Course Series*. Economic Geology Publishing Company, pp. 147-164.
- Lapakko, K.A., White, W.W., 2000. Modification of the ASTM 5744-96 kinetic test. In: *Proceedings of Fifth International Conference on Acid Rock Drainage; Society for Mining, Metallurgy, and Exploration*: Littleton, Colorado, 2000; pp. 631-639.
- Levenspiel, O., 1972. *Chemical Reaction Engineering*, 2nd ed., John Wiley & Sons, New York, 361–371.
- Limpert, E., Stahel, W.A., Abbt, M., 2001. Log-normal distributions across the sciences: keys and clues. *BioScience* 51(5), 341-352.
- Malmström, M.E., Berglund, S., Jarsjö, J., 2008. Combined effects of spatially variable flow and mineralogy on the attenuation of acid mine drainage in groundwater. *Appl. Geochem.* 23, 1419-1436.
- Malmström, M.E., Destouni, G., Banwart, S.A., Stromberg, B.H.E., 2000. Resolving the scale-dependence of mineral weathering rates. *Environ. Sci. Technol.* 34(7), 1375-1378.
- Marescotti, P., Azzali, E., Servida, D., Carbone, C., Grieco, G., De Capitani, L., Lucchetti, G., 2010. Mineralogical and geochemical spatial analyses of a waste-rock dump at the Libiola Fe-Cu sulphide mine (Eastern Liguria, Italy). *Environ. Earth Sci.* 61, 187-199.
- Matheron, G., 1963. Principles of geostatistics. *Econ. Geol.* 58, 1246-1266.

- Mayer, K.U., 1999. *A numerical model for multicomponent reactive transport in variably saturated porous media*. Ph.D. thesis, University of Waterloo, 286 p.
- Mayer, K.U., Frind, E.O., Blowes, D.W., 2002. Multicomponent reactive transport modeling in variably saturated porous media using a generalized formulation for kinetically controlled reactions. *Water Resour. Res.* 38(9), 13-1–21.
- Mehrer, H., Dependence of diffusion on temperature and pressure. 2007. In: *Diffusion in Solids: Fundamentals, Methods, Materials, Diffusion-Controlled Processes*. Berlin; New York: Springer, pp. 127-149.
- Molson, J.W., Fala, O., Aubertin, M., Bussiere, B., 2005. Numerical simulation of pyrite oxidation and acid mine drainage in unsaturated waste rock piles. *J. Contam. Hydrol.* 78, 343-371.
- Morse, J.W., Arvidson, R.S., 2002. The dissolution kinetics of major sedimentary carbonate minerals. *Earth-Sci. Rev.* 58, 51-84.
- Nagy, K.L., 1995. Dissolution and precipitation kinetics of sheet silicates. In: White, A.F. and Brantley, S.L. (Eds.), *Chemical Weathering Rates of Silicate Minerals*, *Rev. Mineral.*, 31, 173-233.
- Neuner, M., Smith, L., Blowes, D.W., Sego, D.C., Smith, L.J.D., Fretz, N., Gupton, M., 2013. The Diavik Waste Rock Project: water flow through waste rock in a permafrost terrain. *Appl. Geochem.* 36, 222–233.
- Nichol, C., Smith, L., Beckie, R., 2005. Field-scale experiments of unsaturated flow and solute transport in a heterogeneous porous medium. *Water Resour. Res.* 41, 1-11.
- Nicholson, R.V., Scharer, J.M., 1998. *Laboratory Studies of Pyrrhotite Oxidation*, MEND Project 1.21.2.

- Nordstrom, D.K., Southam, G., 1997. Geomicrobiology of sulfide mineral oxidation. *Rev. Mineral. Geochem.* 35, 361–390.
- Parbhakar-Fox, A., Lottermoser, B.G., 2015. A critical review of acid rock drainage prediction methods and practices. *Miner. Eng.* Vol. 82, 107-124.
- Parkhurst, D.L., Appelo, C.A.J., 1999. PHREEQCi (*version 2*) – A computer program for speciation, batch reaction, one dimensional transport, and inverse geochemical calculations: U.S. Geological Survey Water-Resources Investigations.
- Pedretti, D., Mayer, K.U., Beckie, R.D., 2017. Stochastic multicomponent reactive transport analysis of low quality drainage release from waste rock piles: Controls of the spatial distribution of acid generating and neutralizing minerals. *J. Contam. Hydrol.* 201, 30-38.
- Pham, N., Segó, D.C., Arenson, L.U., Blowes, D.W., Amos, R.T., Smith, L., 2013. The Diavik Waste Rock Project: Measurement of the thermal regime of a waste-rock test pile in a permafrost environment. *Appl. Geochem.* 36 (2013) 234-245.
- Roden, E.E., 2008. Microbiological control on geochemical kinetics 1: fundamentals and case study on microbial Fe(III) oxide reduction. In: Brantley, S.L., Kubicki, J.D., White, A.F. (Eds.), *Kinetics of Water-Rock Interaction*. Springer Science+Business Media, pp. 335-415.
- Rohwerder, T., Gehrke, T., Kinzler, K., Sand, W., 2003. Bioleaching review part A: progress in bioleaching: fundamentals and mechanisms of bacterial metal sulfide oxidation. *Appl. Microbiol. Biotechnol.* 63, 239-248.
- Sapsford, D.J., Bowell, R.J., Dey, M., Williams, K.P., 2009. Humidity cell tests for the prediction of acid rock drainage. *Miner. Eng.* 22, 25-36.

- Schippers, A., Sand, W., 1999. Bacterial leaching of metal sulfides proceeds by two indirect mechanisms via thiosulfate or via polysulfides and sulfur. *Appl. Environ. Microbiol.* 65(1), 319–321.
- Schlichter, C.S., 1905. Field measurements of the rate of movement of underground waters. U.S. Geol. Surv. Water Supply Paper 140.
- Sinclair, S.A., Pham, N., Amos, R.T., Segó, D.C., Smith, L., Blowes, D.W., 2015. Influence of freeze-thaw dynamics on internal geochemical evolution of low sulfide waste rock. *Appl. Geochem.* 61, 160-174.
- Singer P.C., Stumm, W., 1970. Acidic mine drainage: the rate-determining step. *Science, New Series*, 167(3921), 1121-1123.
- Smith, L.J.D., Moncur, M.C., Neuner, M., Gupton, M., Blowes, D.W., Smith, L., Segó, D.C., 2013a. The Diavik Waste Rock Project: Design, construction, and instrumentation of field-scale experimental waste-rock piles. *Appl. Geochem.* 36, 187-199.
- Smith, L.J.D., Blowes, D.W., Jambor, J.L., Smith, L., Segó, D.C., Neuner, M., 2013b. The Diavik Waste Rock Project: particle size distribution and sulfur characteristics of low-sulfide waste rock. *Appl. Geochem.* 36, 200–209.
- Smith, L.J.D., Bailey, B.L., Blowes, D.W., Jambor, J.L., Smith, L., Segó, D.C., 2013c. The Diavik Waste Rock Project: Initial geochemical response from a low sulfide waste rock pile. *Appl. Geochem.* 36, 210–221.
- Stockwell, J., Smith, L., Jambor, J.L., Beckie, R., 2006. The relationship between fluid flow and mineral weathering in heterogeneous unsaturated porous media: a physical and geochemical characterization of a waste-rock pile. *Appl. Geochem.* 21, 1347-1361.

- Su, D., Mayer, K.U., MacQuarrie, K.T.B., 2017. Parallelization of MIN3P-THCm: A high performance computational framework for subsurface flow and reactive transport simulation. *Environ. Modell. Softw.* 95, 271-289.
- Sudicky, E.A., 1986. A natural gradient experiment on solute transport in a sand aquifer: spatial variability of hydraulic conductivity and its role in the dispersion process.
- Sudicky, E.A., Illman, W.A., Goltz, I.K., Adams, J.J., McLaren, R.G., 2010. Heterogeneity in hydraulic conductivity and its role on the macroscale transport of a solute plume: from measurements to a practical application of stochastic flow and transport theory. *Water Resour. Res.* 46, W01508.
- Terzaghi, K., 1925. *Erdbaumechanik auf bodenphysikalischer grundlage*, Deuticke, Wien.
- Turcke, M.A., Kueper, B.H., 1996. Geostatistical analysis of the Borden aquifer hydraulic conductivity field. *J. Hydrol.* 178, 223-240.
- U.S. Environmental Protection Agency, 1997. *The log normal distribution in environmental applications*. By Singh, A.K., Singh, A., Engelhardt, M. Office of Research and Development; Office of Solid Waste and Emergency Response. Technology Support Center Issue, EPA/600/S-97/006.
- Walter, A.L., Frind, E.O., Blowes, D.W., Ptacek, C.J., Molson, J.W., 1994. Modeling of multicomponent reactive transport in groundwater 1. Model development and evaluation. *Water Resour. Res.* 30(11), 3137-3148.
- Webster, R., Oliver, M.A., 2001. *Geostatistics for Environmental Scientists*, John Wiley & Sons, West Sussex, England, 271 p.

- White, A.F., Blum, A.E., Bullen, T.D., Vivit, D.V., Schulz, M., Fitzpatrick, J., 1999. The effect of temperature on experimental and natural chemical weathering rates of granitoid rocks. *Geochim. Cosmochim. Acta*, 63(19/20), 3277-3291.
- Wilson, D., Amos, R.T., Blowes, D.W., Langman, J.B., Smith, L., Segó, D.C. 2018a. The Diavik Waste Rock Project: A conceptual model for temperature and sulfide-content dependent geochemical evolution of waste rock – laboratory scale. *Appl. Geochem.* 89, 160-172.
- Wilson, D., Amos, R.T., Blowes, D.W., Langman, J.B., Smith, L., Segó, D.C., 2018b. The Diavik Waste Rock Project: Scale-up of a reactive transport model for temperature and sulfide-content dependent geochemical evolution of waste rock. *Appl. Geochem.* 96, 177-190.
- Woodbury, A.D., Sudicky, E.A., 1991. The geostatistical characteristics of the Borden aquifer. *Water Resour. Res.* 27(4), 533-546.
- Wunderly, M.D., Blowes, D.W., Frind, E.O., Ptacek, C.J., 1996. Sulfide mineral oxidation and subsequent reactive transport of oxidation products in mine tailings impoundments: a numerical model. *Water Resour. Res.* 32, 3173-3187.
- Yanina, S.V., Rosso, K.M., 2008. Linked reactivity at mineral-water interfaces through bulk crystal conduction. *Science* 320(5873), 218-222.
- Zak, J., 2017. *Hydrologic investigations of waste rock test piles in a permafrost environment*. M.Sc. thesis, University of British Columbia, 175 p.
- Zhang, D.X., Lu, Z.M., 2004. Stochastic delineation of well capture zones. *Stochastic Environmental Res.* 18, 39-46.